



Virginia Commonwealth University
VCU Scholars Compass

Theses and Dissertations

Graduate School

2018

Colloidal Synthesis and Photophysical Characterization of Group IV Alloy and Group IV-V Semiconductors: Ge_{1-x}Sn_x and Sn-P Quantum Dots

Venkatesham Tallapally
Virginia Commonwealth University

Follow this and additional works at: <https://scholarscompass.vcu.edu/etd>

 Part of the [Inorganic Chemistry Commons](#), and the [Materials Chemistry Commons](#)

© The Author

Downloaded from

<https://scholarscompass.vcu.edu/etd/5568>

This Dissertation is brought to you for free and open access by the Graduate School at VCU Scholars Compass. It has been accepted for inclusion in Theses and Dissertations by an authorized administrator of VCU Scholars Compass. For more information, please contact libcompass@vcu.edu.

Colloidal Synthesis and Photophysical
Characterization of Group IV Alloy and Group
IV-V Semiconductors:
 $\text{Ge}_{1-x}\text{Sn}_x$ and Sn-P Quantum Dots.

A dissertation submitted in partial fulfillment of the requirements for the
degree of Doctor of Philosophy at Virginia Commonwealth University.

by

Venkatesham Tallapally

Advisor: Indika U. Arachchige

Associate Professor, Department of Chemistry

Virginia Commonwealth University

Richmond Virginia, 23284-2006

United States



VCU

VIRGINIA COMMONWEALTH UNIVERSITY

Copyright © 2018 by Venkatesham Tallapally

All rights reserved

Acknowledgements

I would like to express my deep appreciation and gratitude to several people for the contributions and support given to me during the period I have been working for this thesis. I am grateful to my parents, though they are not educated, they believed that education is the main asset to move forward in society. More importantly, they figured the spark and interest in me towards education and gave me complete freedom to pursue it. I am thankful to my brothers Raju, and Kishan and sister Renuka and for their unconditional support. A special thanks to Mamatha, I am grateful to have her as my supportive and understanding better half.

I would like to express my profound sense of gratitude to my doctoral supervisor Dr. Arachchige, Associate professor, Department of Chemistry, Virginia Commonwealth University for his unwavering guidance, constructive criticism, and strong motivation. It is an honor to work under such a helpful, knowledgeable, and enthusiastic professor. I truly appreciate the feedback giver for each and every research aspect allowed me to complete this highest degree. The most important things I have learnt from Dr. Arachchige are, organize the work and prioritize them according to their importance. As a doctoral student one should possess a unique way of problem solving skills, Dr. Arachchige influenced me with his systematic approach towards a challenge.

Graduate studies and research are always challenging and sometimes stressful, a friendly atmosphere is so important, I am lucky to have such a wonderful lab mates. I am especially grateful to Dr. Richard Esteves, Dr. Lamia Nahar, Dr. Xiaonan Gao, and Minh Ho, who helped me at beginning of my graduate research in lab. Especially, Dr. Richard

Esteves advise was very precise yet so much informative which helped me throughout my journey in lab. Dr. Lamia Nahar treated me like her brother by not only helping with initial research but also made me to feel comfortable in lab. Later in my doctoral degree, I have had chance to interact with new good lab mates, Ebthesam, Dilhara, and Chris. I wish great luck to the two newest members of the lab Ashish Nag and Rachel, who will be following up on my work with $\text{Ge}_{1-x}\text{Sn}_x$ and hope they can take it to new dimensions.

I can't simply thank my best and childhood friends, B. N Goud, K. Venkatesh, Sarpanch Raju, T. Raju and Shivarathri for their continuous support and sharing happy or sad moments. I owe a special thanks to my school teachers, Lingareddy and Durgesham for continuous motivation. I would like to thank my MSc classmates, B. Srikanth, B. Devender, and G. Bhasker who are there for me anytime. I thank my Hyderabad roommates, M. Balakrishna, M. Abhilash, Ch. Venkat, D. Venkat, and Kuma for sharing the best moments with me. A special thanks to one of my best friend Damma Devender, for his invaluable personal and professional support, especially in tough times.

Finally, I would like to thank my friends in US, Vamshi, Srikanth, Krishna, Kavitha Reddy, and Maruthi and friends in Richmond, Aravind, Badri, Deepak, Rahul, and Veeren and my buddy friends Ravi, Sunil, Ganesh and Vineeth for their support throughout my graduate studies.

TABLE OF CONTENTS

LIST OF FIGURES	viii-xii
LIST OF TABLES	xii
LIST OF SCHEMES	xii
ABSTRACT	xiii-xvi
CHAPTER 1. Introduction.....	1-28
1.1 Semiconductors	
1.2 Group IV Semiconductor alloys	
1.3 Quantum confinement	
1.4 Synthesis of Ge _{1-x} Sn _x alloys	
1.5 Colloidal Synthesis	
1.6 Synthesis of Ge _{1-x} Sn _x Alloy Nanocrystals	
1.7 Metal Phosphides	
1.8 Group IV-V Semiconductors	
1.9 Tin Phosphides	
1.10 Synthesis of Tin Phosphides	
1.11 Thesis Statement	
CHAPTER 2. Characterization Techniques.....	29-50
2.1 Powder X-Ray Diffraction (XRD)	
2.2 Transmission Electron Microscopy (TEM)	
2.3 Energy Dispersive Spectroscopy (EDS)	
2.4 X-Ray Photoelectron Spectroscopy (XPS)	
2.5 Raman Spectroscopy	

2.6	UV-Visible absorption spectroscopy (Uv-Vis)	
2.7	Diffuse Reflectance Spectroscopy (DRA)	
2.8	Photoluminescence Spectroscopy (PL)	
2.9.	Fourier Transform Infrared (FT-IR) Absorption Spectroscopy	
2.10.	Time-Resolved Photoluminescence (TRPL)	
CHAPTER 3.	Ge _{1-x} Sn _x Alloy Quantum Dots with Composition-Tunable Energy Gaps and Near-Infrared Photoluminescence.....	51-82
3.1	Introduction	
3.2	Experimental Section	
3.3	Results and Discussion	
3.4	Conclusion	
CHAPTER 4.	Photophysical Properties of Ultra-Small Ge _{1-x} Sn _x Alloy Quantum Dots	83-94
4.1	Introduction	
4.2	Experimental Section	
4.3	Results and Discussion	
4.4	Conclusion	
CHAPTER 5.	Multivariate Synthesis of Tin Phosphide Nanoparticles: Temperature, Time, and Ligand Control of Size, Shape, and Crystal Structure.....	95-138
5.1	Introduction	
5.2	Experimental Section	
5.3	Results and Discussion	
5.4	Conclusion	
CHAPTER 6.	Conclusions and Prospectus.....	139-144

REFERENCES	145-162
VITA	163-167

List of Figures

Figure 1.1. A schematic demonstration of the energy gap difference between conductors, semiconductors and insulators.....	3
Figure 1.2. Direct and Indirect bandgap structures illustrating the differences in momentum space (k) of the lowest point in the conduction band and highest point of the valence band.....	5
Figure 1.3. A schematic of Sn alloying on the band structure of Ge.....	8
Figure 1.4. Continuous energy bands in bulk and discrete energy levels in semiconductor nanoparticles.....	10
Figure 1.5. Key steps in the fabrication of $Ge_{1-x}Sn_x$ thin films using non-selective and selective etching process.....	12
Figure 1.6. Schematic of La-Mer nucleation model for mechanism of formation of uniform particles in solution.....	14
Figure 1.7. Overview of utilization of the main phosphorus (P) sources for the synthesis of metal phosphide nanoparticles.....	19
Figure 1.8. A schematic diagram of solvothermal synthesis setup.....	22
Figure 1.9. A Schematic view of motion of the ball and powder mixture.....	24
Figure 2.1. Diagram of a standard vacuum X-ray tube.....	30
Figure 2.2. Electronic shell diagram of electronic transitions for X-ray production.....	32
Figure 2.3. Diffraction of X-rays by parallel crystal planes.....	33
Figure 2.4. Schematic illustration of X-ray diffraction instrument.....	34

Figure 2.5.	A simplified scheme of all possible interactions of an electron beam with a target substrate.....	36
Figure 2.6.	Diagram of X-ray photoelectron spectrometer with a hemispherical detector.....	39
Figure 2.7.	Block diagram of Raman spectrometer.....	41
Figure 2.8.	A schematic of lighter atom replaced by heavier atom results in increase in bond length, subsequently Raman vibrational frequency decreases...	41
Figure 2.9.	Schematic of a multi-source double beam UV-Vis spectrometer.....	42
Figure 2.10.	A schematic illustration of absorption followed by fluorescence and phosphorescence processes under the effect of light energy.....	46
Figure 2.11.	A typical FT-IR set-up utilizing a Nernst Glower source, a Michelson interferometer and a pyroelectric detector.....	48
Figure 2.12.	Schematic diagram of the experimental setup of a fluorescence lifetime imaging microscope time-resolved photoluminescence.....	50
Figure 3.1.	PXRD patterns of $\text{Ge}_{1-x}\text{Sn}_x$ alloy QDs with varying Sn composition.....	58
Figure 3.2.	Raman spectra of $\text{Ge}_{1-x}\text{Sn}_x$ alloy QDs with varying Sn compositions.....	59
Figure 3.3.	Representative low-resolution TEM images of $\text{Ge}_{1-x}\text{Sn}_x$ alloy QDs with varying Sn composition.....	61
Figure 3.4.	Size histograms of $\text{Ge}_{1-x}\text{Sn}_x$ alloy QDs with varying Sn composition.....	62
Figure 3.5.	Representative TEM images of $\text{Ge}_{1-x}\text{Sn}_x$ alloy QDs with varying Sn composition.....	63
Figure 3.6.	Representative low-resolution TEM images of $\text{Ge}_{1-x}\text{Sn}_x$ alloy QDs with varying Sn composition.....	64
Figure 3.7.	High resolution TEM images of $\text{Ge}_{1-x}\text{Sn}_x$ alloy QDs.....	65

Figure 3.8.	Dark filed TEM image of $\text{Ge}_{0.888}\text{Sn}_{0.112}$ alloy QDs along with STEM-EDS elemental maps of Ge, Sn, and an overlay of Ge and Sn.....	66
Figure 3.9.	Dark field TEM image of ~ 15 nm $\text{Ge}_{0.919}\text{Sn}_{0.091}$ alloy QD along with STEM/EDS elemental maps of Ge, Sn, and an overlay of Ge and Sn.....	67
Figure 3.10.	Representative Ge ($3d_{5/2}$) and Sn ($3d_{5/2}$) XPS spectra of $\text{Ge}_{0.888}\text{Sn}_{0.112}$ alloy QDs.....	69
Figure 3.11.	X-ray photoelectron spectra (survey scan) of $\text{Ge}_{0.888}\text{Sn}_{0.112}$ alloy QDs....	70
Figure 3.12.	Representative SEM-EDS spectrum of $\text{Ge}_{0.909}\text{Sn}_{0.091}$ alloy QDs.....	70
Figure 3.13.	FT-IR spectra of $\text{Ge}_{1-x}\text{Sn}_x$ alloy QDs synthesized HDA/ODE.....	71
Figure 3.14.	Representative X-ray photoelectron spectra of $\text{Ge}_{0.909}\text{Sn}_{0.091}$ alloy QDs..	72
Figure 3.15.	Solid state diffuse reflectance spectra of $\text{Ge}_{1-x}\text{Sn}_x$ alloy QDs with varying Sn composition.....	74
Figure 3.16.	Solution absorption spectra (Tauc-indirect) of $\text{Ge}_{1-x}\text{Sn}_x$ alloy QDs as a function of Sn composition.....	75
Figure 3.17.	Room-temperature solid-state photoluminescence spectra of $\text{Ge}_{1-x}\text{Sn}_x$ alloy QDs with varying Sn compositions.....	78
Figure 3.18.	Experimental energy gaps of $\text{Ge}_{1-x}\text{Sn}_x$ alloy QDs as a function of Sn composition.....	79
Figure 3.19.	PL transients at 295 K and 15 K for $\text{Ge}_{1-x}\text{Sn}_x$ alloy QDs with varying Sn compositions.....	80
Figure 4.1.	PXRD patterns of tetragonal-Sn and cubic Ge along with $\text{Ge}_{1-x}\text{Sn}_x$ QDs with varying Sn composition.....	87
Figure 4.2.	Average lattice constant of the 1.4, 2.1 and 2.7 nm diameter $\text{Ge}_{1-x}\text{Sn}_x$ QDs calculated using the LDA relaxed atomic structures compared with experimental measurements of $\text{Ge}_{1-x}\text{Sn}_x$ QDs.....	88

Figure 4.3.	A representative Low Resolution TEM images of Ultra-Small $\text{Ge}_{1-x}\text{Sn}_x$ QDs with varying Sn composition.....	89
Figure 4.4.	Solid-state Absorption Spectra of Ultra-Small $\text{Ge}_{1-x}\text{Sn}_x$ QDs with varying Sn composition.....	90
Figure 4.5.	Solid-state Photoluminescence Spectra of Ultra-Small $\text{Ge}_{1-x}\text{Sn}_x$ QDs with varying Sn composition	91
Figure 4.6.	Room Temperature Time Resolved PL Spectra of Ultra-Small $\text{Ge}_{1-x}\text{Sn}_x$ QDs with varying Sn composition.....	92
Figure 5.1.	Powder XRD pattern of the product obtained from the reaction of SnCl_2 and TOP at 350 °C for 3 h.....	101
Figure 5.2.	Powder XRD pattern of the product obtained from the reaction of SnCl_2 and $(\text{TMSi})_3\text{P}$ at 180 °C for 3 min.....	102
Figure 5.3.	Powder XRD pattern of the product obtained from the reaction of SnCl_2 and $(\text{TMSi})_3\text{P}$ with DDT at 180 °C for 12 h.....	103
Figure 5.5.	A representative powder XRD pattern of amorphous to partially crystalline Sn_4P_3 NPs produced at 180 °C for 5 min.....	103
Figure 5.6.	TEM images of amorphous to partially crystalline Sn_4P_3 NPs synthesized at 180 °C without TBP.....	104
Figure 5.7.	Powder XRD pattern of the product obtained from the reaction of SnI_4 and $(\text{TMSi})_3\text{P}$ at 180 °C for 3 min in the presence of 12 mM TBP.....	108
Figure 5.8.	Powder XRD pattern of the product obtained from the reaction of SnI_4 and $(\text{TMSi})_3\text{P}$ at 180 °C for 3 min in the presence of 4 mM of TOP.....	109
Figure 5.9.	Powder XRD pattern of (a) the product obtained from the reaction of SnI_4 and $(\text{TMSi})_3\text{P}$ at 220 °C for 15 min.....	110
Figure 5.10.	PXRD patterns of hexagonal SnP NCs produced at 250 °C.....	112

Figure 5.11. TEM images of the hexagonal SnP NCs produced at 250 °C.....	113
Figure 5.12. Representative TEM images of the phase pure hexagonal SnP NCs synthesized at 250 °C.....	114
Figure 5.13. Low resolution and high resolution TEM images of the hexagonal SnP NCs prepared at 250 °C.....	115
Figure 5.14. A representative SEM/EDS spectrum of the hexagonal SnP NCs synthesized at 250 °C without the use of TBP for 60 seconds.....	116
Figure 5.15. TEM images of the trigonal Sn ₃ P ₄ NPs grown at 100 °C in the presence of 4 mM TBP.....	117
Figure 5.16. HRTEM images of trigonal Sn ₃ P ₄ NPs synthesized at 100 °C for 3 min using SnI ₄ and (TMSi) ₃ P in the presence of TBP.....	118
Figure 5.17. Representative SEM/EDS spectrum of trigonal Sn ₃ P ₄ NPs synthesized at 100 °C with 4 mM TBP for 60 sec.....	121
Figure 5.18. Solid state diffuse reflectance spectra of smaller, trigonal Sn ₃ P ₄ NPs...	122
Figure 5.19. Diffuse reflectance spectra (converted to absorption using Kubelka-Munk remission function) of trigonal Sn ₃ P ₄ NPs.....	123
Figure 5.20. Representiavtive TEM images of trigonal Sn ₃ P ₄ NPs.....	124
Figure 5.21. Representative SEM/EDS spectrum of trigonal Sn ₃ P ₄ NPs.....	125
Figure 5.22. FT-IR spectra of rhombohedral Sn ₄ P ₃ NCs, hexagonal SnP NCs, and trigonal Sn ₃ P ₄ NPs.....	126
Figure 5.23. XPS of Sn(3d _{5/2}) and P(2p) regions of rhombohedral Sn ₄ P ₃ NCs, hexagonal SnP NCs, and trigonal Sn ₃ P ₄ NPs.....	127
Figure 5.24. X-ray photoelectron spectrum (survey scan) of rhombohedral Sn ₄ P ₃ NCs produced at 180 °C for 3 min.....	128

Figure 5.25. X-ray photoelectron spectrum (survey scan) of hexagonal SnP NCs produced at 250 °C for 5 seconds.....	129
Figure 5.26. X-ray photoelectron spectrum (survey scan) of trigonal Sn ₃ P ₄ NPs produced at 100 °C for 3 min.....	130
Figure 5.27. X-ray photoelectron spectra of rhombohedral Sn ₄ P ₃ NCs, hexagonal SnP NCs, and trigonal Sn ₃ P ₄ NPs.....	134
Figure 5.28. PXRD patterns of trigonal Sn ₃ P ₄ NPs synthesized with TBP at 100 °C for 3 min along with trigonal Sn ₃ P ₄ NPs annealed at different temperatures.....	136

List of Tables

Table 1.1.	List of widely used semiconductors and their applications.....	6
Table 1.2.	List of metal phosphides and their associated properties.....	18
Table 1.3.	Energy gaps of single layer Group IV-V (IV = Si,Ge, and Sn; V = N and P) materials.....	20
Table 3.1.	The molar ratio of GeI_2 , SnCl_2 , and n-BuLi used in the synthesis $\text{Ge}_{1-x}\text{Sn}_x$ alloy QDs.....	21
Table 3.2.	Comparison of the elemental composition, crystallite and primary particle size, and room temperature solid-state absorption onsets and photoluminescence peak maxima for $\text{Ge}_{1-x}\text{Sn}_x$ Alloy QDs.....	55
Table 3.3.	Time constants extracted from biexponential decay Fit to PL transients of near IR emitting $\text{Ge}_{1-x}\text{Sn}_x$ Alloy QDs.....	76
Table 4.1.	Time constants extracted from biexponential decay Fit to PL transients of Ultra-Small $\text{Ge}_{1-x}\text{Sn}_x$ Alloy QDs.....	92
Table 5.1.	Primary particle size, core crystal size, thickness of the amorphous shell, and crystallite size of hexagonal SnP NCs produced at 250 °C for different growth times.....	118

List of Schemes

Scheme 3.1.	An Illustration of the synthesis of near infrared emitting $\text{Ge}_{1-x}\text{Sn}_x$ alloy QDs.....	56
Scheme 4.1.	An Illustration of the Synthesis of Ultra-Small $\text{Ge}_{1-x}\text{Sn}_x$ alloy QDs.....	86
Scheme 5.1.	Reaction protocols for the synthesis of size, shape, and phase controlled rhombohedral Sn_4P_3 , hexagonal SnP, and trigonal Sn_3P_4 NPs.....	104

ABSTRACT

Colloidal Synthesis and Photophysical Characterization of Group IV Alloy and Group IV-V Semiconductors: Ge_{1-x}Sn_x and Sn-P Quantum Dots.

by

Venkatesham Tallapally

A dissertation submitted in partial fulfillment of the requirements for the degree of Doctor of Philosophy at Virginia Commonwealth University.

Advisor: Indika U. Arachchige

Associate Professor, Department of Chemistry

Nanomaterials, typically less than 100 nm size in any direction have gained noteworthy interest from scientific community owing to their significantly different and often improved physical properties compared to their bulk counterparts. Semiconductor nanoparticles (NPs) are of great interest to study their tunable optical properties, primarily as a function of size and shape. Accordingly, there has been a lot of attention paid to synthesize discrete semiconducting nanoparticles, of where Group III-V and II-VI materials have been studied extensively. In contrast, Group IV and Group IV-V based nanocrystals as earth abundant and less-non-toxic semiconductors have not been studied thoroughly. From the class of Group IV, Ge_{1-x}Sn_x alloys are prime candidates for

the fabrication of Si-compatible applications in the field of electronic and photonic devices, transistors, and charge storage devices. In addition, $\text{Ge}_{1-x}\text{Sn}_x$ alloys are potentials candidates for bio-sensing applications as alternative to toxic materials. Tin phosphides, a class of Group IV-V materials with their promising applications in thermoelectric, photocatalytic, and charge storage devices. However, both aforementioned semiconductors have not been studied thoroughly for their full potential in visible (Vis) to near infrared (NIR) optoelectronic applications. In this dissertation research, we have successfully developed unique synthetic strategies to produce $\text{Ge}_{1-x}\text{Sn}_x$ alloy quantum dots (QDs) and tin phosphide (Sn_3P_4 , SnP , and Sn_4P_3) nanoparticles with tunable physical properties and crystal structures for potential applications in IR technologies.

Low-cost, less-non-toxic, and abundantly-produced $\text{Ge}_{1-x}\text{Sn}_x$ alloys are an interesting class of narrow energy-gap semiconductors that received noteworthy interest in optical technologies. Admixing of α -Sn into Ge results in an indirect-to-direct bandgap crossover significantly improving light absorption and emission relative to indirect-gap Ge. However, the narrow energy-gaps reported for bulk $\text{Ge}_{1-x}\text{Sn}_x$ alloys have become a major impediment for their widespread application in optoelectronics. Herein, we report the first colloidal synthesis of $\text{Ge}_{1-x}\text{Sn}_x$ alloy quantum dots (QDs) with narrow size dispersity ($3.3\pm 0.5 - 5.9\pm 0.8$ nm), wide range of Sn compositions (0–20.6%), and composition-tunable energy-gaps and near infrared (IR) photoluminescence (PL). The structural analysis of alloy QDs indicates linear expansion of cubic Ge lattice with increasing Sn, suggesting the formation of strain-free nanoalloys. The successful incorporation of α -Sn into crystalline Ge has been confirmed by electron microscopy, which suggests the homogeneous solid solution behavior of QDs. The quantum confinement effects have

resulted in energy gaps that are significantly blue-shifted from bulk Ge for $\text{Ge}_{1-x}\text{Sn}_x$ alloy QDs with composition-tunable absorption onsets (1.72–0.84 eV for $x=1.5\text{--}20.6\%$) and PL peaks (1.62–1.31 eV for $x=1.5\text{--}5.6\%$). Time-resolved PL (TRPL) spectroscopy revealed microsecond and nanosecond timescale decays at 15 K and 295 K, respectively owing to radiative recombination of dark and bright excitons as well as the interplay of surface traps and core electronic states. Realization of low-to-non-toxic and silicon-compatible $\text{Ge}_{1-x}\text{Sn}_x$ QDs with composition-tunable near IR PL allows the unprecedented expansion of direct-gap Group IV semiconductors to a wide range of biomedical and advanced technological studies.

Tin phosphides are a class of materials that received noteworthy interest in photocatalysis, charge storage and thermoelectric devices. Dual stable oxidation states of tin (Sn^{2+} and Sn^{4+}) enable tin phosphides to exhibit different stoichiometries and crystal phases. However, the synthesis of such nanostructures with control over morphology and crystal structure has proven a challenging task. Herein, we report the first colloidal synthesis of size, shape, and phase controlled, narrowly disperse rhombohedral Sn_4P_3 , hexagonal SnP, and amorphous tin phosphide nanoparticles (NPs) displaying tunable morphologies and size dependent physical properties. The control over NP morphology and crystal phase was achieved by tuning the nucleation/growth temperature, molar ratio of Sn/P, and incorporation of additional coordinating solvents (alkylphosphines). The absorption spectra of smaller NPs exhibit size-dependent blue shifts in energy gaps (0.88–1.38 eV) compared to the theoretical value of bulk Sn_3P_4 (0.83 eV), consistent with quantum confinement effects. The amorphous NPs adopt rhombohedral Sn_4P_3 and hexagonal SnP crystal structures at 180 and 250 °C, respectively. Structural and surface

analysis indicates consistent bond energies for phosphorus across different crystal phases, whereas the rhombohedral Sn_4P_3 NPs demonstrate Sn oxidation states distinctive from those of the hexagonal and amorphous NPs owing to complex chemical structure. All phases exhibit $\text{N}(1s)$ and $\nu_{(\text{N-H})}$ energies suggestive of alkylamine surface functionalization and are devoid of tetragonal Sn impurities.

CHAPTER 1

INTRODUCTION

Materials with at least one of their dimensions are in the range 1-100 nm are generally referred to as nanomaterials and their physical properties are in between bulk solids and atomic/molecular systems.^{1,2} Nanoparticles are of greatest interest because their properties are entirely different or sometimes superior to their bulk counterparts as they differ in size and morphology.³ The unique behavior of nanoparticles allowing the existence of a new and multidisciplinary science, nanoscience and nanotechnology.^{1,3} The research efforts related to nanomaterials for their potential applications have seen a tremendous growth in the last three decades.¹ The art of making nanoparticles has been known dated back to 4th century.^{2,4} A first synthesis of ruby colored gold nanoparticles in laboratory was known in 1857 by Michael Faraday.² Developing a unique synthetic methodology for nanoparticles is a key step uncover their size and shape dependent properties.

The research efforts on nanomaterials have risen exponentially in recent years owing to their promising physical properties and potential applications in advanced technologies.^{3,4} For instance, the unique physical and chemical properties of semiconductor nanoparticles (NPs) resulted in quantization of energy levels and tunable absorption and emission properties.⁵ The surface atoms have fewer coordinate atoms adjacent to them and unsaturated sites or more dangling bonds compared to the bulk atoms.^{1,6} Reduction in size to nanoscale regimes increases the ratio of atoms present on the surface of NPs. As a consequence, the surface atoms have direct influence on the

electronic structure and physical properties of NPs. Moreover, increase in the surface area enhances the catalytic activity due to exposure of a number of active sites present on the surface of the NP.^{1,7} The modification of physical parameters such as size, shape, and surface characteristics have been shown to effectively tune the physical properties for their applications.⁷

1.1 Semiconductors

Semiconductors are a class of materials that displays an intermediate conductivity between conductors and insulators (Figure 1.1).¹ Semiconductors have a small to moderate gap between their valance band (VB) and conduction band (CB), typically between 0.3 – 4.0 eV. Typically, a semiconductor is composed of an extended network of ordered atoms that form a number of molecular orbitals with similar energy, resulting in the formation of a continuous band.^{1 5}The bandgap/energy gap (E_g) in a semiconductor can be understood similar to the molecular orbital theory for individual molecule, thus E_g can be defined as the minimum energy required to excite an electron from highest occupied molecular orbitals (HOMO) to lowest unoccupied molecular orbitals (LUMO). In bulk, the number of discrete HOMO levels become the valance band and the LUMO levels become the conduction band. A material's electronic and optical properties are then classified by the gap between the band levels (Figure 1.1).^{1,4}

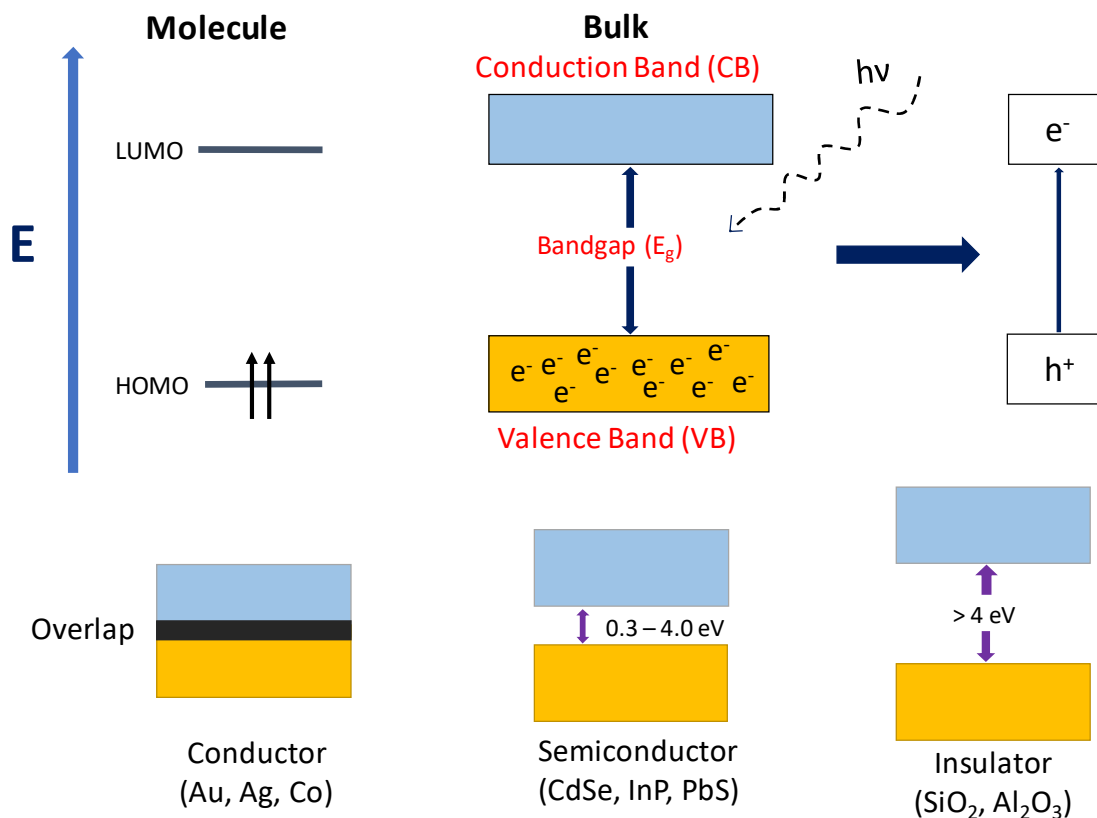


Figure 1.1. A schematic demonstration of the energy gap difference between conductors, semiconductors and insulators, E = Energy, HOMO = Highest occupied molecular orbital, and LUMO = Lowest unoccupied molecular orbital.

In conductors (metals), electrons in the valence band can flow easily through the conduction band as the bands overlap, resulting in zero bandgap. In semiconductors, upon excitation, an electron jumps from valence band to conduction band and the gap between both bands defined as energy gap.⁴ The excitation of electron can be achieved through an applied current or photon absorption. It is difficult for larger bandgap energy electrons to excite from VB to CB, resulting in lower probability for those electrons to conduct. Depending on energy gap, a material's optical and electronic properties are classified.⁸ In insulators, VB and CB are separated by high energy (>4.0 eV), neither

photon nor applied thermal energy can excite the electron. However, each above discussed material types serves the purpose depending on the electronic device.⁴

The incident photon energy must be higher than the energy gap of the material to excite the electron across the bands. As a result of the excitation, an electron jumps from the valance band to the conduction band leaving a positively charged hole behind.¹ This electron-hole pair becomes the charge carrier when it is incorporated into a circuit as it extracts the electron. An exciton is formed when the electron-hole pair are not separated. The exciton is also termed as electrostatic bound state of electron-hole pair. Exciton plays a major role in developing a semiconducting device such as LEDs and solar cell. In nanoscience, excitons also referred to as Bohr radius (a_B).^{1,4} Bohr radius is the natural physical distance of an electron and hole within the crystal. Each semiconductor has a specific distance depending on its properties as can be characterized by equation 1.1, where ϵ is the dielectric coefficient, e is the elementary charge m_e^* is the mass of electron and m_h^* is the mass of hole.⁵ Depending on the above-mentioned material properties, Bohr radius ranges from 1-150 nm. Bohr radius must be taken into consideration in developing a semiconductor device.

$$a_B = \frac{h^2 \epsilon}{e^2} \left[\frac{1}{m_e^*} + \frac{1}{m_h^*} \right] \quad (1.1)$$

There are two types of bandgap semiconductors, direct bandgaps and indirect bandgaps depending on photo excitation requirements (Figure 1.2).^{1,7,9} In direct bandgap semiconductors, the highest point of the valence band is in the same momentum plane as the lowest point of the conduction band. The excitation phenomenon is very simple in

direct bandgaps, so the electrons can easily be excited across the gap by any photon with sufficient energy. For this reason, the direct bandgap semiconductors readily absorb incident light, and reemit depending on appropriate conditions.^{1,9-11}

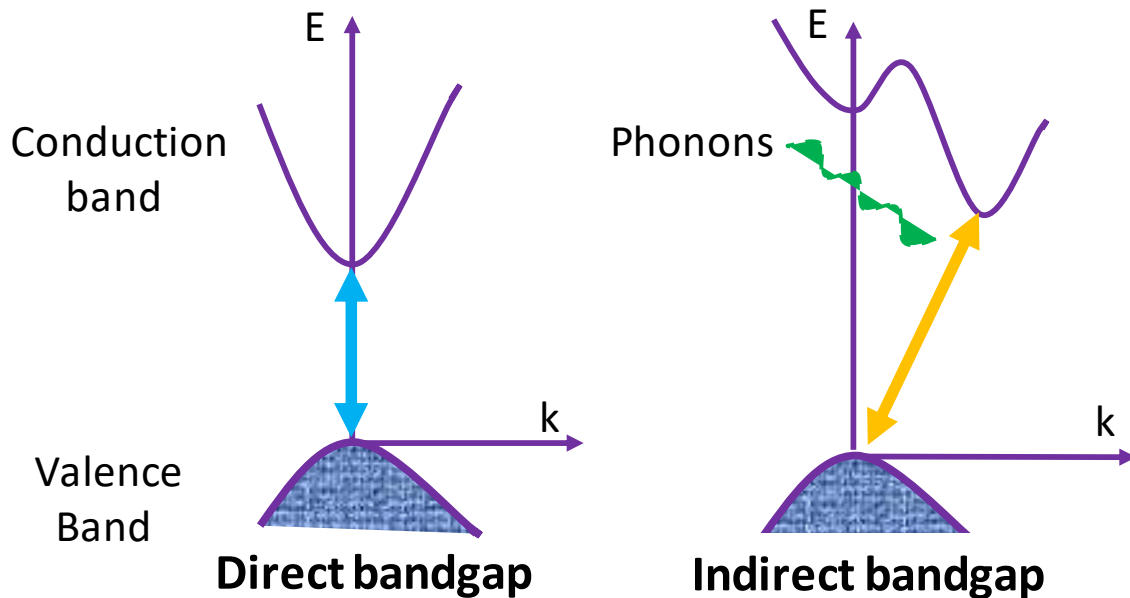


Figure 1.2. Direct and Indirect bandgap structures illustrating the differences in momentum space (k) of the lowest point in the conduction band and highest point of the valence band, E = Energy and k = Crystal momentum.

Unlike the direct bandgaps, in indirect bandgap, the highest point of valence band and lowest point of conduction band are not in same momentum plane. In order to excite an electron from valence band to conduction band, the electron needs to change its momentum.¹¹ As the photons does not carry momentum, a phonon interaction is required. The lattice vibrations in crystal are the phonons and they occur in relatively small quantities when compared to photons. In indirect bandgaps, it requires a phonon in addition to incident photon leaves the low probability of exciting an electron across the

bands. The same applies to relax the excited electron from conduction band to valence band. Both types, direct and indirect bandgap semiconductors can be found in Table 1.1.

Table 1.1 List of Widely Used Semiconductors and their Applications^{1,4,11-17}

Group	Compound	Type	Bandgap (eV)	Structure	Applications
IV	Si	indirect	1.12	Diamond cubic	Photovoltaics, Integrated circuits
IV	Ge	indirect	0.67	Diamond cubic	Power electronics
III-V	GaN	direct	3.44	Zinc blend	LEDs
III-V	GaAs	direct	1.43	Zinc blend	Integrated circuits
III-V	InP	direct	1.35	Zinc blend	Transistors
II-VI	CdSe	direct	1.74	Wurtzite	Photovoltaics
II-VI	CdS	direct	2.42	Wurtzite	Photovoltaics
II-VI	ZnO	direct	3.37	Wurtzite	Photocatalytic
II-VI	ZnS	direct	3.91	Wurtzite	Photocatalytic
IV-VI	PbS	direct	0.37	NaCl	Infrared sensors
IV-VI	PbTe	direct	0.32	NaCl	Infrared sensors
IV-VI	SnS	direct	1.30	Wurtzite	Photocatalytic
II-V	Zn ₃ P ₂	direct	1.50	Tetragonal	Photovoltaic
Oxide	TiO ₂	direct	3.02	Rutile	Photocatalytic
Oxide	Cu ₂ O	direct	2.17	Cubic	Rectifier diodes
IV-V	Sn ₃ P ₄	indirect	0.83	Trigonal	Thermoelectric

1.2 Group IV Semiconductor Alloys

Group IV semiconductors (Si and Ge) are nontoxic class of materials with their potential applications in solar photoconversion and related optoelectronic technologies such as photodetectors, LEDs, and biological imaging.^{3,7,18,19} Si and Ge technologies are highly compatible with each other. Both (Si and Ge) have indirect bandgaps, which limiting their efficiency. However, it is possible to induce a transition from indirect to direct bandgap by expanding crystal structures.^{9,10} As a consequence of the crystal expansion, the interatomic spacing increases which results in alteration of orbital overlaps and density of states.¹⁰ The lattice expansion can be achieved using epitaxy, but it is expensive. Alternative approach is alloying with larger atoms into the crystal which cause in expanding the lattice. To serve this purpose, tin is in the same group, has similar chemistry to both elements with cubic structure, also an earth abundant and non-toxic.^{9,11}

1.2.1 Ge_{1-x}Sn_x Alloys

Elemental tin incorporation into Ge or Si to form an alloy is a topic that has been studied for decades.²⁰ Especially over the last decade, a significant development has been made. Theoretical studies on Ge have shown that a direct gap can be induced with the incorporation of 6.3-11% tin.^{11,21-24} The large discrepancies (~14-19%) in lattice constants and much higher cohesion energies of Si and Ge compared to that of α -Sn makes them difficult to achieve homogeneous alloys.^{25,26} In addition to this, the admixture of α -Sn ($E_g = 0.08$ eV) significantly reduces the energy gaps of Ge_{1-x}Sn_x alloys (0.35–0.80 eV for $x = 15.0$ – 0.00 %).^{21,27}

1.2.2 Indirect to Direct Bandgap Transition in $\text{Ge}_{1-x}\text{Sn}_x$ Alloys

Photoluminescence plays an important role in determining the transition of indirect bandgap to direct.¹⁰ As seen in Figure 1.2 and above discussion, the process of excitation and relaxation in a direct gap is more efficient, which results in a significant increase of quantum yield should.^{10,20} The high quantum yields indicate the direct bandgap induction.¹¹ Experiments have shown this effect in high quality $\text{Ge}_{1-x}\text{Sn}_x$ alloy films.^{11,23} Number of studies have explored the transition via strain, excitation density, temperature, and doping.^{23,28,29} Tin incorporation brings the direct gap to lower energy making it the favorable transition. Numerous studies have shown that after reaching the critical point of tin concentration, significant increase in photoluminescence occurred for compressively strained $\text{Ge}_{1-x}\text{Sn}_x$ alloy films.³⁰ As can be seen in Figure 1.3, a direct correlation between strained $\text{Ge}_{1-x}\text{Sn}_x$ alloys remains an indirect band gap and transitioned to direct band gap upon relaxation.²¹

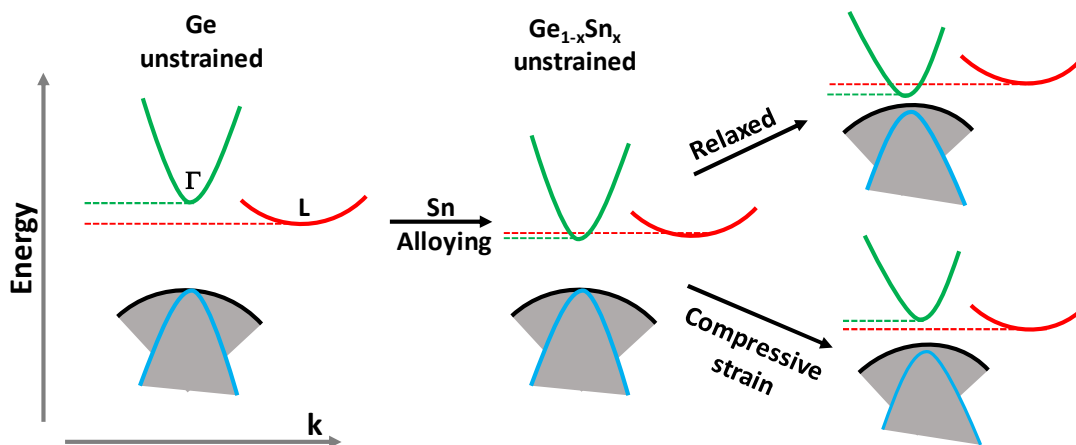


Figure 1.3. A schematic of Sn alloying on the band structure of Ge with A schematic of the different band structures (Γ for direct and L for indirect) for unstrained Ge, compressively strain $\text{Ge}_{1-x}\text{Sn}_x$ and relaxed.

Theory and experiments on thin films suggest that the bandgap energy with respect to alloy composition has a nearly linear relationship. As a result, $\text{Ge}_{1-x}\text{Sn}_x$ films bandgap decreases from 0.67 eV (pure Ge) to ~0.35 eV for 15% Sn.²¹ Further Sn incorporation promotes the metallic character of direct-gap $\text{Ge}_{1-x}\text{Sn}_x$ alloys, eliminating any potential application in visible to near IR optoelectronics. In order to produce higher band gap $\text{Ge}_{1-x}\text{Sn}_x$ alloys more suitable for absorption and emission applications, quantum confinement effect can be utilized.^{31,32}

1.3 Quantum Confinement

When the size of a semiconductor material becomes comparable or smaller than the Bohr radius, the physical separation (distance) of the excitons become smaller, then the material undergoes the quantum confinement effect.^{1,33} It is also defined by the size of the material which is smaller than that of the Bohr radius (a_B , Equation 1.1), where a_B is the distance an excited electron can travel from its corresponding hole. By meeting this condition, it becomes relevant for excitons to the particle in a box model to consider the size vs energy relationship. When this condition is met, the particle in a box model becomes relevant for excitons when considering the size vs energy relationship. The size confinement in bulk, nanoparticles in comparison to HOMO and LUMO levels of molecules can be seen in Figure 1.4.^{4,11}

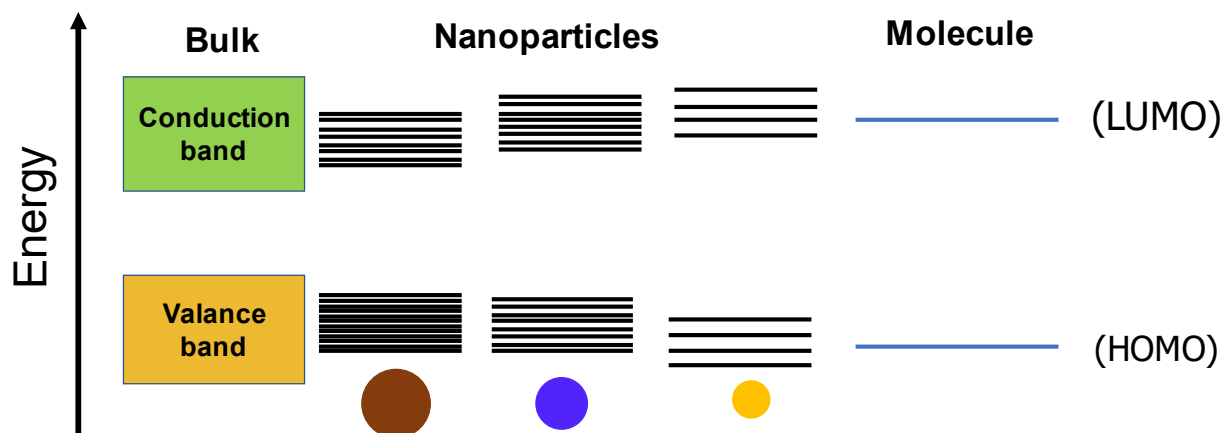


Figure 1.4. Continuous energy bands in bulk and discrete energy levels in semiconductor nanoparticles with respect to molecular orbital theory for a single molecule.

The energy separation between the valence band and conduction band increases as particle size decreases (Figure 1.4) as the electrons and holes are physically confined in smaller area. This brings the changes in band energy (ΔE) in the confinement range. This inversely proportional relationship between the bandgap energy change (ΔE) and the particle size under quantum confinement effect can be explained by Equation 1.2.¹

$$\Delta E = \frac{h^2 \pi^2}{2R^2} \left[\frac{1}{m_e^*} + \frac{1}{m_h^*} \right] - \frac{1.8e^2}{\epsilon R} \quad (1.2)$$

In this equation few assumptions were taken into consideration such as charge carrier masses and dielectric constants. However, it provides a decent estimation of change in bandgap energy in accordance with particle size and confinement effects. The ability to tune the size of material to tune the energy gap is one of the major driving force behind

development of semiconducting nanocrystals. The size at which confinement effects are observed is highly dependent on material properties and can range from 1-150 nm.^{1,25} Thus, development of diverse synthesis methods which provide tunable sizes is of great importance in semiconductor research.

1.4 Synthesis of $\text{Ge}_{1-x}\text{Sn}_x$ alloys

Nanoparticles synthesis is a challenging task as the particles possess high surface to volume ratio which leads to high reactivity and unstable surfaces. With their due importance, there have been numerous reports describing synthesis of different nanoparticles with size, morphology, and composition control.^{34,35} Synthesis approaches are of mainly two types: (1) top down and (2) bottom up approach.^{36,37} In top down synthesis, the bulk materials reduced to nanoscale in size through physical or chemical method. Bottom up synthetic techniques are numerous and diverse, which includes solid state, solution phase, vapor phase, and solid-solution-vapor interface approaches where atoms or ions reacts with other atoms or ions.^{13,37,38}

As mentioned earlier, the major setback for $\text{Ge}_{1-x}\text{Sn}_x$ alloys is poor solubility of Sn into Ge lattice.^{25,39} Thin films of $\text{Ge}_{1-x}\text{Sn}_x$ alloys produced via non-equilibrium growth method and epitaxy overcame the solubility issue.⁴⁰ The first successful report on $\text{Ge}_{1-x}\text{Sn}_x$ thin films is a top down approach. In this process at first, 30 nm thick films were produced and then ion etching was utilized to remove Ge capping layer. While etching Ge capping layer, $\text{Ge}_{1-x}\text{Sn}_x$ layer also slowly getting etched (Figure 1.5).²¹ Etching time is critical here, when longer etching times resulted in destroyed the Ge pillar which released the $\text{Ge}_{1-x}\text{Sn}_x$ disk. Certainly, these disks are confined in one direction and show no quantum confinement effects.²¹

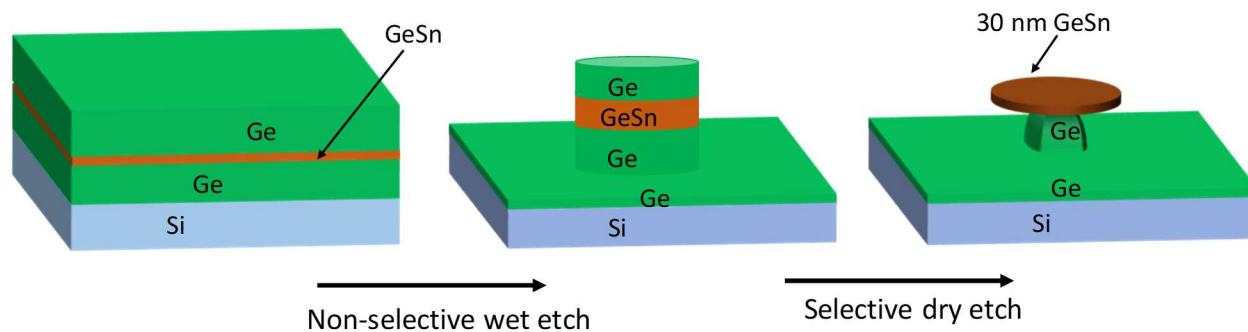


Figure 1.5. Key steps in the fabrication of $\text{Ge}_{1-x}\text{Sn}_x$ thin films using non-selective and selective etching process.

1.5 Colloidal Synthesis

Solution phase synthesis provides a number of variables to control in the nanoparticle synthesis.^{1,41} The solvent can be selected based on the solubility of precursor material. The surfactants are used as solvent as well as to control the growth of crystal by passivating on the surface. Temperature and pressure can be used to achieve desired crystal phase.^{11,42} Reducing agent is useful in decomposing the precursor(s), especially by competing with surfactants, which alone can act as reducing agent to control the nucleation.^{31,32}

Depending on the solvent, solution-based syntheses are considered two types: (1) aqueous and (2) non-aqueous. In aqueous solvent syntheses, water is the main and versatile solvent. Most of noble metal nanoparticle syntheses utilizes water as solvent along with above mentioned precursor, surfactants, and reducing agent.^{43,44} The main disadvantage with the synthesis with water as solvent is that temperature and oxygen sensitive materials. As the water boiling point is 100 °C, the reactions which requires temperature higher than that are limits it's use in the synthesis of semiconducting

nanocrystals. Most of the semiconductors (except oxide ones) are oxygen sensitive, hence water is poor choice of solvent. Thus, non-aqueous solvents have import role in the wet chemical synthesis, where the choice of solvents is more diverse and the boiling point of the solvent as well (up to 350 °C).¹² Long chain hydrocarbons of alkanes, alkenes, alkynes, thiols, phosphines serve this purpose and this approach is termed as colloidal synthesis.^{42,45-47}

In a typical colloidal synthesis, there are mainly three steps involved, nucleation, growth, and isolation of the nanoparticles.¹ The classical La-Mer model is used to explain the synthesis of nanoparticles in solution (Figure 1.6).⁴⁸ A swift injection of reactants into coordinating solvent which is at high temperature creates an unstable supersaturation in the reaction flask allows the formation of nuclei. By maintaining or increasing the reaction temperature, the nuclei consumes the newly formed nuclei from the continuous decomposition of the precursor leads to growth of the particles. Understanding the growth process is critical to control the final size of the nanoparticles. Along with temperature, reaction time also plays an important role in the growth process. Consequently, a secondary growth process occurs as the newly formed small nanoparticles possess high surface energy and is called as Ostwald ripening.⁴⁸ During the Ostwald ripening, small crystals merges dissolves back into solution and deposits on the larger particles. This later stage growth has different effects on the nanoparticle morphology. Alternatively, small crystals can also merge to form larger ones. If small crystals coalesce and connect randomly to result in a polycrystalline particle which has high degree of defects. On the other hand, if the lattices of each crystal match up to fuse results in a single crystal. One more important aspect of oriental attachment is that nanorods, nanowires, and other

morphologies can be produced.⁴⁸ Therefore, to have better control over growth kinetics, the key reaction parameters such as precursor ratios, reaction temperature, growth time, and capping ligands should be adjusted.^{1,48}

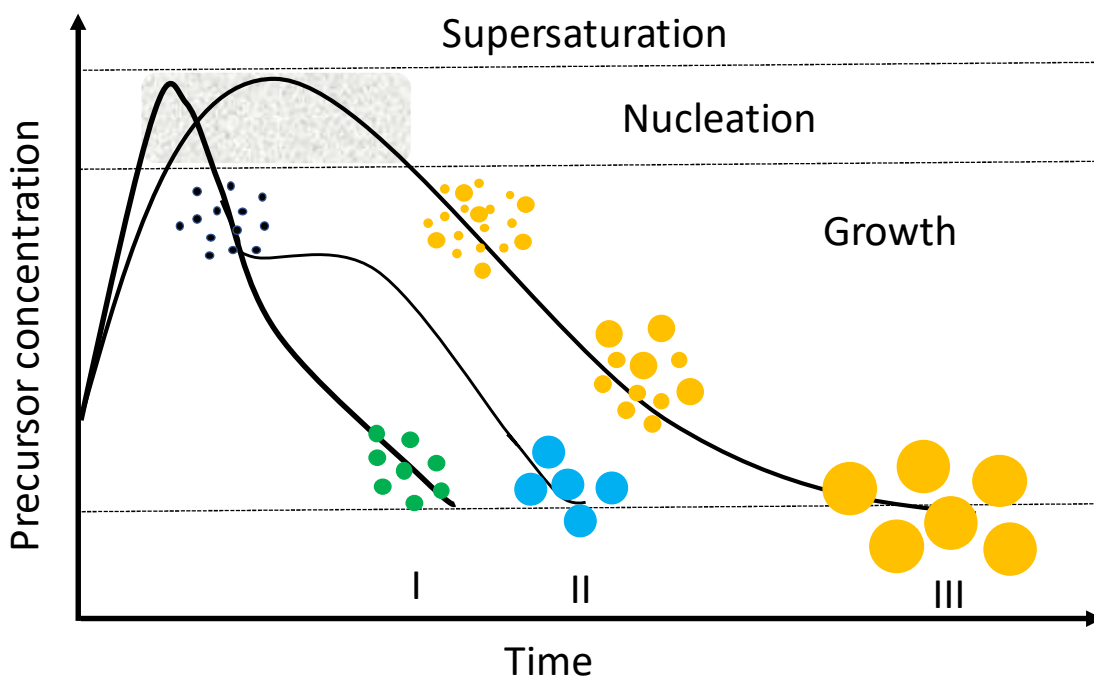


Figure 1.6. Schematic of La-Mer nucleation model for mechanism of formation of uniform particles in solution. curve I: single nucleation and uniform growth by diffusion; curve II: nucleation, growth and aggregation of smaller subunits; curve III: multiple nucleation events and Ostwald ripening growth.

1.6 Synthesis of $\text{Ge}_{1-x}\text{Sn}_x$ Alloy Nanocrystals

Owing to lack of proper synthetic methodologies, $\text{Ge}_{1-x}\text{Sn}_x$ alloy nanocrystals have slowly been developed. The primary reason for the slow development is the low solubility of Sn.²¹ However, as discussed in earlier, the thin film technology overcomes the solubility

issue but resulted in reducing the bandgap into mid IR region which limits their wide spread applications.²¹ To solve both solubility and opening up the energy gap to NIR-visible range our group first reported the synthesis of $\text{Ge}_{1-x}\text{Sn}_x$ alloy QDs.³¹ This first colloidal synthesis GeI_2 and SnCl_2 were utilized as precursors to produced homogeneous $\text{Ge}_{1-x}\text{Sn}_x$ alloys with three distant size regimes with Sn composition up to 28%. The larger set of $\text{Ge}_{1-x}\text{Sn}_x$ alloys with sizes in the range of 15-23 nm exhibit negligible confinement effects with energy gaps (0.2-0.4 eV) that are red-shifted from bulk Ge (0.67 eV) and are similar to $\text{Ge}_{1-x}\text{Sn}_x$ thin film alloys.³¹ A set of smaller yet polydisperse alloy QDs with sizes in the range of 3.4-4.6 nm display decent size confinement effects with Sn composition tunable energy gaps (1.29–0.75 eV for $x = 0$ –11.0%).³¹ Later, researchers at Los Alamos National Laboratory employed GeI_2 and Tin(II) bis(trimethylsilyl)amide ($\text{Sn}(\text{HMDS})_2$) for the Production of size and composition controlled homogenous $\text{Ge}_{1-x}\text{Sn}_x$ alloy nanocrystals.³² Increase in Sn concentration was achieved up to 42% by compromising the nanocrystal sizes in the range of 7-12 nm allowing the optical properties in the near-mid IR absorption (1.04-0.72 eV for $x = 0$ -40%) and mid-IR PL (0.58-0.45 eV for $x = 36$ -38%).³² These two colloidal syntheses provided a platform to extend their optical properties in new scale by adjusting the size and composition.

A set of ultra-small, strongly confined $\text{Ge}_{1-x}\text{Sn}_x$ alloy QDs of particle sizes in the range of 1.85-2.28 nm with composition tunable optical properties in visible range (absorption: 2.05-1.56 eV and PL: 2.00-1.72 eV for $x = 1.8$ –23.6%) was reported.⁴⁹ Optical transition energies and carrier dynamics of the ultra-small QDs were also investigated using steady-state and time-resolved photoluminescence (PL) spectroscopy.⁵⁰ Carrier dynamics of the alloy QDs indicate slow decay of PL at 15 K

owing to radiative recombination of dark excitons which are spin forbidden and carriers trapped at the surface states. At room temperature 295 K, The PL decays are ~ 3 orders of magnitude faster (9–28 ns) due to the bright excitons which are thermally activated and carrier de-trapping from surface states.⁵⁰ Further, using hybrid functional calculations and experimental characterization on the ultra-small $\text{Ge}_{1-x}\text{Sn}_x$ alloy QDs, indicate admixing of α -Sn significantly enhances the oscillator strengths to result in brightly emissive alloy QDs with high absorption and emission efficiency.⁴⁷ However, owing to less size control as increasing Sn concentration and polydispersity of samples show no measurable PL in NIR region. More recently, $\text{Ge}_{1-x}\text{Sn}_x/\text{CdS}$ core/shell QDs have been employed to produce NIR PL.⁵¹ The core/shell QDs show broad-band NIR PL with neither size (8–13 nm) nor composition ($x = 5\text{--}25\%$) dependent tunability. To address the size and composition PL tunability in the pursuit of high absorption and bright emission $\text{Ge}_{1-x}\text{Sn}_x$ alloy QDs, we have developed a unique colloidal synthetic strategy and the detailed discussion will be in chapter 3.

1.7 Metal Phosphides

Metal phosphides (MPs) have received tremendous interest as a class of materials that exhibit a range of physical properties of both fundamental and technological interest depending on their chemical identity and crystal phase.^{12,52-58} Synthetic techniques of MPs transitioned from bulk to nanoparticle ones occurred during the period 1960-2000.¹² The major driving force for this renewal was to achieve tunable bandgaps in semiconductors. In fact, number of MPs are semiconductors.¹² In 1952, Welker suggested that indium phosphide (InP) could be potential candidate as a semiconductor

in electronic devices. Later, InP, GaP, and their alloys with arsenide have become major entities in their applications such as photoemitting diodes, microwave oscillators, and signal enhancers in biological field.^{12,59} The quest for MPs originated from the field of III-V semiconductors, where the bandgaps were successfully tuned by controlling the particle size. However, further extension to other metals to form variety of phosphides triggered the development of specific synthetic routes, which adapted to size and morphology control, both in terms of precursors and processes. Table 1.2 shows the list of MPs and their applications, in specific view of their semiconducting, magnetic, and catalytic properties.^{12,53,60,61}

Table 1.2. List of metal phosphides and their associated properties.

Metal Phosphide	Property
InP	Semiconducting
GaP	Semiconducting
Cd ₃ P ₂	Semiconducting
Zn ₃ P ₂	Semiconducting
SnP ₃	Semiconducting
SnP	Semiconducting
Sn ₃ P ₄	Semiconducting
GeP	Semiconducting
FeP ₃	Semiconducting
CoP ₂	Semiconducting
NiP ₂	Semiconducting
RhP ₂	Semiconducting
MnP	Ferromagnetic
Fe ₃ P	Ferromagnetic
FeP	Anti-ferromagnetic
W ₃ P	Superconducting
Rh ₂ P	Superconducting, Catalytic
Fe ₂ P	Catalytic
Ni ₂ P	Catalytic
MoP	Catalytic
WP	Catalytic
Co ₂ P	Catalytic
Sn ₄ P ₃	Catalytic

Synthetic routes became more and more empirical in most of the cases for MPs. For metal precursor choices, halides, carbonyls, acetates, and acetylacetonates are taken stoichiometric ratios. phosphorus precursor is critical in achieving the desired metal phosphide, Figure 1.7 overviews the use of the phosphorus precursors in the synthesis of MP nanoparticles.¹² MPs synthesized using four major P-sources, among them trioctyl phosphine (TOP) and tris(trimethylsilyl)phosphine ((TMSi)₃P) produced variety of phosphides with size, shape, and phase control.^{12,62-64}

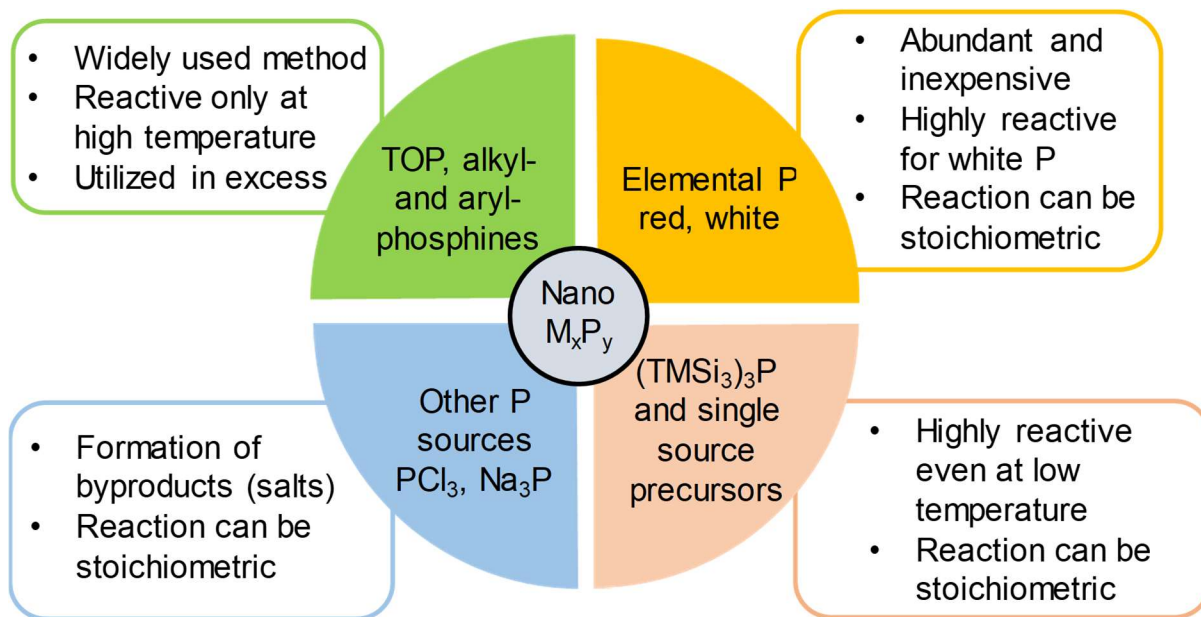


Figure 1.7. Overview of utilization of the main phosphorus (P) sources for the synthesis of metal phosphide nanoparticles.¹²

1.8 Group IV-V Semiconductors

Even though InP and GaP semiconductors were the most studied Group III-V materials in the 1960–2000 period, other phases were also investigated, such as Cd₃P₂ (Group II-V).¹² Recently Zn₃P₂ (Group II-V) also reported for its tunable optical properties

and related photovoltaic applications.^{61,62,65} Group IV-V materials are due in this regard with tunable energy gaps for their potential applications in optoelectronic and thermoelectric fields.^{14,53} Theoretical studies show that these Group IV-V materials are also semiconductors. In particular, IV = Si, Ge, and Sn; V = N and P single layer materials energy gaps are shown in Table 1.5.⁶⁶ However, earlier to this dissertation study, due to lack of proper synthetic methodologies, Group IV-V material's experimental values are not reported. We made a successful attempt to synthesize Sn-P system and reported experimental, tunable energy gaps in NIR region will be discussed in next section and chapter 4.

Table 1.3. Energy gaps of Group IV-V (IV = Si,Ge, and Sn; V = N and P) materials.⁶⁶

Group IV element	Group V element	Energy gap of Group IV-V material (eV)*
Si	N	2.73
	P	2.17
Ge	N	2.56
	P	2.07
Sn	N	1.88
	P	2.17

*Calculated from Heyd-Scuseria-Ernzerhof (HSE06) hybrid function.

1.9 Tin Phosphides

Tin phosphides make up a class of materials that have their potential applications in charge storage, photocatalysis, and thermoelectric devices.^{53,67-69} Owing to dual stable oxidation state of tin (Sn^{2+} and Sn^{4+}), tin phosphides exists in four stoichiometries: (1)

Rhombohedral Sn_4P_3 , (2) Hexagonal SnP , (3) Trigonal Sn_3P_4 , (4) Trigonal SnP_3 .¹⁴ Theoretical studies describe that except the metal rich Sn_4P_3 , the other stoichiometries (SnP , Sn_3P_4 , and SnP_3) are semiconductors. Numerous reports indicate, tin phosphides extensively studied for battery applications. Layered crystal structure makes them promising anode materials for Li and Na ion batteries (LIBs & NaIBs). conducting nature and their main applications can be seen Table 1.3.1.^{14,53,66}

Table 1.4. Different crystal phase of Tin phosphides and Their Potential Applications

Tin Phosphide	Crystal Phase	Conductivity	Applications
Sn_4P_3	Rhombohedral	Metallic	Photocatalytic, anode material in Li- & Na-ion batteries
SnP	Hexagonal	Semiconducting	Anode material in Li- & Na-ion batteries
Sn_3P_4	Trigonal	Semiconducting	Thermoelectric
SnP_3	Trigonal	Semiconducting	Anode material in Li- & Na-ion batteries

1.10 Synthesis of Tin Phosphides

Tin phosphides can be synthesized through different approaches: (1) solvothermal, (2) chemical vapor deposition, and (3) mechanochemical (ball milling).^{67,70,71} Among them solvothermal and mechanochemical synthetic approaches are widely utilized to produce tin phosphides.

1.10.1 Solvothermal method

solvothermal method can be defined as “a chemical reaction in an organic solvent closed system under high temperature and high-pressure conditions”.⁵³ Typically, this process requires temperature higher than that of the boiling point of the solvent. In lieu of a non-aqueous solvent, water can be utilized as solvent and this method is called as hydrothermal process.⁶⁸ Hydrothermal process is limited to the preparation of hydroxides, oxyhydroxides, and oxides. Solvothermal process is inevitable for non-oxide materials as it excludes water as solvent. In addition, metastable yet kinetically stable phases instead thermodynamically stable phases are often isolated in solvothermal method. A schematic of this process is shown in Figure 1.8.^{68,70}

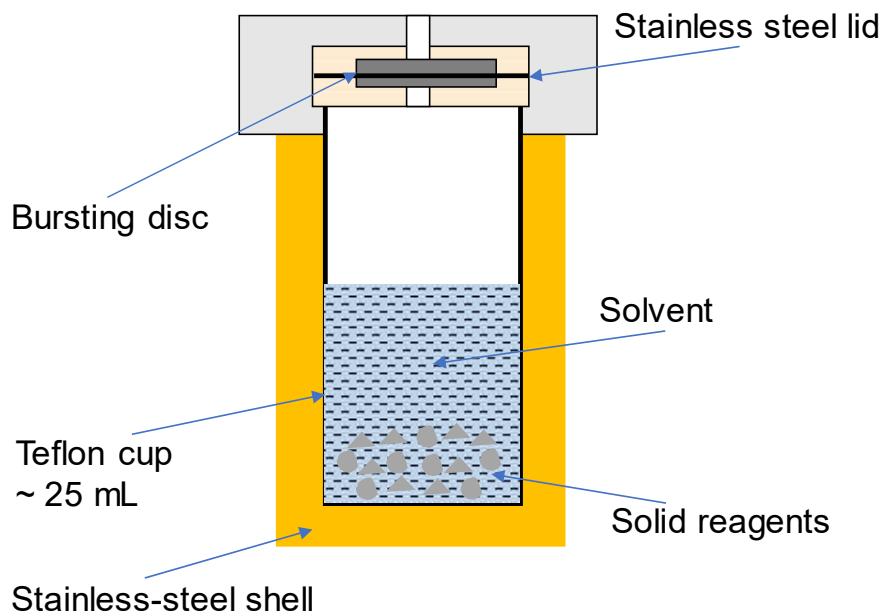


Figure 1.8. A schematic diagram of solvothermal synthesis setup.

In this method, the solid reactants (tin/tin halides and yellow/red/white phosphorus) are placed in a stainless-steel autoclave filled with an organic solvent

(ethanol/ethylenediamine/dimethyl formamide) to carry out the reaction.⁶⁸ The Teflon-lined autoclave is critical for high temperature and pressure conditions. In addition, it exhibits a strong resistance towards strong acids and sustains in alkaline media as well. During the earlier course the reaction, the reduced viscosity of solvent increases the diffusion process favors the crystal growth.⁷² The solvothermal method favored the synthesis of rhombohedral Sn₄P₃. However, controlling the size to nanoscale is still a challenge in the solvothermal method.

1.10.2 Mechanochemical or ball milling method

Mechanochemical process is also termed as ball milling, a process where mixture of powders is placed in the ball mill is subjected to high-energy collision from the balls.³⁶ This process was developed by Benjamin in late 1960. A high energy mechanical ball milling was shown a promising technique to produce tin phosphides (Figure 1.9). During the ball milling, a uniform environment is created, which allows the synthesis of homogeneous monophasic solid solutions of tin phosphides via mixing of Sn and P powder precursors.³⁷ The mechanochemical process involves mechanical activation of chemical reactions during ball milling at relatively low temperatures.^{36,37} Milling of precursor powders leads to the formation of a nanoscale composite structure of the starting materials, which react during milling.^{36,73} The resulting nanoparticles are collected simply by selective removal of the matrix phase. This technique has unique advantages: (1) relative simplicity in operation, and (2) ease to create desired phase of tin phosphides such as SnP₃, Sn₃P₄, SnP, and Sn₄P₃ for which Sn and P precursors taken stoichiometrically.^{67,69} The main disadvantages of this method include, (1) contamination from balls, typically made of stainless-steel or zirconium (tungsten carbide can be used

to address the impurities issue but is expensive to deal with), and (2) size control is also a major issue.³⁶

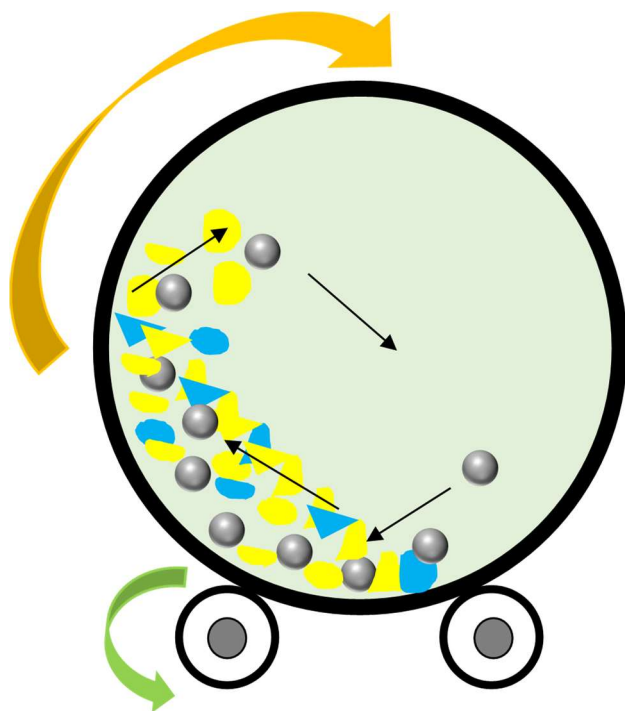


Figure 1.9. A Schematic view of motion of the ball and powder mixture.

As the both above mentioned syntheses resulted in polydisperse samples and the physical properties of tin phosphides have not been reported properly owing to lack of unique methodology which controls crystal phase, size, and morphology.

1.10.3 Wet chemical synthesis

Nanoparticle synthesis requires an additional control on the surface states to limit the growth of the crystals which allows to control the final size and shape of the particles.¹ They relied for instance on the use of organic capping ligands in wet chemical routes. Prior to this dissertation study, only hexagonal $\text{SnP}_{0.94}$ was synthesized via colloidal

synthetic strategy.^{67,74} Tin acetate ($\text{Sn}(\text{OAc})_2$) and trioctyl phosphine (TOP) were utilized as precursors and trioctyl phosphine oxide (TOPO) as surfactant and solvent at elevated reaction temperature ($390\text{ }^\circ\text{C}$) for 1 h.⁷⁴ However, the resulted tear-drop shaped particles are in micron size ($\sim 0.5\text{ }\mu\text{m}$). Apart from size control, another major challenge with this colloidal synthetic route is that reaction temperature ($390\text{ }^\circ\text{C}$) which is difficult to achieve and maintain for 1 h with choice of solvents we have (TOP and TOPO in this case). Though the Bohr radius of the semiconducting tin phosphides (SnP_3 , Sn_3P_4 , SnP) are not known to date, certainly the micro meter size is nowhere near to achieve the quantum size confinement effects. Thus, we have developed a unique synthetic strategy to control over size, shape, crystal structure at low to moderate temperature ($100\text{-}250\text{ }^\circ\text{C}$). In this wet chemical synthesis, oleylamine (OLA) and oleic acid (OA) were employed as surfactant mixture and SnI_4 and tris(trimethylsilyl)phosphine ($(\text{TMSi})_3\text{P}$) as starting materials. By manipulating the reaction parameters, such as temperature, precursors ratio, and additional coordinating ligands the control over crystal phase, size, and morphology of tin phosphides were achieved. More importantly, quantum size effects were observed, and the energy gaps were tuned in NIR region. These observations will be discussed in chapter 4.

1.11 Thesis Statement

There are two main goals to be achieved in this dissertation study to develop unique synthetic strategies for $\text{Ge}_{1-x}\text{Sn}_x$ alloys and tin phosphides. The first goal is to develop a wet colloidal synthesis to produce $\text{Ge}_{1-x}\text{Sn}_x$ alloy QDs and perform physical and optical characterizations to understand structure properties relationships (Goal 1). The second

goal is to develop a unique synthetic methodology to produce different phases of tin phosphides in nanoscale and probe their size dependent optical properties.

The development of non-equilibrium $\text{Ge}_{1-x}\text{Sn}_x$ alloys in nanoscale is critical to achieve new functionalities, especially the formation of a direct bandgap in a conventional indirect bandgap elemental semiconductor (Goal 1). However, to synthesize $\text{Ge}_{1-x}\text{Sn}_x$ alloy QDs, a special care has to be taken in terms of choice of precursors with moderate reactivity, strong reducing agent, and surfactants with strong affinity towards Ge and Sn. As such careful investigation to produce $\text{Ge}_{1-x}\text{Sn}_x$ alloy nanocrystals using GeI_2 and SnCl_2 as precursors, oleylamine (OLA) as surfactant, n-butyllithium (BuLi) as reducing agent triggered the alloy QDs research to further explore their size and composition dependence on physical and optical properties. The set of ultra-small (~ 2 nm) $\text{Ge}_{1-x}\text{Sn}_x$ alloy QDs with composition tunable visible PL provided important ground work for synthesis and understanding of 3.3-5.9 nm alloy QDs allows to expand the optical emission to NIR region (Goal 1). By expanding photoluminescence into NIR region, especially in the range of 1.3-1.9 eV is ideal for bio-imaging applications. In addition, these NIR alloy QDs are potential alternatives to commercial toxic NIR QDs in therapeutic application.

Goal 1 is expected to be achieved through the utilization of hexadecylamine (HDA) as capping ligand in lieu of OLA, since HDA provided a better control over size and dispersity for pure Ge nanocrystals. The optimal concentration of OLA as surfactant results in ~ 2 -3 nm QDs with tunable optical properties in visible region. Our own observation by lowering the OLA concentration to produce alloy QDs sizes above 3 nm instead produced polydisperse samples. In order to produce precise size QDs within 3-6

nm, HDA as surfactant and varied amounts of BuLi will be employed. The successful alloying effects can be confirmed using PXRD on the as prepared samples, which show a systematic shift of diffraction peaks of cubic Ge towards lower 2θ angle. Along with PXRD, Raman peak shift and increase in Ge d-spacing values through HRTEM indicate a successful alloying of Sn. Homogeneous distribution of Sn and Ge throughout the QD further confirms the alloy formation (Goal 1). Composition tunable optical properties absorption of the as prepared solid alloy QDs can be probed using solid-state absorbance and photoluminescence measurements. A significant blue shift of energy gaps from bulk Ge and $\text{Ge}_{1-x}\text{Sn}_x$ thin films indicate strong size confinement effects. Relaxation pathways of the excited electrons provided by time resolved photoluminescence (TRPL) measurements along with their temperature dependence of TRPL provide significant detail on carrier dynamics of alloy QDs.

There are no reports on the synthesis of tin phosphides in nanoscale until this dissertation study (Goal 2). The second goal is expected to be achieved through the selection of choice of the precursors via colloidal synthesis using OLA as surfactant. Our own observation with SnCl_2 as Sn precursor and $(\text{TMSi})_3\text{P}$ resulted in single phase (rhombohedral Sn_4P_3) with no control over size. Sn precursor such as SnI_4 is helpful by decomposing slowly compared to SnCl_2 is expected to slow down the nucleation and growth of the nanoparticles. As $(\text{TMSi})_3\text{P}$, a highly reactive P-source the temperature dependent study is critical to achieve size control and different tin phosphide phases. In addition to reaction temperature, the other reaction parameters such as precursor ratio, additional coordinating solvents, and reaction time could provide size, shape, crystal phase control (Goal 2). PXRD along with HRTEM are important tools to confirm the crystal

phase of the nanoparticles. As tin possess a stable Sn^{2+} , and Sn^{4+} oxidation states, these formal charges of the as prepared different phases of nanoparticles can be confirmed using XPS measurements. Theoretical reports indicate, P-rich tin phosphides (SnP_3 , Sn_3P_4 , and SnP) are semiconductors. The optical absorbance on as synthesized nanoparticles provide a first ever experimental evidence of their energy gaps. In addition, by employing a systematic reaction time offer size tunability allows to tunable optical properties (Goal 2).

CHAPTER 2

CHARACTERIZATION TECHNIQUES

Several characterization methods and techniques are required to investigate the structural, chemical, optical and physical properties of the materials. In this chapter, all material characterizations employed to probe aforementioned properties of material will be discussed. Primarily, powder X-ray diffraction (PXRD) was utilized to confirm the structure, transmission electron microscopy (TEM) for particle size and high resolution TEM (HRTEM) to image lattice fringes which further confirms the crystal structure. Materials compositional analysis was done using scanning electron microscopy (SEM) coupled with an energy dispersive spectroscopy (EDS). Techniques such as Raman, thermogravimetric analysis (TGA), and X-ray photoelectron spectroscopy (XPS) provided diverse understandings of surface chemistry and functionalization of the surface. The optical properties of materials characterized by solution UV-Vis, solid-state diffuse reflectance spectroscopy, and photoluminescence measurements.

2.1 Powder X-ray Diffraction

Powder X-Ray Diffraction (PXRD) is an important tool which provides information about the crystallinity and phase of a material. Every crystalline material diffracts distinctively, and thus provides a diffraction pattern that serve as a “fingerprint” for that specific material.⁷⁵ Crystal structures are defined as a periodic arrangement of atoms with identical repeating units. A wide script of descriptors has been developed for crystal systems including orientation, symmetry, unit cells, atomic arrangements, and atomic distances.⁷⁵⁻⁷⁸ The X-ray wavelengths are comparable to the inter atomic spacing in

crystals, and so the atoms in a crystal act as scattering centers which result in diffraction. X-rays are produced inside an X-ray tube when high energy electrons collide with a metal target. X-ray tube consists of three main components: (i) a source of electrons (ii) a high accelerating voltage and (iii) a metal target (Figure 2.1).⁷⁸ A tungsten filament, which acts as a cathode, generates electrons upon heating by a filament current of about 100-150 mA. The electrons are directed across the X-ray tube at high velocities to the metal target (anode) by a high accelerating voltage on the order of 30,000 – 50,000 volts.

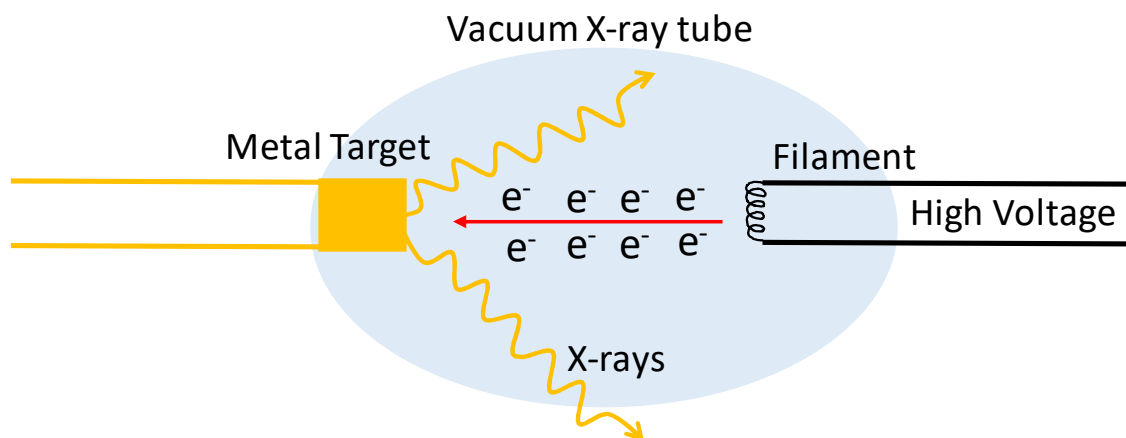


Figure 2.1. Diagram of a standard vacuum X-ray tube.

Metal target (commonly Cu) generates X-rays upon collision with high energy electrons and they pass through highly transparent windows made of beryllium.^{77,78} The kinetic energy associated with the high velocity electrons is converted into heat in the target and need to be cooled to stop melting. The efficiency of X-ray tubes is increased when the metal target is rotated continuously, thus exposing a fresh target metal to the incident electrons uninterrupted. X-ray radiation generated inside the X-ray tube can be classified into two different components: (i) white radiation, which covers a broad

spectrum of wavelengths and (ii) one or more monochromatic radiations. White radiation is produced when the high velocity electrons hit a road block in the form a metal target, resulting in loss of energy, a part of which is converted into electromagnetic radiation. The monochromatic X-rays that are commonly used in all diffraction experiments are generated by a diverse process that includes ionization of the target metal atoms.^{77,78}

When the accelerated electrons strike the metal target, they ionize some of the Cu 1s (K shell) electrons (Figure 2.2). An electron from the outer orbitals (2p or 3p) falls to the vacant orbital and the transitions, which has a fixed energy, results in emission of characteristic X-rays. The 2p → 1s transition is called the K α transition (1.5418 Å) and it is more intense than the 3p → 1s transition, K β (1.3922 Å), because the K α transition occurs with greater frequency.^{58,77} A monochromator is used as a filter to ensure a selected wavelength is used for the diffraction experiments. Crystals comprise regularly repeating structures that act as optical gratings. When X-rays hit a sample, some of them are reflected at angles equal to the angle of incidence by planes on the surface of the sample, while some pass through and are reflected by the inner planes.

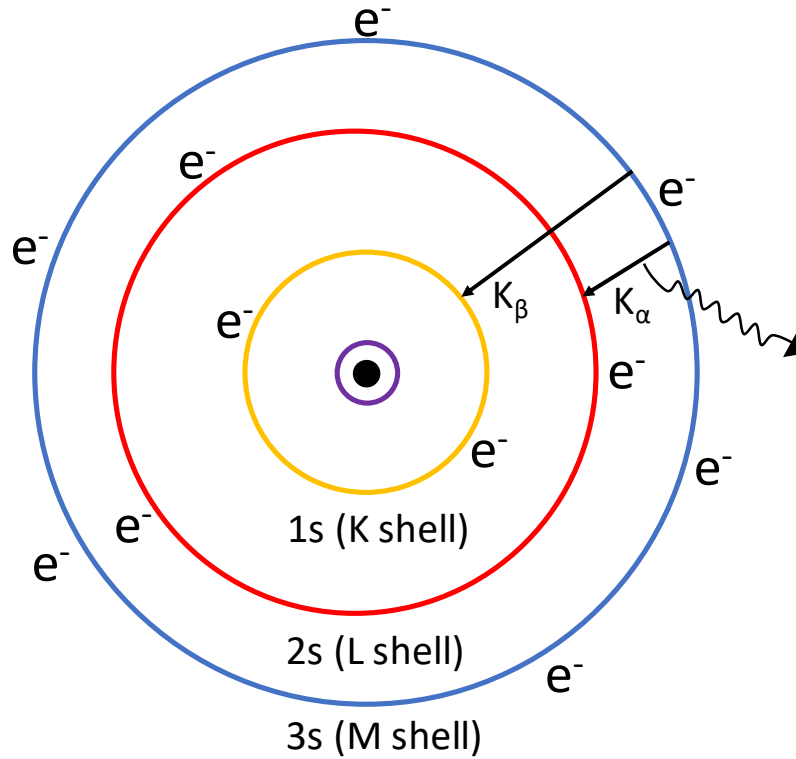


Figure 2.2. Electronic shell diagram of electronic transitions for X-ray production.^{77,78}

The reflected X-rays reinforce each other results in constructive interference if they are in phase or cancel out results in destructive interference if they are not in phase (Figure 2.3). Consider two X-ray beams A and B hitting a sample, X-ray beam A gets diffracted as A' by an atom on the surface plane while B passes through the surface plane and is diffracted as B' by an atom in the interior plane. Only when AA' and BB' are in phase the scattering of the X-rays is considered a diffracted beam.

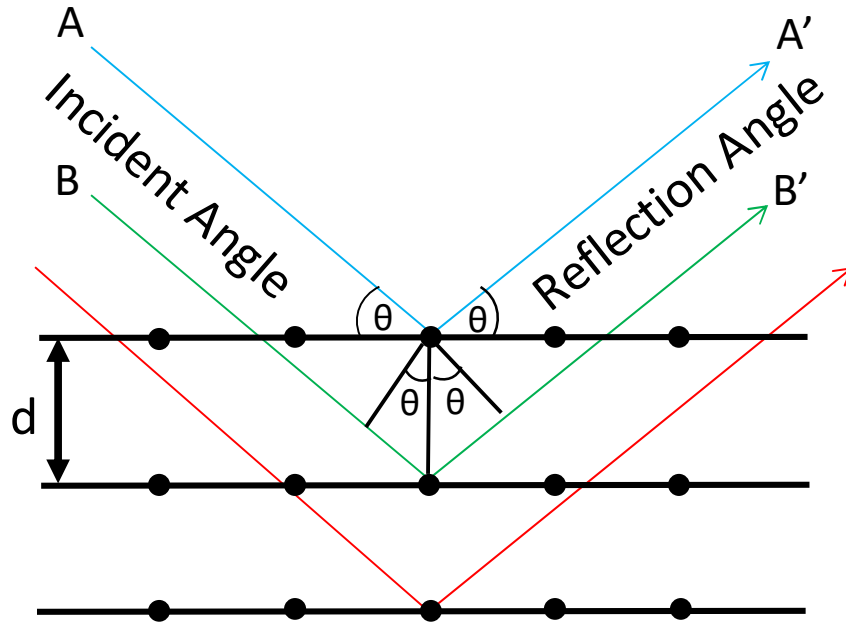


Figure 2.3. Diffraction of X-rays by parallel crystal planes.^{77,78}

The conditions which leading to coherent diffraction allows us to apply the Bragg Law (equation 2.1) where n is the order of reflection, λ is X-ray wavelength, d is the distance between two incident beams, and θ is the angle between the incident beam and the surface to the crystal. The interfering waves which result from the narrow line widths of diffraction peaks produced across thousands of planes canceling out diffraction from non-Bragg angles.^{77,78}

$$n\lambda = 2d \sin\theta \quad (2.1)$$

In nanocrystals, the broadening of the diffraction peaks is due to not enough lattice planes to create beneficial interference. The size of a crystal is determined by utilizing Scherrer equation (2.2), which takes the advantage of the line broadening. The crystal

size is t , λ is the wavelength of the X-ray, B is the full width half maxima (FWHM) of the peak and θ is the diffraction angle.^{77,78}

$$t = \frac{0.9 \lambda}{B \cos \theta} \quad (2.2)$$

Samples in this dissertation study were analyzed using a Philips X'Pert Pro, running Cu K α monochromatized radiation ($\lambda = 1.5418 \text{ \AA}$). The powdered samples were loaded onto a low background Si sample holder with a spinning stage to improve sample averaging (Figure 2.4). Instrumental line broadening was measured with a Si standard and accounted for in any calculations.

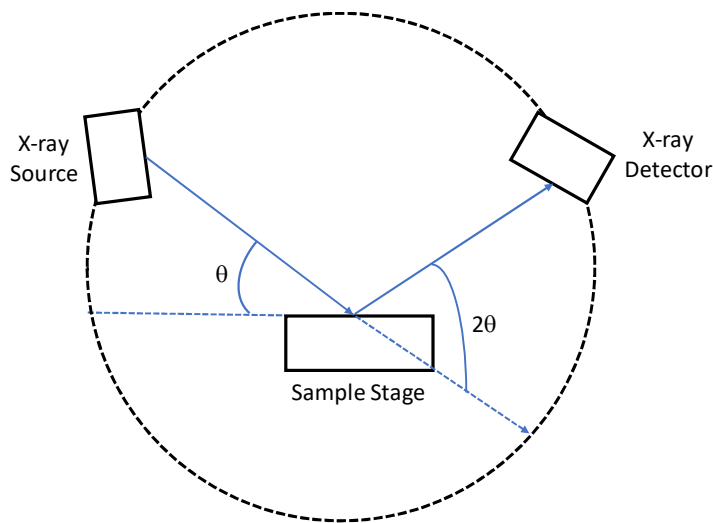


Figure 2.4. Schematic illustration of X-ray diffraction instrument.^{58,77,78}

2.2 Transmission Electron Microscopy

TEM is a commonly used technique for observing material's size and morphology in nanoscale. In semiconducting nanocrystals, one of the most substantial topics is size dependent properties. There are several ways to determine the size of a nanocrystal

including dynamic light scattering (DLS), diffraction. However most of these only provide a 'virtual' size of the sample. Transmission electron microscopy (TEM) stands out in its capacity to provide an actually 'physical' representation of nanoparticle size. TEM show not only size but also the morphology and structure of nanoparticle, something the earlier mentioned techniques cannot provide. High resolution TEM has the ability to resolve crystal lattice arrangements and even individual atoms which can be combined with X-ray spectroscopy to provide elemental identification.⁷⁹

TEM utilizes the electron source similar to X-ray tube (Figure 2.1). A tungsten filament is heated up with extreme high voltage (80-400 kV) under vacuum resulting in the emission of electrons. In TEM, the electrons are focused through a series of magnetic lenses to directly probe a sample, whereas in X-ray tube the electrons are used to produce X-rays.⁷⁹ In basic imaging, the electron beam is spread out across the sample, some of the electrons are blocked by the sample and a negative is created by the unhindered electrons. To offer the best possible contrast the sample holder must be significantly thin with a low electron cross section, in most cases, a thin carbon film from 3-30 nm supported by a Cu mesh is adequate for this purpose. When the electron beam, a host of interaction are possible and essentially all occur concurrently (Figure 2.5). TEM instrument is so versatile as it involves number of interactions, with accurate control of the beam through focusing lenses and detection methods a numerous of information can be collected from a single sample. The TEM basic imaging as already described, in which transmitted electrons strike a detector below the sample. The change in the focus of the beam after sample interaction, it is possible to detect scattered and notably diffracted electrons for selected area electron diffraction (SAED) patterns providing data of crystal

structure. As the sample is bombarded with high energy electrons, some of the atoms will undergo excitations and resulting in emitting X-rays similar to X-rays produced in tubes.⁷⁹

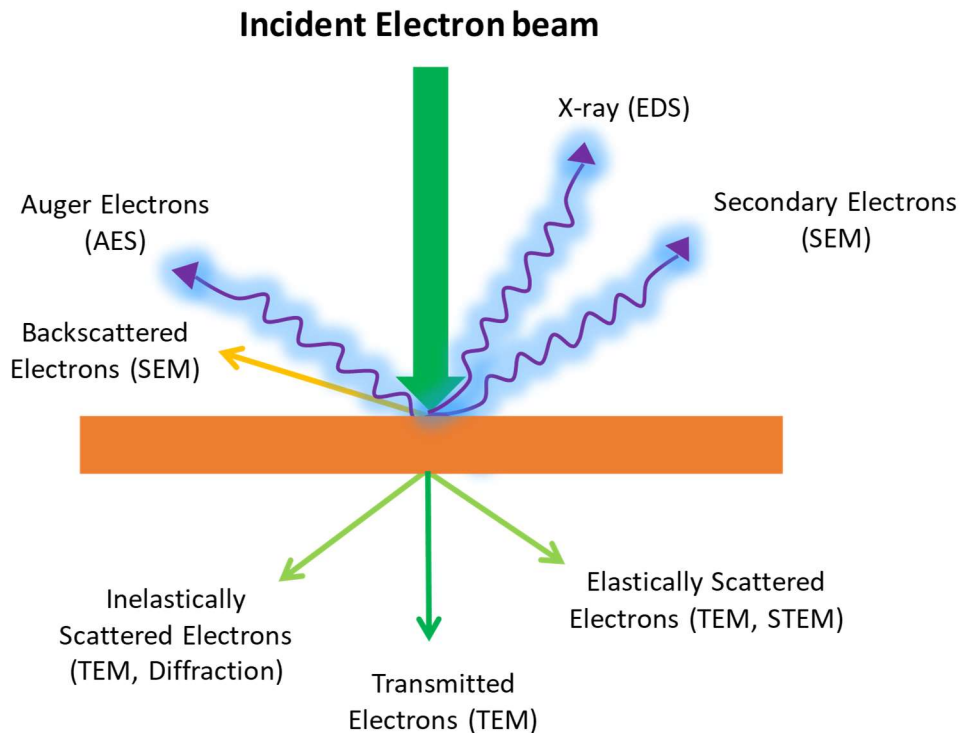


Figure 2.5. A simplified scheme of all possible interactions of an electron beam with a target substrate.⁷⁹

The X-rays produced from an element is unique and can be useful in determining the composition through energy dispersive spectroscopy (EDS) with a detector positions above the sample. Few electrons are re-emitted or backscattered from the sample, those are typically not used in a TEM but are important for SEM.⁷⁹

Several instruments have been used in this study to acquire basic imaging i.e. low resolution TEM (LRTEM), HRTEM, diffraction, and elemental maps. A Zeiss Libra 120 was utilized to acquire LRTEM at 120 kV and SAED as well. FEI Titan 8300 microscope

equipped with a Gatan 794 multi-scan camera operating at 200 kV used to acquire elemental maps. A separate FEI Titan 8300 electron microscope operating at 300 kV was used to collect HRTEM. All the samples in this study, were prepared by dropping a dilute solution (similar dilution to solution UV-Vis) of nanocrystals dispersed in hexanes onto an ultra-thin carbon coated Cu TEM grid after the removal of the Formvar layer by washing with chloroform (CHCl_3).

2.3 Energy Dispersive Spectroscopy

Energy dispersive spectroscopy (EDS) within a SEM or TEM provides the average composition of a sample. One advantage with EDS technique is it can monitor a much larger area of sample at once.⁷⁹ X-rays emitted from excited atoms are measured in EDS. Each element has unique atomic energy levels, it is possible to qualitatively analyze elemental composition. The emission of X-rays from substrates has already been described in sections 2.1 and 2.2 and Figure 2.5. In both TEM and SEM, the electron beams are used for imaging are simultaneously exciting the sample and subsequently inducing X-ray emission. The limitations of EDS are typically the energy of the incident electrons, spectral overlap, and range of the detectors.⁷⁹

In this study, dried powder nanocrystal samples were spread onto a conductive carbon tape attached to an aluminum stub. No further sample preparation was needed before loading the samples into Hitachi SU-70 running at 20 kV accelerating voltage. The compositions obtained from the EDS measurements averaged over five separate areas.

2.4 X-ray Photoelectron Spectroscopy

Nanoparticles are known for large surface to volume ratios with as much as 60% of atoms being on the surface of the particle. The surface chemistry plays a vital role in

many nanoparticle properties. X-ray photoelectron spectroscopy (XPS) is one of the most powerful techniques for surface analysis.⁸⁰ XPS is one of the few methods of identifying atomic composition, detail on their bonding environment, and oxidation state of the elements.^{81,82} Moreover, even though it is a surface technique, the X-rays penetration depth is around 5-10 nm. Therefore, in small enough nanocrystals, both the surface and the core of the particle is measured.⁸⁰

Similar to X-ray tube (Figure 2.1), XPS also uses X-rays as source to bombard the surface, as the X-ray photons strike with atomic electrons they are kicked out as photoelectrons.⁸⁰ The energy required to kick out the electrons is equivalent to the electrons binding energy. The unique electron binding energy of each element allows to differentiate elements, individual orbitals, and chemical environment. A high-level vacuum is compulsory for accurate XPS measurements. The ultra-high vacuum requirement has driven the design of XPS instruments. To avoid contamination during outgassing, samples are loaded through a preparation chamber which pumps samples down (Figure 2.6). The analysis chamber is maintained under a constant level of ultra-high vacuum. The analysis chamber is equipped with certain extra items for charge control such as ion beams for etching and Argon flow. Al K α is the X-ray source of choice due to its production of high energy and narrow line width. The analyzed high-energy photoelectrons require a method to maintain sensitivity and adequately resolve closely spaced peaks. The hemispherical analyzer can switch between the desired effects though variable voltage which will affect the path length of the electron for detection.⁸⁰

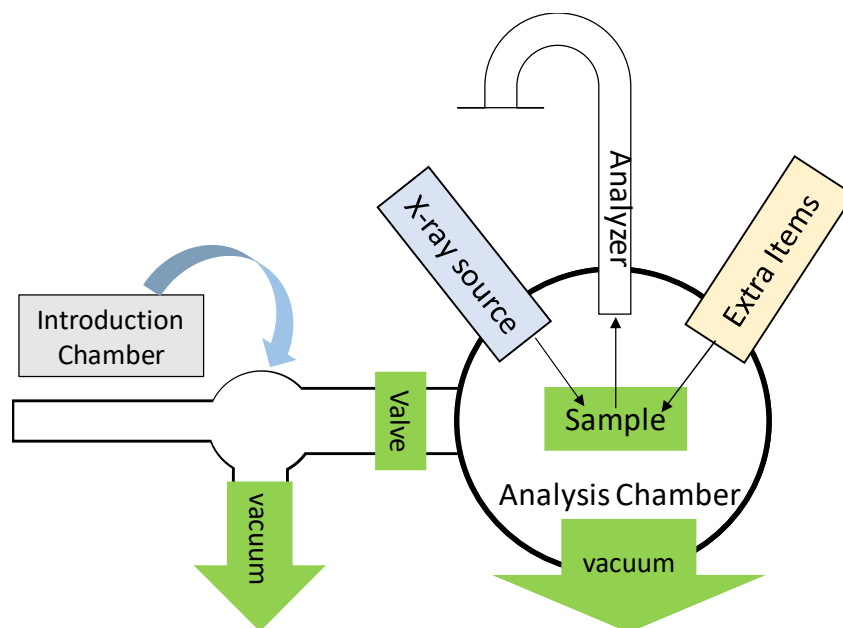


Figure 2.6. Diagram of X-ray photoelectron spectrometer with a hemispherical detector.⁸⁰

In this study, a Thermofisher ESCALAB 250 equipped with Al $\text{K}\alpha$ source. Dried powder nanocrystals were pressed onto indium foil and taped to an aluminum sample holder with conductive carbon tape. To avoid oxidation and atmospheric contamination, samples were stored and prepared in a glove box then loaded into the instrument using an air free sample loader. The pass energy was 20 keV and an average of 30 scans was used. Charge correction was carried out with adventitious carbon and double checked against indium.

2.5 Raman Spectroscopy

Raman spectroscopy has been developed to probe molecular vibrations that can provide substantial information on chemical makeup of a sample. Raman is a unique spectroscopy, it measures changes in energy of scattered photons.⁸³ The scattering

phenomenon occurs by the photons interaction with a molecules vibrational induced dipole.⁸³ As molecular vibrations are well known for many organic and inorganic compounds, Raman can be used to screen nanoparticle systems for surface ligands, unwanted amorphous impurities, and more importantly changes in composition.⁸³

The fundamental physics behind the Raman measurement is its biggest limitation. Photon interactions with phonon's have a very low probability which is impaired by how infrequent phonon are in comparison to incident photons. To obtain a reasonable signal is collected it is necessary to input extremely high intensity of photon, that is why Raman instruments utilize laser sources (Figure 2.7).⁸³ When the photons hit the sample some of them are inelastically scattered, the scattered light is then channeled through a grating and the change in energy with respect to the incident beam, is measured called as the Raman shift. The control behind this lays in the dependency on vibrational modes of sample. For example, if the molecules being examined are visualized as two balls connected by a spring it is easy to understand why (Figure 2.8). The Raman shift is proportional to the frequency and amplitude of the vibrations between the two balls. If the mass of one of the balls changes or the distance between them the frequency will decrease resulting in a smaller Raman shift.⁸³

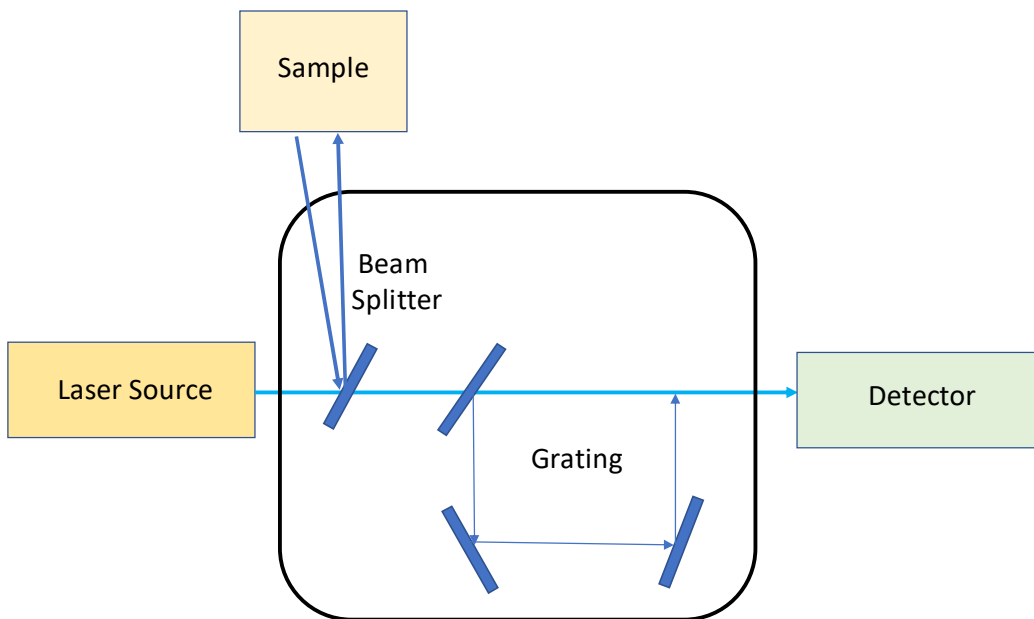


Figure 2.7. Block diagram of Raman spectrometer.⁸³

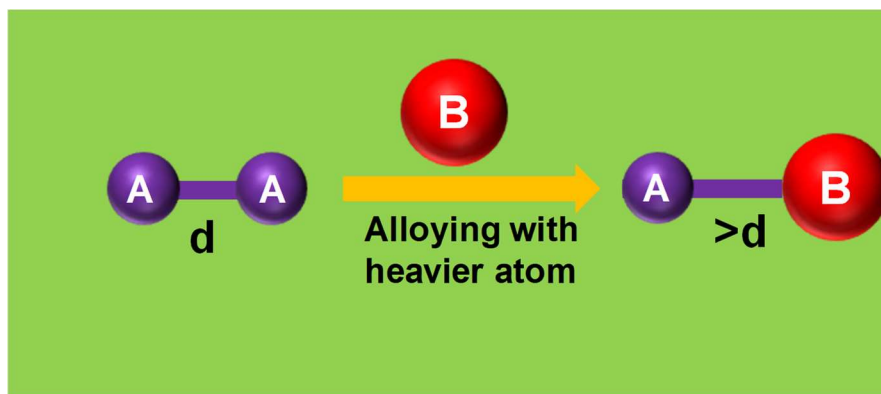


Figure 2.8. A schematic of lighter atom (A) replaced by heavier atom (B) results in increase in bond length, subsequently Raman vibrational frequency decreases.

In this dissertation study, powdered samples were analyzed with a 532 nm laser in a Horiba LABram HR Evolution Confocal Raman Spectrometer. Nanocrystal powder samples were placed on an aluminum substrate and maintained 50-100% laser strength to probe the structural changes in the sample.

2.6 UV-Visible absorption spectroscopy

UV-Vis spectroscopy provides absorption/reflectance of compounds and materials in ultraviolet-visible spectral region (200 – 800 nm). Measuring the optical transitions of compounds and materials using UV-Vis is one of the oldest method to study chemical physics. Energy levels in compounds: HOMO-LUMO for molecules and bandgaps for materials, are studied by measuring across the UV-Vis region and monitoring light input vs transmitted light. The set up includes a series of mirrors and beam splitters allowing to simultaneous measurements of a sample with respective to a reference (Figure 2.9).^{1,84}

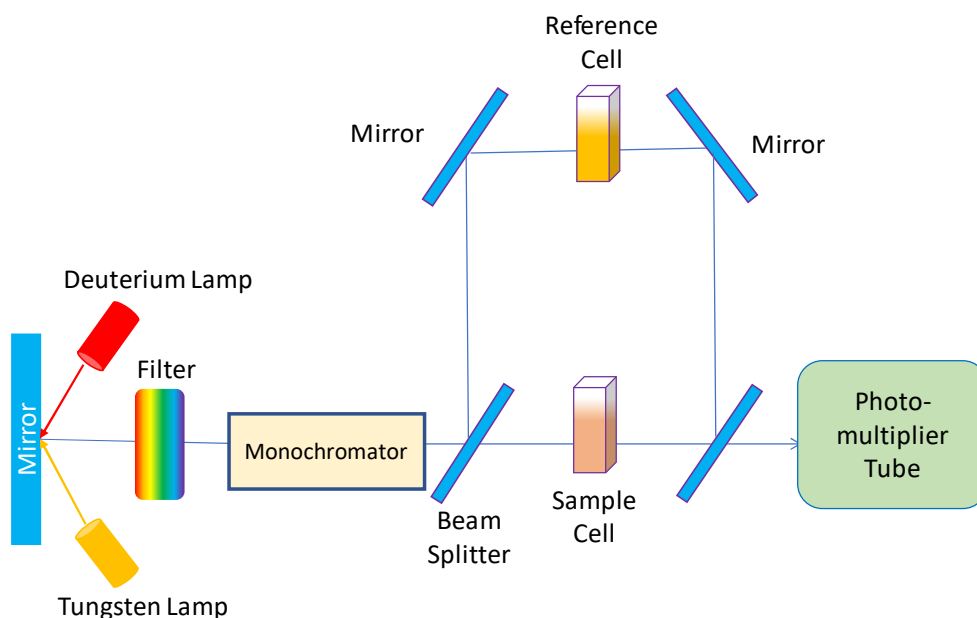


Figure 2.9. Schematic of a multi-source double beam UV-Vis spectrometer.

The absorption value is basically the difference between sample and reference values. Typically, the measurement is carried out with the analyte dissolved in an optically transparent solvent. The absorption is related to the concentration (c) of the analyte, the

path length (l) through the solution, and the molar absorptivity (ϵ) of the analyte by the Beer-Lambert Law (equation 2.3).^{1,84}

$$A = \epsilon lc \quad (2.3)$$

The onset of the absorption can be equated to the bandgap in semiconductors. Below the onset value, it does not have enough energy to induce excitation from valence band to the conduction band. Also, beyond the onset value, the absorption can be related to the density of states. In nanocrystals, this technique plays an important role and can be utilized to explore the changes in gap energy as a function of size of nanoparticle and quantum confinement.^{1,85}

In this study, all solution-based measurements were performed soon after the isolation of as prepared nanoparticles. The samples were dissolved in CHCl_3 and transferred to a quartz cuvette. Absorption spectra were collected in a Cary 6000i UV-Vis-NIR spectrometer (Agilent Technologies).

2.7 Diffuse Reflectance Spectroscopy

Diffuse reflectance spectroscopy analyzes the scattered light in the form of reflectance which occur in addition to absorption from a sample. From a practical standpoint, majority of semiconducting applications utilize solid samples. It is important to have a better understanding of light mater interactions of an aggregated solid, diffuse reflectance spectroscopy serve this purpose. In this reflectance spectroscopy, the reflected light is recollected and can be evaluated by utilizing Kubelka-Munk remission function (equation 2.4).^{86,87} In this method, the percent reflectance (R) is equated to a

pseudo-absorption coefficient (K/S) which is similar to that obtained through transmission experiments.^{86,87}

$$f_{KM}(R) = \frac{(1-R)^2}{2R} = \frac{K}{S} \quad (2.4)$$

To estimate the bandgap of semiconductors, Kubelka-Munk function is only one method which does not account for the type of transition occurring, meaning that the measurements are taken in reflectance and the outcome is absorbance.⁸⁷ Tauc analysis is another method to probe bandgaps in which the absorption probabilities are based on crystal momentum and photon-phonon interactions. Applying the Tauc equation to reflectance the absorption coefficient (α) is similar to k/s term from the Kubelka-Munk formula.⁸⁸ By using the absorption ($\alpha h\nu$) and density of states $(h\nu - E_g)^{1/n}$ in semiconductors, the Tauc equation can be seen equation 2.5, where $h\nu$ is the energy of an incident photon, A is proportionality coefficient, and E_g is the bandgap. The exponent n value is dependent on the interband transition being modeled, $\frac{1}{2}$ for allowed indirect, 2 for allowed direct.⁸⁸

$$(\alpha h\nu)^n = A (h\nu - E_g) \quad (2.5)$$

The practical difficulty with Tauc equation was that never meant for application to nanocrystals since it was developed for bulk semiconductors. Though it has been accepted for nanocrystals in literature, the Tauc analysis results should be taken with careful consideration.⁸⁸

In this dissertation study, energy-gaps were estimated by Tauc and Kubelka-Munk. In both methods, absorbance value is considered as the intersection point of the linear

extrapolation of the absorption onset and baseline. The nanocrystals were dispersed in a BaSO₄, a non-absorbing medium to minimize the scattering. All measurements were performed with a Cary 6000i UV-Vis-NIR spectrometer (Agilent Technologies) equipped with an internal DRA 2500 integrating sphere.

2.8 Photoluminescence Spectroscopy

Photoluminescence (PL) refers to emission of light by excited molecules that absorb energy from an excitation source. This emission spectroscopy is a very well-known technique for the analysis of the electronic structure and photophysical properties of semiconductor NCs. Photo and electrical excitations are of the greatest interest in semiconductor nanocrystals owing to their potential applications in devices such as solar cells, LEDs, detectors, and sensors.^{5,89}

Number of electronic states are involved in the excitation and emission process due to rotational and vibrational energy levels. Upon excitation, an electron is bumps from a singlet ground state (S_0) to an excited singlet state (S_1).⁵ The relaxation of the excited electron occurs from S_1 to S_0 through the release of a photon is called fluorescence (Figure 2.10).⁸⁹ The energy of the released photon will directly correspond to the energy-gap between the two states involved in the process. The relaxation occurs rapidly typically on the order nano-micro second time scales. However, fluorescence is not the only pathway that an excited electron can relax through. If the excitation energy is higher than that of the energy-gap, the excited electron must first relax from the higher energy levels through a non-radiative process. Release of heat energy in the form of molecular vibration is one form of non-radiative relaxation. Intersystem crossing to an excited triplet state (T_1) is another pathway of non-radiative processes.^{89,90} Typically, triplet states are formed by

impurities or defects and have lower energy than the S_1 state. The Intersystem crossing (ISC) process and subsequent phosphorescence results in much longer lifetimes (3-5 orders of magnitude) for the excited states than that of fluorescence.

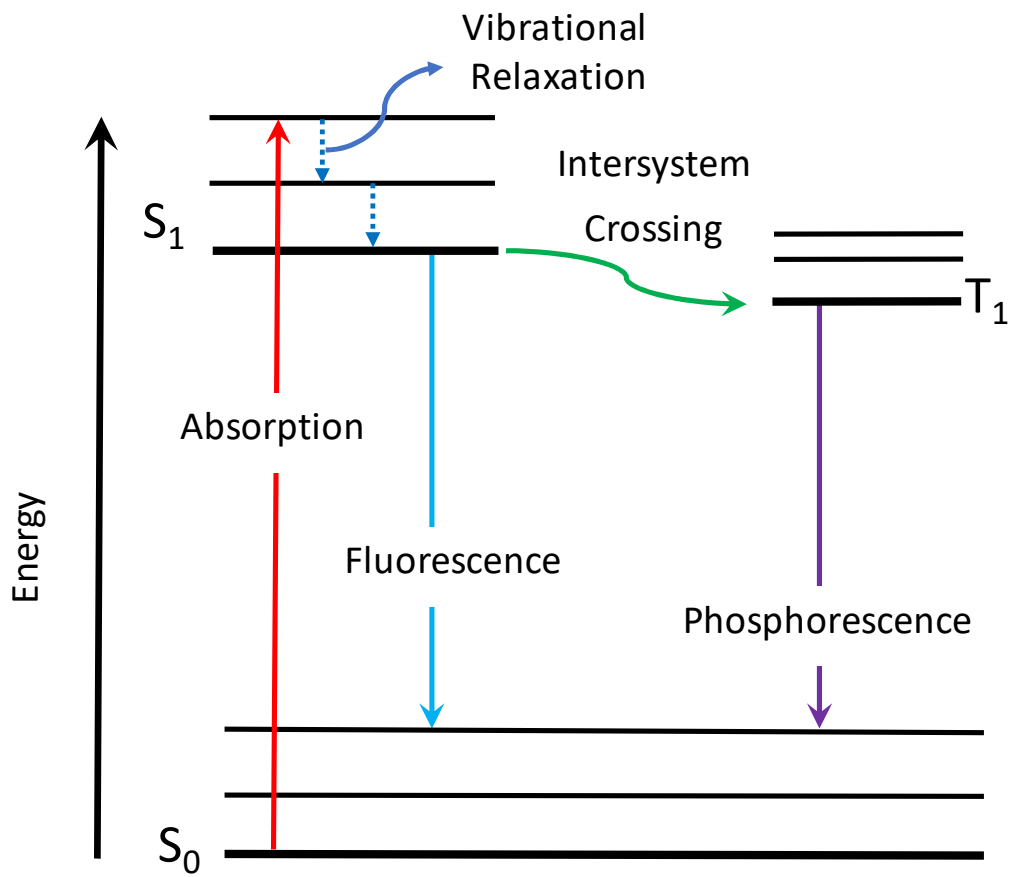


Figure 2.10. A schematic illustration of absorption followed by fluorescence and phosphorescence processes under the effect of light energy.⁸⁹

Quantum confined nanocrystals PL measurements are used to probe size and composition dependent optical properties.⁸⁹ To understand energy levels and excitonic behavior is advantageous in semiconducting devices designing. Time resolved PL (TRPL) measurements can be employed using ultra-fast spectroscopy.⁹¹ By combining temperature and excitation density studies, it is possible to develop overall understanding

on light-mater interactions of nanocrystals.⁹⁰ In this study, A frequency doubled Ti: sapphire laser (385 nm wavelength, 150 fs pulse width, and 160 kHz to 80 MHz repetition rate) was utilized as excitation source to record steady-state PL and TRPL spectra of nanocrystals dispersed in CCl₄ and drop casted (~5 μL increments of solution for a thick layer) onto clean Si substrates.

2.9. Fourier Transform Infrared (FT-IR) Absorption Spectroscopy

Infrared spectroscopy is a commonly used spectroscopic technique that measures IR frequencies of chemical functional groups of a sample by positioning the sample in the optical path of an incident IR light.^{34,64,92} Infrared spectroscopy typically involves transitions between vibrational or rotational energy levels that have low energy (4000 – 400 cm⁻¹). The compound must undergo a net change in dipole moment in order to absorb IR radiation. By using the interferometer and Fourier transform data processing, FT-IR has been proven a convenient, inexpensive, fast and non-destructive material characterization technique. A representative a simple illustration of a typical FT-IR set-up shown in Figure 2.11, which includes; (i) the Nernst glower source, (ii) the Michelson interferometer, and (iii) the triglycine sulfate pyroelectric detector.⁹² The Michelson interferometer contains a KBr beam splitter.^{86,93} To generation of an interferogram, both fixed and movable mirrors are essential. Since nanocrystals possesses high surface to volume ratio, FT-IR is one of earliest and most popular techniques to probe surface chemical activities. As molecular vibrations are dependent on the surrounding chemical bonds involved, each molecule exhibits a unique vibrational absorption frequency that referred as a “fingerprint” of that specific material. Nowadays, the main use of FT-IR in nanoparticle characterization is the identification of specific functional groups, surface

bound solvents, and surfactants present on the surface. The FT-IR spectra of all the samples in this study were recorded using a Nicolet 670 Fourier transform infrared (FT-IR) instrument equipped with a single reflection diamond ATR attachment.^{86,92,94}

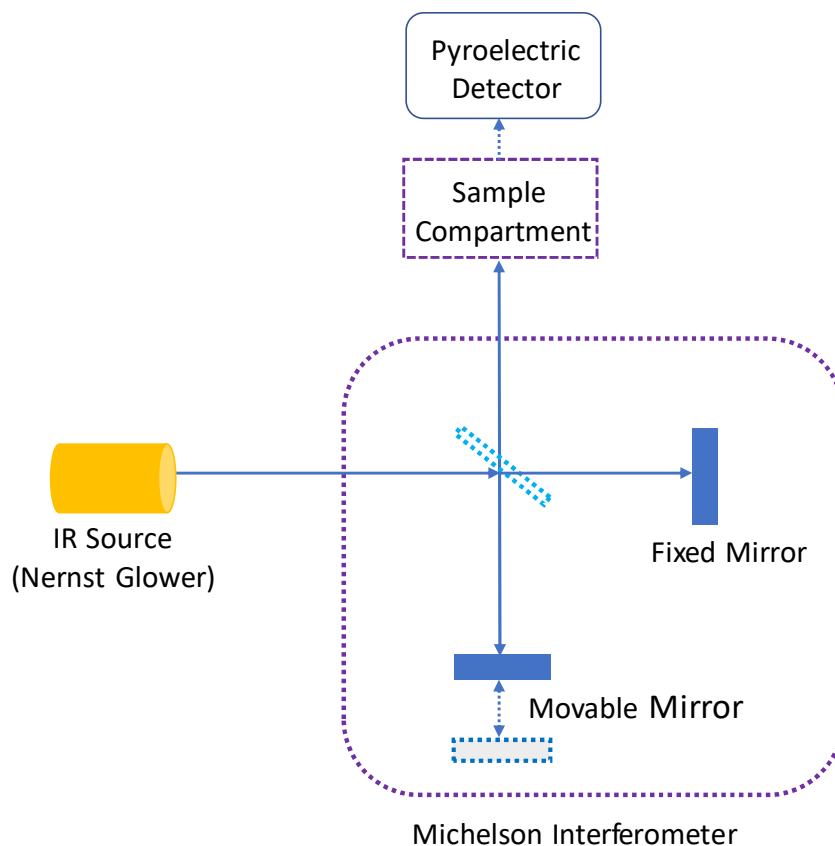


Figure 2.11. A typical FT-IR set-up utilizing a Nernst Glower source, a Michelson interferometer and a pyroelectric detector.⁹²

2.10. Time-Resolved Photoluminescence (TRPL)

Time Resolved Photo-Luminescence (TRPL) is an experimental technique measured by exciting luminescence from a sample with a pulsed light source. Then, recording the subsequent decay of photoluminescence as a function of time.⁹¹ The electron-hole pair generated by the short pulse of light decay to lower energy level of the

measuring sample and can subsequently recombine to emit light. The light emitted in this process is composed of a set of wavelengths corresponding to transition energies of the sample. Consequently, to measure the transition energies and their lifetimes, the optical spectrum provides the means as a function of time. As the decay times are on the order of picoseconds or microseconds, the intensity of light emitted is generally weak. A conventional spectrum analyzer cannot offer required resolution. So, it is necessary to use a streak camera to provide better resolution.⁹¹

As can be seen in Figure 2.12, TRPL via time-correlated single photon counting (TCSPC) is specifically suited for fast charge carrier dynamics for III-V or II-VI semiconductors.⁹¹ In TCSPC, it can be measurable that the time between sample excitation by a pulsed laser and the arrival of the emitted photon using a detector. A defined “start” signal requires in TCSPC to provide the electronics steering the laser pulse/photodiode, and a defined “stop” signal as well to allow the detection with single-photon sensitive detectors. The time decay measurement is repeated many a times for the interpretation of the fluorophores emission. The delay times are collected into a histogram which plots the occurrence of emission over time.⁹¹

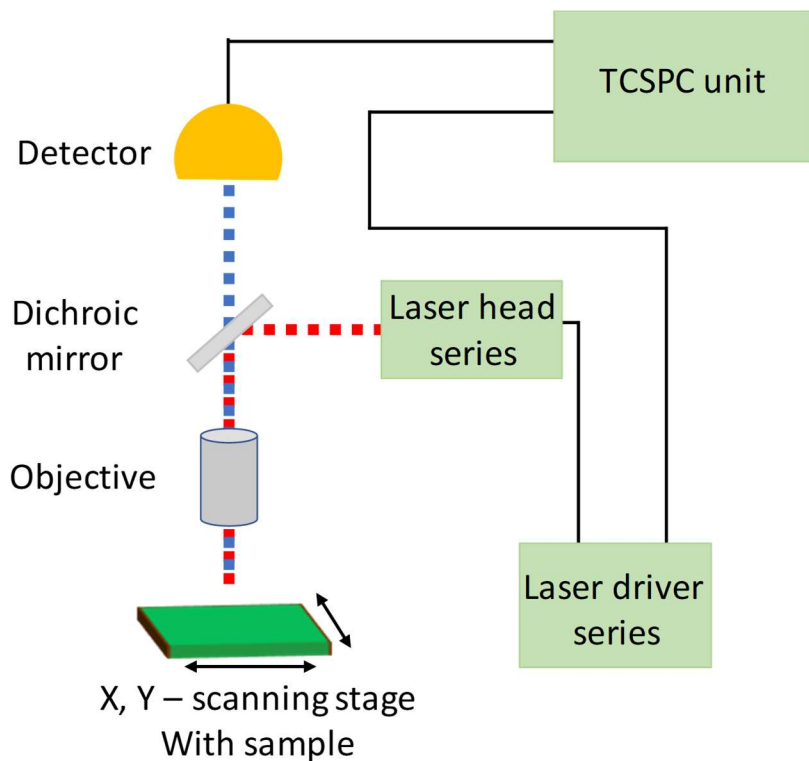


Figure 2.12. Schematic diagram of the experimental setup of a fluorescence lifetime imaging microscope time-resolved photoluminescence.⁹¹

CHAPTER 3

Ge_{1-x}Sn_x Alloy Quantum Dots with Composition-Tunable Energy Gaps and Near-Infrared Photoluminescence

3.1 Introduction

Group-IV semiconductors show immense potential in a number of optical technologies including solar energy conversion, photo-detection, chemical sensing, and imaging.^{16,95-97} However, indirect energy gaps of crystalline Si (1.1 eV) and Ge (0.67 eV) limit their widespread application in optical devices, significantly decreasing the absorption cross section and emission efficiency.^{16,96} Thus, a number of different methods, including application of mechanical stress,⁴⁰ heteroepitaxial growth,⁹⁸⁻¹⁰⁰ and alloying with Sn,^{21,23,101} have been investigated to produce direct gap Group IV semiconductors with promising photophysical properties. Specifically, admixing of α -Sn into crystalline Si and Ge has been shown to decrease the energy of the Γ (direct) valley of conduction band relative to the L (indirect) valley producing direct bandgap Si_{1-x}Sn_x or Ge_{1-x}Sn_x alloys.^{21,23,100-102} This transition stems from the expansion of cubic Si and Ge structure induced by α -Sn, the diamond-like structural equivalent to Si and Ge.¹⁰² Theoretical and experimental reports suggest an indirect to direct-gap cross over in bulk Ge_{1-x}Sn_x when Sn composition reaches 6.3–11%.^{21-24,102,103} In addition, incorporation of

Sn enhances the electron and hole mobility, making direct-gap $\text{Ge}_{1-x}\text{Sn}_x$ alloys promising candidates for high speed optoelectronics.^{104,105} Unfortunately, the fabrication of homogeneous alloys has proven difficult, because of large discrepancies (~14-19%) in lattice constants and much higher cohesion energies of Si and Ge compared to that of α -Sn.¹⁰⁶ Moreover, the admixture of α -Sn (bandgap (E_g) = 0.08 eV) significantly reduces the energy gaps (0.35–0.80 eV for $x = 15.0$ – 0.00 %)⁹ and promotes the metallic character of direct-gap $\text{Ge}_{1-x}\text{Sn}_x$ alloys, eliminating any potential application in visible to near IR optoelectronics.

To promote direct-gap behavior and expand the optical range, quantum confinement effects have been utilized to produce low-dimensional nanostructures of $\text{Ge}_{1-x}\text{Sn}_x$ alloys.^{31,32,49-51} Quantum dots (QDs) and nanowires (NWs) of $\text{Ge}_{1-x}\text{Sn}_x$ have been reported both at strongly-confined and weakly-confined size regimes that promote wider direct energy gaps from visible to near IR spectrum.^{31,32,49-51,105,107-109} Recently, our group reported the first colloidal synthesis of $\text{Ge}_{1-x}\text{Sn}_x$ alloy QDs with varying sizes (~2-23 nm) and Sn compositions ($x = 0$ –28%).²⁰ The larger $\text{Ge}_{1-x}\text{Sn}_x$ alloys (15–23 nm) exhibit minimum or no confinement effects and absorption energy gaps (0.2–0.4 eV) that are red-shifted from bulk Ge, similar to those reported for bulk $\text{Ge}_{1-x}\text{Sn}_x$ thin film alloys. In contrast, smaller $\text{Ge}_{1-x}\text{Sn}_x$ alloy QDs (~2–5 nm) show strong confinement effects with composition-tunable absorption onsets and visible PL, exclusively for ultra-small QDs (1.8–2.2 nm).^{20-23,47} A recent theoretical study suggests that admixture of α -Sn into Ge significantly increases the oscillator strengths, with the potential to produce brightly emissive QDs with high molar absorptivity and PL efficiency.⁴⁷ Nonetheless, size- and composition-dependent PL properties of near IR emitting $\text{Ge}_{1-x}\text{Sn}_x$ QDs have not been

properly quantified to date, owing in part to high polydispersity of as-synthesized particles and significantly low PL quantum yields.³¹ More recently, inorganic passivation of $\text{Ge}_{1-x}\text{Sn}_x$ QDs has been attempted to produce $\text{Ge}_{1-x}\text{Sn}_x/\text{CdS}$ core/shell QDs.⁵¹ However, resultant alloys exhibit broad-band IR PL with no size (8–13 nm) or composition ($x = 5\text{--}25\%$) dependent tunability. As such, the synthesis of $\text{Ge}_{1-x}\text{Sn}_x$ alloys with enhanced near IR absorption and tunable near IR PL has proven a challenging task to further expand the optical window of direct-gap and silicon-compatible Group IV alloys.

Herein, we report the first colloidal synthesis of narrowly disperse ($3.3 \pm 0.5\text{--}5.9 \pm 0.8$ nm), near IR emitting (1.62–1.31 eV) $\text{Ge}_{1-x}\text{Sn}_x$ alloy QDs with wide range of Sn compositions ($x = 1.5\text{--}20.6\%$) via alkyllithium reduction of precursor halides (GeI_2 and SnCl_2). Control over QD diameter and composition was achieved by employing hexadecylamine (HDA) as the surfactant and changing the molar ratio of halides: reducing agent. The absorption energy gaps were tuned over a wide spectral region (1.72–0.84 eV) for narrowly disperse $\text{Ge}_{1-x}\text{Sn}_x$ QDs with $x = 1.5\text{--}9.1\%$. As-synthesized alloy QDs exhibit intense near IR emissions (1.62–1.31 eV for $x = 1.5\text{--}5.6\%$) and a clear red shift in PL energy with increasing Sn composition. It was found consistently that at room temperature (295 K) the PL decay of the alloy QDs was on the order of 10–20 ns, while it was ~ 3 orders of magnitude slower (1–10 μs) at low temperature (15 K). Such temperature dependence of carrier dynamics suggests clearly distinguishable contributions from dark and bright excitons as well as the interplay between surface traps and core electronic states.

3.2 Experimental Section

3.2.1 Materials. Germanium diiodide (99.99+ %) and tin dichloride (99.9985 %) were purchased from Strem Chemicals and Alfa Aesar, respectively. n-butyllithium (BuLi, 1.6 M in hexane) was purchased from Sigma Aldrich. 1-octadecene (ODE, 90%) was purchased from Fisher Scientific. 1-Hexadecylamine (HDA), toluene, CCl₄, and methanol of ACS grade were purchased from Acros. ODE was dried at 120 °C under vacuum for 1 h. Methanol and toluene were dried over molecular sieves and Na, respectively and distilled under N₂ prior to use.

3.2.2 Synthesis of 3-6 nm Ge_{1-x}Sn_x Alloy QDs.

In a typical synthesis of 3–6 nm Ge_{1-x}Sn_x QDs, 3.00 g of HDA in a 50 mL three neck round bottom flask was fitted with a condenser and degassed under vacuum at 115 °C for 1 h. This set up was cooled to room temperature and transferred to a nitrogen glovebox. Then, appropriate amounts of GeI₂ and SnCl₂, 0.6 mmol of metal total, were combined with HDA and the sealed set up was connected to a Schlenk line. This mixture was degassed at 115 °C for 1 h to produce a homogeneous orange color solution. Then the reaction was flushed with nitrogen for 15 min and the temperature was raised to 230 °C, at which point 1.16–1.48 mmol (Table 3.1) of BuLi in 3.0 mL of ODE was swiftly injected. The injection caused a temperature drop to 209–213 °C and the mixture was reheated to 300 °C within 15 min to produce Ge_{1-x}Sn_x alloy QDs. The flask was then rapidly cooled with compressed air to ~100 °C and 10 mL of freshly distilled toluene was added. Then, 10 mL of freshly distilled methanol was added, followed by centrifugation at 4000g to precipitate the alloy QDs. The supernatant was discarded and the QD precipitate

was purified by dispersing in toluene and subsequent precipitation with methanol 2–3 times under ambient conditions.

Table 3.1. The molar ratio of GeI₂, SnCl₂, and n-BuLi used in the synthesis of 3.3 ± 0.5–5.9 ± 0.8 nm Ge_{1-x}Sn_x (x = 1.5 – 20.6%) alloy QDs. The total moles of GeI₂ and SnCl₂ was fixed at 0.6 mmol.

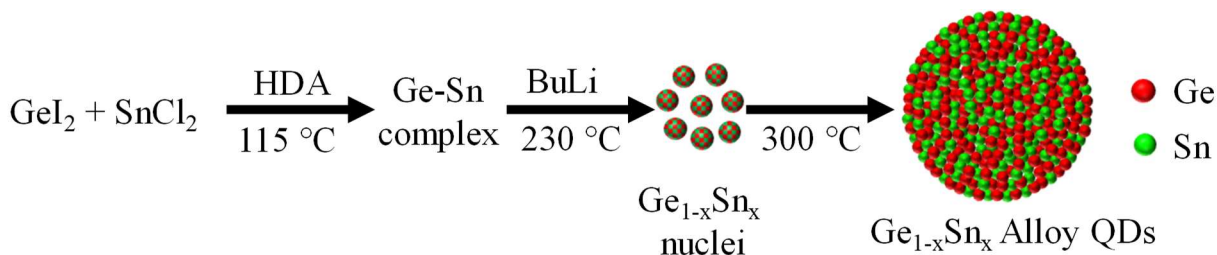
Sample	GeI ₂ (mmol)	SnCl ₂ (mmol)	n-BuLi (mmol)
Ge _{0.985} Sn _{0.015}	0.591	0.0090	1.48
Ge _{0.981} Sn _{0.019}	0.5886	0.0114	1.46
Ge _{0.973} Sn _{0.027}	0.5838	0.0162	1.43
Ge _{0.966} Sn _{0.034}	0.5796	0.0204	1.42
Ge _{0.958} Sn _{0.042}	0.5748	0.0252	1.40
Ge _{0.944} Sn _{0.056}	0.5664	0.0336	1.38
Ge _{0.936} Sn _{0.064}	0.5619	0.0381	1.36
Ge _{0.921} Sn _{0.079}	0.5526	0.0474	1.34
Ge _{0.909} Sn _{0.091}	0.5454	0.0546	1.30
Ge _{0.888} Sn _{0.112}	0.5328	0.0672	1.25
Ge _{0.846} Sn _{0.154}	0.5076	0.0924	1.20
Ge _{0.794} Sn _{0.206}	0.4764	0.1236	1.16

3.3 Results and Discussion

The lattice mismatch between Ge and Sn (~14%) causes a great challenge to produce homogeneous Ge_{1-x}Sn_x alloys.^{9,23} Because of its covalent bonding nature Ge requires high temperature (300-400 °C) to crystallize whereas Sn melts above 231 °C.¹¹⁰⁻

¹¹² Hence these two elements are poorly miscible (~1% equilibrium solubility of Sn in bulk Ge) in the solid state. With consideration of aforementioned complications, we have developed a unique synthetic strategy to produce $3.3 \pm 0.5 - 5.9 \pm 0.8$ nm $\text{Ge}_{1-x}\text{Sn}_x$ alloy QDs with Sn content up to 20.6%. Colloidal synthesis provides a unique platform to incorporate significant Sn into Ge without altering its diamond cubic structure and simultaneously expanding the energy gaps owing to unique size confinement effects. Previous wet-chemical reports utilized oleylamine/octadecene as the surfactant/solvent and constant amount of reducing agent (n-butyllithium, BuLi) to produce 3.4–4.6 nm $\text{Ge}_{1-x}\text{Sn}_x$ alloy QDs.³¹ However, the fixed amount of n-BuLi resulted in minimum control over nanocrystal size (size dispersity = 15–25% for $x = 0.0 - 11.0\%$) because Sn promotes the growth of larger polydisperse QDs.³¹ Herein, by manipulating the nucleation and growth kinetics, a modified synthetic strategy has been developed to produce phase-pure $\text{Ge}_{1-x}\text{Sn}_x$ alloy QDs with narrow size dispersity (11–15%) and nearly spherical morphology (Scheme 3.1). The size and composition of the alloy QDs were effectively controlled by varying the amount of n-BuLi across wide a range of Sn compositions (0.58–0.75 mmol of n-BuLi for $x = 20.6-1.5\%$) to equalize the growth effects of Sn.

Scheme 3.1. An Illustration of the Synthesis of Near Infrared Emitting $\text{Ge}_{1-x}\text{Sn}_x$ Alloy QDs.



Powder X-ray diffraction (PXRD) patterns of $\text{Ge}_{1-x}\text{Sn}_x$ alloy QDs indicate the phase purity of particles and Bragg reflections corresponding to diamond cubic Ge structure (Figure 3.1A). No diffraction peaks corresponding to GeO_2 , $\alpha\text{-Sn}$, or $\beta\text{-Sn}$ (tetragonal Sn) impurity phases were detected suggesting the production of homogeneous alloys. The major diffraction peaks were indexed to (111), (220), and (311) planes of diamond-cubic Ge (JCPDS # 01-089-5011). The peak broadening is quite significant as a result of Scherrer scattering, consistent with the synthesis of nanoalloys.¹¹³ The crystallite sizes computed using Scherrer formula are in the range of $2.01 \pm 0.2 - 3.82 \pm 0.2$ nm for $x = 1.5\text{--}20.6\%$. With increasing Sn, diffraction patterns shift to lower 2θ angles owing to expansion of cubic Ge structure by $\alpha\text{-Sn}$. Unlike the bulk lattice constants, which show significant bowing, average lattice parameters calculated from diffraction patterns indicate near linear expansion of the cubic Ge structure with increasing Sn, consistent with the Vegard's rule (Figure 3.1B).¹¹⁴ Lattice constants for cubic Ge and $\alpha\text{-Sn}$ are 5.66 and 6.49 Å, respectively. In contrast, as-synthesized alloy QDs exhibit intermediate lattice parameters of 5.64–5.85 Å, further supporting the synthesis of strain-free, homogeneous nanoalloys.

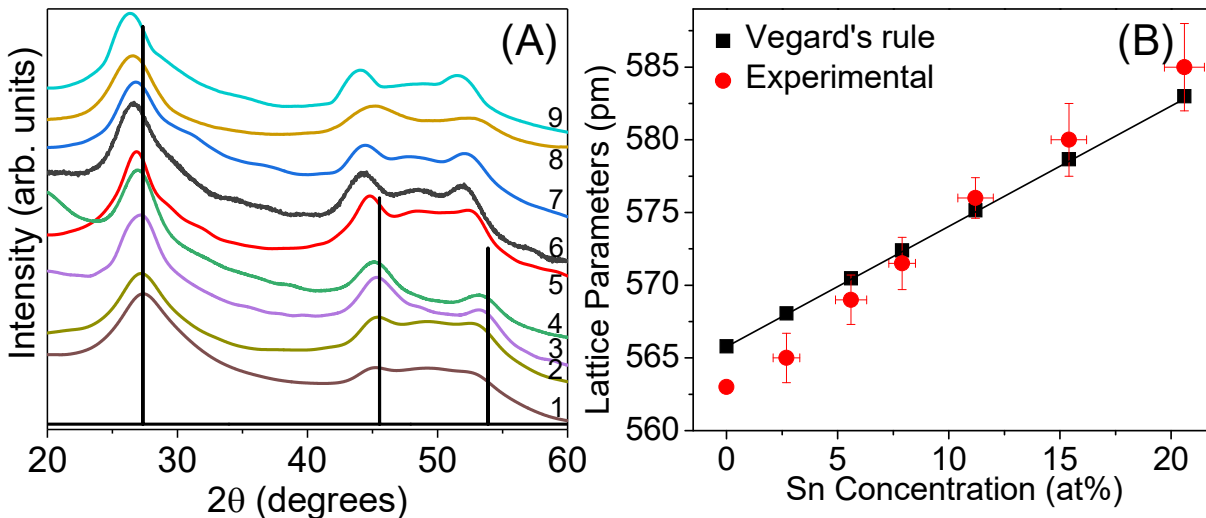


Figure 3.1. (A) PXR D patterns of $\text{Ge}_{1-x}\text{Sn}_x$ alloy QDs with varying Sn composition: (1) $x = 1.5\%$, (2) $x = 2.7\%$, (3) $x = 5.6\%$, (4) $x = 6.4\%$, (5) $x = 7.9\%$, (6) $x = 9.1\%$, (7) $x = 11.2\%$, (8) $x = 15.4\%$, and (9) $x = 20.6\%$. The ICDD-PDF overlay of diamond cubic Ge (JCPDS # 01-089-5011) is shown as vertical black lines. (B) A plot illustrating the variation of experimental (obtained from PXR D analysis) and theoretical (calculated using Vegard's rule) lattice parameters of selected QDs as a function of Sn composition. Experimental lattice parameters and Sn compositions were obtained from analysis of 3–5 individually prepared samples.

Raman spectroscopy was utilized to further study the alloying effects in $\text{Ge}_{1-x}\text{Sn}_x$ QDs. Crystalline Ge exhibits a Raman peak at 300 cm^{-1} that corresponds to the optical phonon mode of Ge–Ge bonds.¹¹⁵ As heavier Sn atoms are incorporated into the Ge crystal, a systematic red shift of Ge–Ge phonon mode is expected.¹¹⁵ Nonetheless, single element Ge QDs exhibit a broad, red shifted Ge–Ge peak at $297\text{--}300\text{ cm}^{-1}$ owing to phonon confinement effects.^{51,116} Therefore, the combined effects of phonon confinement

and Sn induced shifting cannot be distinguished preventing quantification of Sn-induced expansion effects in the alloy. However, a systematic red shift of the Ge–Ge phonon mode (295–287 cm^{-1} for $x = 0.000$ – 0.206) with increasing heavier Sn atoms is observed for 3.3 ± 0.5 – 5.9 ± 0.8 nm alloy QDs, consistent with the weakening (or lengthening) of the Ge–Ge bond and lattice constants computed from Vegard’s law (Figure 3.2B). The broadening of Ge–Ge peak is consistent with the increased alloy disorder and size confinement effects.^{49,86}

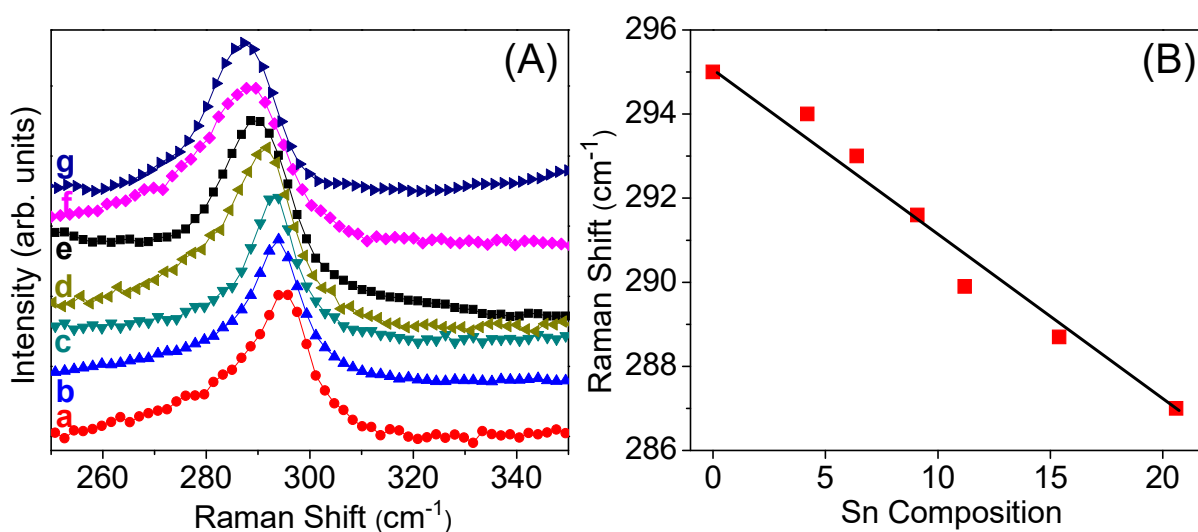


Figure 3.2. (A) Raman spectra of $\text{Ge}_{1-x}\text{Sn}_x$ alloy QDs with varying Sn compositions: (a) $x = 0.00\%$, (b) $x = 4.2\%$, (c) $x = 6.4\%$, (d) $x = 9.1\%$, (e) $x = 11.2\%$. (f) $x = 15.4\%$, and (g) $x = 20.6\%$. (B) A plot illustrating the systematic red-shifting of Ge–Ge optical phonon mode with increasing Sn composition.

TEM was used to investigate the morphology and size dispersity of alloy QDs. The LRTEM images of as-synthesized particles show narrow size dispersity (3.3 ± 0.5 – 5.9 ± 0.8 nm) and near spherical morphology across varying Sn compositions (Figure 3.3A–F). No size selective precipitation steps were employed during the isolation and purification

of samples. A slight increase in particle size with increasing Sn composition was noted possibly due to Sn-induced growth of QDs.³¹ The narrow size distribution of as-synthesized QDs was confirmed through size analysis of 150–200 particles across multiple individually prepared samples, which yields dispersity of 11–15% (Figure 3.4–3.6). In contrast, prior reports of $3.4 \pm 0.4 - 4.6 \pm 1.2$ nm $\text{Ge}_{1-x}\text{Sn}_x$ alloy QDs, produced in oleylamine, are reported to exhibit much higher size dispersity of 15–25%. The improved size and size dispersity control is attributed to strong interaction between $\text{Ge}_{1-x}\text{Sn}_x$ and HDA, which prevents the growth of larger polydisperse particles. In addition, HRTEM images of $\text{Ge}_{1-x}\text{Sn}_x$ alloy QDs indicate the single crystalline nature of particles with a lattice spacing of 3.32–3.41 Å for $x = 2.7\text{--}20.6\%$, consistent with an expanded (111) plane of cubic Ge (3.3 Å, Figure 3.7).

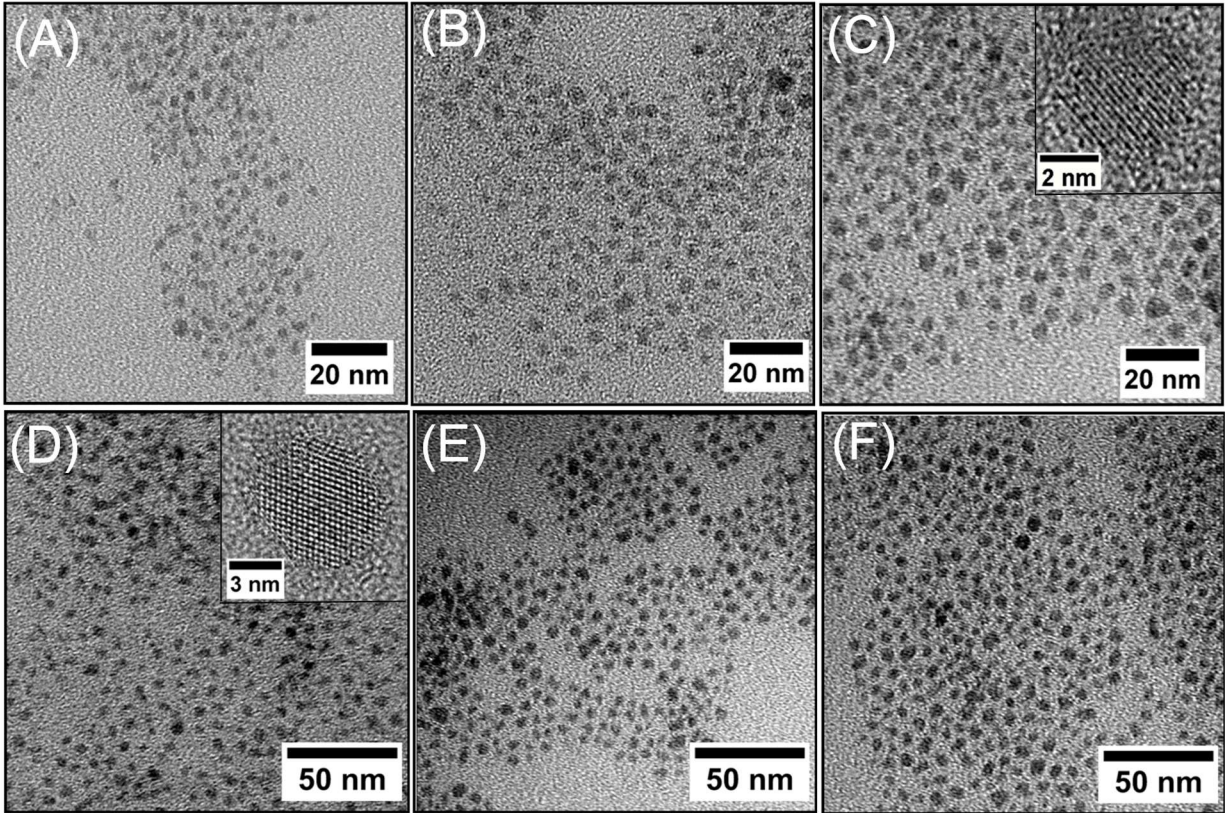


Figure 3.3. Representative low-resolution TEM images of $\text{Ge}_{1-x}\text{Sn}_x$ alloy QDs with varying Sn composition: (A) $x = 1.5\%$, (B) $x = 5.6\%$, (C) $x = 7.9\%$, (D) $x = 11.2\%$, (E) $x = 15.4\%$, and (F) $x = 20.6\%$. Insets in C and D show the high resolution TEM Images of selected QDs.

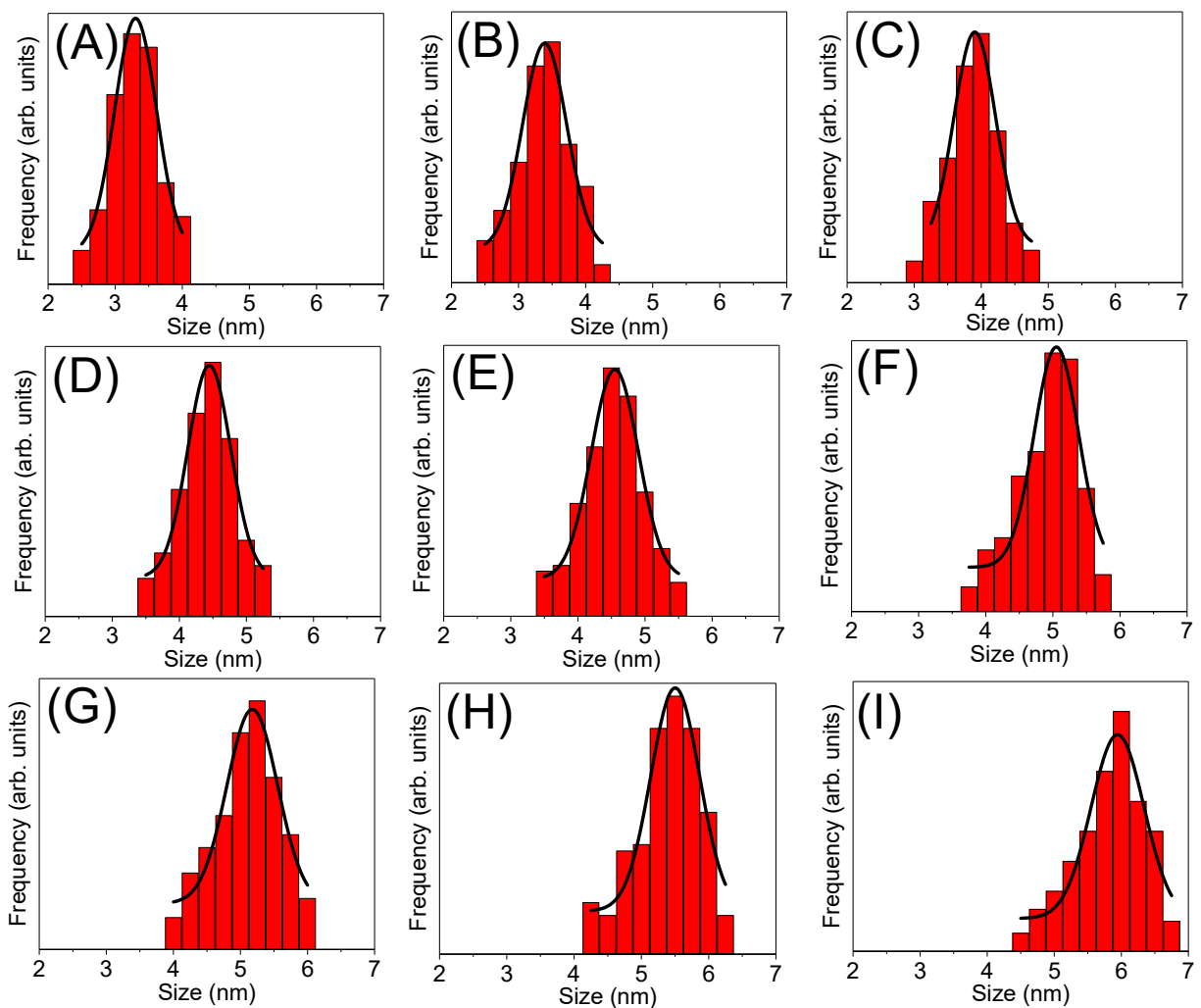


Figure 3.4. Size histograms of $\text{Ge}_{1-x}\text{Sn}_x$ alloy QDs with varying Sn composition: (A) $x = 1.5\%$, (B) $x = 2.7\%$, (C) $x = 4.2\%$, (D) $x = 5.6\%$, (E) $x = 7.9\%$, (F) $x = 9.1\%$, (G) $x = 11.2\%$, (H) $x = 15.4\%$, and (I) $x = 20.6\%$.

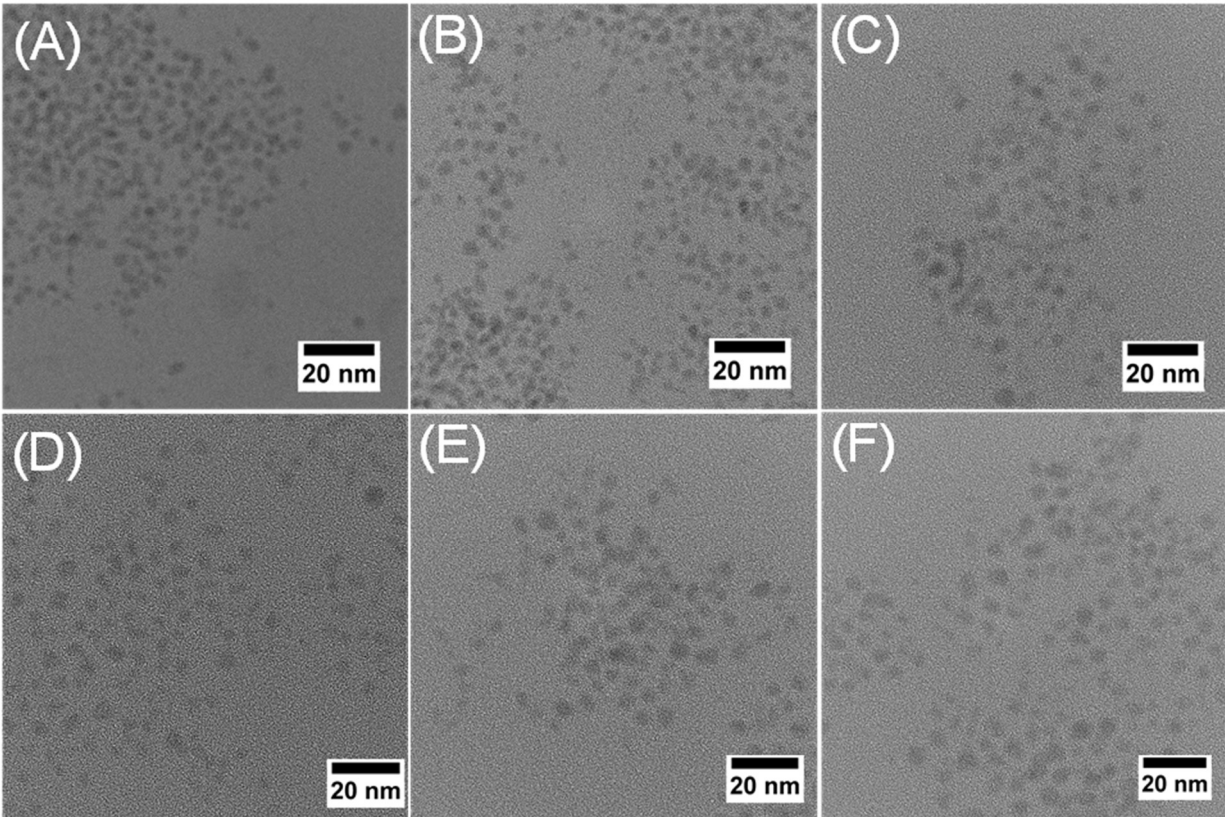


Figure 3.5. Representative TEM images of $\text{Ge}_{1-x}\text{Sn}_x$ alloy QDs with varying Sn composition: (A) $x = 2.7\%$, (B) $x = 5.6\%$, (C) $x = 7.9\%$, (D) $x = 11.2\%$, (E) $x = 15.4\%$, and (F) $x = 20.6\%$.

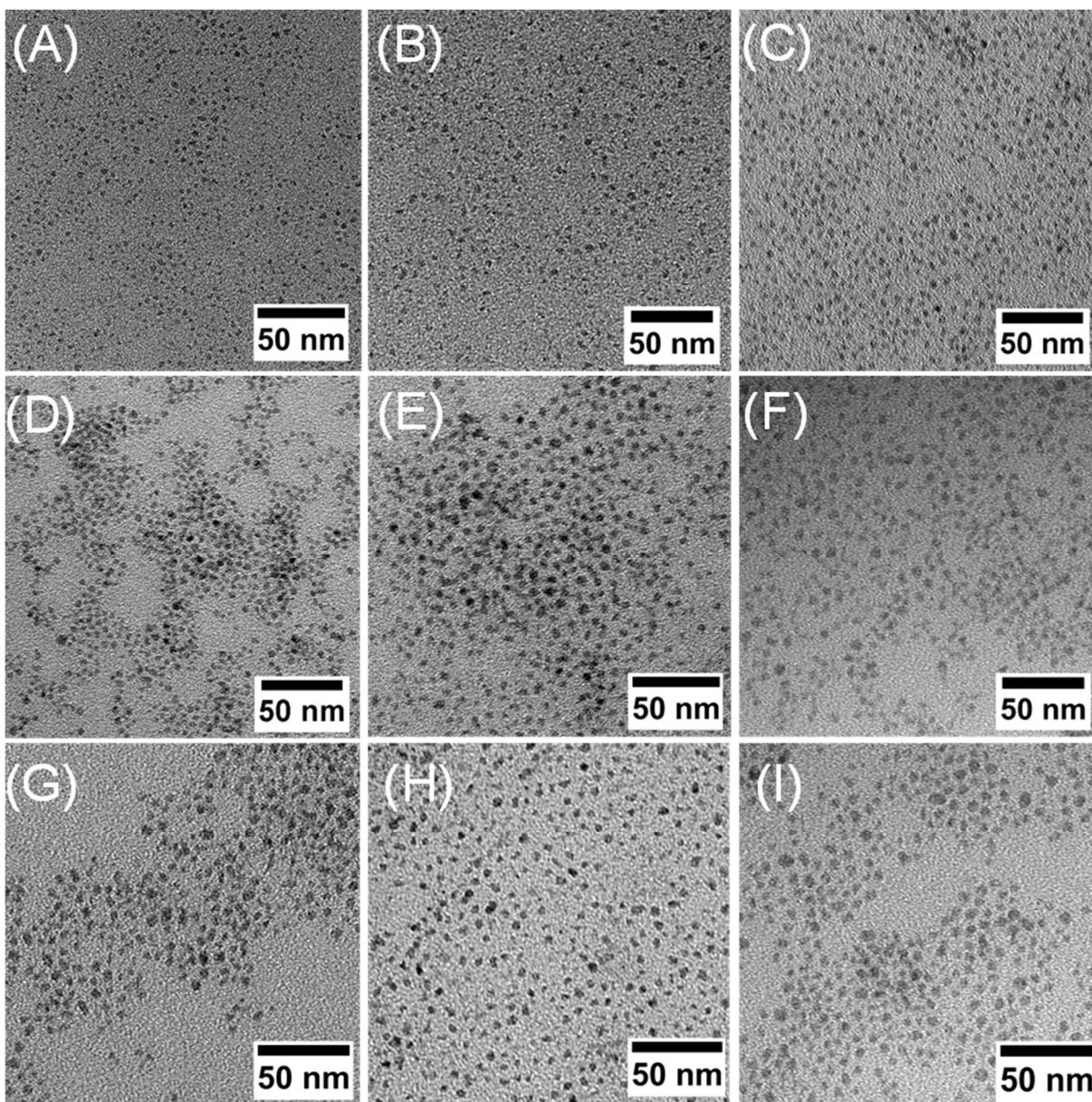


Figure 3.6. Representative low-resolution TEM images of $\text{Ge}_{1-x}\text{Sn}_x$ alloy QDs with varying Sn composition: (A) $x = 1.5\%$, (B) $x = 2.7\%$, (C) $x = 4.2\%$, (D) $x = 5.6\%$, (E) $x = 7.9\%$, (F) $x = 9.1\%$, (G) $x = 11.2\%$, (H) $x = 15.4\%$, and (I) $x = 20.6\%$.

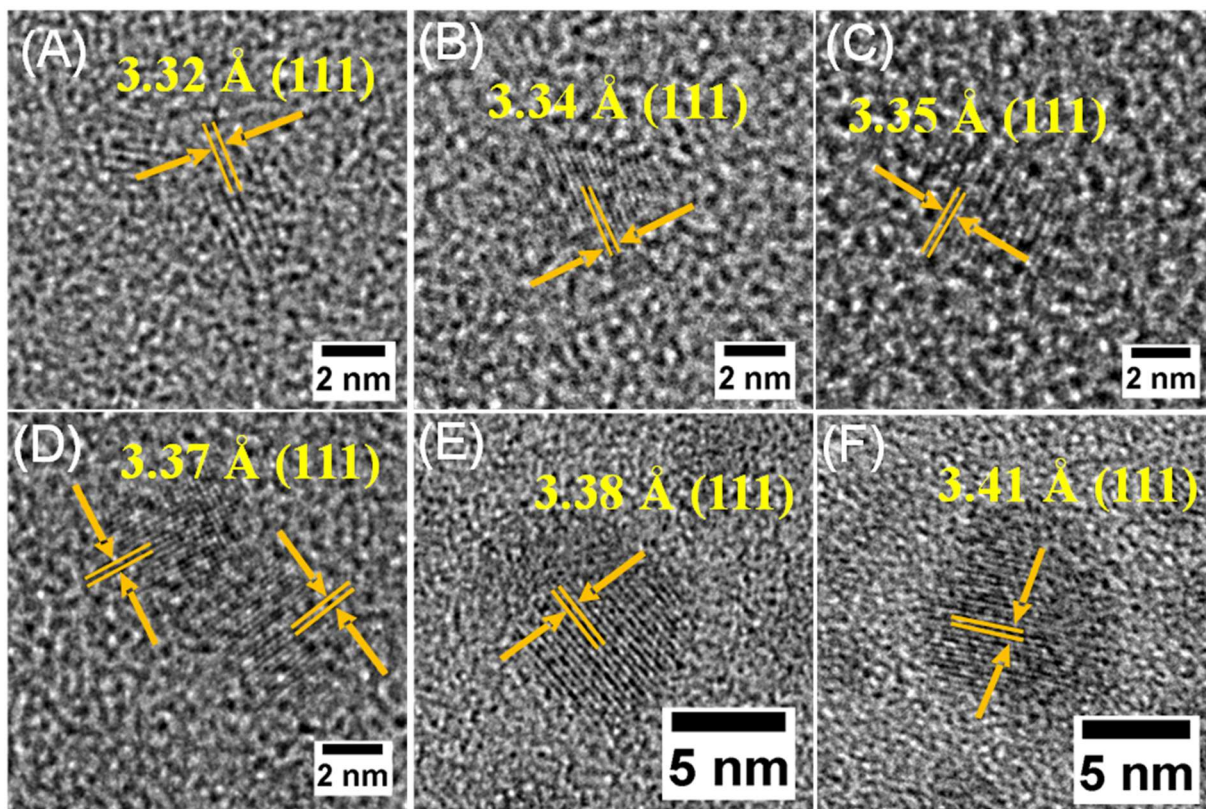


Figure 3.7. High resolution TEM images of $\text{Ge}_{1-x}\text{Sn}_x$ alloy QDs displaying lattice fringes corresponding to expanded (111) plane of diamond cubic Ge: (A) $x = 2.7\%$ (B) $x = 5.6\%$, (C) $x = 7.9\%$, (D) $x = 11.2\%$, (E) $x = 15.4\%$, and (F) $x = 20.6\%$.

High-angle annular dark-field (HAADF) images and STEM-EDS elemental maps were utilized to probe the homogeneous solid solution behavior of $\text{Ge}_{1-x}\text{Sn}_x$ QDs. Elemental mapping of near IR emitting alloy QDs was difficult due to extremely small size ($3.3 \pm 0.5 - 5.9 \pm 0.8$ nm) and complete destruction of particles is often noted under the high energy beam. Therefore, a set of larger polydisperse (8-20 nm) alloy nanocrystals was produced, by extending the growth temperature (10 min.) at 300°C , solely for STEM-EDS analysis. Elemental maps of 8-20 nm $\text{Ge}_{0.888}\text{Sn}_{0.112}$ alloy QDs indicate homogeneous distribution of Ge and Sn in the entire crystal, suggesting the solid solution behavior (Figure 3.8 and Figure 3.9). Therefore, the smaller near IR emitting alloy QDs,

which act as seeds for the growth of larger polydisperse (8-20 nm) particles, should also be homogeneous, consistent with prior reports on colloiddally synthesized $\text{Ge}_{1-x}\text{Sn}_x$ nanoalloys.^{32,49,105,107,108} It should be noted while elemental maps were recorded from larger QDs that provide high counts from individual particles, the elemental composition of near IR emitting alloy QDs were obtained from multiple individually prepared 3.3 ± 0.5 – 5.9 ± 0.8 nm alloy particles and the average values are shown in Table 3.2.

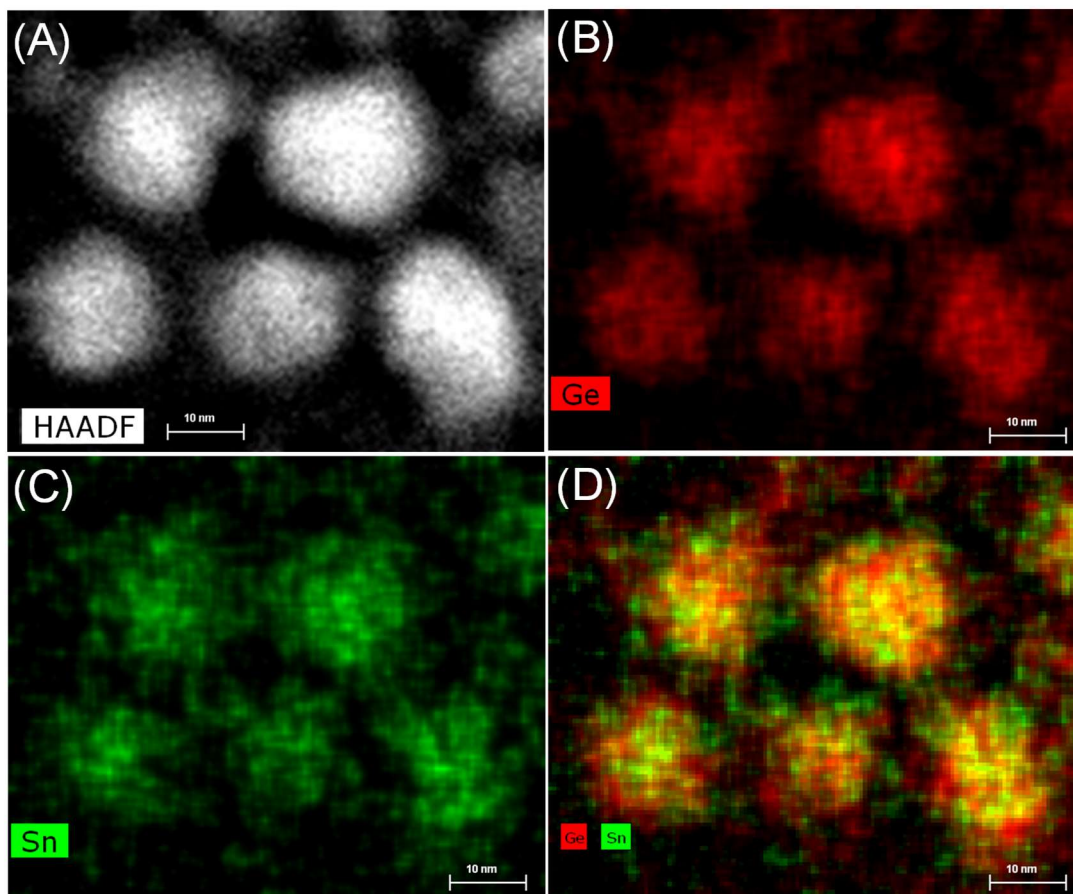


Figure 3.8. (A) Dark field TEM image of 8–20 nm $\text{Ge}_{0.888}\text{Sn}_{0.112}$ alloy QDs along with STEM-EDS elemental maps of (B) Ge, (C) Sn, and (D) an overlay of Ge and Sn indicating the homogeneous distribution of elemental components throughout the alloy lattice.

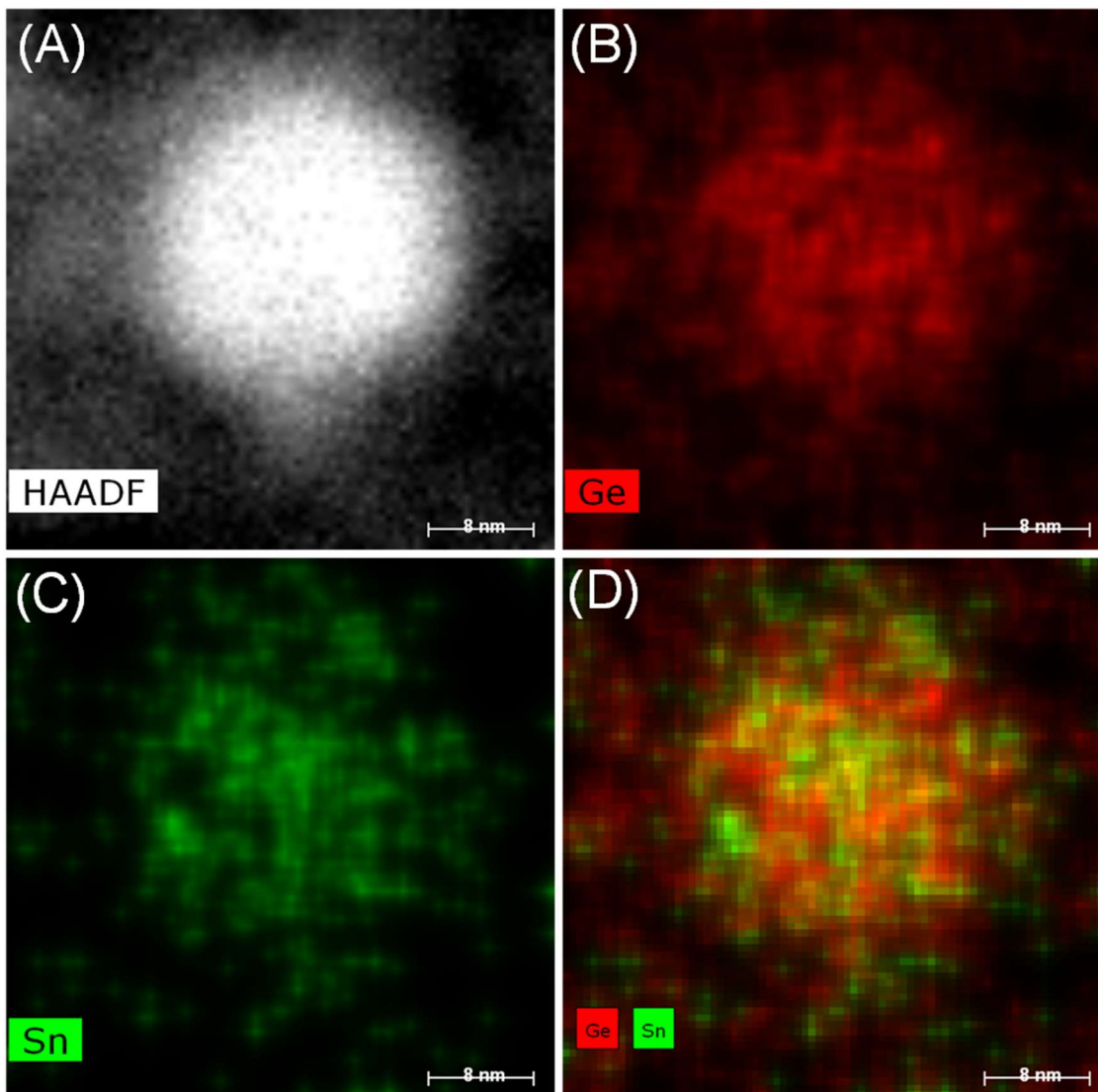


Figure 3.9. (A) Dark field TEM image of ~ 15 nm $\text{Ge}_{0.919}\text{Sn}_{0.091}$ alloy QD along with STEM/EDS elemental maps of (B) Ge, (C) Sn, and (D) an overlay of Ge and Sn, indicating the homogeneous distribution of elemental components throughout the alloy lattice.

The binding energies of Ge and Sn obtained from XPS spectra are consistent with prior reports of $\text{Ge}_{1-x}\text{Sn}_x$ nanoalloys (Figure 3.10).^{31,49} The survey XPS spectra exhibit peaks corresponding to Ge, Sn, C, and O with no other impurities, consistent with the EDS analysis (Figure 3.11 and Figure 3.12). The peak at 28.4 eV in the Ge $3d_{5/2}$ spectra

can be attributed to Ge(0), which has been shifted from the expected value of 29.4 eV, likely due to surface charging effects.¹¹⁷ The peak at 31.2 eV is likely arising from surface Ge²⁺ species coordinated to alkylamine and alkene passivating ligands.^{31,32} Consistent with XPS data, FTIR spectra of alloy QDs indicates the presence of HDA on QD surface (Figure 3.13). Occasionally, a minor peak at 34.0 eV is observed in Ge 3d_{5/2} spectra, which can be attributed to Ge⁴⁺ likely produced by surface oxidation (Figure 3.14). The examination of the Sn (3d_{5/2}) region indicates similar behavior with both core Sn⁰ (483.9 eV) and surface Sn^{2+/4+} (485.6 eV) species bound to stabilizing ligands.^{31,32,42,118} It is important to note that no GeO_x or SnO_x impurities were detected in PXRD and Raman spectra of QDs (Figure 3.1A and Figure 3.2A). However, the presence of higher oxidation state peaks (*i.e.* Ge⁴⁺ and Sn⁴⁺ in particular) can also be attributed to minor oxide impurities produced via surface oxidation.^{31,32,49} Nonetheless, similar core and surface species were noted in Ge (3d and 2P) and Sn (3d) spectra of alloy QDs with varying Sn compositions, consistent with prior reports of Ge_{1-x}Sn_x nanoalloys.^{31,32,49}

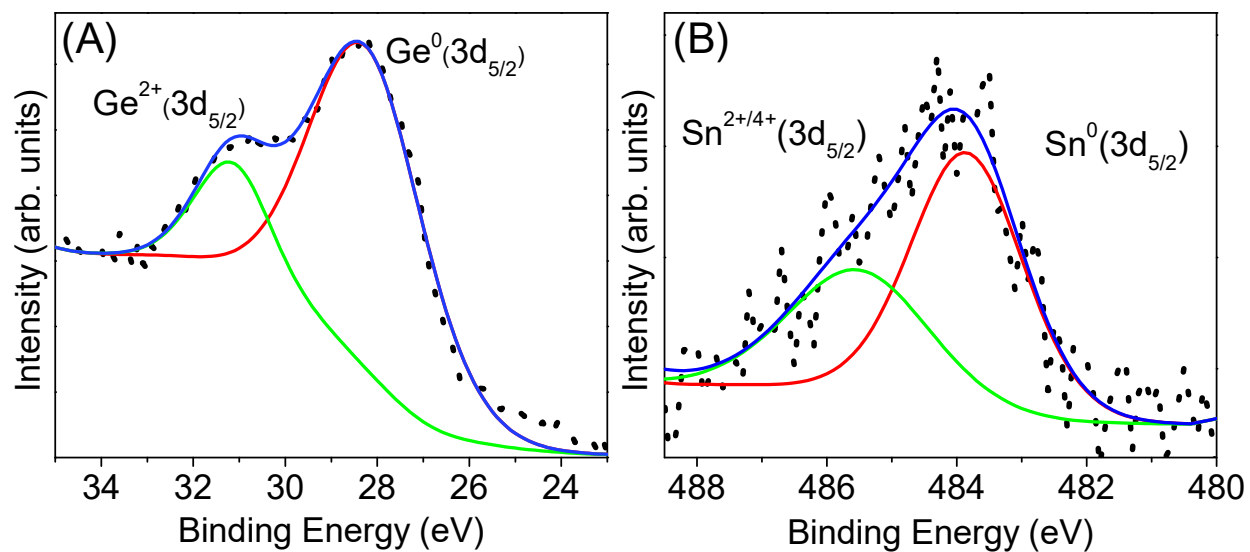


Figure 3.10. Representative (A) Ge (3d_{5/2}) and (B) Sn (3d_{5/2}) XPS spectra of Ge_{0.888}Sn_{0.112} alloy QDs. Dotted lines represent the spectral data and the red and green lines are fitted deconvolutions of core Ge⁰/Sn⁰ and different oxidation states (Ge²⁺, Sn²⁺ and Sn⁴⁺) of surface species, respectively. Blue lines are spectral envelopes.

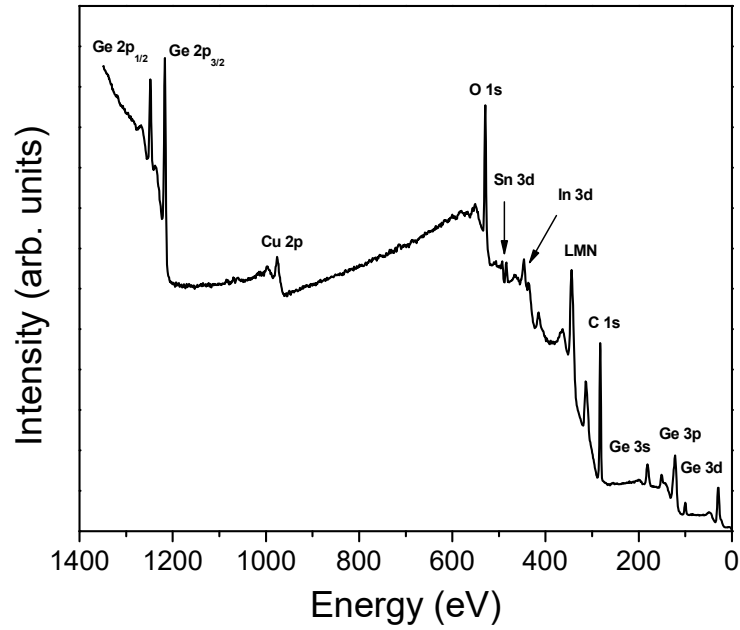


Figure 3.11. X-ray photoelectron spectra (survey scan) of $\text{Ge}_{0.888}\text{Sn}_{0.112}$ alloy QDs. Similar survey scans were obtained from QDs with other compositions.

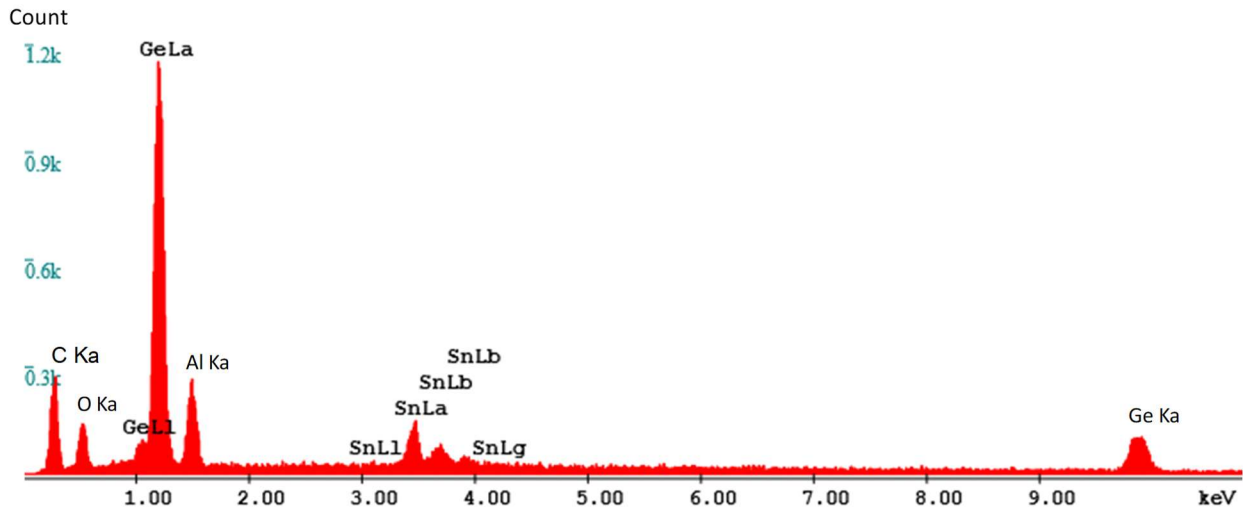


Figure 3.12. Representative SEM-EDS spectrum of $\text{Ge}_{0.909}\text{Sn}_{0.091}$ alloy QDs. The X-ray peak corresponding to aluminum (Al) is arising from sample holder.

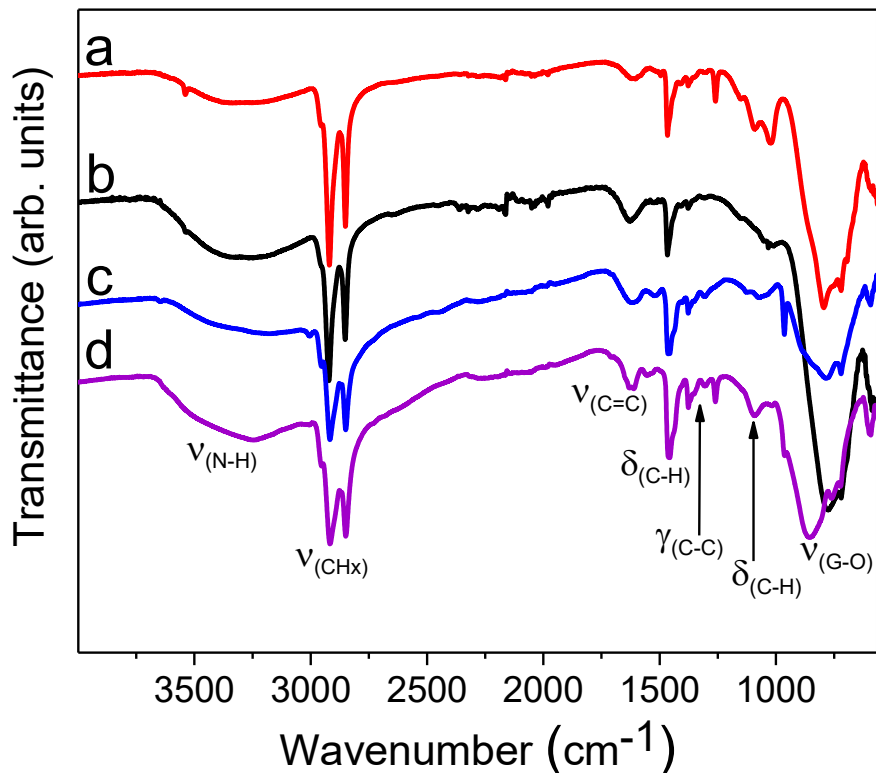


Figure 3.13. FT-IR spectra of $\text{Ge}_{1-x}\text{Sn}_x$ alloy QDs synthesized HDA/ODE. (a) $x = 0.015$, (b) $x = 0.056$, (c) $x = 0.112$, and (d) $x = 0.206$. The peaks at 2920 and 2850 cm^{-1} are arising from C–H asymmetric and symmetric stretching vibrations of alkyl chains, respectively.¹⁹ The vibrations at 1361–1460 cm^{-1} corresponds to C–H bending $\delta_{(\text{CH}_x)}$ modes of alkyl chains.¹¹⁹ A broader peak observed at 1622 cm^{-1} can be assigned to $\nu_{(\text{C}=\text{C})}$ whereas the weak band at ~ 3300 cm^{-1} can be attributed to $\nu_{(\text{N}-\text{H})}$ further indicating the presence of HDA on the QD surface. A broad band observed at 790–860 cm^{-1} can be attributed to $\nu_{(\text{Ge}-\text{O})}$ arising from adsorbed surface oxygen species¹⁹, consistent with XPS O(1s) spectrum shown in Figure 3.14.

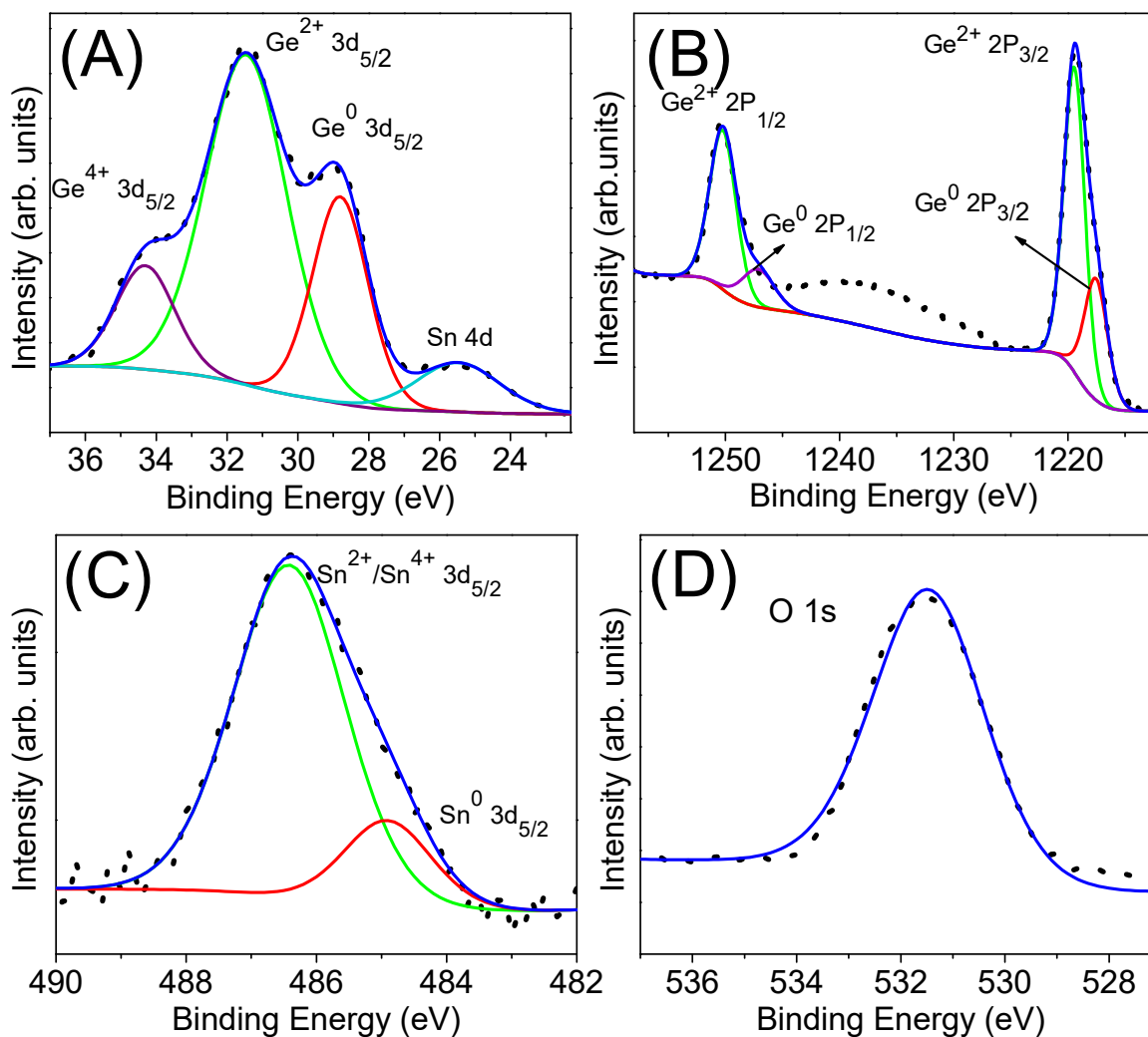


Figure 3.14. Representative X-ray photoelectron spectra of $\text{Ge}_{0.909}\text{Sn}_{0.091}$ alloy QDs displaying the (A) Ge(3d), (B) Ge(2P), (C) Sn(3d), and (D) O(1s) spectral regions. Dotted lines are spectral data, solid red and green lines are fitted deconvolutions, and blue lines are spectral envelopes. The peak at 531.5 eV in O(1s) spectrum corresponds to adsorbed H_2O .

Solid state diffuse reflectance (converted to absorption) spectroscopy was utilized to probe the absorption onsets of alloy QDs and effects of size confinement. The energy gaps obtained from Kubelka Munk⁸⁷ analysis indicate strong quantum confinement effects

in $3.3 \pm 0.5 - 5.0 \pm 0.7$ nm $\text{Ge}_{1-x}\text{Sn}_x$ QDs with well-defined absorption onsets from 1.72–0.84 eV for $x = 1.5\text{--}9.1\%$ compositions (Figure 3.15). A clear red-shift in absorption onset is noted with increasing Sn content for QDs with similar average size, consistent with Sn induced lowering of energy gaps. The solid-state energy gaps of alloy QDs with higher Sn content ($x > 9.1\%$) could not be probed because of the instrumental limitations. Thus, solution absorption spectra were recorded to estimate the energy gaps over a wide range of Sn compositions (0–20.6%). The solution phase energy gaps estimated using Tauc function,^{6,32,87,88,95,120} yield values from 2.05–0.90 eV for $x = 1.5\text{--}20.6\%$ compositions (Figure 3.16). However, the energy gaps obtained from solid-state absorption spectra (Kubelka–Munk analysis) are in close agreement with the gap energies estimated from PL measurements (Figure 3.17 and Table 3.2). It should also be noted that both solid-state and solution-state energy gaps of $\text{Ge}_{1-x}\text{Sn}_x$ alloy QDs are significantly larger than those reported for bulk $\text{Ge}_{1-x}\text{Sn}_x$ thin film alloys (0.35–0.80 eV for $x = 15.0\text{--}0.00\%$),⁹ consistent with the expected quantum confinement effects.

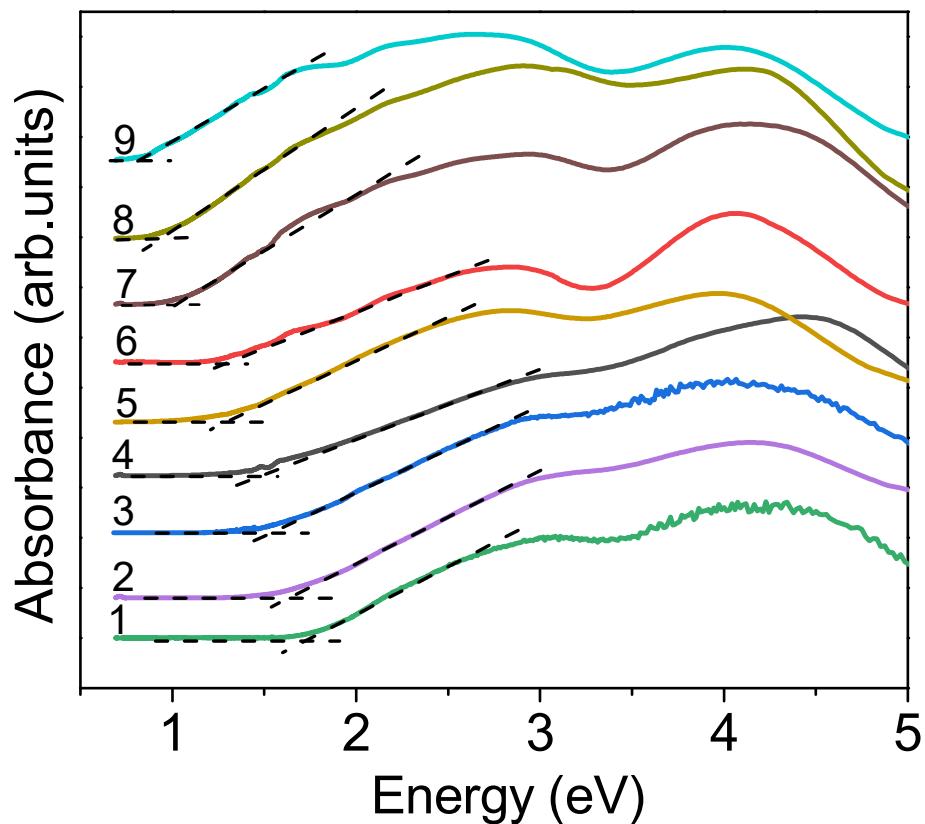


Figure 3.15. Solid state diffuse reflectance spectra (converted to absorption using Kubelka–Munk remission function) of $\text{Ge}_{1-x}\text{Sn}_x$ alloy QDs with varying Sn composition: (1) $x = 1.5\%$ (1.72 eV), (2) $x = 1.9\%$ (1.61 eV), (3) $x = 2.7\%$ (1.52 eV), (4) $x = 3.4\%$ (1.48 eV), (5) $x = 4.2\%$ (1.30 eV), (6) $x = 5.6\%$ (1.22 eV), (7) $x = 6.4\%$ (1.02 eV), (8) $x = 7.9\%$ (0.94 eV), and (9) $x = 9.1\%$ (0.84 eV). Corresponding absorption onset values are shown in parentheses.

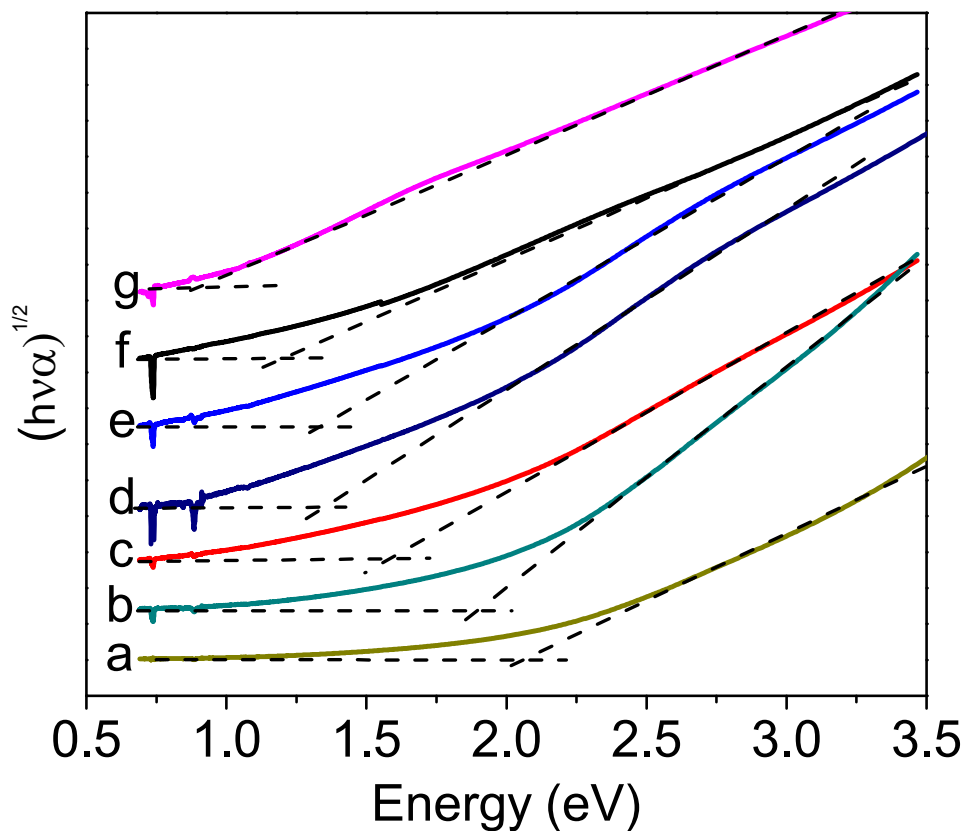


Figure 3.16. Solution absorption spectra (Tauc-indirect) of $\text{Ge}_{1-x}\text{Sn}_x$ alloy QDs as a function of Sn composition: (a) $x = 1.5\%$ (2.05 eV), (b) $x = 2.7\%$ (1.90 eV), (c) $x = 5.6\%$ (1.58 eV), (d) $x = 9.1\%$ (1.35 eV), and (e) $x = 11.2\%$ (1.33 eV), (f) $x = 15.4\%$ (1.19 eV), and (g) $x = 20.6\%$ (0.90 eV). Corresponding energy gaps are shown in parentheses.

Table 3.2. Comparison of the Elemental Composition, Crystallite and Primary Particle Size, and Room Temperature Solid-State Absorption Onsets and Photoluminescence Peak maxima for $3.3 \pm 0.5 - 5.9 \pm 0.8$ nm $\text{Ge}_{1-x}\text{Sn}_x$ Alloy QDs.

Sample	Sn Composition (x) ^a	Particle Size (nm) ^b	Crystallite Size ^c (nm)	Energy gap (eV) ^d	PL Peak Position (eV)
1	0.015	3.3 ± 0.5 nm	1.9 ± 0.2	1.72	1.62
2	0.019	3.4 ± 0.5 nm	2.1 ± 0.2	1.61	1.52
3	0.027	3.5 ± 0.6 nm	2.2 ± 0.2	1.52	1.43
4	0.034	3.7 ± 0.5 nm	2.4 ± 0.2	1.48	1.38
5	0.042	3.9 ± 0.6 nm	2.8 ± 0.2	1.30	1.34
6	0.056	4.4 ± 0.7 nm	2.8 ± 0.2	1.22	1.31
7	0.064	4.5 ± 0.6 nm	2.9 ± 0.2	1.02	n/a ^f
8	0.079	4.6 ± 0.8 nm	3.0 ± 0.3	0.94	n/a ^f
9	0.091	5.0 ± 0.7 nm	3.3 ± 0.2	0.84	n/a ^f
10	0.112	5.2 ± 0.6 nm	3.5 ± 0.3	n/a ^e	n/a ^f
11	0.154	5.5 ± 0.8 nm	3.6 ± 0.3	n/a ^e	n/a ^f
12	0.206	5.9 ± 0.8 nm	3.8 ± 0.2	n/a ^e	n/a ^f

^aElemental compositions were obtained from EDS analysis of multiple individually prepared samples and averaged values are presented. ^bAverage particle sizes were calculated from 150–200 individual QDs from TEM images of multiple individually prepared samples. ^cCrystallite sizes were calculated by applying the Scherrer formula to (111), (220), and (311) reflections of PXRD patterns and average values are presented. ^dEnergy gaps were estimated from extrapolating the first major absorption onset to the intersection point of the baseline using linear fits. ^eOnset cut off due to detector limitation. ^fNo detectable PL was noted.

Solid-state emission spectra of $\text{Ge}_{1-x}\text{Sn}_x$ alloy QDs exhibit composition tunable PL peak energies in the near IR spectrum (1.62–1.31 eV for $x = 0.015$ – 0.056 , Figure 3.17). Consistent with absorption studies, a clear red shift in PL maxima was noted with increasing Sn composition. The PL peak energies are red shifted from those reported for ultra-small (1.8–2.2 nm) $\text{Ge}_{1-x}\text{Sn}_x$ alloy QDs (2.0–1.72 eV for $x = 1.8$ – 23.6%), owing to larger particles produced in the current study.^{49,50} It is important to note that this is the first report on tunable near IR emitting $\text{Ge}_{1-x}\text{Sn}_x$ alloy QDs with wide range of Sn compositions. Previous studies on 6–11 nm $\text{Ge}_{1-x}\text{Sn}_x/\text{CdS}$ core/shell QDs with 5 and 25% Sn compositions showed broad-band PL (800–1200 nm) with no tunability as a function of size or composition.⁵¹ Likewise, larger (9–10 nm) $\text{Ge}_{1-x}\text{Sn}_x$ alloy QDs with high Sn content ($x = 36$ – 39%) are reported to exhibit broad and weak PL in the deep IR region (~ 0.45 – 0.55 eV).³² In contrast, alloy QDs reported in this study exhibit wide tunability of near IR PL across different Sn compositions. Moreover, the solid-state absorption onsets are in close agreement with the PL peak maxima, suggesting that the PL results from fundamental direct energy gap transitions (Figure 3.18). However, PL from QDs with Sn content higher than 5.6% could not be probed possibly due to poor surface passivation and/or weaker confinement effects, resulting in higher degree of non-radiative recombination. As such, efforts are currently underway to utilize different surface passivation strategies to eliminate surface defects, enhanced the PL efficiency, and improve the chemical and optical stability of QDs with higher Sn compositions.

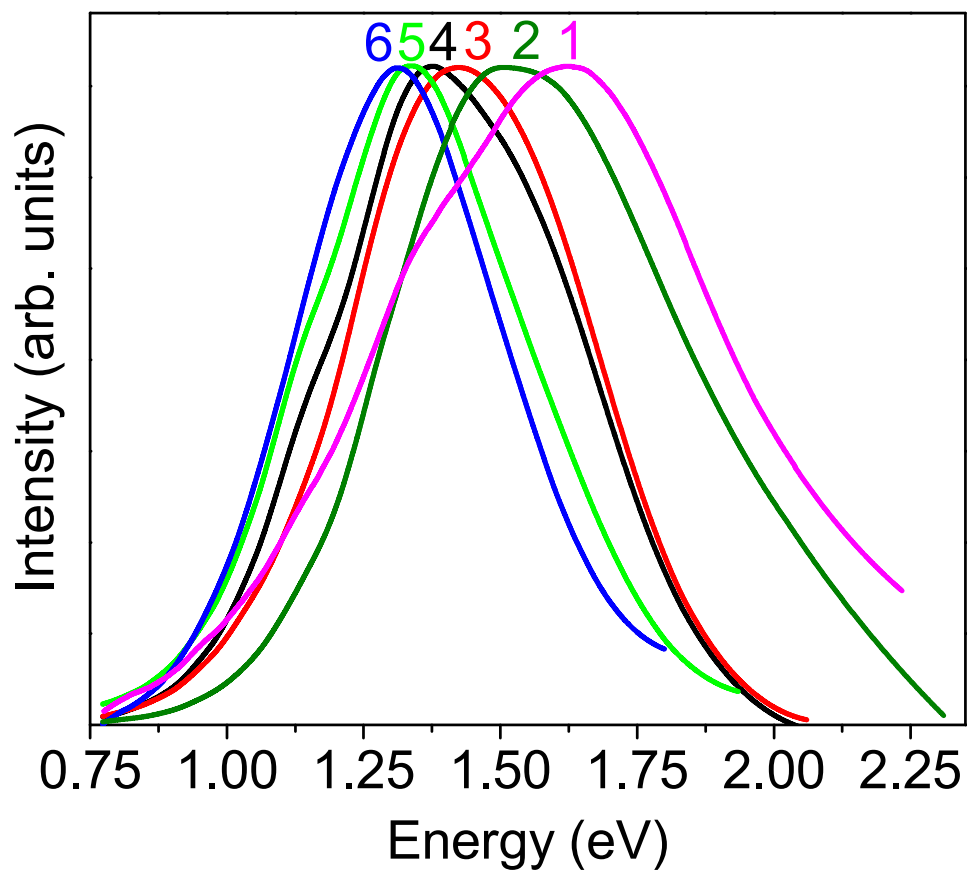


Figure 3.17. Room-temperature solid-state photoluminescence spectra of Ge_{1-x}Sn_x alloy QDs with varying Sn compositions: (1) x = 1.5% (1.62 eV), (2) x = 1.9% (1.52 eV), (3) x = 2.7% (1.43 eV), (4) x = 3.4% (1.38 eV), (5) x = 4.2% (1.34 eV), and (6) x = 5.6% (1.31 eV). Corresponding PL peak maxima are shown in parentheses.

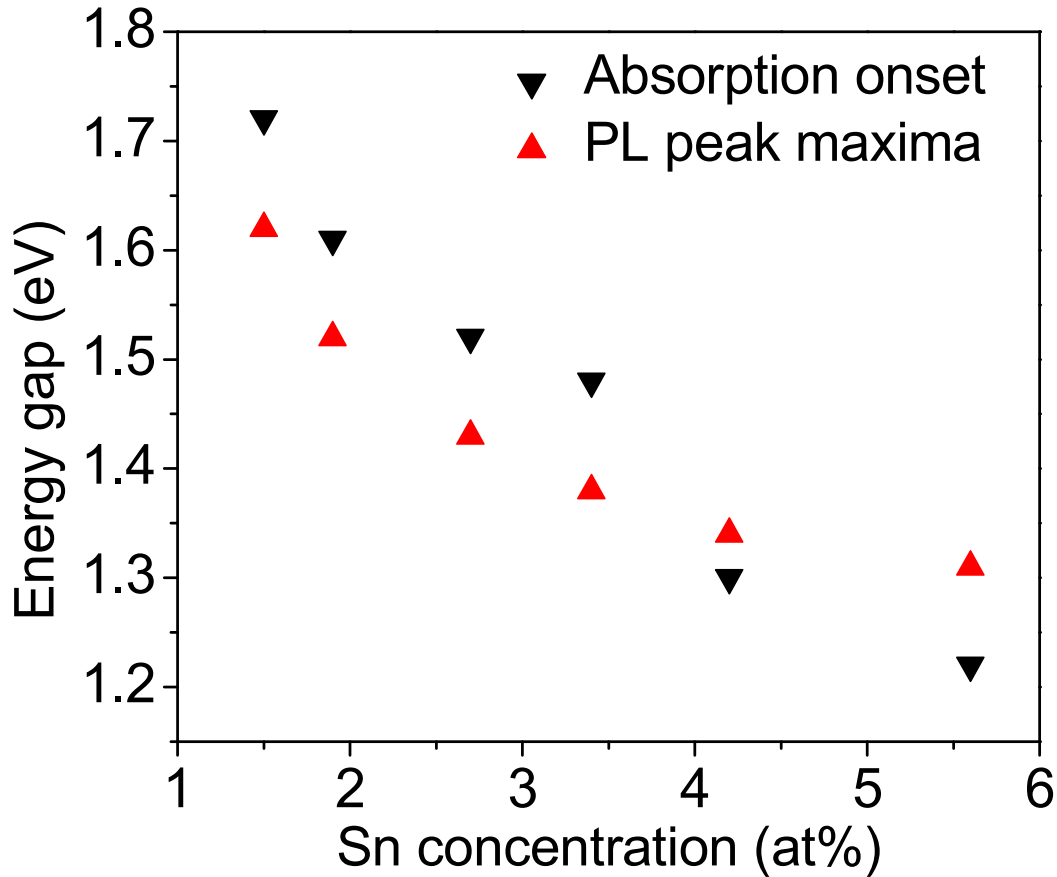


Figure 3.18. Experimental energy gaps of $3.2 \pm 0.2 - 5.7 \pm 0.5$ nm $\text{Ge}_{1-x}\text{Sn}_x$ alloy QDs as a function of Sn composition ($x = 1.5-5.6\%$). Data were obtained from room-temperature solid-state absorption and photoluminescence (PL) studies.

To investigate carrier relaxation pathways and further understand the origin of near IR PL, temperature dependent time-resolved PL experiments were performed. Figure 3.19 shows the PL transients measured for $\text{Ge}_{1-x}\text{Sn}_x$ alloy QDs with $x = 1.9\%$, 4.2% , and 5.6% at 295 K and 15 K. All transients are well described by biexponential decay fits, providing fast decay constants of $\tau_{\text{fast}} = 8-11.7$ ns and slow decay constants of $\tau_{\text{slow}} = 80-119$ ns at room temperature (295 K, Table 3.3). In contrast, the PL decays are much slower at 15 K: $\tau_{\text{fast}} = 1-1.6$ μs , $\tau_{\text{slow}} = 7.8-10.8$ μs . This drastic difference can

be explained by a combined effect of surface trap states and dark-bright exciton splitting in QDs.^{49,50} The spin-forbidden dark exciton recombination is slow at 15 K, and increased thermal energy at room temperature makes bright excitonic states accessible, improving the recombination rates. Moreover, slow recombination at 15 K may also be partially due to charge trapping at the surface states, which can lead to long carrier times owing to separation of photoexcited carriers. Nearly an order of magnitude reduction in PL intensities at 295K compared to those at 15 K suggests a dominant role of nonradiative recombination at increased temperatures. While it is outside the scope of this report, further studies are currently underway to differentiate the individual contributions from different carrier relaxation pathways to better understand the origin of near IR PL.

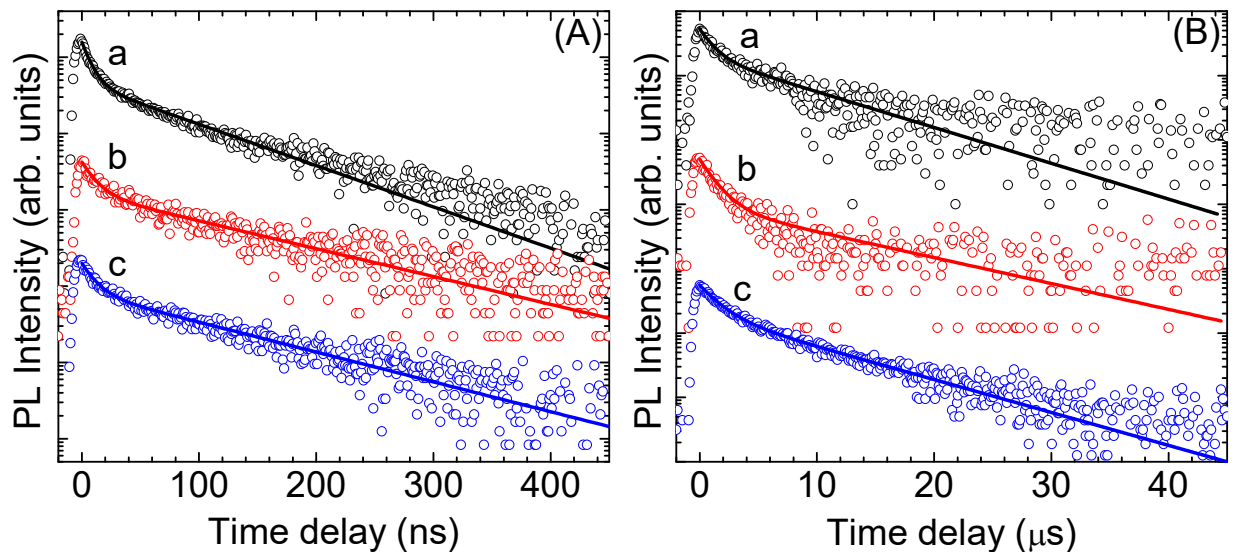


Figure 3.19. PL transients at (A) 295 K and (B) 15 K for Ge_{1-x}Sn_x alloy QDs with varying Sn compositions: (a) $x = 1.9\%$, (b) $x = 4.2\%$, and (c) $x = 5.6\%$. The solid lines are biexponential fits.

Table 3.3. Time Constants Extracted from Biexponential Decay Fit ($A_{fast} e^{-t/\tau_{fast}} + A_{slow} e^{-t/\tau_{slow}}$) to PL Transients of Near IR Emitting Ge_{1-x}Sn_x Alloy QDs.

@295 K	τ_{fast} (ns)	τ_{slow} (ns)	A_{fast}/A_{slow}
x = 0.019	8.0 ± 0.2	80.2 ± 1.3	2.44
x = 0.042	11.7 ± 0.8	119.1 ± 4.2	1.54
x = 0.056	11.5 ± 0.6	111.1 ± 2.7	1.41
@15 K	τ_{fast} (μs)	τ_{slow} (μs)	A_{fast}/A_{slow}
x = 0.019	1.1 ± 0.1	7.8 ± 0.4	1.64
x = 0.042	1.3 ± 0.1	10.8 ± 1.1	4.27
x = 0.056	1.6 ± 0.1	8.5 ± 0.2	1.78

3.3 Conclusions

In conclusion, for the first time we have successfully produced narrowly dispersed Ge_{1-x}Sn_x alloy QDs with wide tunability of Sn compositions (0–20.6%) and composition-tunable near IR absorption and intense PL. The diameter of alloy QDs was tuned by varying the molar ratio of precursor halides: n-BuLi minimizing the size dispersity to ~11–15%, across varying Sn compositions. The lattice parameters computed from PXRD analysis indicate near linear expansion of diamond cubic Ge structure with increasing Sn content, suggesting the formation of strain-free nanoalloys. The successful incorporation of α-Sn into cubic Ge has been further confirmed by PXRD patterns, STEM-EDS elemental maps, and Raman spectroscopy studies. The quantum confinement effects have resulted in energy gaps that are significantly blue-shifted from bulk Ge_{1-x}Sn_x thin film counterparts for alloy QDs with composition-tunable absorption onsets (1.72–0.84 eV for

$x = 1.5\text{--}20.6\%$) and PL maxima (1.62–1.31 eV for $x = 1.5\text{--}5.6\%$) primarily in the near IR spectrum. The temperature dependent TRPL spectroscopy suggests microsecond and nanosecond PL decays at 15 K and 295 K, respectively owing to radiative recombination of dark and bright excitons and carriers trapped at surface states. The colloidal synthesis reported here has expanded the optical window of direct-gap $\text{Ge}_{1-x}\text{Sn}_x$ alloy QDs into near IR spectrum allowing less-toxic, earth abundant, and silicon-compatible Group IV elements for application in a broad range of electronic and photonic technologies.

CHAPTER 4

Photophysical Properties of Ultra-Small $\text{Ge}_{1-x}\text{Sn}_x$

Alloy QDs

4.1 Introduction

In an effort to expand the spectral range and to improve the efficiency of the optical transitions, recently there has been increased interest in the synthesis of alloy nanostructures to exploit the size confinement effects.^{31,32,47,49} Taking advantage of the low-temperature colloidal synthesis and nucleation and growth control, we have reported the synthesis of 3.3-5.9 nm homogeneous $\text{Ge}_{1-x}\text{Sn}_x$ nanoalloys. The photophysical properties of the aforementioned 3.3-5.9 nm alloy QDs exhibit composition tunable NIR optical properties were discussed exclusively in chapter 3. To probe the optical properties of alloy QDs that show enormously high quantum confinement effects, we have developed the synthesis of ultra-small $\text{Ge}_{1-x}\text{Sn}_x$ alloy QDs (2.1-2.7 nm) with composition ($x = 4.3\text{-}12.5\%$) tunable absorption and orange to red color emission. More importantly, by synthesizing the alloy QDs in 2-3 nm size regime resulted in photoluminescence in visible region. Temperature dependent, time resolved photoluminescence (PL) spectroscopy has been utilized to study the carrier dynamics of $\text{Ge}_{1-x}\text{Sn}_x$ QDs, which suggest micro second decay of PL at 15 K, likely due to slow recombination of dark excitons and carriers trapped at surface states, and roughly one order of magnitude faster recombination with increasing Sn concentration to 23.6%.⁴⁷ Increasing temperature to 295 K led to three orders of magnitude faster decay (nanosecond) owing to the thermal

activation of bright excitons and carrier de-trapping from surface states. In addition to expansion of optical window into visible region, ultra-small QDs exhibit an opposite PL energy splitting (ΔE) compare to NIR QDs. Ultra-small, 2-3 nm samples PL peaks at room temperature are blue-shifted ($\Delta E = 35-50$ meV) compared to those at 15 K, whereas NIR (3.3-5.9 nm) samples PL peaks are red-shifted ($\Delta E = 30-56$ meV) at room temperature compared to those at 15 K. Alternatively, post synthetic surface passivation of ultra-small QDs with oleic acid resulted in 8-fold PL enhancement. Oleic acid surface passivated samples PL peaks are blue-shifted ($\Delta E \sim 50$ meV) compared to those of not treated ones, consistent with the samples at room temperature.

4.2 Experimental Section

Materials. Germanium diiodide (99.99+ %) and tin dichloride (99.9985 %), were purchased from Strem Chemicals and Alfa Aesar, respectively. N-butyllithium (BuLi) 1.6 M in hexane was purchased from Sigma Aldrich and stored in a N₂ glove box at < 5°C. 1- octadecene (ODE, 90%) was purchased from Fisher Scientific. Oleylamine (OLA, >98% primary amine) and oleic acid (OA) were purchased from Sigma Aldrich. Toluene, chloroform, carbon tetrachloride, and methanol of ACS grade were purchased from Acros. OLA and ODE were dried by heating at 120 °C under vacuum for one hour prior to storage in a N₂ glovebox. Methanol and toluene were dried over molecular sieves and Na, respectively and distilled prior to use. Caution: n-butyllithium is highly pyrophoric and ignite in air so must be handled in air free conditions by properly trained personnel. Carbon tetrachloride is highly toxic, and its use should be minimized to limit exposure.

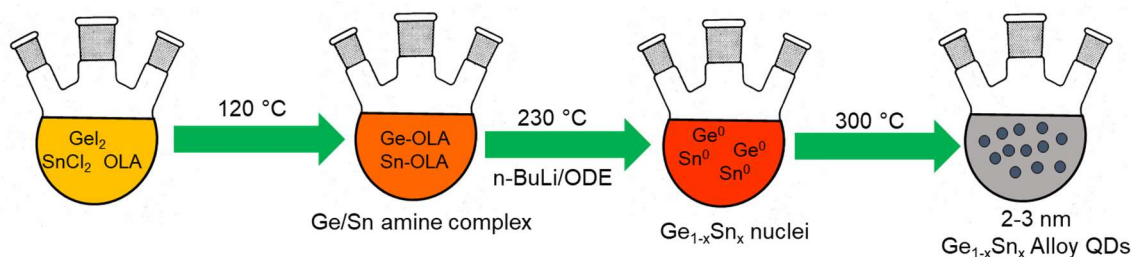
4.2.1 Synthesis of ~ 2nm Ge_{1-x}Sn_x Quantum Dots

In a typical synthesis of 1.8-2.3 nm Ge_{1-x}Sn_x QDs, appropriate amounts of GeI₂ and SnCl₂, 0.6 mmol of metal total, were combined with 20 mL of OLA in a 50 mL three neck flask inside a glovebox. The sealed set up was transferred to a Schlenk line and degassed under vacuum at 120 °C to produce a homogeneous orange color solution. The reaction temperature was then raised to 230 °C under nitrogen and 0.5-0.9 mL of BuLi in 3.0 mL of ODE was swiftly injected. The temperature dropped to 209-213 °C and the mixture was reheated to 300 °C within 10-14 min to produce Ge_{1-x}Sn_x alloy QDs. The flask was then rapidly cooled with compressed air to ~100 °C and 10 mL of freshly distilled toluene was added. Then, 60-90 mL of freshly distilled methanol was added, followed by centrifugation at 4000g for 5-10 min to precipitate the alloy QDs. The supernatant was discarded, and the precipitate was purified by dispersing in toluene and subsequent precipitation with methanol.

4.3 Results and Discussion

Ge_{1-x}Sn_x alloy QDs with sizes in the range of 2-3 nm (ultra-small) were produced with Sn composition ranging from 4.3-12.5% to probe tunable visible PL and extreme size confinement effects. Photophysical properties of 2-3 nm QDs were compared with 4-6 nm QDs reported previously. To induce strong size confinement effects in 2-3 nm QDs, oleylamine (OLA) was employed as the surfactant by following a route reported by our group.⁴⁹ In a typical synthesis, GeI₂ and SnCl₂ (0.6 mmol in total) were co-reduced using 1.5-1.3 mmol of n-butyl lithium (n-BuLi) at 230 °C to form Ge-Sn nuclei, followed by growth of the alloy nuclei at 300 °C (Scheme 4.1). In order to equalize the growth effects of Sn, varied amounts of n-BuLi (1.5-1.3 mmol for x = 4.3-12.5%) was employed.

Scheme 4.1. An Illustration of the Synthesis of $\text{Ge}_{1-x}\text{Sn}_x$ alloy QDs^a



^aCo-reduction of Ge and Sn precursor halides dissolved in oleylamine (OLA), followed by the growth of resulting $\text{Ge}_{1-x}\text{Sn}_x$ alloy nuclei at $300\text{ }^\circ\text{C}$ has been successfully utilized to produce homogeneous $\text{Ge}_{1-x}\text{Sn}_x$ alloy QDs.

Powder X-ray diffraction (PXRD) was utilized to confirm the structural homogeneity of alloy QDs and the absence of the undesirable byproduct impurities. PXRD patterns of $\text{Ge}_{1-x}\text{Sn}_x$ alloy QDs suggest that the as-synthesized 2-3 QDs are consisting of diamond cubic crystal structure similar to 4-6 nm QDs reported previously.^{31,49} No $\alpha\text{-Sn}$, or $\beta\text{-Sn}$ (tetragonal Sn) impurity phases detected indicate successful Sn incorporation into Ge lattice to form homogeneous alloys (Figure 4.1).^{26,102} As Sn content increases, a systematic shift of diffraction peaks towards lower 2θ angles suggest the larger Sn incorporation into smaller Ge. A significant broadening of cubic Ge diffraction peaks indicates small crystallite size of the alloys QDs. In addition, disorder in alloy couple with strain in the lattice can also contribute further broadening of Bragg's reflections.⁴⁹ Thus, calculating the crystallite size using Scherrer's formula and lattice parameters are not accurate for the broad peaks. However, experimental lattice constants for somewhat larger 4-6 nm QDs synthesized with similar synthesis were obtained. Here we obtain experimental lattice constants using the powder X-ray diffraction patterns of alloy QDs.

However, diffraction peak positions of (111), (220), and (311) Bragg reflections were accurately determined and the lattice constants were calculated by applying the Bragg's equation to all peaks (Figure 4.2). The experimental lattice parameters obeying Vegard's rule and are in close agreement with theoretical studies using local density approximation (LDA) for 1.4-2.7 nm $\text{Ge}_{1-x}\text{Sn}_x$ QDs.⁴⁷

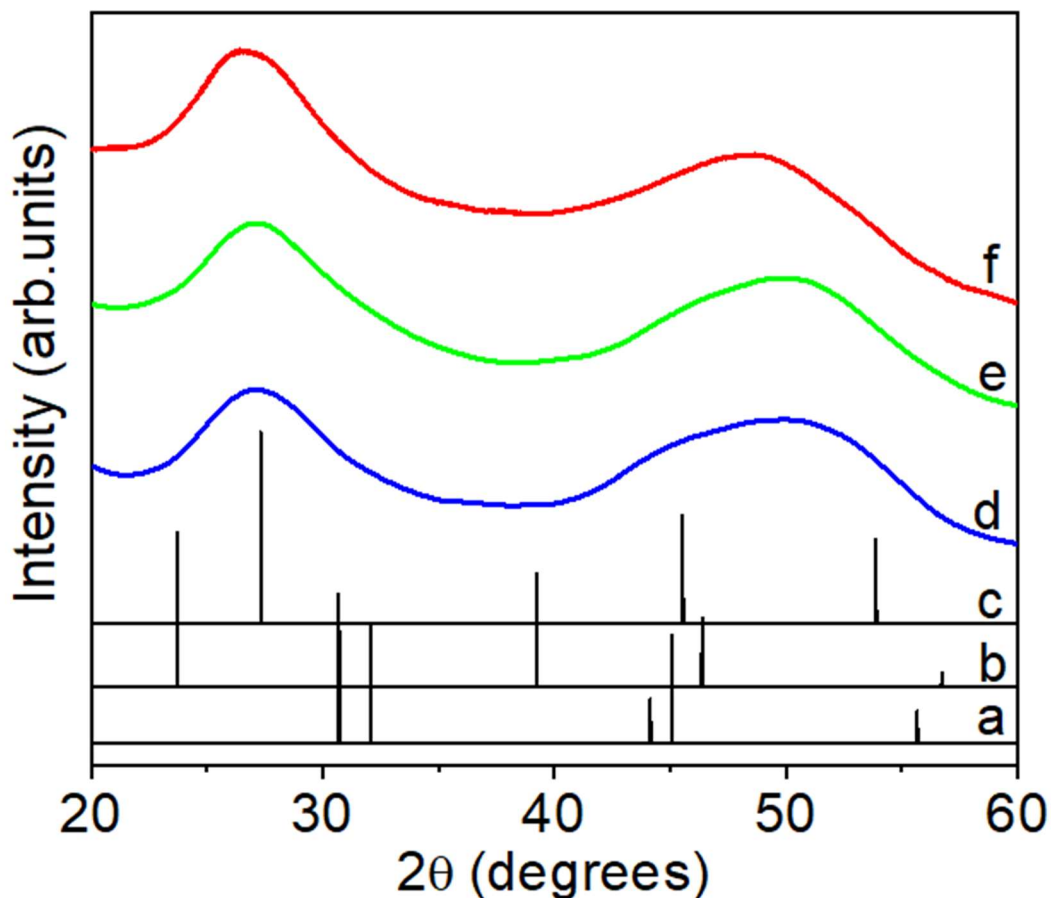


Figure 4.1. PXRD patterns of (a) b-Sn, (b) a-Sn, (c) cubic Ge (JCPDS # 01-089-5011) along with $\text{Ge}_{1-x}\text{Sn}_x$ QDs with varying Sn composition: (d) $x = 4.3\%$, (e) $x = 8.1\%$, and (f) $x = 12.5\%$.

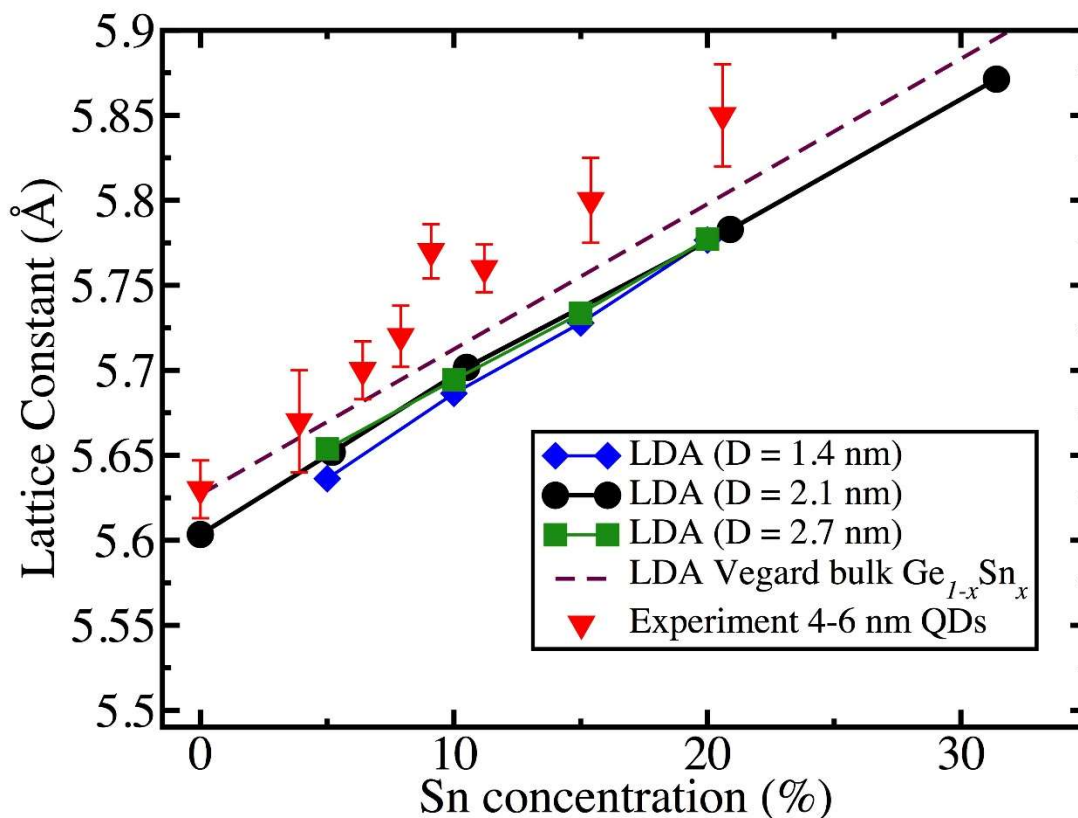


Figure 4.2. Average lattice constant of the 1.4, 2.1 and 2.7 nm diameter $Ge_{1-x}Sn_x$ QDs calculated using the LDA relaxed atomic structures compared with experimental measurements of 4-6 nm $Ge_{1-x}Sn_x$ QDs. Dashed line shows the Vegard's rule for the bulk $Ge_{1-x}Sn_x$ alloy, obtained from LDA.⁴⁷

TEM was utilized to investigate the size and morphology of alloy QDs (Figure 4.2). The LRTEM images of as-synthesized particles show near spherical morphology and fairly narrow size dispersity ($2.1 \pm 0.3 - 2.7 \pm 0.4$ nm for $x = 4.3-12.5\%$). Due to Sn-induced growth of alloy QDs, a slight increase in particle size with increasing Sn composition was noted.³¹ The size analysis of 100-150 particles across multiple individual

samples indicate narrow size distribution (14-15% for 2-3 nm QDs) of as-synthesized QDs.

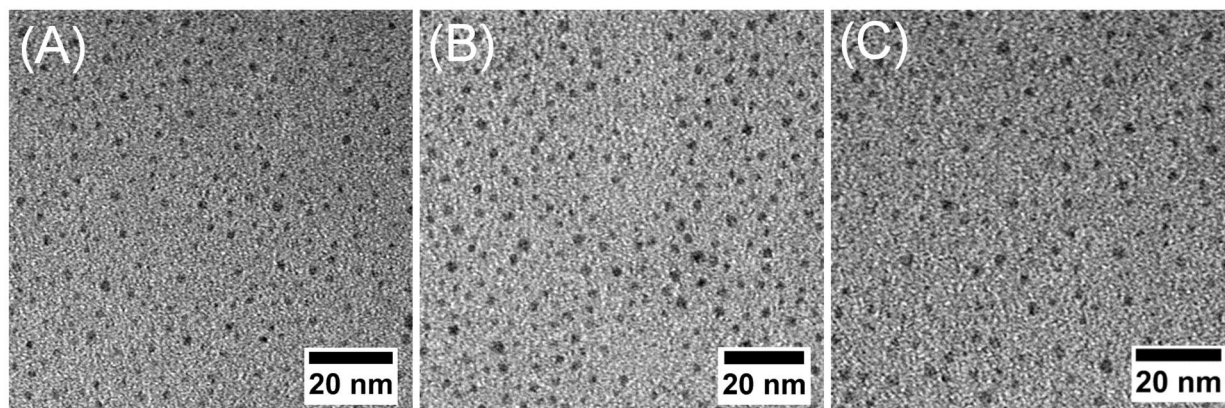


Figure 4.3. Representative low-resolution TEM images of $\text{Ge}_{1-x}\text{Sn}_x$ alloy QDs with varying Sn composition: (A) $x = 4.3\%$ (2.1 ± 0.4 nm), (B) $x = 8.1\%$ (2.4 ± 0.6 nm), and (C) $x = 12.5\%$ (2.7 ± 0.5 nm). Corresponding average particle sizes are shown in parentheses.

Absorption measurements were carried out on solid samples using solid state diffuse reflectance (converted to absorption) spectroscopy. The absorbance (energy gap) of the alloy QDs were estimated from Kubelka-Munk analysis indicate strong quantum confinement effects in ultra-small QDs with well-defined onsets in the visible spectrum (Figure 3A).^{86,87} The energy gaps of ultra-small $\text{Ge}_{1-x}\text{Sn}_x$ QDs are in visible region ranging from 1.92-1.75 eV for $x = 4.3$ -12.5%. In contrast, 4-6 nm QDs reported in the chapter 3 show onsets in the NIR region (1.72 eV-0.84 eV for $x = 1.5$ -9.1%). However, a clear red-shift in absorption onset is noted with increasing Sn composition because of Sn induced lowering of energy gaps.

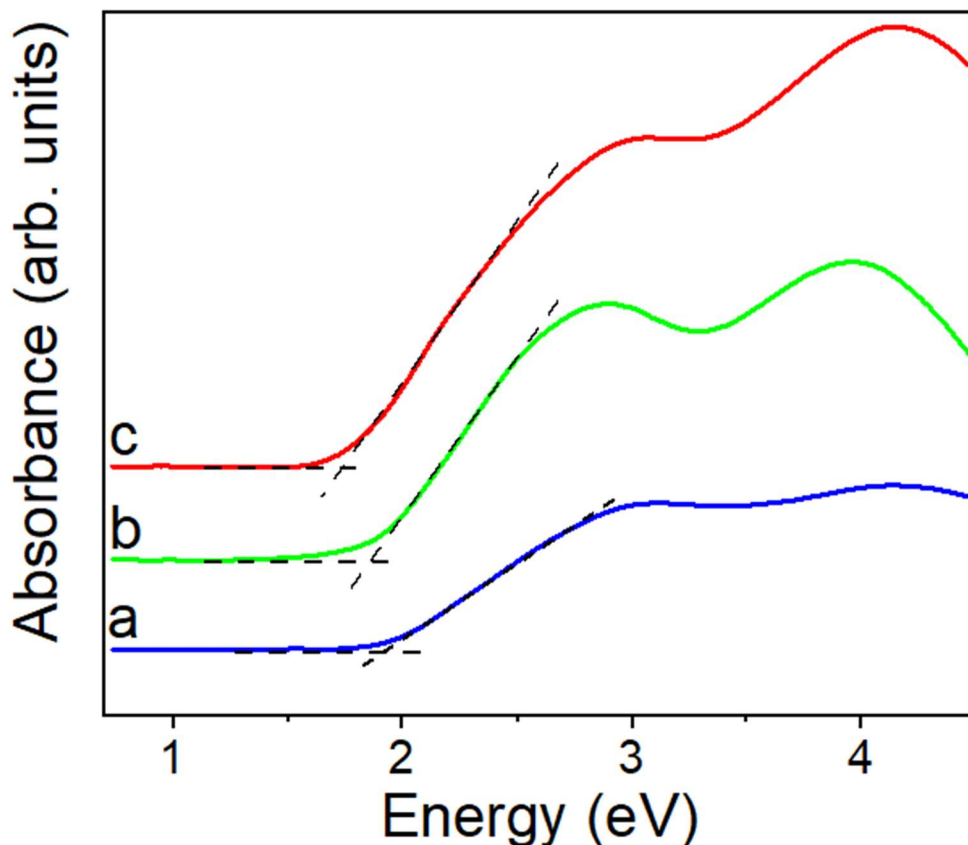


Figure 4.4. Solid state diffuse reflectance spectra (converted to absorption using Kubelka–Munk remission function) of $\text{Ge}_{1-x}\text{Sn}_x$ alloy QDs with varying Sn composition: (a) $x = 4.3\%$ (1.92 eV), (b) $x = 8.1\%$ (1.86 eV), and (c) $x = 12.5\%$ (1.75 eV). Corresponding energy gaps are shown in parentheses.

The ultra-small QDs produced in this study exhibit high intensity PL both in solution state and solid state. However, consistent with solid-state absorption, the PL of the samples measured in solid state using steady-state photoluminescence spectroscopy. The ultra-small alloy QDs exhibit composition tunable PL peak energies in the visible spectrum (2.0–1.86 eV for $x = 4.3\text{--}12.5\%$, Figure 4.5). A systematic red shift in PL maxima was noted with increasing Sn composition, consistent with absorption onsets. The Room-

temperature time-resolved photoluminescence (TRPL) spectra of $\text{Ge}_{1-x}\text{Sn}_x$ alloy QDs show a nanosecond decay, consistent with earlier reports (Figure 4.6 and Table 4.1).

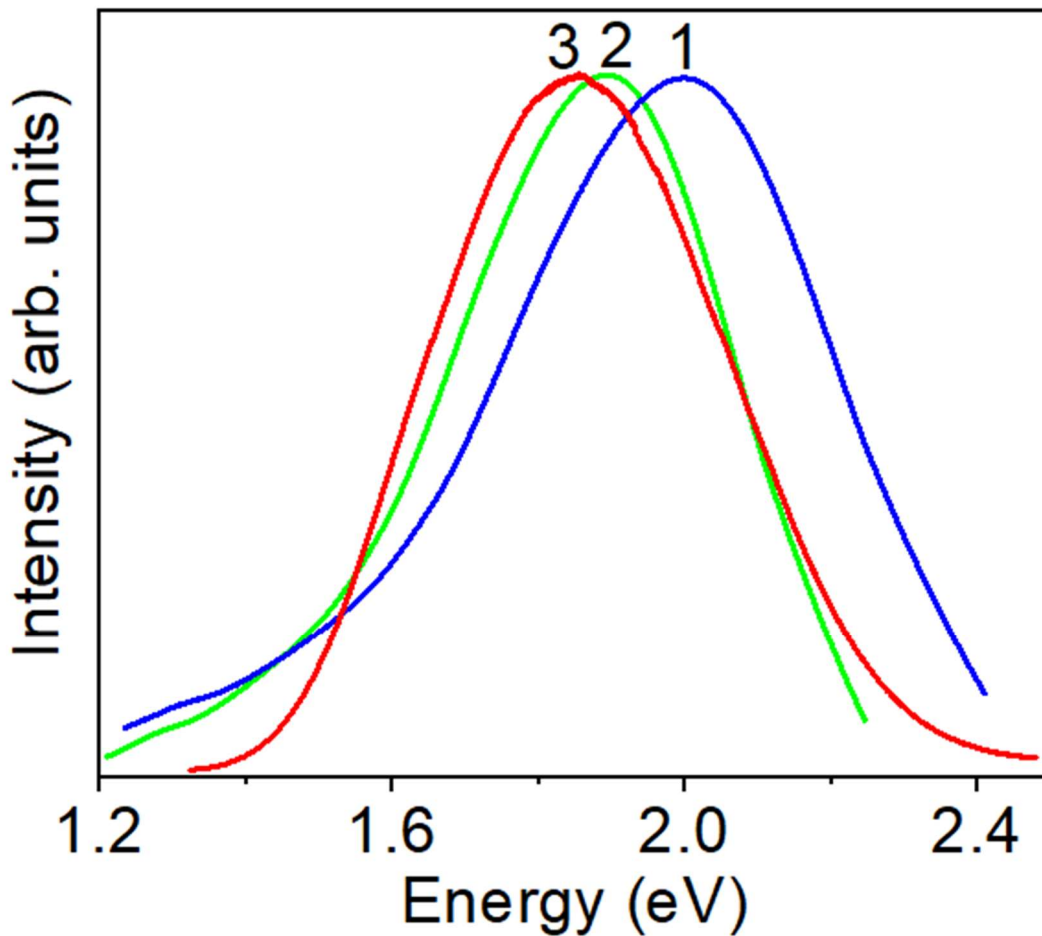


Figure 4.5. Room-temperature solid-state photoluminescence spectra of $\text{Ge}_{1-x}\text{Sn}_x$ alloy QDs with varying Sn compositions: (1) $x = 4.3\%$ 2.00 eV), (2) $x = 8.1\%$ (1.89 eV), and (3) $x = 12.5\%$ (1.86 eV). Corresponding PL peak maxima are shown in parentheses.

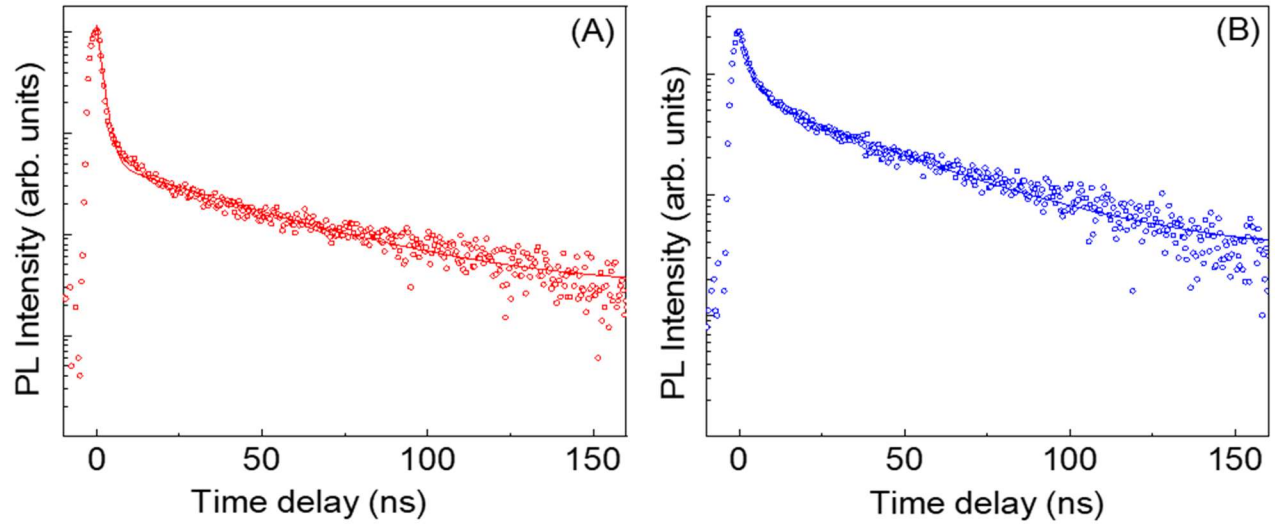


Figure 4.6. Room-temperature time-resolved photoluminescence (TRPL) spectra of $\text{Ge}_{1-x}\text{Sn}_x$ alloy QDs with varying Sn compositions: (A) $x = 8.1\%$ (2.00 eV) and (B) $x = 13.1\%$.

Table 4.1. Time Constants Extracted from Biexponential Decay Fits (

$A_{fast} e^{-t/\tau_{fast}} + A_{slow} e^{-t/\tau_{slow}}$) to PL Transients of Visible Emitting $\text{Ge}_{1-x}\text{Sn}_x$ Alloy QDs.

$\text{Ge}_{1-x}\text{Sn}_x$ (x%)	τ_{fast} (ns)	τ_{slow} (ns)	A_{fast}/A_{slow}
8.1	0.15 ± 0.01	1.16 ± 0.05	8.2
13.1	1.57 ± 0.03	39.45 ± 5.49	22.4

4.3.1 Surface Passivation to Enhance Visible Photoluminescence Brightness of Ultra-small $\text{Ge}_{1-x}\text{Sn}_x$ Alloy QDs

Additional surface passivation of as prepared alloy QDs was carried out using oleic acid. The as prepared samples were dispersed in toluene first, followed by 3 mL of oleic acid and stir the mixture for 24 h. Interestingly, PL intensities of the oleic acid treated samples exhibit a significant enhancement. However, this enhancement is less for already bright samples (Figure 4.7), whereas for the samples with low PL intensities show a 8-fold enhancement (Figure 4.8).

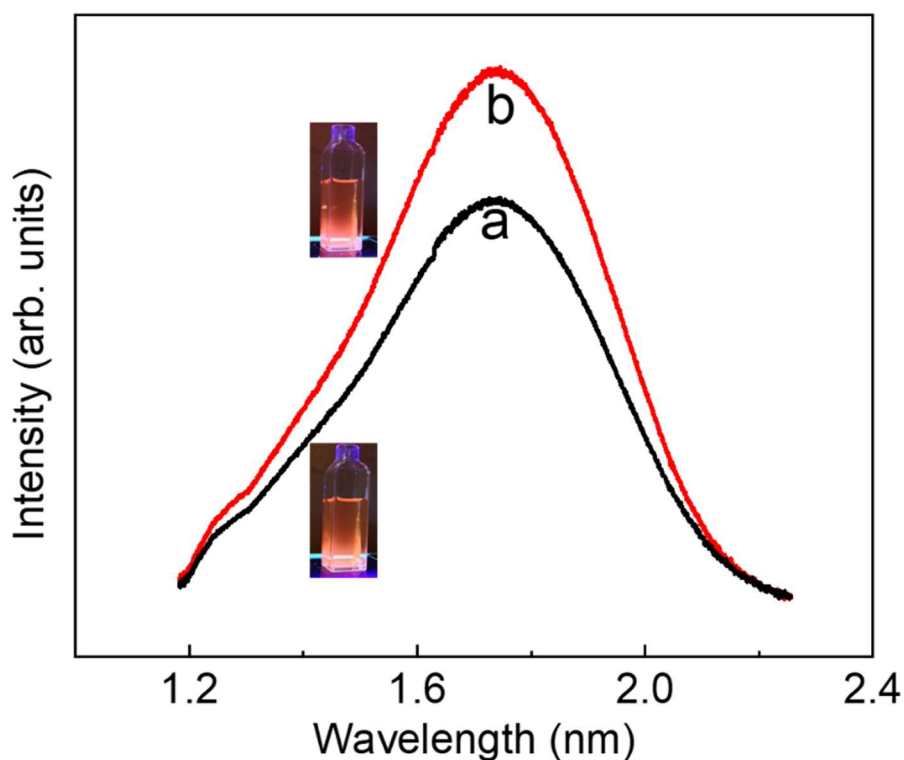


Figure 4.7. Room-temperature solid-state photoluminescence spectra of $\text{Ge}_{1-x}\text{Sn}_x$ alloy QDs ($x = 13.1\%$, 1.74 eV) exhibit visible PL: (a) As prepared QDs and (b) post-synthetic additional surface passivation using oleic acid results in 1.2-fold PL enhancement. The insets show bright red color PL for both as prepared and oleic acid treated QDs.

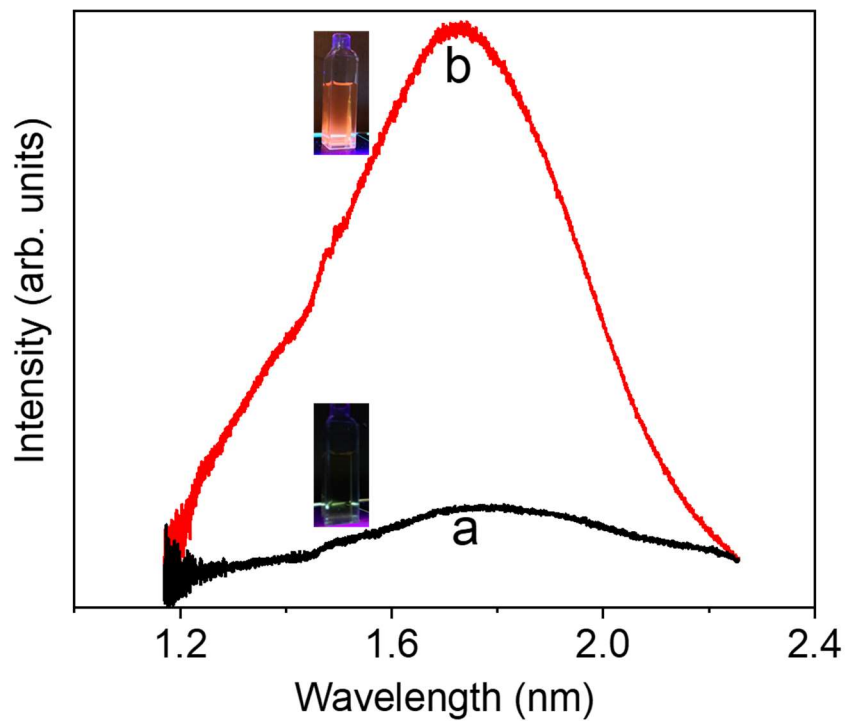


Figure 4.6. Room-temperature solid-state photoluminescence spectra of Ge_{1-x}Sn_x alloy QDs ($x = 13.1\%$, 1.74 eV) exhibit visible PL: (a) As prepared QDs and (b) post-synthetic additional surface passivation using oleic acid results in 8-fold PL enhancement. The insets show bright red color PL for oleic acid treated sample compared to as prepared one.

To understand and explain the above-mentioned enhancement with oleic acid along with temperature dependence of PL, theoretical studies are currently underway.

CHAPTER 5

Multivariate Synthesis of Tin Phosphide

Nanoparticles: Temperature, Time, and Ligand

Control of Size, Shape, and Crystal Structure

5.1 Introduction

Tin phosphides have gained significant interests as a class of materials that exhibit a range of physical properties of both fundamental and technological interest depending on their chemical identity and crystal phase. For instance, tin-rich rhombohedral Sn_4P_3 is metallic in nature whereas phosphorus-rich trigonal SnP_3 , hexagonal SnP , and highly disordered Sn_3P_4 are narrow bandgap semiconductors.^{14,121-124} These distinct properties make them attractive as low-cost, earth abundant catalytic, photocatalytic, and semiconductor materials depending sensitively on the electronic structure, stoichiometry, and crystal phase.^{14,125} Scaling down the size to nanoscale regimes has been shown to augment these properties, providing an incentive to develop robust and reproducible syntheses that enable control over morphology and crystal phase.¹² Despite considerable understanding of bulk physical properties, nanoscale properties of tin phosphides are poorly understood to date, owing in part to lack of well-developed syntheses that enable precise control over size, shape, and crystal phase.

The metal rich Sn_4P_3 possess a layered crystal structure, which makes it promising as high capacity, cycle-stable anode material for Li- and Na-ion batteries.^{69,126-129}

Moreover, because of tin rich crystal structure, rhombohedral Sn_4P_3 is also known as a promising material in photocatalytic degradation of organic compounds and alkylation of silanes.¹²⁵ In contrast, the phosphorus-rich, trigonal Sn_3P_4 is a narrow bandgap semiconductor that exhibits a transition from n-type to p-type below 150 K, with potential application in thermoelectrics.¹⁴ Conversely, for bulk SnP, there is no known stable phase at ambient conditions whereas the existence of a metastable/high pressure phase has been reported.^{71,130} Nonetheless, recent reports on colloidal syntheses of tin phosphides have yielded micron-sized, hexagonal SnP particles with unique morphologies and physical (charge storage) properties.^{74,131} Despite significant differences in fundamental properties, the crystal structures of Sn_3P_4 and Sn_4P_3 are remarkably similar and indicate the presence of two distinct Sn atoms: Sn(1) atoms are octahedrally coordinated by phosphorus atoms whereas Sn(2) atoms confine a [3+3] coordination consisting of three phosphorus and three Sn(2) atoms.¹⁴ Theoretical studies of Sn_3P_4 suggest an indirect bandgap of 0.83 eV, owing to the presence of filled bonding and nonbonding states and vacant antibonding states.^{14,132} Therefore, optoelectronic transitions are expected in between those energy levels resulting in semiconducting properties.

Among tin phosphides, the synthesis of rhombohedral Sn_4P_3 has been studied both as extended solids and micron-sized particles.^{69,125-129} Phase pure Sn_4P_3 has been produced by direct reaction of metallic tin with red phosphorous at elevated temperatures,¹²¹⁻¹²⁴ hydrothermal and solvothermal syntheses,^{53,68,70,72} chemical or pulsed vapor deposition,¹³³ and mechanical milling.^{69,127-129} Specifically, high energy mechanical milling has been widely studied for the synthesis of agglomerated, micron-sized Sn_4P_3 powders/particles as anode material for Li- and Na-ion batteries.^{69,127-129} The

first synthesis of Sn_4P_3 nanorods has been reported by Xie et al. where aggregated bundles of anisotropic particles were obtained via solvothermal method with no control over growth mechanics.⁷⁰ Later, micron-sized, aggregated Sn_4P_3 spheres, tubes, hollow nanostructures, and polycrystalline powders with high degree of size dispersity have also been produced via solvothermal synthesis.^{53,68,72} In contrast, only a handful of efforts on colloidal synthesis of tin phosphide NPs are reported. Kim et al. exploited alkylphosphines and tin acetate to produce teardrop-shaped, hexagonal $\text{SnP}_{0.94}$ microcrystals for Li-ion battery applications.⁷⁴ Aso et al. utilized thermal decomposition of tin salts in high boiling alkylamine and phosphines to produce hexagonal $\text{SnP}_{0.94}$ along with tetragonal Sn impurities.¹³¹ However, neither reported comprehensive physical characterization of tin phosphide NPs nor achieved nanoscale control over size, shape, and crystal structure. To our knowledge, the synthesis of phosphorus rich Sn_3P_4 and SnP_3 phases on the nanoscale has not been reported.

Herein, we report the first colloidal synthesis of rhombohedral Sn_4P_3 , hexagonal SnP , and trigonal Sn_3P_4 NPs with control over size, shape, and crystal structure using a generalized chemical route. The NP morphology and crystal phase were tuned by varying the nucleation and growth temperature, altering the Sn/P molar ratio of the reaction, and/or using the additional coordinating solvents. A significantly smaller set of quantum confined tin phosphide NPs was produced at low temperatures (100 °C), which undergo trigonal Sn_3P_4 to rhombohedral and hexagonal phase transitions at 180 and 250 °C, respectively. The surface characterization of tin phosphide NPs suggests the presence of three distinct oxidation states of tin (Sn^0 484.8 eV, Sn^{2+} 486.4 eV and Sn^{4+} at 487.4 eV) across multiple phases reported. However, the analysis of P(2p) region indicates that the

P-Sn bond is only marginally sensitive to the oxidation states of tin observed in distinct crystal phases.

5.2 Experimental Section

5.2.1 Materials: Oleylamine (OLA), 1-octadecene (ODE), 1-dodecanethiol (DDT), and tri-n-butylphosphine (TBP) were purchased from Acros. Tin(II) chloride, tin(IV) iodide (99.998%) and oleic acid (OA) were purchased from Alfa Aesar. Tris(trimethylsilyl)phosphine ((TMSi)₃P, 10 wt% in hexane) and tri-n-octylphosphine (TOP) were purchased from Strem Chemicals. Oleylamine and 1-octadecene were degassed and dried under vacuum at 120 °C for 2 h. Toluene was dried with Na and methanol was dried with molecular sieves and both were distilled under nitrogen before use. All other chemicals were used as received without further purification. *[Caution: (TMSi)₃P is pyrophoric and will immediately ignite in air. TBP has the potential to generate pyrophoric phosphorus. Therefore, only properly trained personnel should carry out this synthesis under air-free conditions.]*

5.2.2 Synthesis of Rhombohedral Sn₄P₃ NCs and Larger, Partially Crystalline

Sn₄P₃ NPs: In a typical synthesis of rhombohedral Sn₄P₃ NCs, stock solutions of (TMSi)₃P/ODE (0.24 mmol of (TMSi)₃P in 1 mL of ODE) and TBP/ODE (1 mL of TBP in 1 mL of ODE) were freshly prepared in a nitrogen glovebox. Anhydrous SnI₄ (0.2 mmol), OLA (5 mL), and OA (25 μL) were taken in a 50 mL three neck flask and degassed at 120 °C for 1 h. Then, the reaction was flushed with nitrogen for 10 min and heated to 180 °C. At this temperature, stock solutions of TBP/ODE and (TMSi)₃P/ODE were swiftly injected. Upon injection, the temperature was dropped to 160–165 °C and allowed to heat back to 180 °C within 3–4 min to produce phase pure, rhombohedral Sn₄P₃ NCs. Larger, partially

crystalline Sn_4P_3 NPs were obtained using the same synthetic protocol with no use of alkylphosphine (TBP).

5.2.3 Synthesis of Hexagonal SnP NCs: In a typical synthesis of hexagonal SnP NCs, a stock solution of $(\text{TMSi})_3\text{P}$ in ODE (0.35 mmol of $(\text{TMSi})_3\text{P}$ in 1 mL of ODE) was prepared in a nitrogen glove box. Ultra-dry SnI_4 (0.2 mmol, 0.125 g), OLA (5 mL), and OA (25 μL) were taken in a 50 mL three neck flask and degassed under vacuum at 120 °C for 1 h. The reaction was flushed with nitrogen and the temperature was raised to 250 °C within 15–20 min. Then, the $(\text{TMSi})_3\text{P}/\text{ODE}$ solution was rapidly injected. The reaction color changed to black within ~2 seconds and the resulting nuclei were grown for 5, 30, 60, and 180 seconds at 250 °C to produce hexagonal SnP NCs with different sizes.

5.2.4 Synthesis of Smaller, Trigonal Sn_3P_4 NPs: In a typical synthesis of smaller trigonal Sn_3P_4 NPs, a stock solution of $(\text{TMSi})_3\text{P}/\text{ODE}$ (0.24 mmol of $(\text{TMSi})_3\text{P}$ in 1 mL of ODE) was freshly prepared in a nitrogen glovebox. Ultra-dry SnI_4 (0.2 mmol, 0.125 g), OLA (5 mL), and OA (25 μL) were mixed in a 50 mL three neck flask and degassed under vacuum at 120 °C for 1 h. Then, the reaction was flushed with nitrogen and 1 mL of TBP in 1 mL of ODE was injected. The injection caused a temperature drop to 108–110 °C and the reaction was cooled to 100 °C under nitrogen. Then, the $(\text{TMSi})_3\text{P}/\text{ODE}$ mixture was rapidly injected. The resultant nuclei were grown at 100 °C for different time intervals (5–180 seconds) to produce trigonal Sn_3P_4 NPs with different sizes.

5.2.5 Isolation and Purification: After desired growth time, the reactions were quenched rapidly by blowing compressed air, followed by the injection of toluene (6–8 mL) at ~80 °C. The resulting NPs were precipitated with excess methanol, followed by centrifugation at 3500g for 5-10 min. The NPs were purified by re-dispersion and re-

precipitation in toluene (2–3 mL) and methanol (10–15 mL), respectively. This process was repeated twice to obtain black color precipitates, which were dried under vacuum prior to further characterization.

5.3 Results and Discussion

5.3.1 Nucleation and Growth Control Tin Phosphide NPs. Although tin phosphides exist in multiple crystal phases, the synthesis of rhombohedral Sn_4P_3 and hexagonal SnP were only reported owing to highly ordered crystal structures and significant applications.^{74,127} Herein, we have systematically explored the possible options for colloidal synthesis of aforementioned phases by employing a number of Sn and P precursors, additional coordinating solvents (TBP and TOP), and varying molar ratio of Sn/P. To produce rhombohedral Sn_4P_3 , tin(II) chloride and TOP were initially employed in OLA/OA/ODE. It has been reported that the amount of alkylamines is critical in obtaining a desired metal phosphide phase when alkylphosphines are employed as the phosphorus-source.^{45,58,134} Therefore, varying molar ratio of Sn: OLA was explored in the synthesis along with TOP. At high concentrations of OLA (i.e. Sn: OLA molar ratio of 0.2: 15.2 mmol), Sn^{2+} is found to be strongly coordinated by alkylamines, hence the reaction with TOP did not produce tin phosphides (or elemental Sn) even at ~ 350 °C, despite the potential to produce reactive phosphorus.^{45,55,135} Lowering the concentration of OLA (i.e. Sn: OLA molar ratio of 0.2: 1.52 mmol) caused the nucleation of tetragonal Sn at ~ 350 °C, as the precursor amino-tin complex is less shielded (Figure 5.1). Therefore, highly reactive $(\text{TMSi})_3\text{P}$ was employed along with a number of Sn halides in OLA/OA/ODE. The advantage of the latter route is that $(\text{TMSi})_3\text{P}$ is a stoichiometric reagent and therefore is helpful in tuning the reaction parameters to optimize the synthesis of desired crystal

phases.^{64,65,136} Initially, metal rich Sn_4P_3 was produced using SnCl_2 and $(\text{TMSi})_3\text{P}$ at 180 °C (Figure 5.2). Although OLA could serve as strongly passivating agents, challenge remained in obtaining smaller Sn_4P_3 nanocrystals (NCs). The PXRD pattern of the reaction product exhibits sharp Bragg's reflections pertaining to the growth of larger Sn_4P_3 particles (40-90 nm). As the nucleation (< 5 seconds) and growth is fast, neither rapid cooling nor incorporation of additional coordinating solvents (DDT, TOP, and TBP) resulted in controlled growth of Sn_4P_3 NCs. The addition of latter two reagents has slowed down the reaction and the nucleation were delayed up to 50–60 seconds.

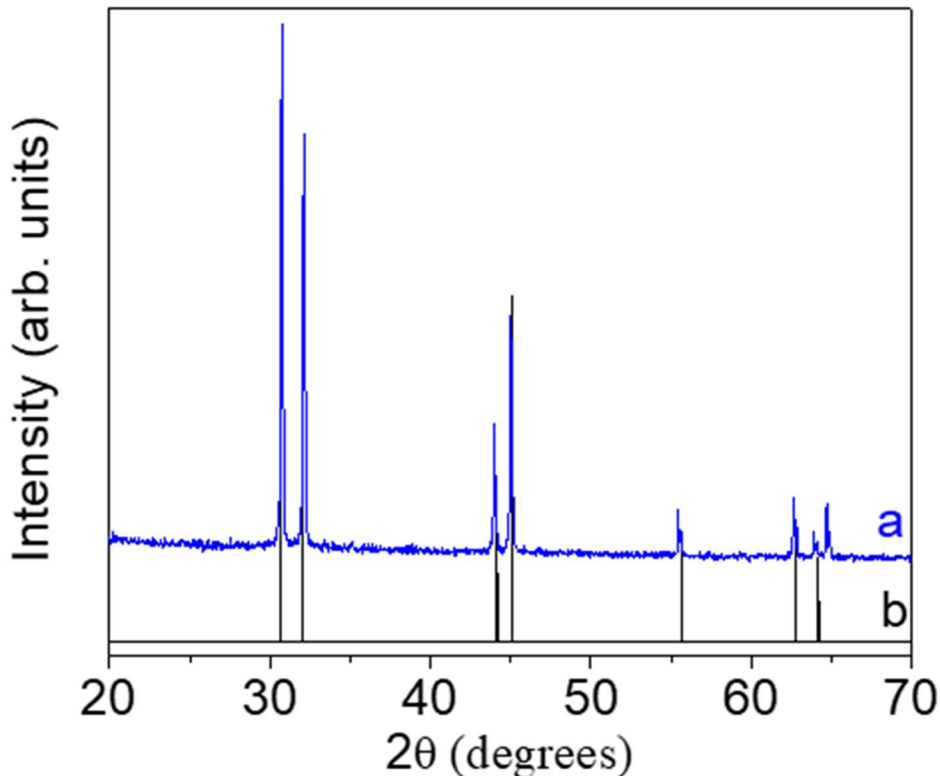


Figure 5.1. (a) Powder XRD pattern of the product obtained from the reaction of SnCl_2 and TOP in OLA/OA/ODE at 350 °C for 3 h along with the (b) ICDD-PDF overlay of tetragonal Sn (JCPDS No. 00-004-0673).

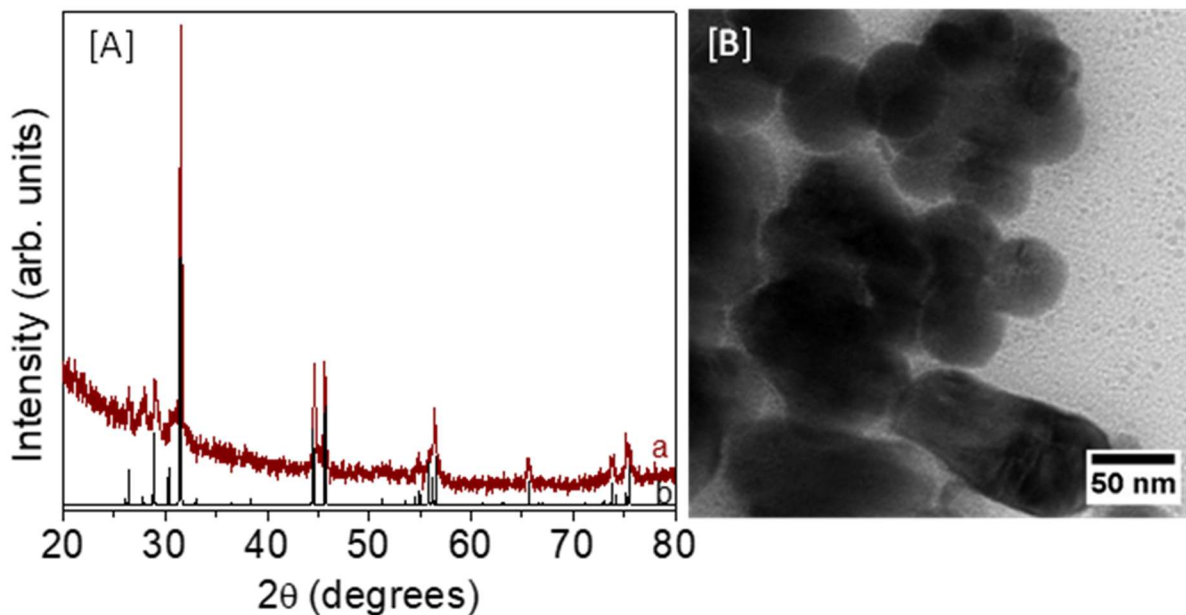


Figure 5.2. (A) (a) Powder XRD pattern of the product obtained from the reaction of SnCl_2 and $(\text{TMSi})_3\text{P}$ in OLA/OA/ODE at 180 °C for 3 min along with the (b) ICDD-PDF overlay of rhombohedral Sn_4P_3 (JCPDS No. 01-073-1820). (B) A representative TEM image of the as-prepared particles.

The incorporation of DDT caused the synthesis of rhombohedral Sn_4P_3 along with orthorhombic SnS impurities as evidenced by structural characterization (Figure 5.3). Likewise, the attempts to alter nucleation and growth using substitute tin halides (SnBr_2 and SnI_2) along with $(\text{TMSi})_3\text{P}$ showed no change in reaction kinetics. However, the use of $\text{SnI}_4/(\text{TMSi})_3\text{P}$ precursors provided significant control over NP growth besides slow nucleation (50–60 seconds). Therefore, SnI_4 and $(\text{TMSi})_3\text{P}$ were employed in the synthesis of tin phosphide NPs with varying size, shape, and crystal structures (Scheme 5.1).

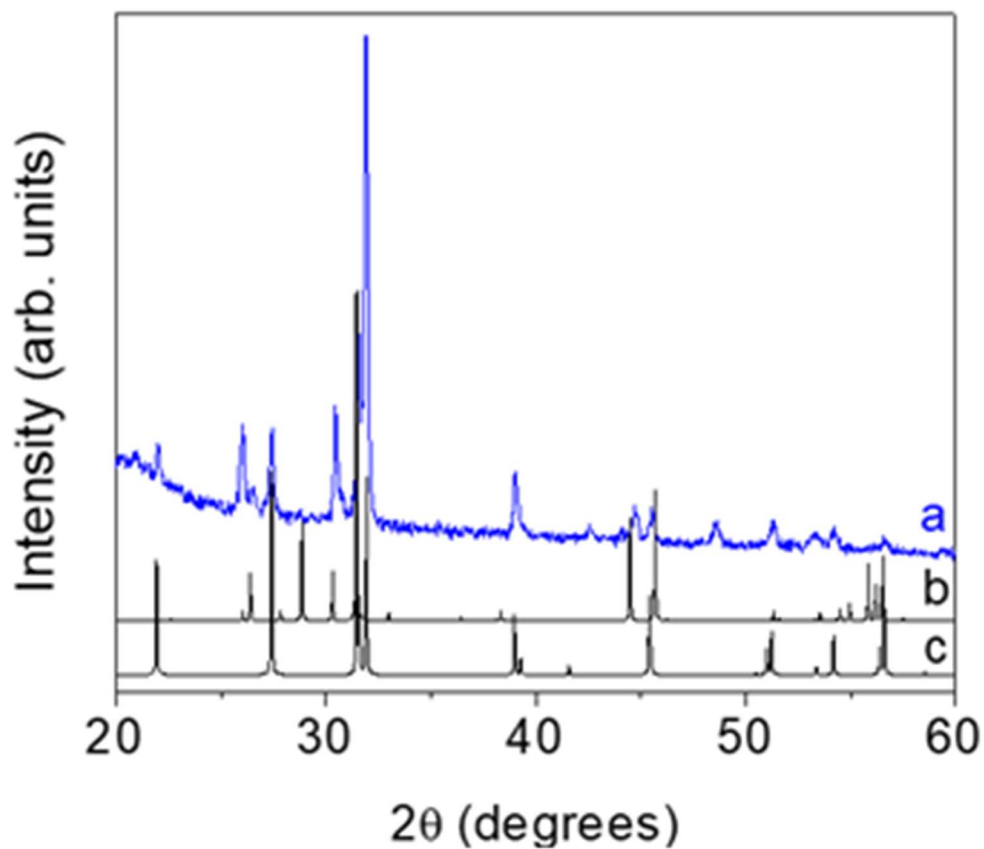
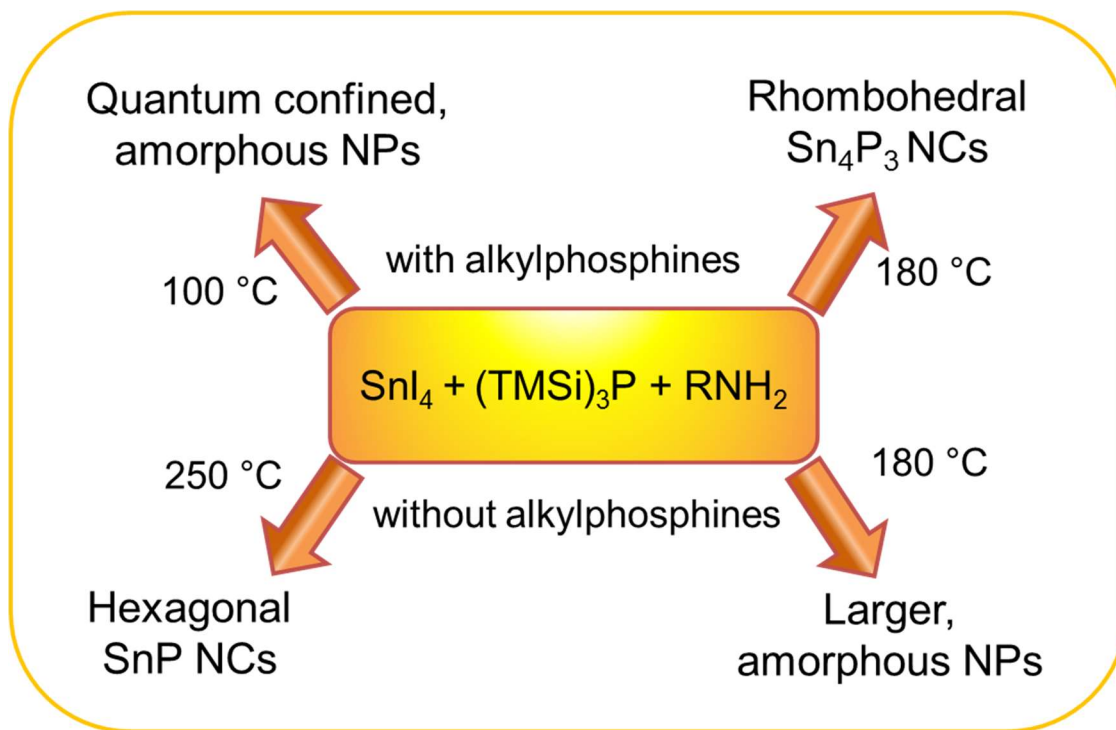


Figure 5.3. (a) Powder XRD pattern of the product obtained from the reaction of SnCl₂ and (TMSi)₃P in OLA/OA/ODE with DDT at 180 °C for 12 h along with the ICDD- PDF overlays of (b) rhombohedral Sn₄P₃ (JCPDS No. 01-073-1820) and (c) orthorhombic SnS (JCPDS No. 39-0354).



Scheme 5.1 Reaction protocols for the synthesis of size, shape, and phase controlled rhombohedral Sn_4P_3 , hexagonal SnP, and trigonal Sn_3P_4 NPs. RNH_2 = oleylamine.

5.3.2 Phase Pure Rhombohedral and Partially Crystalline Sn_4P_3 NPs. In a typical synthesis of partially crystalline Sn_4P_3 NPs, $\text{SnI}_4:(\text{TMSi})_3\text{P}$ molar ratio of 1: 1.2 was allowed to react in OLA/OA/ODE at 180 °C for 1–10 min to produce NPs with desired sizes. When the reactions were performed without OA, resultant particles exhibit high degree of size dispersity. However, the use of OA has allowed us to control the NP size in a much narrower regime (18.7 ± 1.5 nm – 35.4 ± 4.9 nm) by manipulating the growth time at 180 °C (Figure 5.6A-D).

The structural analyses of the reaction products suggest the presence of amorphous to partially crystalline Sn_4P_3 NPs. The PXRD and SAED patterns indicate broad and ambiguous diffraction, likely because of the lack of long-range crystal order

and the possible presence of amorphous domains (Figure 5.5).³⁵ Conversely, HRTEM reveals lattice fringes with a d spacing of 0.31 nm, corresponding to the (105) plane of the rhombohedral Sn₄P₃ crystal structure (Figure 5.5). The elemental analyses indicate Sn/P atomic ratios of 57.4–58.6/42.6–41.4 (Sn/P ~ 1.38) for all samples, which are in close agreement with the atomic composition of rhombohedral Sn₄P₃ (Figure 5.5). Remarkably, phase pure crystalline Sn₄P₃ NCs can also be produced at 180 °C in the presence of TBP (Figure 5.6E, F). Scherrer analysis of rhombohedral Sn₄P₃ NCs indicates an average crystallite size of 35.2 ± 0.2 nm,⁷⁶ which is in close agreement with size estimated from TEM images (38.4 ± 4.8 nm, Figure 5.6E). The Sn₄P₃ crystallites exhibit flower-like morphology caused potentially by the agglomeration of smaller NPs. Further attempts to produce size tunable Sn₄P₃ NCs were not successful and resulted in larger, polydisperse mixed phases of crystalline tin phosphides (Figure 5.7-5.9).

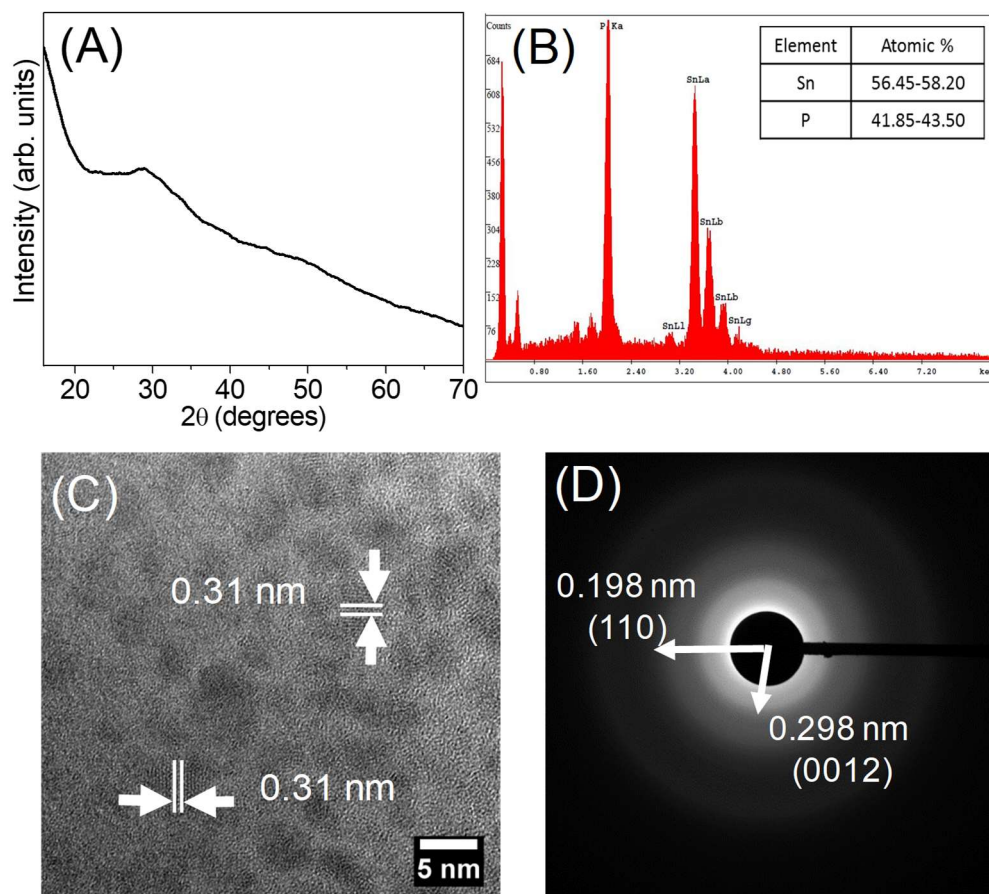


Figure 5.5. (A) A representative powder XRD pattern of amorphous to partially crystalline Sn_4P_3 NPs produced at 180 °C for 5 min using SnI_4 and $(\text{TMSi})_3\text{P}$ precursors, without the use of alkylphosphines (TBP or TOP). (B) SEM/EDS spectrum of the corresponding Sn_4P_3 NPs along with (C) HRTEM, and (D) the selected area electron diffraction pattern recorded from 200 nm x 200 nm area of the sample indicating short-range crystalline order of rhombohedral Sn_4P_3 . The broad and not well-defined peaks in the PXRD is due to lack of long-range crystalline order. The average Sn: P atomic ratio obtained from 5 individual measurements of the same sample are also shown suggesting the growth of Sn_4P_3 particles.

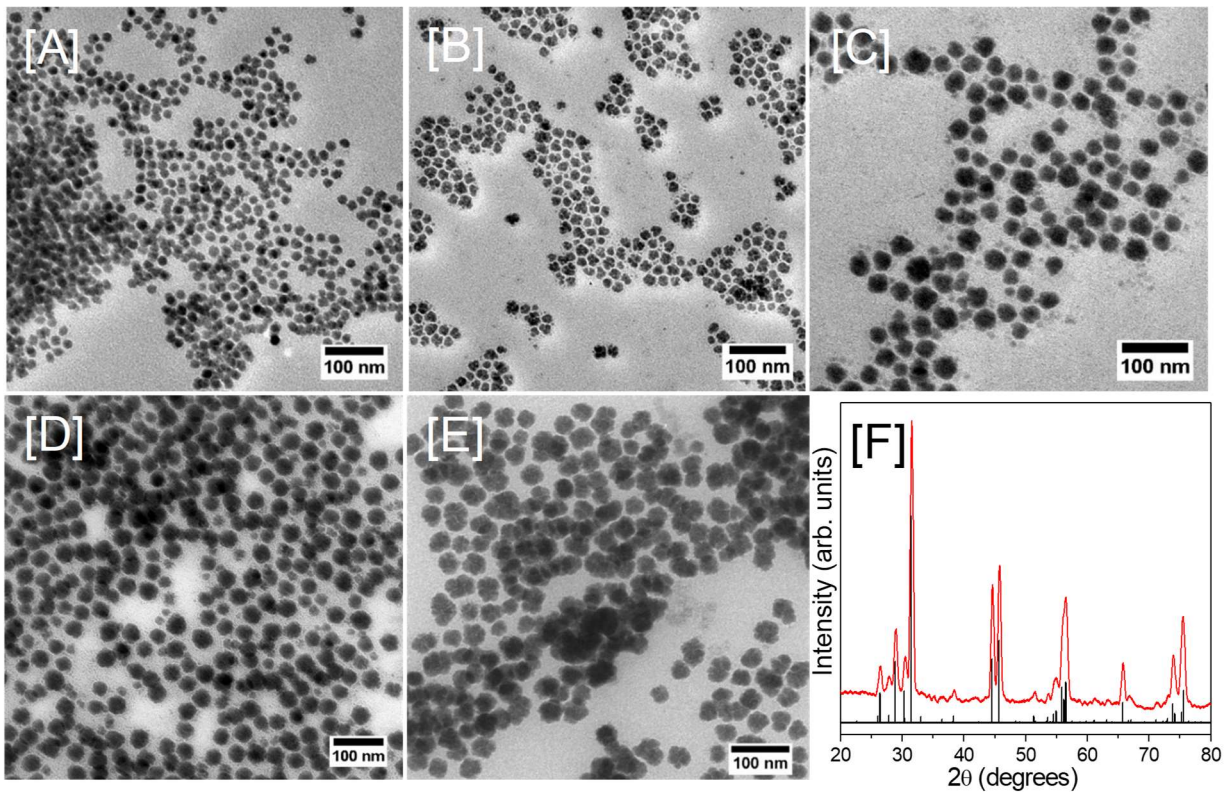


Figure 5.6. TEM images of amorphous to partially crystalline Sn_4P_3 NPs synthesized in the OLA/OA/ODE system at 180 °C without TBP for growth times of (A) 5 s (18.7 ± 1.5 nm), (B) 1 min (19.5 ± 3.4 nm), (C) 5 min (26.7 ± 4.2 nm), and (D) 10 min (35.4 ± 4.9 nm). (E) Representative TEM image and (F) PXRD pattern of the phase pure, rhombohedral Sn_4P_3 NCs (38.4 ± 4.8 nm) produced in the OLA/OA/ODE system at 180 °C with 4 mM TBP. The ICDD–PDF overlay of rhombohedral Sn_4P_3 (JCPDS Card No. 01-073-1820) is shown as vertical black lines.

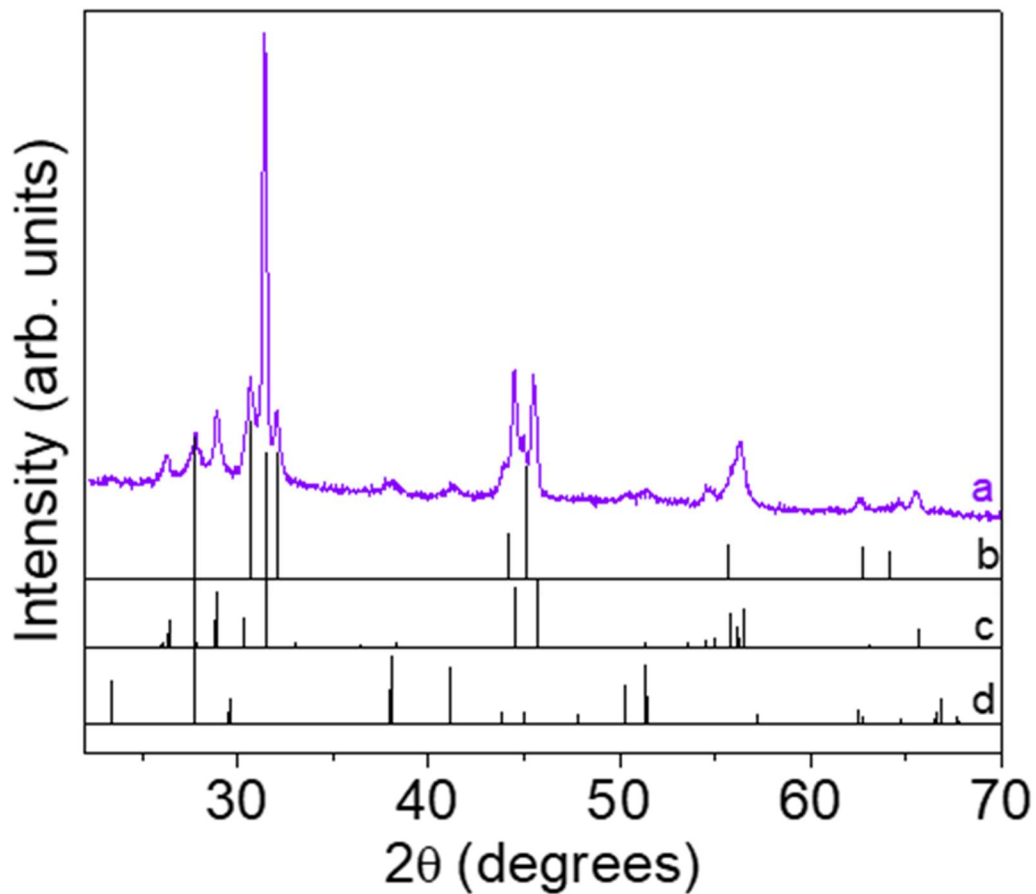


Figure 5.7. (a) Powder XRD pattern of the product obtained from the reaction of SnI₄ and (TMSi)₃P in OLA/OA/ODE at 180 °C for 3 min in the presence of 12 mM TBP. ICDD-PDF overlays of (b) tetragonal tin (JCPDS No. 00-004-0673), (c) rhombohedral Sn₄P₃ (JCPDS No. 01-073-1820), and (d) hexagonal SnP (JCPDS No. 03-065-9787) are also shown.

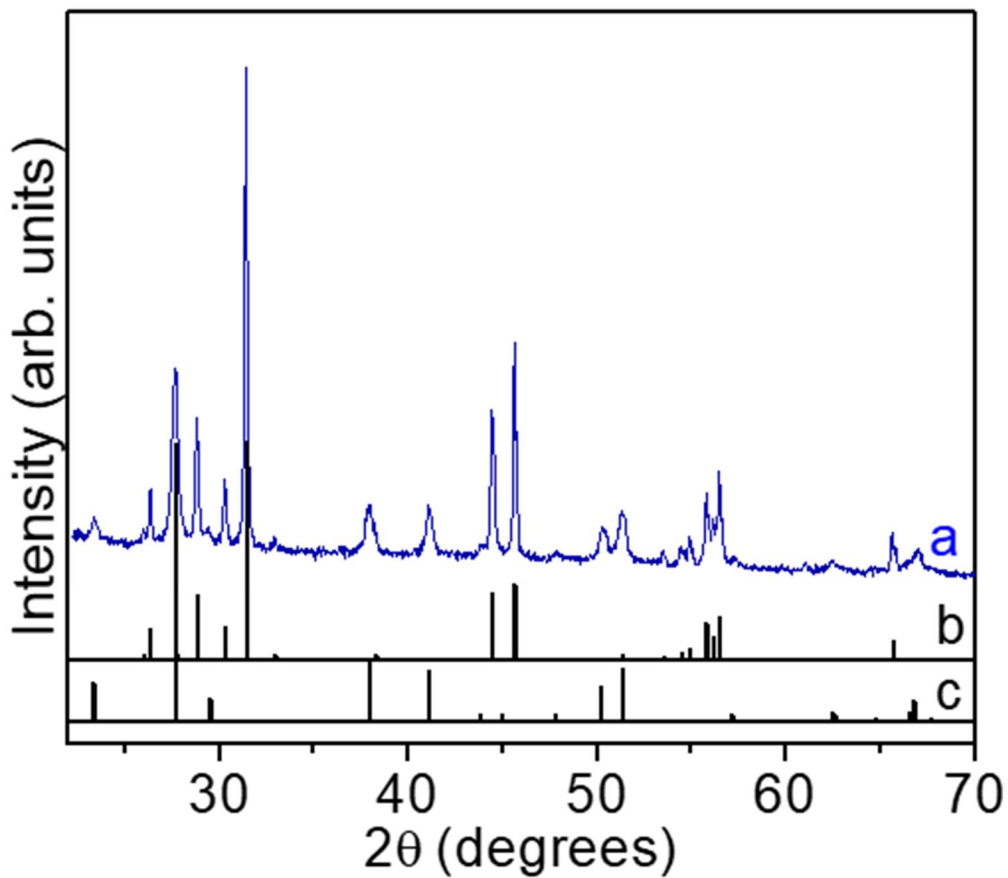


Figure 5.8. (a) Powder XRD pattern of the product obtained from the reaction of SnI_4 and $(\text{TMSi})_3\text{P}$ in OLA/OA/ODE at $180\text{ }^\circ\text{C}$ for 3 min in the presence of 4 mM of TOP. ICDD-PDF overlays of (b) rhombohedral Sn_4P_3 (JCPDS No. 01-073-1820) and (c) hexagonal SnP (JCPDS No. 03-065-9787) are also shown.

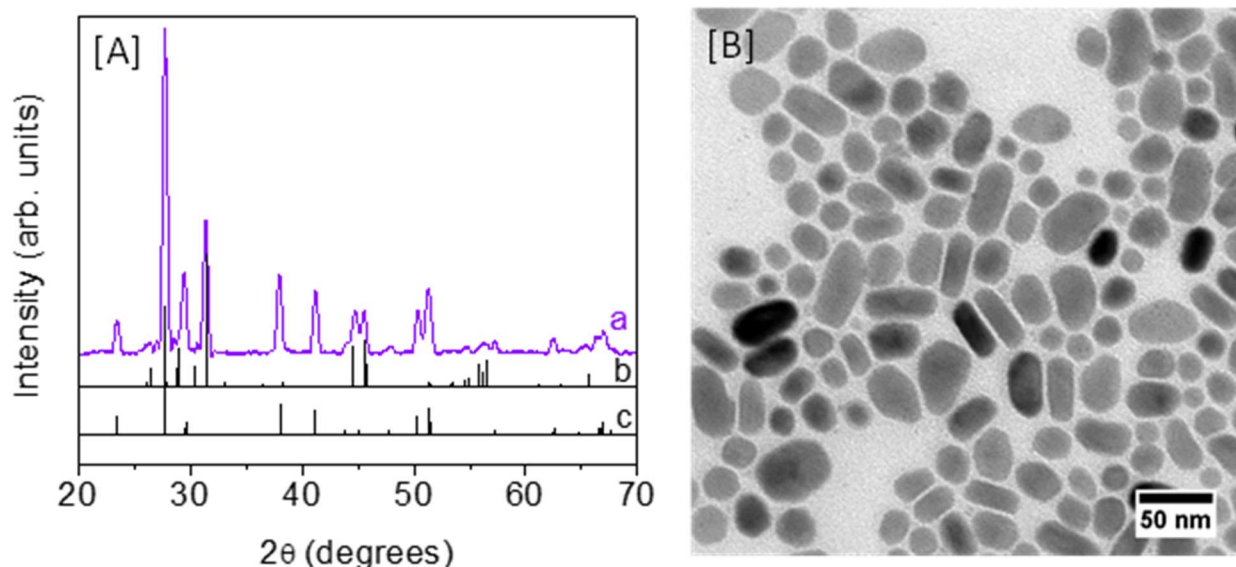


Figure 5.9. (A) Powder XRD pattern of (a) the product obtained from the reaction of SnI_4 and $(\text{TMSi})_3\text{P}$ in OLA/OA/ODE at 220 °C for 15 min. ICDD-PDF overlays of (b) rhombohedral Sn_4P_3 (JCPDS No. 01-073-1820) and (c) hexagonal SnP (JCPDS No. 03-065-9787) are also shown. (B) A representative TEM image of the as-prepared particles.

4.3.3 Role of TBP in Prompting the Crystallinity of Sn_4P_3 . To uncover the key factors critical for inducing crystallinity in Sn_4P_3 , a series of control experiments were implemented. With no TBP, the NPs produced at 180 °C were partially crystalline, whereas fully crystalline rhombohedral Sn_4P_3 NCs were produced in the presence of TBP. It was also revealed that the amount of TBP is critical in the synthesis of phase pure Sn_4P_3 NCs. In our observation, 4 mM of TBP is sufficient to attain rhombohedral Sn_4P_3 NCs with no additional impurities. Further increasing TBP (8-12 mM) has slowed down the nucleation, hence required longer growth times (5-10 min) to attain the crystallinity. The reactions carried out with 8-12 mM TBP produced rhombohedral Sn_4P_3 along with tetragonal Sn and hexagonal SnP impurity phases (Figure 5.7). Long chain alkylphosphines (TOP) have also been used in lieu of TBP yet resulted in mixed phases

of Sn_4P_3 and SnP (Figure 5.8). It is likely that the coordination of the alkylphosphines to Sn^{4+} precursors plays an important role in the crystal growth and both the length of alkyl chain and the amount of phosphines used in the synthesis is highly sensitive for the production of phase pure Sn_4P_3 . The reason for this remarkable contrast in structure can potentially be attributed to the *in-situ* generation of Sn(IV)-TBP complexes such as Sn-phosphanediide cages.¹³⁷ Since TBP is a weakly coordinating ligand, it can potentially produce Sn(IV)-TBP complexes that control the ordered growth of tin phosphide nuclei. A similar phenomenon has been reported in the synthesis of Ge NCs, where hexamethyldisilazane (HMDS) has been used to produce diamond-like cubic Ge in lieu of amorphous NPs.¹¹² In the above report, the formation of Ge-HMDS complex and subsequent ordered crystal growth is presumed to induce the crystallinity of Ge NCs. With further increasing the growth temperature ($>180\text{ }^\circ\text{C}$), hexagonal SnP NCs were obtained with trace amounts of rhombohedral Sn_4P_3 NCs (Figure 5.9). It is important to note that the reactions performed at $190\text{-}240\text{ }^\circ\text{C}$ consistently resulted in mix phases of SnP and Sn_4P_3 . TEM images of the mixed phases produced at $220\text{ }^\circ\text{C}$ indicate the presence of short rods and oblong-shaped particles. The typical length of nanorods is $40\text{-}60\text{ nm}$ whereas the width is $15\text{-}25\text{ nm}$. In contrast, oblong-shaped particles are $\sim 20\text{-}80\text{ nm}$ in diameter.

5.3.4 Synthesis of Phase Pure Hexagonal SnP NCs. Phase pure, hexagonal SnP NCs were produced in OLA/OA/ODE at $250\text{ }^\circ\text{C}$ when $\text{SnI}_4:(\text{TMSi})_3\text{P}$ precursor ratio of $1: 1.75$ is employed in the synthesis. The narrowly disperse, spherical SnP NPs with wider tunability of sizes were obtained by varying the growth time at $250\text{ }^\circ\text{C}$. The structural analyses of the reaction product indicate the presence of hexagonal SnP with significant

line broadening consistent with the growth of smaller crystallites (Figure 5.10). No extraneous Bragg reflections corresponding to tetragonal Sn or other tin phosphide impurities were detected suggesting that as-synthesized NCs are phase pure. Conversely, the rhombohedral Sn_4P_3 impurities were often detected in reactions performed below 250 °C (Figure 5.9).

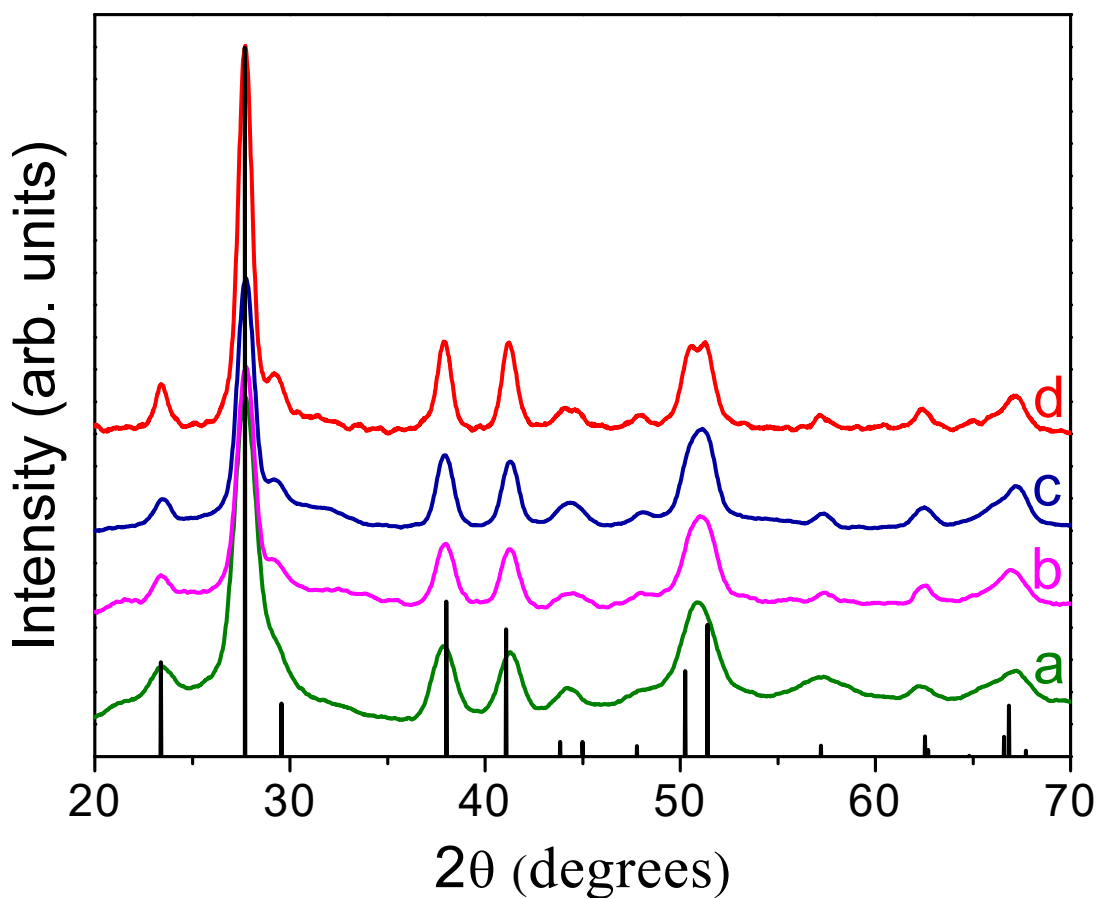


Figure 5.10. PXRD patterns of hexagonal SnP NCs produced in OLA/OA/ODE at 250 °C for (a) 5, (b) 30, (c) 60, and (d) 180 seconds. ICDD-PDF overlay of hexagonal SnP (JCPDS No. 03-065-9787) is shown as vertical black lines.

TEM was employed to investigate the morphological evolution of hexagonal SnP NCs as a function of growth time (Figure 5.11). The NCs produced at 250 °C exhibit spherical morphology and narrow size dispersity with average size in the range of $12.2 \pm 1.2 - 20.0 \pm 2.9$ nm. Additional TEM images of SnP NCs produced at different time intervals are shown in Figure 4.12 and Figure 4.13. At shorter growth times (< 30 sec.), SnP NCs exhibit narrower size dispersity (8-10%) however, with increasing growth time anisotropic nanostructures were also produced likely due to Ostwald ripening. The anisotropic growth of SnP NCs is accompanied by a slight change in morphology from spherical to quasi-spherical and cuboidal shapes (Figure 5.11A-D). Interestingly, the particle size estimations from TEM images were not consistent with the crystallite sizes obtained from Scherrer calculations (Table 5.1).⁷⁶ This discrepancy can be attributed to the presence of an amorphous tin phosphide shell around hexagonal SnP core crystals, which is evident in low resolution TEM images (Figure 5.13). Additionally, HRTEM images of all samples indicate the single crystalline SnP core with an amorphous shell and a lattice spacing of 0.32 nm, corresponding to (011) plane of hexagonal SnP (Figure 5.11E). However, the crystallite size increases with increasing growth time similar to primary particle size obtained from TEM analyses. Moreover, a slight decrease in amorphous shell thickness (from 1.7 to 1.4 nm) is noted with increasing growth time, possibly due to coarsening of the amorphous shell. The selected area electron diffraction patterns of SnP NCs exhibit the main diffraction rings corresponding to the hexagonal structure type (Figure 5.11F). The elemental analysis based on SEM/EDS indicates Sn:P atomic ratios of 48.7-50.5: 51.3-49.5 % for NCs produced at different times, consistent with the stoichiometry of hexagonal SnP (Figure 5.14).

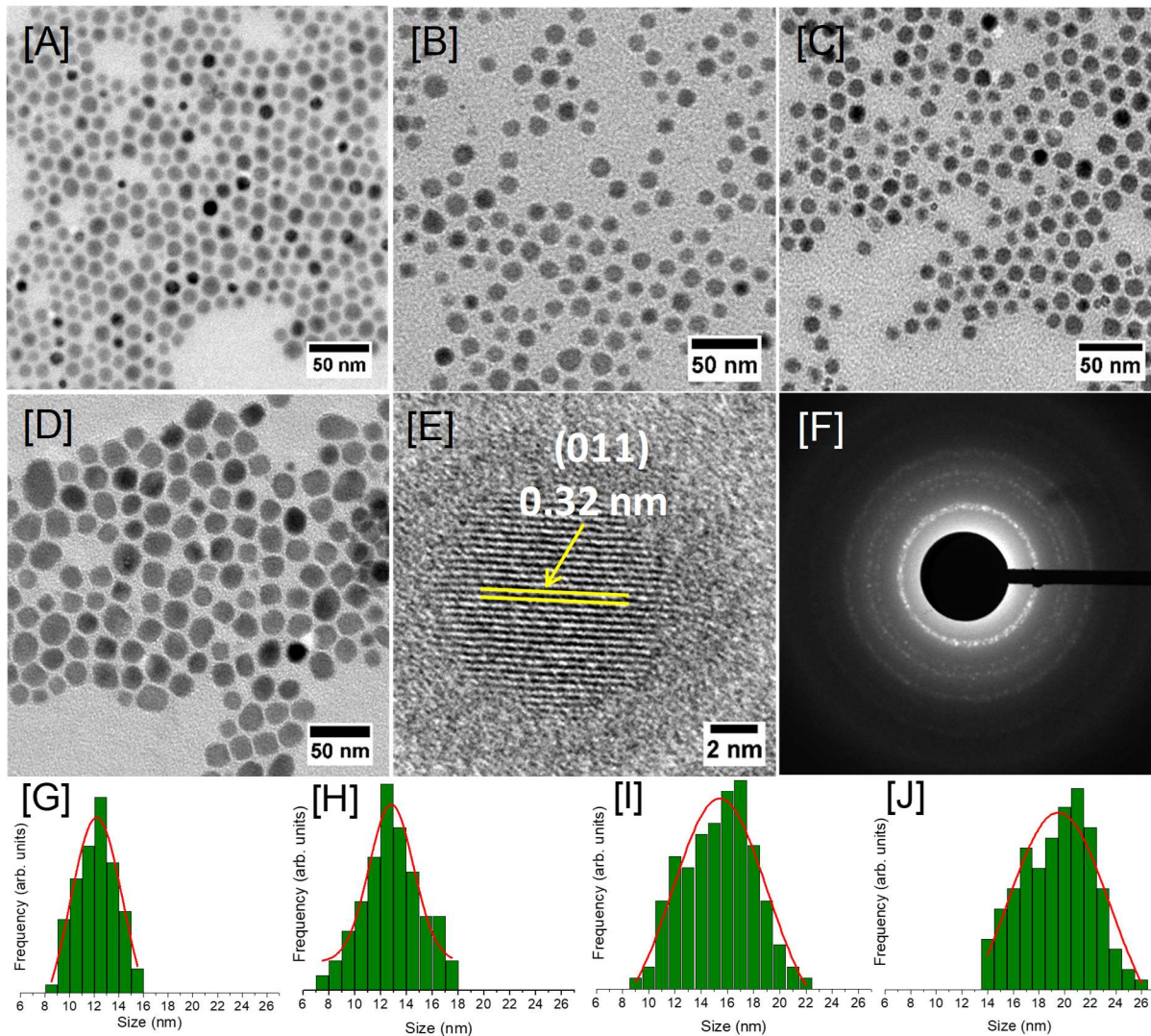


Figure 5.11. TEM images of the hexagonal SnP NCs produced in OLA/OA/ODE at 250 °C for [A] 5 sec. (12.2 ± 1.2 nm) [B] 30 sec. (12.9 ± 1.7 nm) [C] 60 sec. (15.9 ± 2.2 nm) and [D] 180 sec. (20.1 ± 2.9 nm). (E) HRTEM of the SnP NCs from part (A) showing (011) lattice spacing. (F) A selected area (~ 200 nm x 200 nm) electron diffraction pattern of the hexagonal SnP NCs shown in part (A). The diffractions rings are indexable to a hexagonal lattice. The size histograms of SnP NCs grown at 250 °C for [G] 5, [H] 30, [I] 60, and [J] 180 sec.

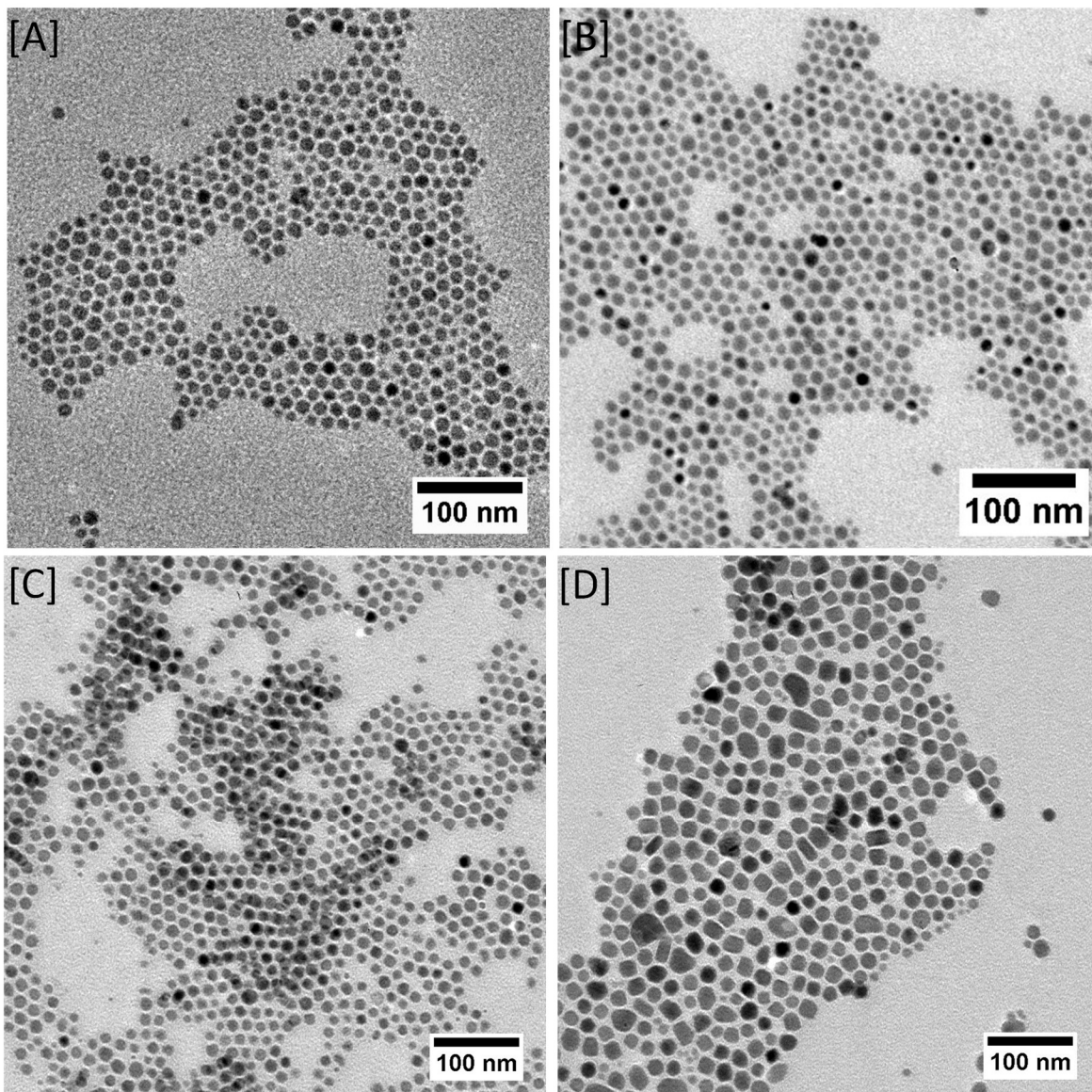


Figure 5.12. Representative TEM images of the phase pure hexagonal SnP NCs synthesized in OLA/OA/ODE at 250 °C for (a) 5, (b) 30, (c) 60, and (c) 180 seconds.

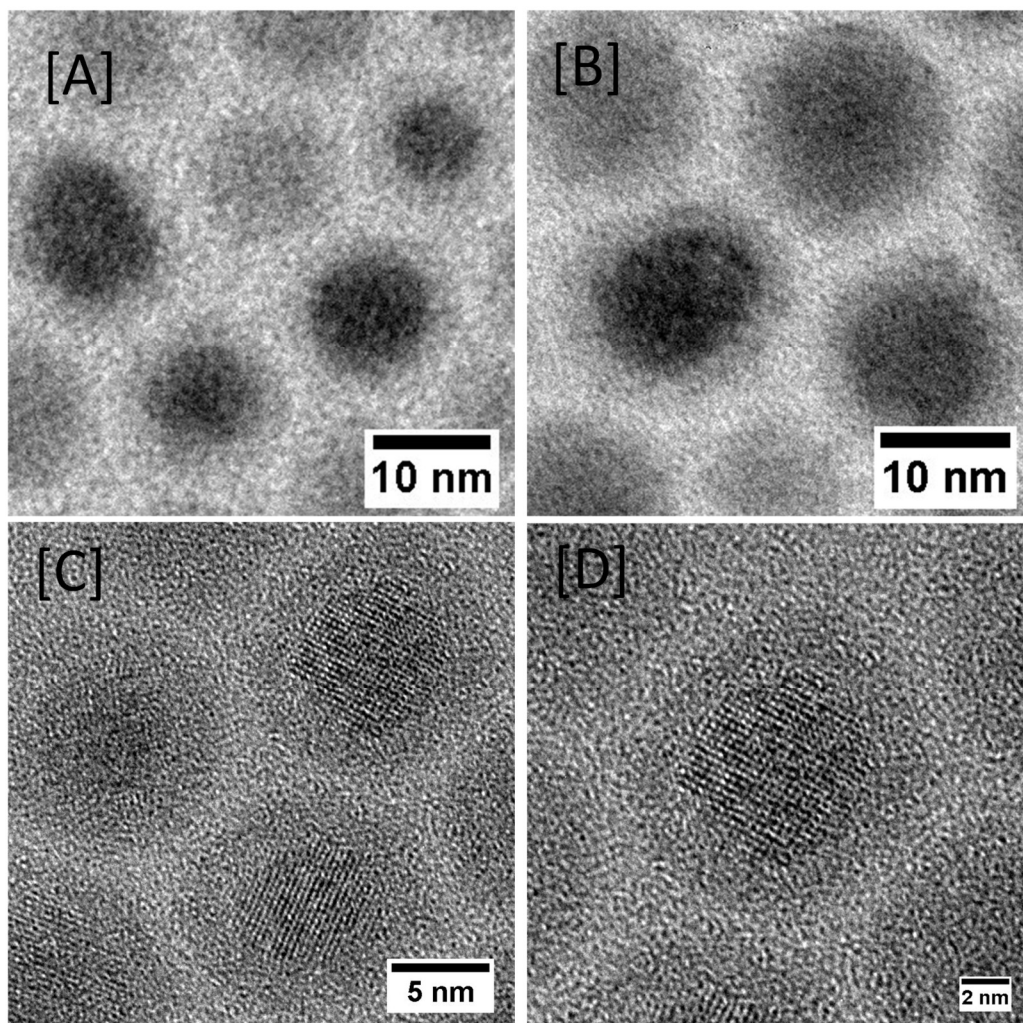


Figure 5.13. Low resolution and high resolution TEM images of the hexagonal SnP NCs prepared in OLA/OA/ODE at 250 °C for (a) 5, (b) 30, (c) 60, and (c) 180 seconds showing the presence of a crystalline SnP core and amorphous shell with varying thickness.

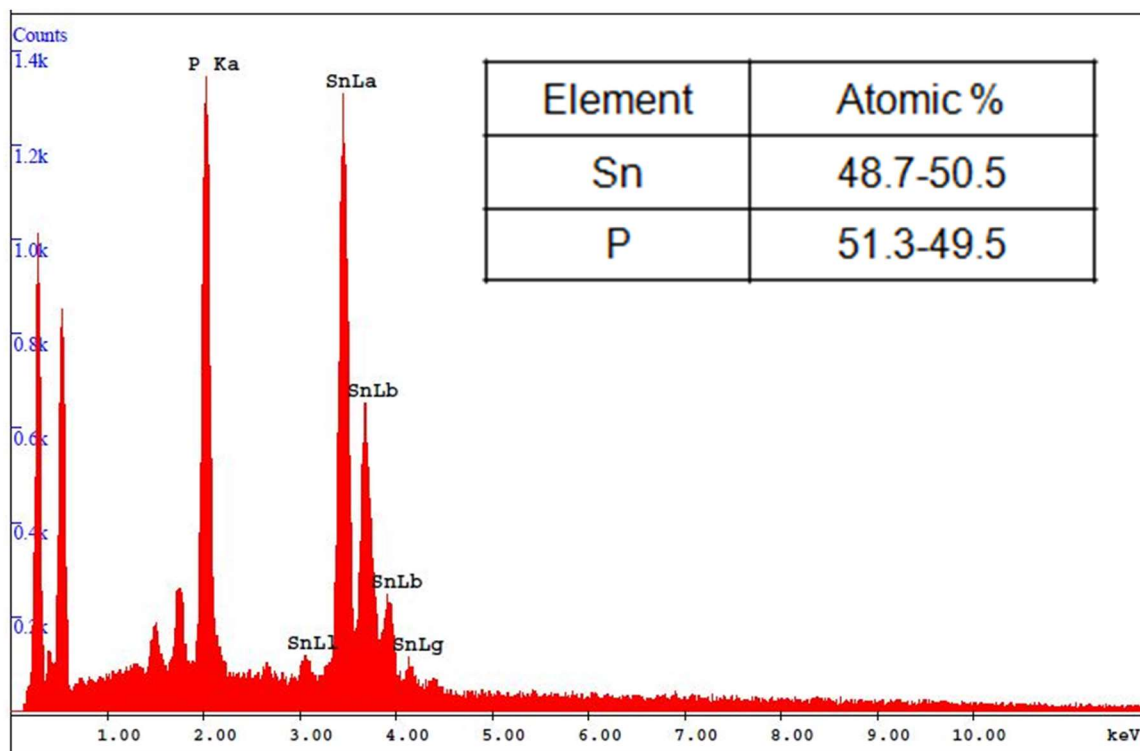


Figure 5.14. A representative SEM/EDS spectrum of the hexagonal SnP NCs synthesized at 250 °C without the use of TBP for 60 seconds. The average Sn: P atomic ratio obtained from 5 individual measurements of the same sample are also shown.

Table 5.1. Primary Particle Size, Core Crystal Size, Thickness of the Amorphous Shell, and Crystallite Size of Hexagonal SnP NCs Produced at 250 °C for different growth times.

Growth Time at 250 °C (seconds)	Primary Particle Size (nm) ^a	Core Size (nm) ^b	Amorphous Shell Thickness (nm) ^c	Crystallite Size from Scherrer Calculations (nm) ^d
5	12.2 ± 1.2	8.7 ± 0.8	1.7 ± 0.2	8.4 ± 0.2
30	12.9 ± 1.7	9.8 ± 0.9	1.5 ± 0.3	9.3 ± 0.2
60	15.9 ± 2.2	12.9 ± 1.7	1.5 ± 0.2	12.1 ± 0.2
180	20.1 ± 2.9	17.2 ± 2.0	1.4 ± 0.4	16.4 ± 0.2

^aPrimary particle size, ^bcore crystal size, and ^camorphous shell thickness were measured from TEM analysis of 150–250 individual NCs. ^dCrystallite size was calculated by applying the Scherrer formula⁷⁶ to (011) reflection after making appropriate correction for instrumental broadening using a Si standard.

5.3.5 Quantum Confinement Effects in trigonal Sn₃P₄ NPs. Synthesis of a significantly smaller set of quantum-confined, tin phosphide NPs was achieved at 100 °C in the presence and absence TBP (Figure 5.15). Notably, the physical and optical characterization of NPs suggests the formation of the trigonal Sn₃P₄ phase. The PXRD patterns of trigonal Sn₃P₄ NPs show diffuse diffraction due to a lack of long-range crystal order and the possible presence of amorphous domains (Figure 5.16). The short-range crystal order of as-synthesized NPs was confirmed by HRTEM that indicates lattice fringes of 0.20 and 0.31 nm corresponding to the (116) and (015) planes of trigonal Sn₃P₄, respectively.²⁶ Diffuse diffraction from the (116) plane is also visible in the SAED patterns (Figure 5.16).²⁶ Additionally, the compositional analyses based on SEM/EDS reveal Sn/P

atomic ratios of 41.8–42.9/58.2–57.1 (Figure 5.17), which are in close agreement with the composition of trigonal Sn_3P_4 (Sn/P ratio of ~ 0.75). Previous reports on tin phosphides suggest that Sn rich phases are metallic whereas P-rich phases are semiconductors. In rhombohedral Sn_4P_3 , all phosphorus atoms exhibit 100% occupancy with octahedral coordination by Sn atoms. Hence, phosphorus atoms do not form any homonuclear bonds, and the structure remains metallic. As such, we did not observe absorption band onsets for Sn_4P_3 NCs. In contrast, the phosphorus-rich phases, SnP and Sn_3P_4 , possess P_2^{4-} dumbbells with Sn^{2+} leading to the formation of $(\text{Sn}^{2+})_2(\text{P}_2^{4-})_1$ and $(\text{Sn}^{4+})_1(\text{Sn}^{2+})_2(\text{P}_2^{4-})_2$ units, respectively.¹ In both structures, the bonding and nonbonding states are filled and the antibonding states are vacant; hence, optoelectronic transitions are expected between those energy levels. As such, the trigonal Sn_3P_4 NPs produced in this study could possibly exhibit size confinement effects similar to those of their tin chalcogenide counterparts reported in the literature (bulk bandgaps of SnS and SnSe are 1.3 and 0.86 eV, respectively).³⁸

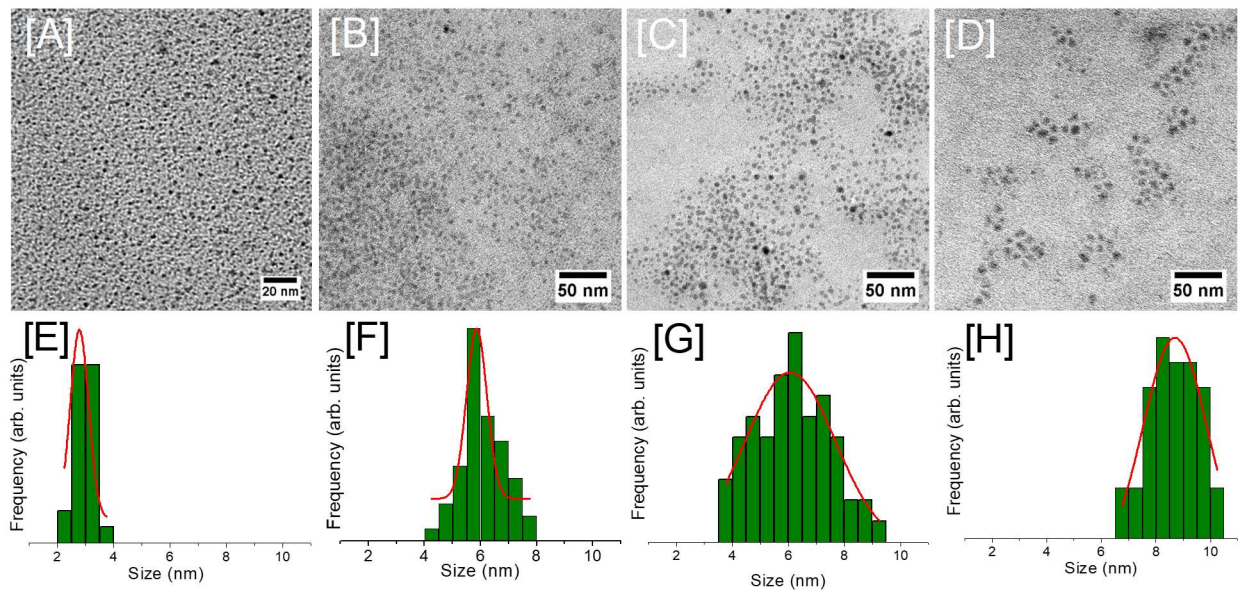


Figure 5.15. TEM images of the trigonal Sn_3P_4 NPs grown in OLA/OA/ODE at 100 °C in the presence of 4 mM TBP for (A) 5 sec. (3.0 ± 0.4 nm) (B) 60 sec. (5.9 ± 0.6 nm) (C) 120 sec. (6.3 ± 0.8 nm) and (D) 180 sec. (8.6 ± 1.8 nm). The size histograms of the as-prepared trigonal NPs grown at 100 °C for [E] 5, [F] 60, [G] 120, and [H] 180 sec. are also shown.

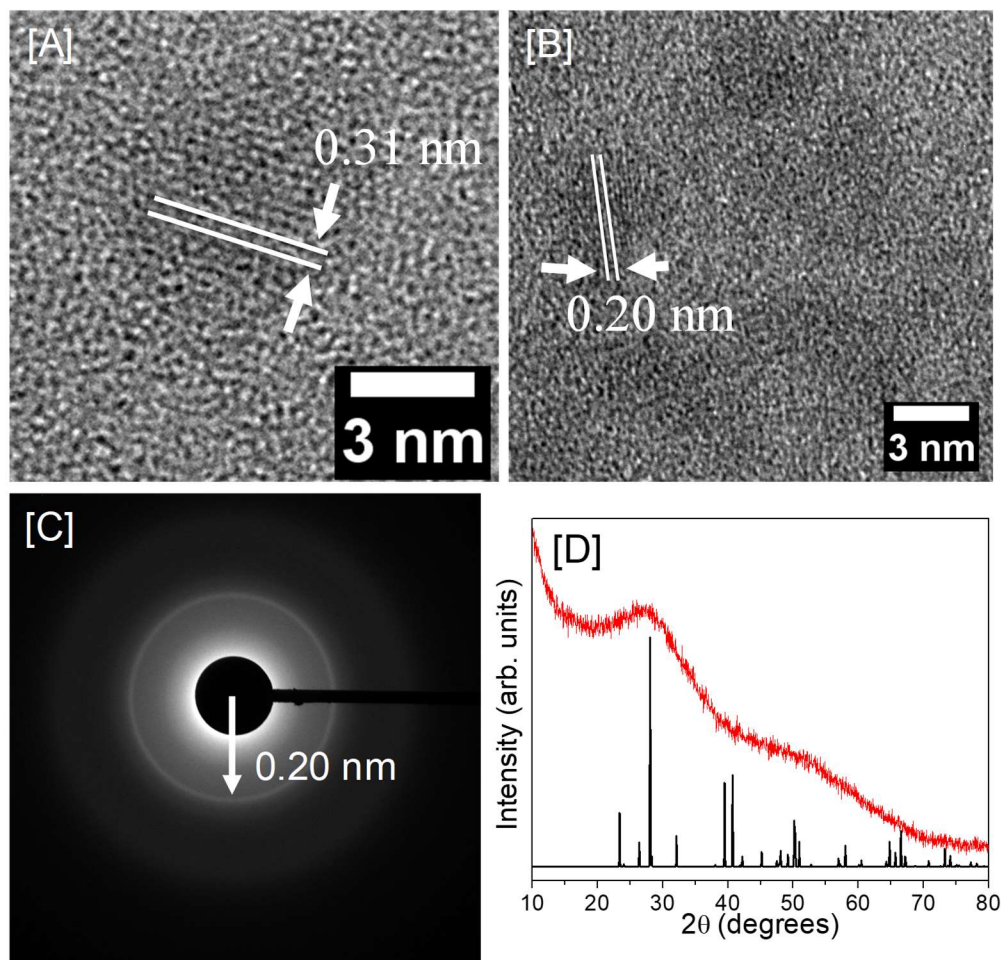


Figure 5.16. (A-B) HRTEM images of trigonal Sn_3P_4 NPs synthesized at 100 °C for 3 min using SnI_4 and $(\text{TMSi})_3\text{P}$ in OLA/OA/ODE in the presence of TBP. (C) SAED and (D) PXRD patterns of the corresponding sample along with ICDD-PDF overlay of trigonal Sn_3P_4 generated from crystal maker (black lines).

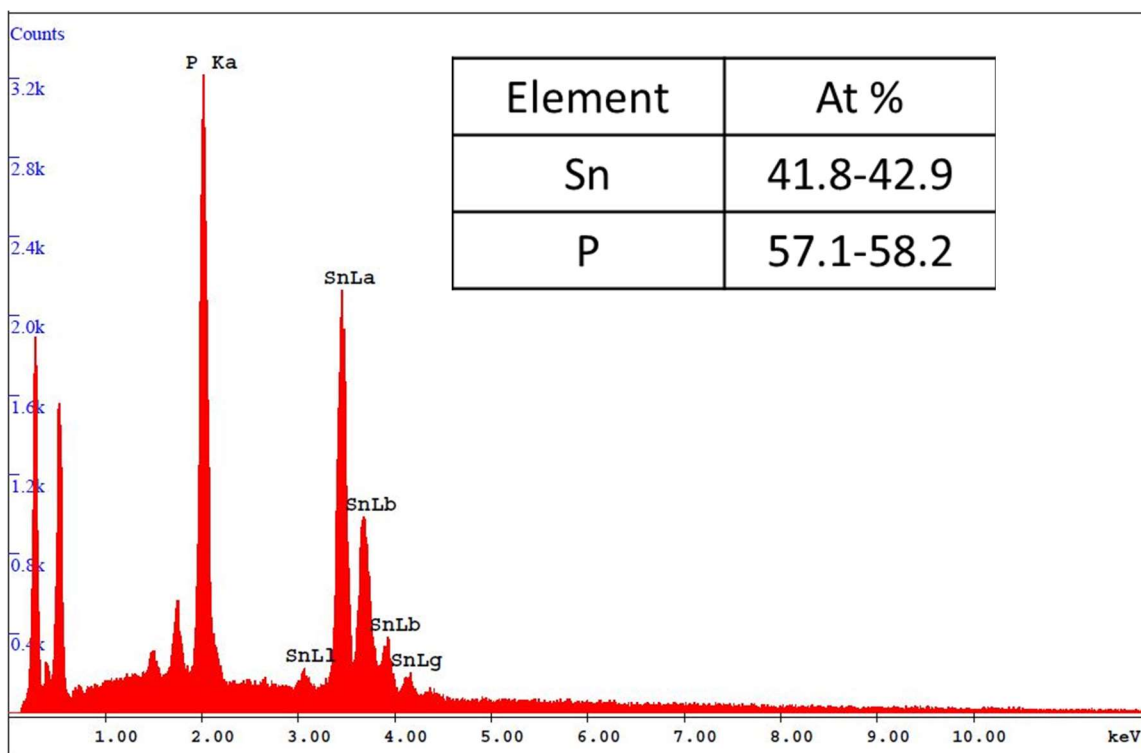


Figure 5.17. Representative SEM/EDS spectrum of trigonal Sn_3P_4 NPs synthesized in OLA/OA/ODE at 100 °C with 4 mM TBP for 60 sec. The average Sn: P atomic ratio obtained from 5 individual measurements of the same sample are also shown.

To examine the size confinement effects, solid state diffuse reflectance spectroscopy was implemented. The absorption spectra of Sn_3P_4 NPs (3.0 ± 0.4 to 8.6 ± 1.8 nm) exhibit bandgap onsets (1.38–0.88 eV) that are blue-shifted from the theoretical value of bulk trigonal Sn_3P_4 [0.83 eV (Figure 5.18)], consistent with the size confinement effects.³⁹ Moreover, a systematic red shift in absorption onsets with an increasing NP size is noted. The confinement effects observed in as synthesized Sn_3P_4 NPs further indicate that the semiconducting, trigonal phase has been produced at 100 °C with an optimal TBP concentration of 4 mM (Figure 5.15).

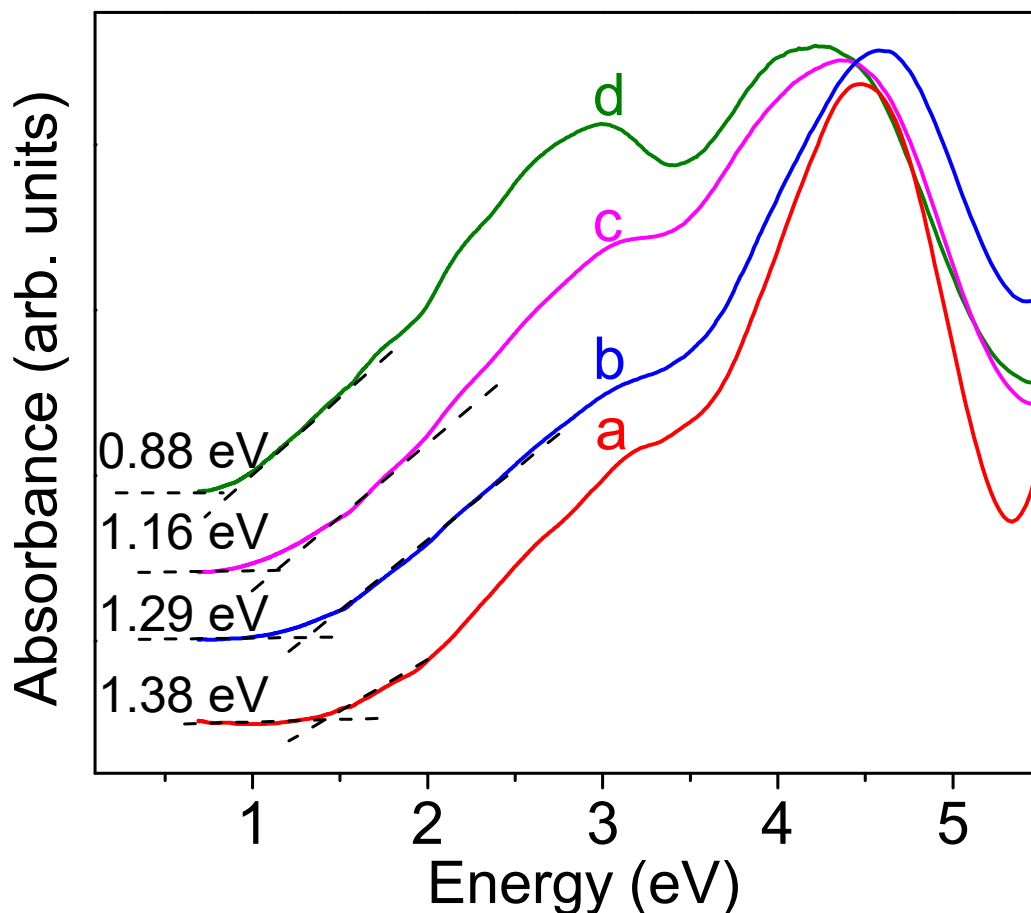


Figure 5.18. Solid state diffuse reflectance spectra (converted to absorption) of smaller, trigonal Sn_3P_4 NPs synthesized in OLA/OA/ODE in the presence of 4 mM TBP at 100 °C for (a) 5 sec., (b) 60 sec., (c) 120 sec., and (d) 180 sec.

To further elucidate the dependence of optical properties on NP size/shape, a series of controlled experiments were implemented, both in the presence and absence of TBP at 100 °C. With no TBP, the bandgaps were tuned in a shorter range (0.78–0.96 eV) for highly polydisperse particles (Figure 5.19). The corresponding TEM images revealed popcorn-shaped NPs with size ranging from 5.2 ± 1.5 – 27.5 ± 3.6 nm (Figure 5.20).

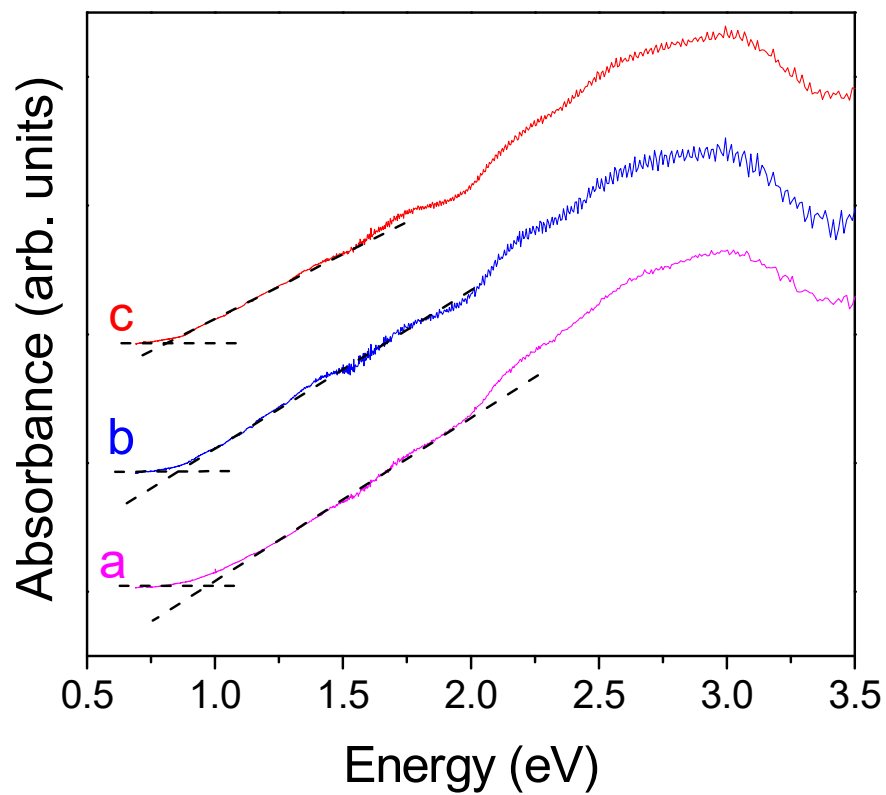


Figure 5.19. Diffuse reflectance spectra (converted to absorption using Kubelka-Munk remission function) of trigonal Sn_3P_4 NPs synthesized in OLA/OA/ODE without TBP at 100 °C for (a) 1, (b) 2, and (c) 3 minutes.

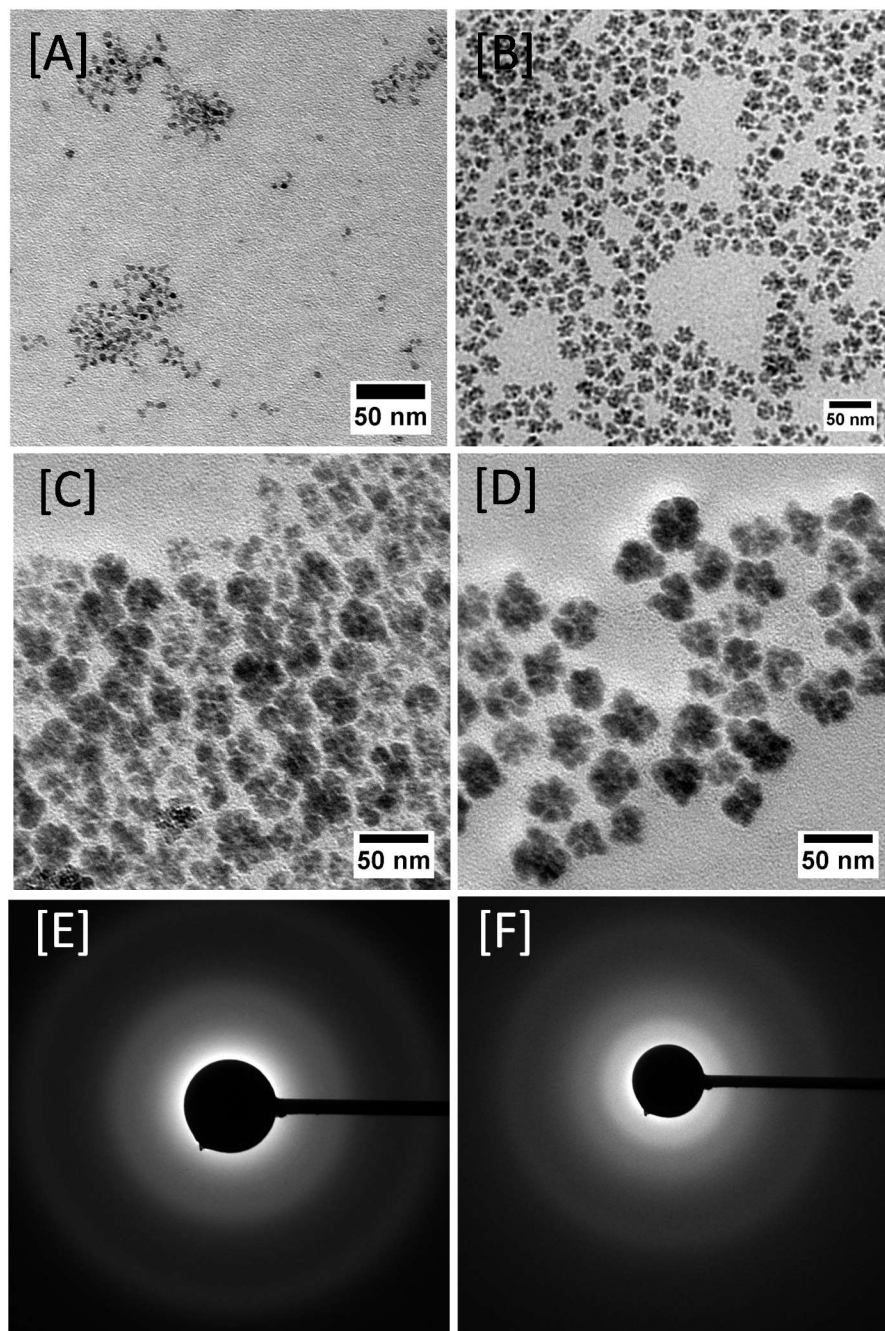


Figure 5.20. Representative TEM images of trigonal Sn_3P_4 NPs synthesized in OLA/OA/ODE at 100 °C without TBP for (A) 5 sec, (B) 1 min, (C) 2 min, and (D) 3 min. (E) and (F) are electron diffraction patterns of NPs shown in (C) and (D), respectively.

It is likely that alkylphosphines can act as additional coordinating solvents and allow the control growth of trigonal Sn_3P_4 NPs at 100 °C. However, further increasing TBP (6 – 12 mM) resulted in the growth of polydisperse NPs that exhibit inconsistent optical properties. It is important to note that smaller, quantum confined NPs ($3.0 \pm 0.4 - 8.6 \pm 1.8$ nm) exhibit Sn: P atomic ratios of 41.8–42.9: 58.2–57.1 % (Figure 5.21), which are in close agreement with the composition of highly disordered Sn_3P_4 (Sn/P ratio is ~ 0.75).

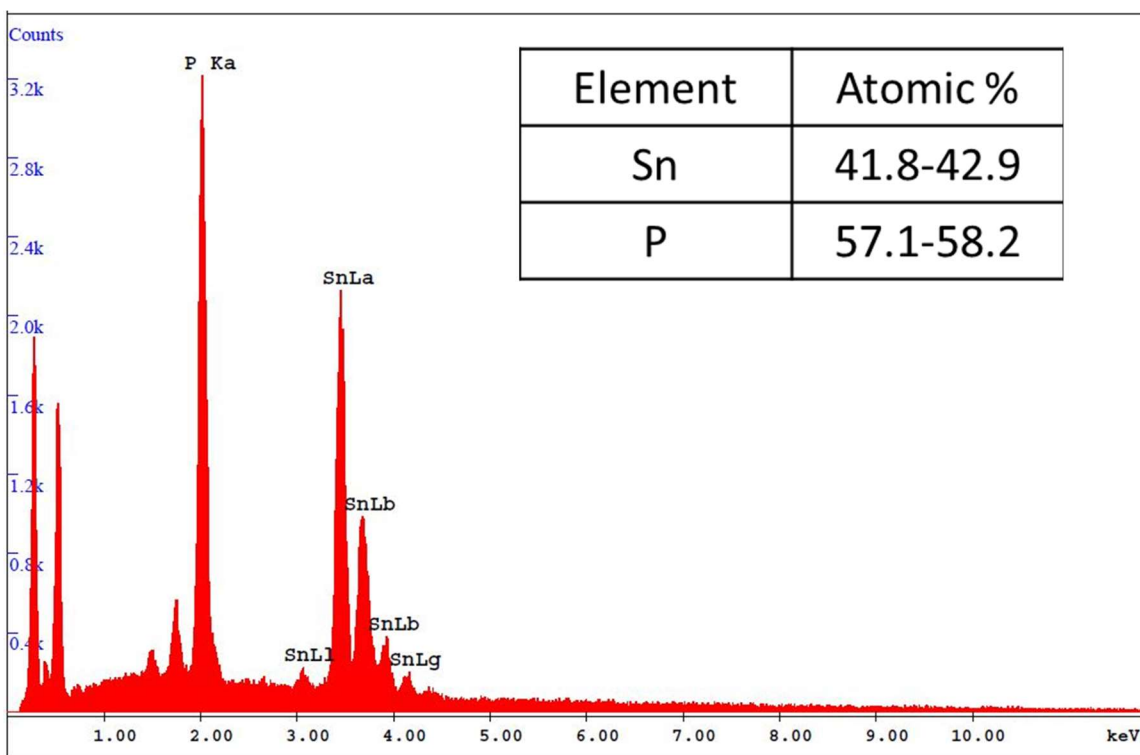


Figure 5.21. Representative SEM/EDS spectrum of trigonal Sn_3P_4 NPs synthesized in OLA/OA/ODE at 100 °C with 4 mM TBP for 60 sec. The average Sn: P atomic ratio obtained from 5 individual measurements of the same sample are also shown.

Theoretical studies suggest that the tin-rich phosphides (i.e. rhombohedral Sn_4P_3) are metallic whereas the phosphorous-rich phosphides (i.e. Sn_3P_4) are semiconducting.¹⁴ In the case of rhombohedral Sn_4P_3 , all phosphorous atoms exhibit 100% occupancy with octahedral coordination by Sn atoms.¹⁴ Hence, phosphorous atoms do not form any homonuclear bonds and the structure remains metallic. As such, we did not observe absorption band onsets for Sn_4P_3 NCs produced at 180 °C. In contrast, the phosphorous-rich phases, SnP and Sn_3P_4 , possess P_2^{4-} dumbbells with Sn^{2+} leading to the formation of $(\text{Sn}^{2+})_2(\text{P}_2^{4-})_1$ and $(\text{Sn}^{4+})_1(\text{Sn}^{2+})_2(\text{P}_2^{4-})_2$ units, respectively.¹⁴ In both structures, the bonding and nonbonding states are filled and the antibonding states are vacant, hence electronic transitions are expected in between those energy levels. Theoretical studies of bulk Sn_3P_4 predict an indirect bandgap of 0.83 eV.¹³² In contrast, the smaller, trigonal Sn_3P_4 NPs produced in this study exhibit bandgap onsets that are blue shifted (0.88-1.38 eV) from theoretical value, consistent with the quantum confinement effects.

The surface properties of tin phosphide NPs were probed by FT-IR (Figure 5.22) and XPS spectroscopy. The FT-IR spectra of all samples exhibit vibrations corresponding to $\nu_{(\text{CH}_x)}$ at 2850 - 2960 cm^{-1} and $\delta_{(\text{CH}_x)}$ modes at 1381-1463 cm^{-1} of alkyl chains. A broader peak at 1620 cm^{-1} arising from $\nu_{(\text{C}=\text{C})}$ and a weaker band at 3420 cm^{-1} corresponding to $\nu_{(\text{N}-\text{H})}$ further indicate the presence of OLA on NP surface.¹³⁸ Besides alkylamines, the peaks at 1261 cm^{-1} and 801 cm^{-1} suggest the presence of $\rho_{[\text{Si}(\text{CH}_3)]}$ and $\nu_{(\text{Si}-\text{C})}$ modes of residual trimethylsilyl species, respectively.¹³⁹ The broad peak at ~ 1020 cm^{-1} can be attributed to $\nu_{(\text{PO}_x)}$ of phosphorous-oxygen, which is further discussed in the XPS analyses.¹³⁹

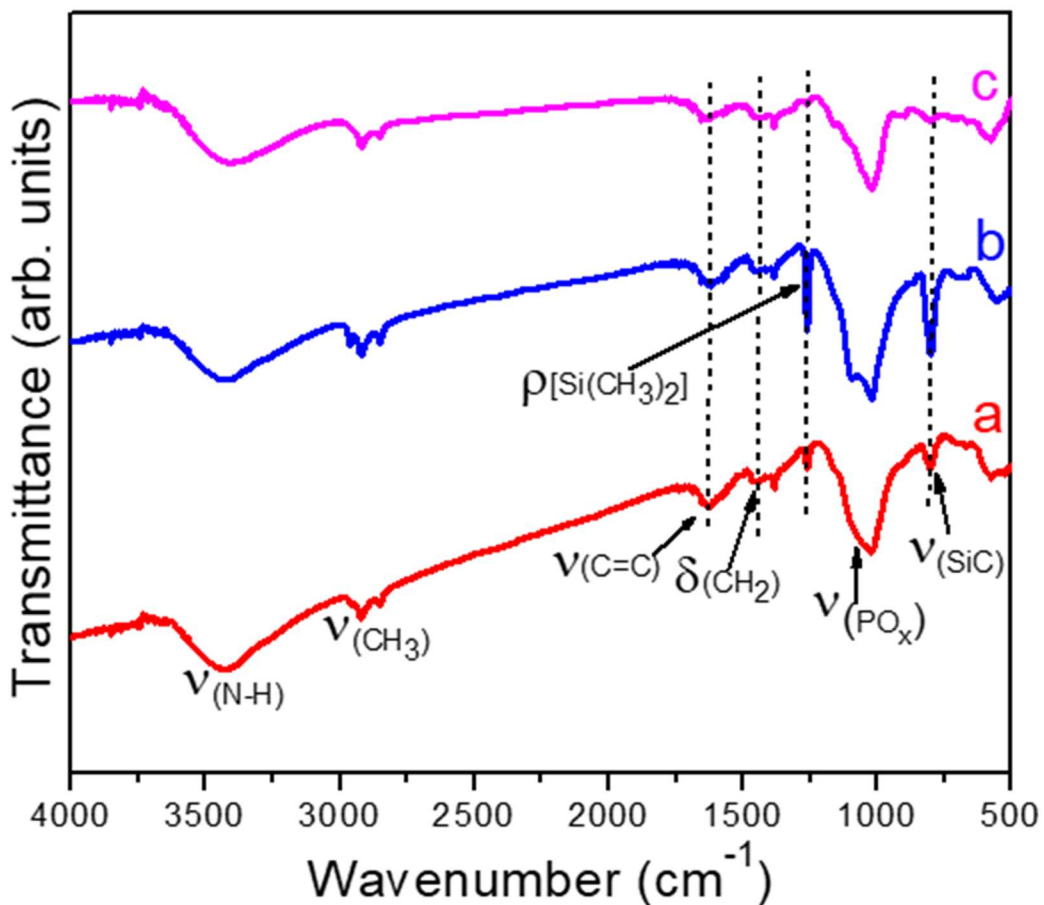


Figure 5.22. FT-IR spectra of tin phosphide NPs synthesized OLA/OA/ODE. (a) rhombohedral Sn_4P_3 NCs produced at 180 °C for 3 min, (b) hexagonal SnP NCs at 250 °C for 5 seconds, and (c) trigonal Sn_3P_4 NPs produced at 100 °C for 3 min.

XPS was performed to determine the oxidation state of tin and phosphorus in rhombohedral Sn_4P_3 , hexagonal SnP, and trigonal Sn_3P_4 NPs (Figure 5.23). Corresponding survey scans are shown in Figure 5.24-5.26.

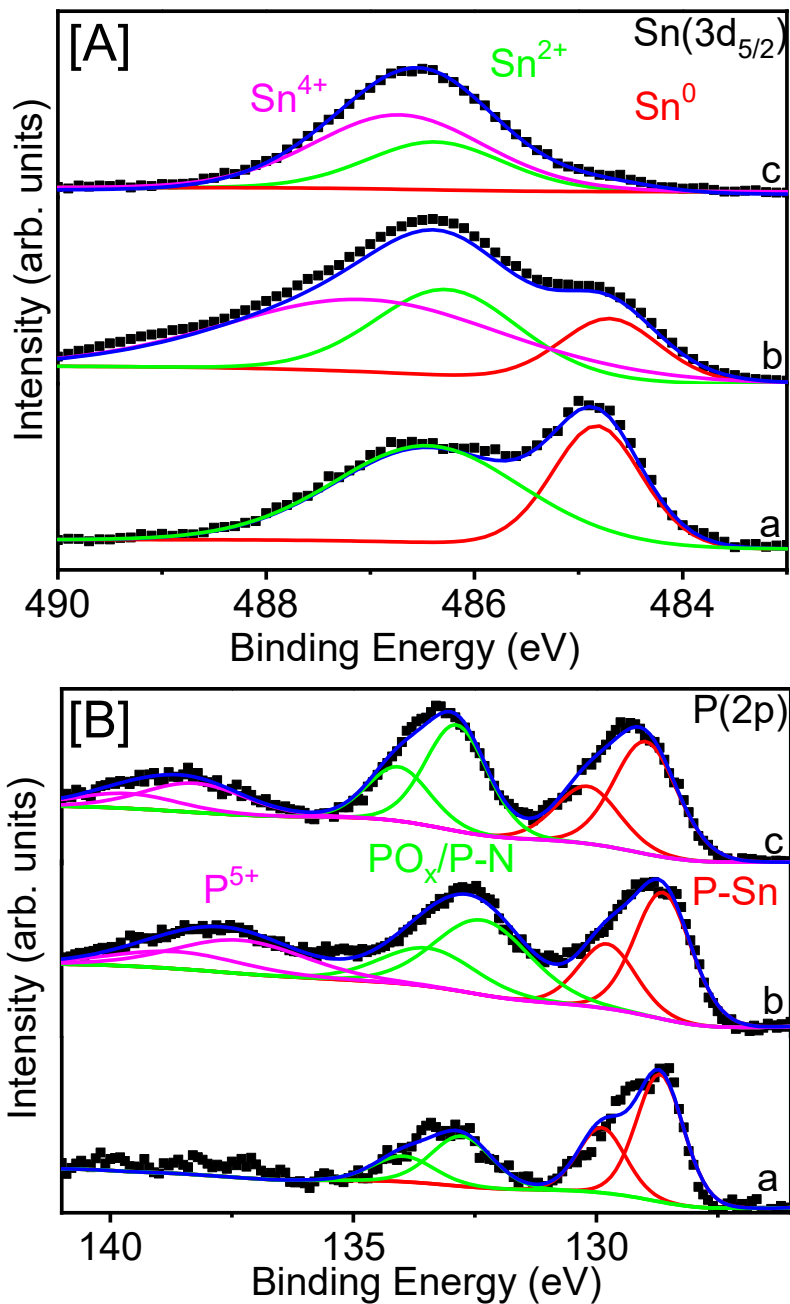


Figure 5.23. XPS of (A) Sn(3d_{5/2}) and (B) P(2p) regions of (a) rhombohedral Sn₄P₃ NCs produced at 180 °C for 3 min, (b) hexagonal SnP NCs produced at 250 °C for 5 seconds, and (c) trigonal Sn₃P₄ NPs produced at 100 °C for 3 min. The dotted squares represent the spectral data and the red, green, and blue lines are fitted deconvolutions.

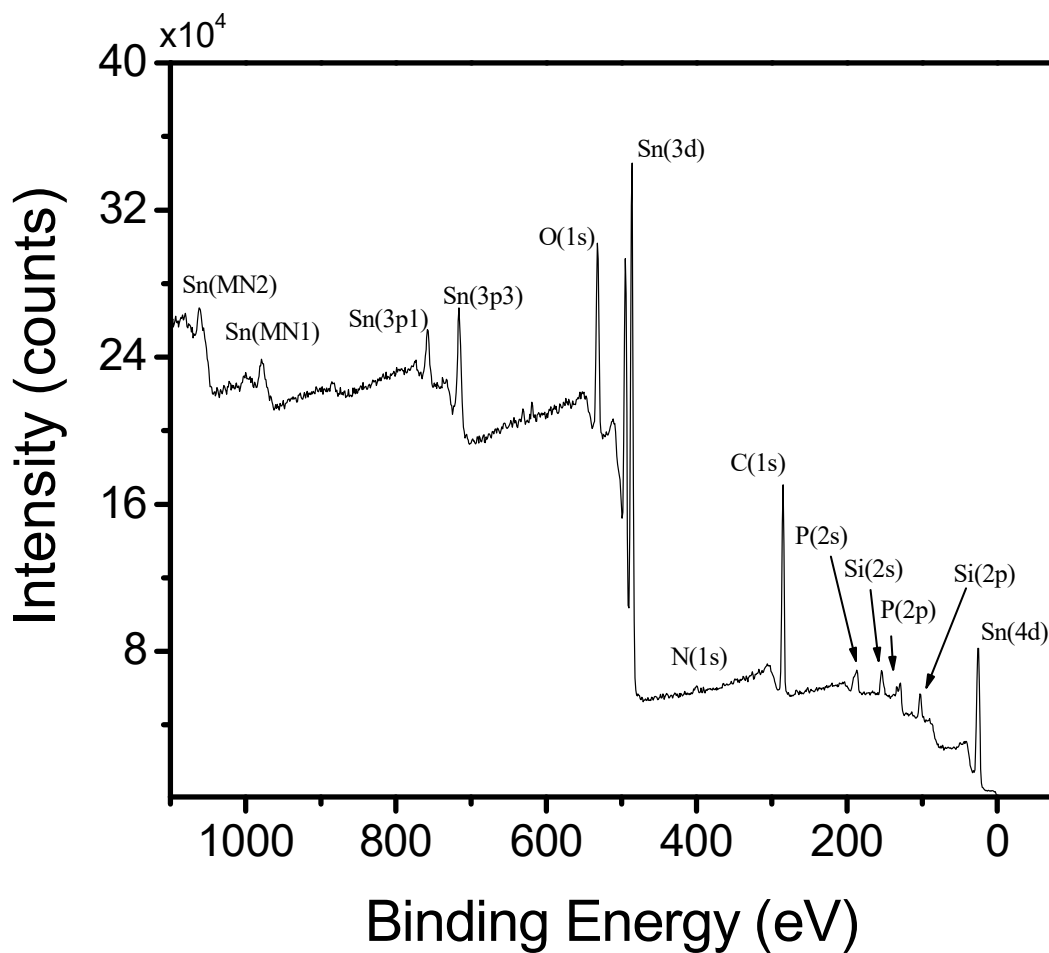


Figure 5.24. X-ray photoelectron spectrum (survey scan) of rhombohedral Sn_4P_3 NCs produced at 180 °C for 3 min.

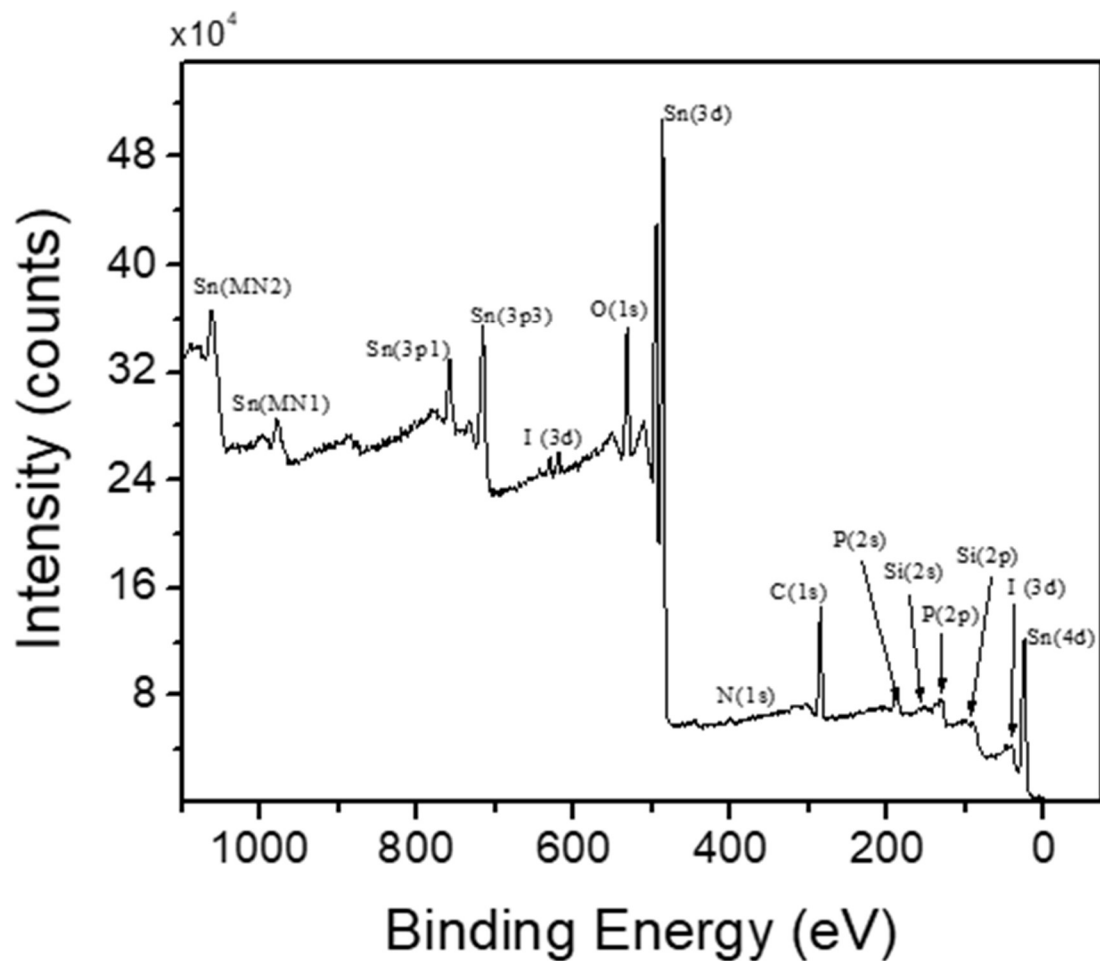


Figure 5.25. X-ray photoelectron spectrum (survey scan) of hexagonal SnP NCs produced at 250 °C for 5 seconds.

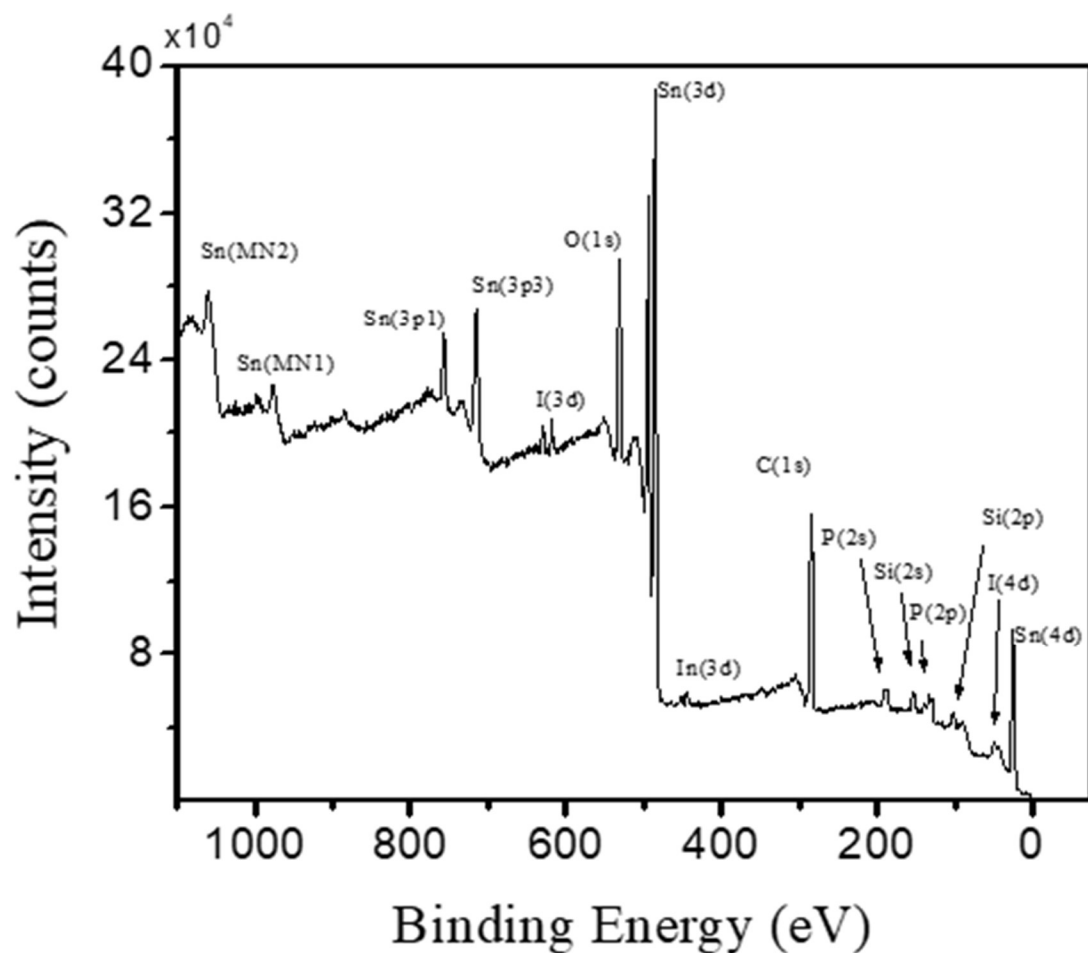


Figure 5.26. X-ray photoelectron spectrum (survey scan) of trigonal Sn_3P_4 NPs produced at 100 °C for 3 min.

The experimental binding energies of $\text{Sn}(3d_{5/2})$ suggest the presence of Sn^0 484.8 eV and Sn^{2+} 486.4 eV in rhombohedral Sn_4P_3 NCs (Figure 5.23A). Literature reports on Sn_4P_3 have used X-ray absorption (XAS) and Mössbauer spectroscopy to investigate the atomic structure and bonding. However, these studies were unable to assign the stoichiometric formal charges to all atoms in the rhombohedral Sn_4P_3 structure.^{14,140} Mössbauer spectroscopy indicates that the bonding energy of Sn in Sn_4P_3 is similar to metallic $\beta\text{-Sn}$ ^{141,142} whereas XAS data suggests the presence of Sn-P and Sn-P-

Sn bonding modes in Sn_4P_3 .⁶⁹ Accordingly, the binding energies observed in Sn_4P_3 , Sn^{2+} 486.4 eV and Sn^0 484.8 eV, likely arise from the two different types of Sn present in the crystal structure.^{14,69} Based on the N(1s) and O(1s) XPS spectra there is an expected contribution of Sn^{2+} from the surface atoms bound to OLA and surface oxides (Figure 5.27A, B).^{31,65} The P(2p) region has a doublet peak at 128.7 eV, which is consistent with metal-phosphide bonds in the Sn_4P_3 structure (Figure 5.23B).^{62,139,143} The peak at 132.7 eV can be assigned to surface P atoms bound to either OLA (P-N) or surface oxides (P-O) similar to prior reports of metal phosphide NCs.^{62,65,139}

In contrast, hexagonal SnP NCs and trigonal Sn_3P_4 NPs display binding energies corresponding to all three oxidation states in the Sn(3d) region (Sn^0 484.8 eV, Sn^{2+} 486.4 eV and Sn^{4+} at 487.4 eV, Figure 4.23A). The presence of all three Sn oxidation states cannot be fully explained by the SnP bonding structure, $(\text{Sn}^{2+})_2(\text{P}_2^{4-})_1$.¹⁴ However, hexagonal SnP has previously been shown to exhibit metallic β -Sn like bonding,¹⁴¹ similar to Sn_4P_3 , which may explain the Sn^0 484.8 eV peak.^{74,142} The presence of Sn^{4+} (487.4 eV) could be accounted for Sn-O bonds present in the O(1s) spectrum (Figure 5.27B). Conversely, if the trigonal Sn_3P_4 NPs are considered to be similar to highly disordered Sn_3P_4 , it can be expected that Sn^{2+} and Sn^{4+} would both be present according to the assignment of formal charges.¹⁴ This suggests the Sn^{4+} could originate from the amorphous shell on the hexagonal SnP core crystals. Furthermore, in both the rhombohedral and hexagonal samples the Sn^0 can possibly be attributed to amorphous Sn species, however this is highly unlikely due to Sn low crystallization temperature.¹⁴⁴

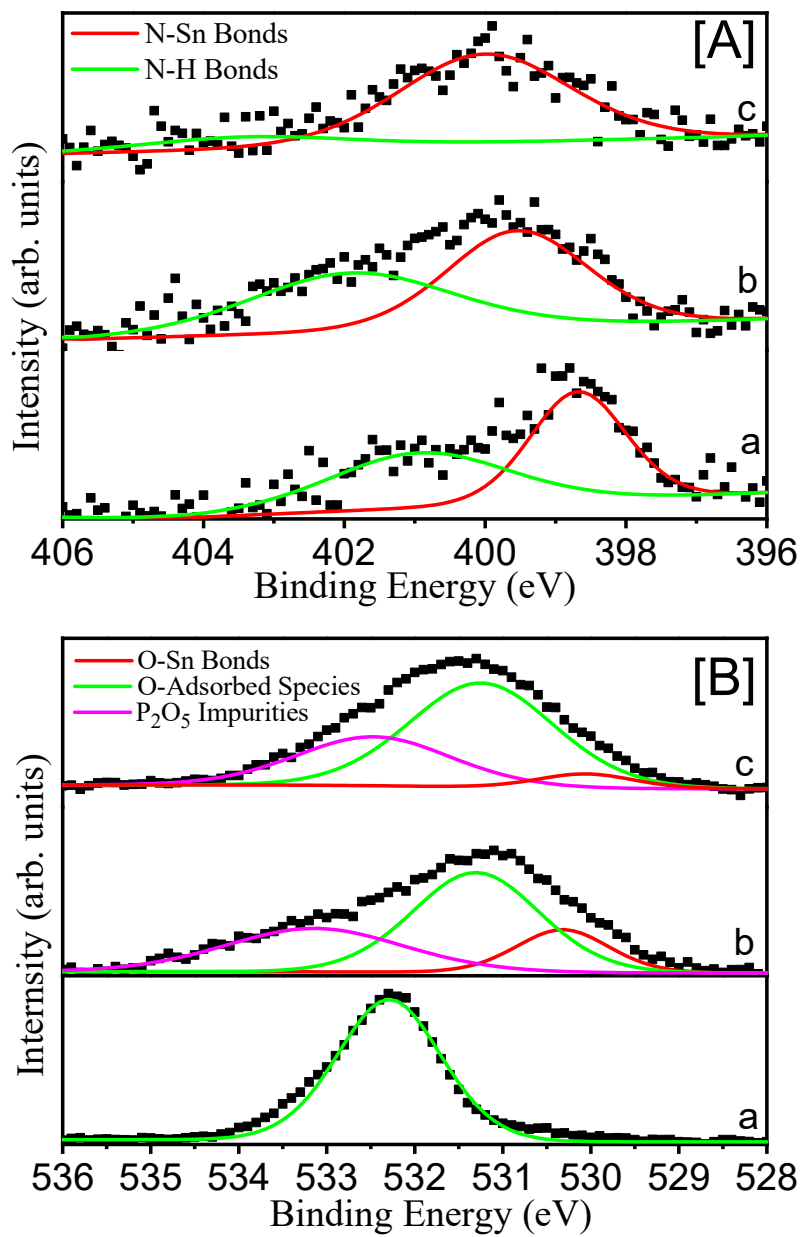


Figure 5.27. X-ray photoelectron spectra of (A) N(1s) and (B) O(1s) regions of (a) rhombohedral Sn₄P₃ NCs produced at 180 °C for 3 min., (b) hexagonal SnP NCs produced at 250 °C for 5 seconds, and (c) trigonal Sn₃P₄ NPs produced at 100 °C for 3 min.

The hexagonal SnP NCs and trigonal Sn₃P₄ NPs exhibit P-Sn bonds, P(2p) 128.9 eV, with little change noticeable between any of the three phases reported (Figure 4.23B). This is possibly due to the small difference between the electronegativity of P (2.19) and Sn (1.96) Pauling constants.⁷⁴ The surfactant ligands (OLA) and oxide species bound to the surface phosphorous atoms (P-N or P-O) are likely the origin of the peak at 132.7 eV. The peak at 137.9 eV can be assigned to P⁵⁺ surface oxides and the corresponding O-P peak is present in the O(1s) spectra of both samples (Figure 5.27B). The exact nature of the P⁵⁺ impurities has not been fully elucidated. It is suspected that poorly passivated surface phosphorus can be readily oxidized during the ambient isolation process with toluene/methanol, contaminating the sample.

4.3.6 Trigonal Sn₃P₄ to Rhombohedral Sn₄P₃ and Hexagonal SnP Phase Transformation via Low Temperature Annealing. To investigate the phase stability of tin phosphide NPs, a systematic annealing study was conducted under rigorous air free conditions. In this study, the smaller, trigonal Sn₃P₄ NPs (3.0 ± 0.4 – 8.6 ± 1.8 nm) were annealed at 150–250 °C for 16–48 h (Figure 5.28). The PXRD patterns of the samples annealed at 150–170 °C for 16–48 h exhibit no changes in structure. In contrast, NPs annealed at 180 °C for 16 h show rhombohedral Sn₄P₃ structure. The phase pure, hexagonal SnP crystallites were only obtained in samples annealed at 250 °C for 16–24 h. In contrast, the trigonal Sn₃P₄ NPs annealed at 190–240 °C exhibit both rhombohedral Sn₄P₃ and hexagonal SnP crystal phases. Therefore, it is likely that the as-synthesized Sn₃P₄ NPs undergo phase transformation to hexagonal SnP via rhombohedral Sn₄P₃ intermediate phase. Consistent with this study, tin phosphide crystallites produced at 180, 220, and 250 °C indicate the presence of rhombohedral Sn₄P₃, a mixture of Sn₄P₃/SnP,

and hexagonal SnP phases, respectively. This suggests that the thermodynamic stability of Sn–P phases changes on the nanoscale. The literature reports on bulk tin phosphides indicate that Sn_4P_3 and Sn_3P_4 phases are stable as extended solids up to $\sim 530^\circ\text{C}$; however, SnP is known as either a high-pressure tetragonal or a metastable hexagonal phase.^{4,14} It is likely that the high surface area/volume ratio and surface ligands of the NPs are responsible for the observed changes in phase stability.

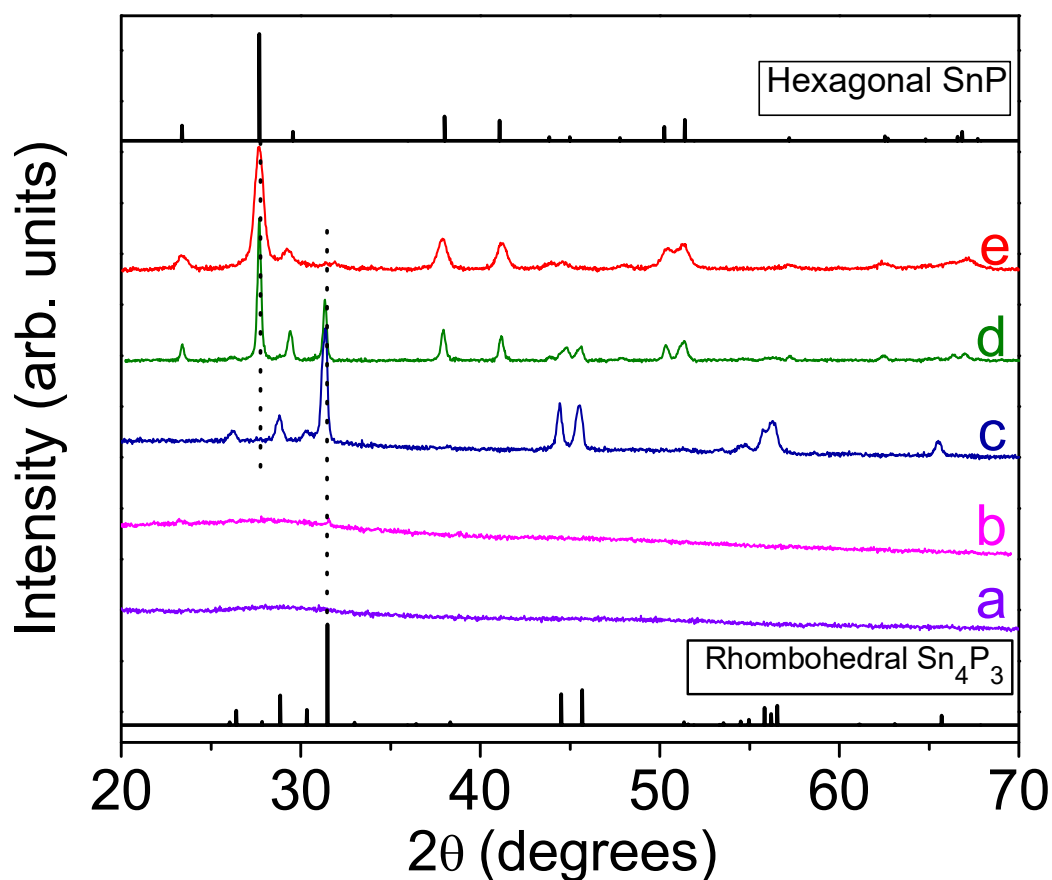


Figure 5.28. PXRD patterns of (a) the trigonal Sn_3P_4 NPs synthesized in OLA/OA/ODE with TBP at 100°C for 3 min along with trigonal Sn_3P_4 NPs annealed at (b) 150°C , (c) 180°C , (d) 230°C , and (e) 250°C for 16 h. The ICDD-PDF overlay of rhombohedral Sn_4P_3 (JCPDS No. 01-073-1820) and hexagonal SnP (JCPDS No. 03-065-9787) are also shown.

5.4 Conclusions

In conclusion, we have reported the first colloidal synthesis of size, shape, and phase controlled, narrowly disperse rhombohedral Sn_4P_3 , hexagonal SnP , and trigonal Sn_3P_4 NPs utilizing a generalized synthetic approach. The control over crystal structure and morphology was achieved by varying the nucleation and growth temperature, stoichiometry of SnI_4 and $(\text{TMSi})_3\text{P}$ precursors, and concentration of additional coordinating solvents (TBP or TOP). Phase pure, rhombohedral Sn_4P_3 NCs were produced at 180 °C in the presence of TBP, whereas amorphous to partially crystalline Sn_4P_3 NPs were achieved at the same temperature with no use of TBP. The role of alkylphosphines as the crystallizing agent has been systematically studied, and 4 mM TBP is found to be optimal for the synthesis of phase pure Sn_4P_3 NCs at 180 °C. In contrast, narrowly disperse, hexagonal SnP NCs with wider tunability of sizes were produced at 250 °C with no use of TBP. A smaller, quantum confined, trigonal Sn_3P_4 NPs ($3.0 \pm 0.4 - 8.6 \pm 1.8$ nm) with size-tunable absorption onsets (0.88 – 1.38 eV) were produced at 100 °C in the presence of TBP. Although each Sn-P phase has unique atomic arrangement, the tin bonding energies of hexagonal SnP NCs and trigonal Sn_3P_4 NPs cannot be distinguished in part due to the presence of amorphous shell on hexagonal core crystals. Conversely, the rhombohedral Sn_4P_3 NCs stand apart in that no Sn^{4+} is detected and the structure consisting only of Sn^{2+} and Sn^0 species. In contrast, the phosphorus bonding energies are consistent across multiple Sn-P phases reported with minimal or no effect from different metal phosphide bonds. The trigonal to rhombohedral phase transition is achieved at 180 °C whereas rhombohedral to hexagonal transition is achieved at 250 °C. The control over NP size, shape, and crystal structure realized through reported colloidal synthesis can be extended to produce other anisotropic

nanostructures of tin phosphides as well as to probe the structure and size/shape dependent charge storage and photocatalytic properties. Specific studies to test these premises are currently underway.

CHAPTER 6

CONCLUSIONS AND PROSPECTUS

In this dissertation study, we have successfully developed synthetic strategies for $\text{Ge}_{1-x}\text{Sn}_x$ alloy QDs with wider tunability of Sn compositions ($x = 1.5\text{-}20.6\%$) and different crystal phases of tin phosphide nanocrystals and studied their composition- and size-dependent physical and photophysical properties (Goal 1 and Goal 2). Both goals have been achieved thoroughly and explored in detail. Their significance is novel and will have potential for their technological advancement.

In chapter 3, we have developed the synthesis of $\text{Ge}_{1-x}\text{Sn}_x$ alloy QDs with size in the range of 3.3-5.9 nm for NIR absorption and emission with Sn composition as high as 20.6%. The structural and surface characterizations on as prepared samples indicate no detectable impurities. Previously, the colloidal synthesis of $\text{Ge}_{1-x}\text{Sn}_x$ alloy QDs were explored (by our group and Los Alamos National Laboratory) for their tunable optical properties, especially, emission in visible and mid IR range. Both the syntheses utilized wet chemical method, but different routes. However, to achieve tunable NIR emission, we have employed GeI_2 and SnCl_2 as precursors, HDA as surfactant, more importantly varied amounts of reducing agent (BuLi). In order to achieve the QDs size within 6 nm, the critical parameter is to adjust the BuLi amount in accordance with Sn composition (1.48-1.16 mmol BuLi for 1.5-20.6% Sn). By doing so, the energy gaps estimated from Kubelka-Munk, a solid-state absorbance were in the range of 1.72-0.84 eV for $x = 1.5\text{-}9.1\%$. Using Tauc analysis, a solution phase absorption, the energy gaps for all the samples ($x = 1.5\text{-}$

20.6%) were in the range of 2.05-0.90 eV. The energy gaps estimated using both the above-mentioned methods are in the widest possible range for $\text{Ge}_{1-x}\text{Sn}_x$ alloy QDs as of today, allow them potential candidates in the relevant technologies. For the first time, a tunable PL was achieved in the range of 1.62-1.31 eV for $x = 1.5-5.6\%$, again this is the broadest range for visible and NIR $\text{Ge}_{1-x}\text{Sn}_x$ alloy QDs. It is important to note that, for bio-imaging the ideal emission wavelength is in the range of 1.9-1.3 eV and our $\text{Ge}_{1-x}\text{Sn}_x$ alloy QDs exhibit PL within this range makes them an alternative to toxic bio-imaging lead (Pb) and tellurium (Te) based QDs. However, PL from alloy QDs with Sn concentration higher than 5.6% could not be probed.

To achieve PL from the alloy QDs with Sn composition higher than 5.6% the following challenge(s) need to be addressed. (1) effective surface passivation and/or (2) strong size confinement effects (for QD size >4.5 nm). In order to minimize non-radiative pathways, treating the as prepared samples with additional capping ligands such as oleic acid or alkylthiol. However, with this post synthetic additional ligand treatment using oleic acid resulted in enhancement in PL intensity by 1-3-fold increment. This PL enhancement is effective for samples with lower intensity. For example, upon oleic acid treatment for 16-24 h, the samples with very low PL intensity exhibited 3-fold increment whereas the samples with bright PL show 1-fold increment. Unfortunately, the oleic acid treatment for samples with Sn content higher than 5.6% could not useful in achieving measurable PL. Thus, it directs to inorganic passivation of the surface by growing a shell on the alloy QDs. Earlier reports on Ge and $\text{Ge}_{1-x}\text{Sn}_x$ alloy nanocrystals suggest that the presence of an epitaxial CdS or ZnS shell enhances the PL intensity significantly. The recent report on $\text{Ge}_{1-x}\text{Sn}_x/\text{CdS}$ core/shell QDs with 6-11 nm core size claim an enhancement in PL intensity.

However, the larger core size QDs resulted a broad-band IR PL with no size (8–11 nm) or composition ($x = 5\text{--}25\%$) dependent tunability. As this dissertation study focused on 3-6 nm alloy QDs, upon successful core-shelling, it is possible to probe tunable PL across the samples ($x = 1.5\text{--}20.6\%$) and to achieve brighter PL. Added advantage with $\text{Ge}_{1-x}\text{Sn}_x$ core and epitaxial growth of CdS or ZnS shell is that there is a potential to incorporate more Sn ($>20.6\%$) by allowing increase in particle size (>6 nm) will also. Another way to induce PL in samples with Sn content, is to effectively reduce the particle size within 4.5 nm for which strong size confinement effects will be expected. The size control in high Sn concentration ($x>5.6\%$) samples can be achieved through careful manipulation of reaction parameters such as concentration of surfactant (HDA) and/or reducing agent (BuLi).

Temperature dependent (295 K and 15 K) time-resolved PL experiments were performed on solid samples to understand carrier relaxation pathways and the origin of NIR PL. At room temperature (295 K), the PL range was 1.62-1.31 eV with decay lifetimes of 80-111 ns due to the thermal energy makes bright excitonic states accessible, resulting in faster recombination rates. In contrast, the PL decays at low temperature (15 K) are much slower with lifetimes of 8-11 μs owing to combined effect of surface trap states and dark-bright exciton splitting in QDs. In addition, nearly an order of magnitude increases in PL intensities at 15 K when compare to the those at 295 K suggests a dominant role of nonradiative recombination at increased temperatures. Interestingly, the PL peak position as a function of Sn content show a systematic red-shift at 15 K when compare to 295 K. The PL splitting energy (ΔE) of 15 K and 295 K is systematically increasing from 30-56 meV as decrease in Sn content from 4.2-3.5%. On the contrary, ~ 2 nm $\text{Ge}_{1-x}\text{Sn}_x$ alloy

QDs show an opposite trend, the visible PL peaks at room temperature are blue-shifted compared to those at 15 K by 35-50 meV for 5.5-12.5% Sn. In the case of ~2 nm QDs, the PL splitting energy is systematically increasing from 30-50 meV as increase in Sn content from 5.5-12.5%. It will be interesting to study the fundamental differences between both visible and NIR PL sets to understand the temperature dependent PL peak shifts. Overall, 3.3-5.9 nm alloy QDs expanded the optical range to NIR.

In chapter 5, we have successfully produced different tin phosphides in nanoscale for the first time. Owing to lack of proper synthetic methodology which could provide the control over size and crystal phase of tin phosphides weren't explored for their full potential in optical, photocatalytic, thermoelectric, and Li-/Na- ion battery applications. In order to produce tin phosphide nanoparticles, we have explored all the possible Sn (SnCl_2 , SnBr_2 , SnI_2 , $\text{Sn}(\text{OAc})_2$, and SnI_4) and P (TOP, TBP, and $(\text{TMSi})_3\text{P}$) precursors. Some combinations weren't fruitful in reacting Sn and P at atomic level, while the other produced either single phase/mixed phase or β -Sn (tetragonal Sn) with less to no control over size of the particles. The success was achieved with a combination of relatively slow decomposing SnI_4 as Sn source and highly reactive $(\text{TMSi})_3\text{P}$ as P precursor.

We have developed a generalized colloidal synthetic approach for the production of size, shape, and phase controlled, narrowly disperse rhombohedral Sn_4P_3 , hexagonal SnP, and trigonal Sn_3P_4 NPs. By adjusting the key reaction parameters such as nucleation and growth temperature, stoichiometry of SnI_4 and $(\text{TMSi})_3\text{P}$ precursors, and concentration of additional coordinating solvents (TBP or TOP) the control over crystal structure and morphology was achieved. It is important to note that both TBP and TOP are potential P-sources in various metal phosphides, but in this synthesis they both as

additional coordinating solvent, induced long range crystallinity in short range crystalline samples. In the presence of TBP, metal-rich rhombohedral Sn_4P_3 NCs were produced at 180 °C whereas with no use of TBP, larger, amorphous to partially crystalline Sn_4P_3 NPs were achieved at the same temperature. The amount of TBP is also critical to achieve single phase nanocrystals and 4 mM of TBP is found to be optimal for the synthesis of phase pure Sn_4P_3 NCs at 180 °C. By changing the reaction temperature to 250 °C, narrowly disperse, highly reproducible hexagonal SnP NCs with wider tunability of sizes were produced with no use of TBP. With a significant reduction in the reaction temperature to 100 °C, a smaller, quantum confined trigonal Sn_3P_4 NPs were produced in the presence of TBP. The P-rich trigonal Sn_3P_4 NPs exhibit size-tunable energy gaps (1.38 – 0.88 eV for 3.0 ± 0.4 – 8.6 ± 1.8 nm). The energy gaps obtained were significantly blue shifted compared to bulk theoretical bandgap (0.83 eV) indicate size confinement effects. There is a potential to expand this optical absorption window from NIR to visible by reducing the particle size below 3 nm. Apart from PXRD and HRTEM data, we have utilized XPS to probe surface and core of the as synthesized NPs. In addition, the formal charges obtained from XPS analysis indicate Sn possess stable Sn^{2+} and Sn^{4+} oxidation states across three phases. To investigate the phase stability of tin phosphide NPs, a systematic annealing study has been carried out. Trigonal-to-hexagonal phase transition is achieved at 250 °C via rhombohedral intermediate phase at 180 °C.

This colloidal synthetic approach can be extended to produce other anisotropic nanostructures of tin phosphides as well. By doing so, structure and size/shape dependent charge storage, photocatalytic, and thermoelectric properties will be studied effectively. To produce tin phosphide nanostructures, one potential way to explore the

utilization of TBP at 180 °C and 250 °C for longer growth times. Since 3 out of 4 stable tin phosphides are synthesized using this wet chemical approach, the remaining P-rich phase (trigonal SnP₃) can also be produced with a systematic investigation, mainly by employing more (>3% (TMSi)₃P) at temperature higher than 250 °C.

Theoretical studies suggest that hexagonal SnP is also a semiconductor, however with the 12-20 nm particle sizes we couldn't probe the experimental energy gaps, due to possibly (1) minimum size confinement effects and/or (2) onset cut off due to detector limitation (energy gaps below 0.68 eV could not be measured). However, with effective control over hexagonal SnP nanocrystal size potentially below 10 nm could induce size confinement effects.

References

- (1) Trindale, T. O.; O'Brien, P.; Pickett, N. L. Nanocrystalline Semiconductors: Synthesis, Properties, and Perspectives. *Chem. Mater.* **2001**, *13*, 3843-3858.
- (2) Quinten, M. Optical Properties of Nanoparticle Systems. *Wiley-VCH Verlag & Co.: Germany* **2011**.
- (3) Claeys, C. S., E. Germanium-Based Technologies From Materials to Devices. *Elsevier: Oxford, UK* **2007**, p 449.
- (4) Sze, S. M. Physics of Semiconductor Devices. 2nd ed.; *John Wiley & Sons* **1981**, *New York, NY*.
- (5) Smith, A. M.; Nie, S. Semiconductor Nanocrystals: Structure, Properties, and Band Gap Engineering. *Acc. Chem. Res.* **2010**, *43*, 190– 200.
- (6) Ganguly, S.; Kazem, N.; Danielle, C.; Kauzlarich, S. M. Colloidal Synthesis of an Exotic Phase of Silicon: The BC8 Structure. *J. Am. Chem. Soc.* **2014**, *136*, 1296–1299.
- (7) Franklin, A. D. Nanomaterials in Transistors: From High-performance to Thin-film Applications. *Science* **2015**, *349*, 10.
- (8) Klajn, R.; Bishop, K. J. M.; Fialkowski, M.; Paszewski, M.; Campbell, C. J.; Gray, T. P.; Grzybowski, B. A. Plastic and Moldable Metals by Self-Assembly of Sticky Nanoparticle Aggregates. *Science* **2007**, *316*, 261-264.
- (9) Ragan, R.; Min, K. S.; Atwater, H. A. Direct Energy Gap Group IV Semiconductor Alloys and Quantum Dot Arrays in $\text{Sn}_x\text{Ge}_{1-x}/\text{Ge}$ and $\text{Sn}_x\text{Si}_{1-x}/\text{Si}$ Alloy Systems. *Mater. Sci. Eng.* **2001**, *79*, 1937-1940.
- (10) Sun, X.; Liu, J.; Kimerling, L. C.; Michel, J. Direct Gap Photoluminescence of n-type Tensile-Strained Ge-on-Si. *Appl. Phys. Lett.* **2009**, *95*, 011911/1-011911/3.

- (11) Eckhardt, C.; Hummer, K.; Kresse, G. Indirect-to-Direct Gap Transition in Strained and Unstrained $\text{Sn}_x\text{Ge}_{1-x}$ Alloys *Phys. Rev. B* **2014**, *89*, 165201/1-165201/9.
- (12) Carencu, S.; Portehault, D.; Boissière, C.; Mézailles, N.; Sanchez, C. Nanoscaled Metal Borides and Phosphides: Recent Developments and Perspectives. *Chem. Rev.* **2013**, *113*, 7981–8065.
- (13) Liu, J. J.; Yang, W. T.; Li, Y. C.; Fan, L. Z. L., Y. F. Electrochemical Studies of the Effects of the Size, Ligand and Composition on the Band Structures of CdSe, CdTe and their Alloy Nanocrystals. *Phys. Chem. Chem. Phys.* **2014**, *16*, 4778-4788.
- (14) Zaikina, J. V.; Kovnir, K. A.; Sobolev, A. N.; Presniakov, I. A.; Kytin, V. G.; Kulbachinskii, V. A.; Olenev, A. V.; Lebedev, O. I.; Van Tendeloo, G.; Dikarev, E. V.; Shevelkov, A. V. Highly Disordered Crystal Structure and Thermoelectric Properties of Sn_3P_4 . *Chem. Mater.* **2008**, *20*, 2476– 2483.
- (15) Guo, Y.; Rowland, C. E.; Schaller, R. D.; Vela, J. NearInfrared Photoluminescence Enhancement in Ge/CdS and Ge/ZnS Core/Shell Nanocrystals; Utilizing IV/II-VI Semiconductor Epitaxy. *ACS Nano* **2014**, *8*, 8334–8343.
- (16) Alivisatos, A. P. Semiconductor Clusters, Nanocrystals, and Quantum Dots. *Science* **1996**, *271*, 933-937.
- (17) Steigerwald, M. I.; Brus, L. E. Semiconductor Crystallites: A Class of Large Molecules. *Acc. Chem. Res.* **1990**, *23*, 183-188.
- (18) Prabakar, S.; Shiohara, A.; Hanada, S.; Fujioka, K.; Yamamoto, K.; Tilley, R. D. Size Controlled Synthesis of Germanium Nanocrystals by Hydride Reducing Agents and Their Biological Applications. *Chem. Mater.* **2010**, *22*, 482-486.

- (19) Nolan, B. M.; Chan, E. K.; Zhang, X.; Muthuswamy, E.; Benthem, K. v.; Kauzlarich, S. M. Sacrificial Silver Nanoparticles: Reducing Ge_2 To Form Hollow Germanium Nanoparticles by Electroless Deposition. *ACS Nano* **2016**, *10*, 5391–5397.
- (20) Mader, K. A.; Baldereschi, A.; Vonkanel, H. Band-structure and Instability of $\text{Ge}_{1-x}\text{Sn}_x$ Alloys. *Solid State Commun.* **1989**, *69*, 1123-1126.
- (21) Gupta, S.; Chen, R.; Huang, Y.-C.; Kim, Y.; Sanchez, E.; Harris, J. S.; Saraswat, K. C. Highly Selective Dry Etching of Germanium over Germanium-Tin ($\text{Ge}_{1-x}\text{Sn}_x$): A Novel Route for $\text{Ge}_{1-x}\text{Sn}_x$ Nanostructure Fabrication. *Nano Lett.* **2013**, *13*, 3783-3790.
- (22) Chen, R.; Lin, H.; Huo, Y.; Hitzman, C.; Kamins, T. I.; Harris, J. S. Increased Photoluminescence of Strain-Reduced, High-Sn Composition $\text{Ge}_{1-x}\text{Sn}_x$ Alloys Grown by Molecular Beam Epitaxy. *Appl. Phys. Lett.* **2011**, *99*, 181125/1-181125/3.
- (23) Gupta, S.; Magyari-Koepe, B.; Nishi, Y.; Saraswat, K. C. Achieving Direct Band Gap in Germanium through Integration of Sn Alloying and External Strain. *J. Appl. Phys.* **2013**, *113*, 073707/1-073707/7.
- (24) Lee, M.-H.; Liu, P.-L.; Hong, Y.-A.; Chou, Y.-T.; Hong, J.-Y.; Siao, Y.-J. Electronic Band Structures of $\text{Ge}_{1-x}\text{Sn}_x$ Semiconductors: A First Principles Density Functional Theory Study. *J. Appl. Phys.* **2013**, *113*, 063517/1-063517/5.
- (25) Fan, J.; Chu, P. K. Group IV Nanoparticles: Synthesis, Properties, and Biological Applications. *Small* **2010**, *6*, 2080-2098.
- (26) Lavine, C. F.; Ewald, A. W. 2-Band Galvanomagnetic Effects In Gray Tin. *J. Phys. and Chem. Solids* **1971**, *32*, 1121-1140.

- (27) Cheng, T. H.; Peng, K. L.; Ko, C. Y.; Chen, C. Y.; Lan, H. S.; Wu, Y. R.; Liu, C. W.; Tseng, H. H. Strain-enhanced Photoluminescence From Ge Direct Transition. *Appl. Phys. Lett.* **2010**, *96*, 211108/1- 211108/3.
- (28) Lin, H.; Chen, R.; Lu, W.; Huo, Y.; Kamins, T. I.; Harris, J. S. Investigation of the Direct Band Gaps in $\text{Ge}_{1-x}\text{Sn}_x$ Alloys with Strain Control by Photoreflectance Spectroscopy. *Appl. Phys. Lett.* **2012**, *100*, 102109/1-102109/4.
- (29) He, G.; Atwater, H. A. Synthesis of Epitaxial $\text{Sn}_x\text{Ge}_{1-x}$ Alloy Films by Ion-Assisted Molecular Beam Epitaxy *Appl. Phys. Lett.* **1996**, *68*, 664-666.
- (30) D'Costa, V. R.; Cook, C. S.; Birdwell, A. G.; Littler, C. L.; Canonico, M.; Zollner, S.; Kouvetakis, J.; Menendez, J. Optical Critical Points of Thin-Film $\text{Ge}_{1-y}\text{Sn}_y$ Alloys: A Comparative $\text{Ge}_{1-y}\text{Sn}_y\text{Ge}_{1-x}\text{Si}_x$ Study. *Phys. Rev. B* **2006**, *73*, 125207/1-125207/6.
- (31) Esteves, R. J. A.; Ho, M. Q.; Arachchige, I. U. Nanocrystalline Group IV Alloy Semiconductors: Synthesis and Characterization of $\text{Ge}_{1-x}\text{Sn}_x$ Quantum Dots for Tunable Bandgaps. *Chem. Mater.* **2015**, *27*, 1559-1568.
- (32) Ramasamy, K.; Kotula, P. G.; Fidler, A. F.; Brumbach, M. T.; Pietryga, J. M.; Ivanov, S. A. $\text{Sn}_x\text{Ge}_{1-x}$ Alloy Nanocrystals: A First Step toward Solution-Processed Group IV Photovoltaics. *Chem. Mater.* **2015**, *27*, 4640–4649.
- (33) Ellingson, R. J.; Beard, M. C.; Johnson, J. C.; Yu, P. R.; Micic, O. I.; Nozik, A. J.; Shabaev, A.; Efros, A. L. Highly Efficient Multiple Exciton Generation in Colloidal PbSe and PbS Quantum Dots. *Nano Lett.* **2005**, *5*, 865-871.
- (34) Zaoui, A.; Ferhat, M.; Certier, M.; Khelifa, B.; Aourag, H. Optical properties of GeSn and SiSn. *Infrared Phys. Technol.* **1996**, *37*, 483-487.

- (35) Biswas, S.; Doherty, J.; Saladukha, D.; Ramasse, Q.; Majumdar, D.; Upmanyu, M.; Singha, A.; Ochalski, T.; Morris, M. A.; Holmes, J. D. Non-equilibrium Induction of Tin in Germanium: Towards Direct Bandgap $\text{Ge}_{1-x}\text{Sn}_x$ Nanowires. *Nat. Commun.* **2016**, *7*, 1-12.
- (36) Nguyen, T. T. N.; He, J. L. Preparation of Titanium Monoxide Nanopowder by Low-energy Wet Ball-milling. *Adv. Powder Technol.* **2016**, *27*, 1868-1873.
- (37) Enayati, M. H.; Mohamed, F. A. Application of Mechanical Alloying/Milling for Synthesis of Nanocrystalline and Amorphous Materials. *Int. Mater. Rev.* **2014**, *59*, 394-416.
- (38) Ismail, R. A.; Sulaiman, G. M.; Abdulrahman, S. A. Preparation of Iron Oxide Nanoparticles by Laser Ablation in DMF Under Effect of External Magnetic Field. *Int. J. Mod. Phys. B* **2016**, *30*, 1650094/1- 1650094/8.
- (39) D'Costa, V. R.; Fang, Y.-Y.; Tolle, J.; Kouvetakis, J.; Menendez, J. Tunable Optical Gap at a Fixed Lattice Constant in Group-IV Semiconductor Alloys *Phys. Rev. Lett.* **2009**, *102*, 107403/1-107403/4.
- (40) Boztug, C.; Sanchez-Perez, J. R.; Cavallo, F.; Lagally, M. G.; Paiella, R. Strained-Germanium Nanostructures for Infrared Photonics. *ACS Nano* **2014**, *8*, 3136-3151.
- (41) Walling, M. A.; Novak, J. A.; Shepard, J. R. E. Quantum Dots for Live Cell and In Vivo Imaging *Int. J. Mol. Sci.* **2009**, *10*, 441-491.
- (42) Tallapally, V.; Esteves, R. J. A.; Nahar, L.; Arachchige, I. U. Multivariate Synthesis of Tin Phosphide Nanoparticles: Temperature, Time, and Ligand Control of Size, Shape, and Crystal Structure. *Chem. Mater.* **2016**, *28*, 5406-5414.

- (43) Gao, X.; Esteves, R. J.; Luong, T. T. H.; Jaini, R.; Arachchige, I. U. Oxidation-Induced Self-Assembly of Ag Nanoshells into Transparent and Opaque Ag Hydrogels and Aerogels. *J. Am. Chem. Soc.* **2014**, *136*, 7993–8002.
- (44) Nahar, L.; Esteves, R. J. A.; Hafiz, S.; Özgür, Ü.; Arachchige, I. U. Metal-Semiconductor Hybrid Aerogels: Evolution of Optoelectronic Properties in a Low Dimensional CdSe/Ag Nanoparticle Assembly *ACS Nano* **2015**, *9*, 9810–9821.
- (45) Muthuswamy, E.; Savithra, G. H. L.; Brock, S. L. Synthetic Levers Enabling Independent Control of Phase, Size, and Morphology in Nickel Phosphide Nanoparticles. *ACS Nano* **2011**, *5*, 2402-2411.
- (46) Arachchige, I. U.; Brock, S. L. Highly Luminescent Quantum-Dot Monoliths. *J. Am. Chem. Soc.* **2007**, *129*, 1840-1841.
- (47) Demchenko, D. O.; Tallapally, V.; Esteves, R. J. A.; Hafiz, S.; Nakagawara, T. A.; Arachchige, I. U.; Özgür, Ü. Optical Transitions and Excitonic Properties of Ge_{1-x}Sn_x Alloy Quantum Dots. *J. Phys. Chem. C* **2017**, *121*, 18299–18306.
- (48) Thanh, N. T. K.; Maclean, N.; Mahiddine, S. Mechanisms of Nucleation and Growth of Nanoparticles in Solution. *Chem. Rev.* **2014**, *114*, 7610-7630.
- (49) Esteves, R. J. A.; Hafiz, S.; Demchenko, D. O.; Ozgur, U.; Arachchige, I. U. Ultra-Small Ge_{1-x}Sn_x Quantum Dots with Visible Photoluminescence. *Chem. Commun.* **2016**, *52*, 11665–11668.
- (50) Hafiz, S. A.; Esteves, R. J. A.; Demchenko, D. O.; Arachchige, I. U.; Özgür, Ü. Energy Gap Tuning and Carrier Dynamics in Colloidal Ge_{1-x}Sn_x Quantum Dots. *J. Phys. Chem. Lett.* **2016**, *7*, 3295–3301.

- (51) Boote, B. W.; Men, L.; Andaraarachchi, H. P.; Bhattacharjee, U.; Petrich, J. W.; Vela, J.; Smith, E. A. Germanium–Tin/Cadmium Sulfide Core/Shell Nanocrystals with Enhanced Near-Infrared Photoluminescence. *Chem. Mater.* **2017**, *29*, 6012–6021.
- (52) Brock, S. L.; Perera, S. C.; Stamm, K. L. Chemical Routes for Production of Transition-Metal Phosphides on the Nanoscale: Implications for Advanced Magnetic and Catalytic Materials. *Chem.—Eur. J.* **2004**, *10*, 3364–3371.
- (53) Liu, S.; Zhang, H.; L., X.; L., M. Synthesis of Hollow Spherical Tin Phosphides (Sn₄P₃) and their High Adsorptive and Electrochemical Performance. *J. Cryst. Growth.* **2016**, *438*, 31-37.
- (54) Li, D.; Senevirathne, K.; Aquilina, L.; Brock, S. L. Effect of Synthetic Levers on Nickel Phosphide Nanoparticle Formation: Ni₅P₄ and NiP₂. *Inorg. Chem.* **2015**, *54*, 7968-7975.
- (55) Popczun, E. J.; McKone, J. R.; Read, C. G.; Biacchi, A. J.; Wiltrout, A. M.; Lewis, N. S.; Schaak, R. E. Nanostructured Nickel Phosphide as an Electrocatalyst for the Hydrogen Evolution Reaction. *J. Am. Chem. Soc.* **2013**, *135*, 9267–9270.
- (56) Yoon, K. Y.; Jang, Y.; Park, J.; Hwang, Y.; Koo, B.; Park, J.-G.; Hyeon, T. J. Synthesis of Uniform-Sized Bimetallic Iron–Nickel Phosphide Nanorods. *Solid State Chem.* **2008**, *181*, 1609-1613.
- (57) Park, J.; Koo, B.; Yoon, K., Y.; Hwang, Y.; Kang, M.; Park, J.-G.; Hyeon, T. Generalized Synthesis of Metal Phosphide Nanorods via Thermal Decomposition of Continuously Delivered Metal–Phosphine Complexes Using a Syringe Pump. *J. Am. Chem. Soc.* **2005**, *127*, 8433-8440.

- (58) Moreau, L.; Ha, D.; Zhang, H.; Hovden, R.; Muller, D. A.; Robinson, R. D. Defining Crystalline/Amorphous Phases of Nanoparticles through X-ray Absorption Spectroscopy and X-ray Diffraction: The Case of Nickel Phosphide. *Chem. Mater.* **2013**, *25*, 2394– 2403
- (59) Seker, F.; Meeker, K.; Kuech, T. F.; Ellis, A. B. Surface Chemistry of Prototypical Bulk II-VI and III-V Semiconductors and Implications for Chemical Sensing. *Chem. Rev.* **2000**, *100*, 2505-2536.
- (60) Callejas, J. F.; McEnaney, J. M.; Read, C. G.; Crompton, J. C.; Biacchi, A. J.; Popczun, E. J.; Gordon, T. R.; Lewis, N. S.; Schaak, R. E. Electrocatalytic and Photocatalytic Hydrogen Production from Acidic and Neutral-pH Aqueous Solutions Using Iron Phosphide Nanoparticles. *ACS Nano* **2014**, *8*, 11101– 11107.
- (61) Lubber, E. J.; Mobarok, M. H.; Buriak, J. M. Solution-Processed Zinc Phosphide (α -Zn₃P₂) Colloidal Semiconducting Nanocrystals for Thin Film Photovoltaic Applications. *ACS Nano* **2013**, *7*, 8136– 8146.
- (62) Mobarok, M. H.; Lubber, E. J.; Bernard, G. M.; Peng, L.; Wasylshen, R. E.; Buriak, J. M. Phase-Pure Crystalline Zinc Phosphide Nanoparticles: Synthetic Approaches and Characterization. *Chem. Mater.* **2014**, *26*, 1925–1935.
- (63) Brock, S. L.; Senevirathne, K. Recent Developments in Synthetic Approaches to Transition Metal Phosphide Nanoparticles for Magnetic and Catalytic Applications. *J. Solid State Chem.* **2008**, *181*, 1552-1559.
- (64) Miao, S.; Hickey, S. G.; Rellinghaus, B.; Waurisch, C.; Eychmüller, A. Synthesis and Characterization of Cadmium Phosphide Quantum Dots Emitting in the Visible Red to Near-Infrared. *J. Am. Chem. Soc.* **2010**, *132*, 5613– 5615.

- (65) Ho, M. Q.; Esteves, R. J. A.; Kerdarnath, G.; Arachchige, I. U. Size-Dependent Optical Properties of Luminescent Zn₃P₂ Quantum Dots *J. Phys. Chem. C* **2015**, *119*, 10576-10584.
- (66) Lin, J. H.; Zhang, H.; Cheng, X.-L.; Miyamoto, Y. Single-Layer Group IV-V and Group V-IV-III-VI Semiconductors: Structural Stability, Electronic Structures, Optical Properties, and Photocatalysis. *Phys. Rev. B* **2017**, *96*, 1-12.
- (67) Kim, Y.; Kim, Y.; Choi, A.; Woo, S.; Mok, D.; Choi, N.-S.; Jung, Y. S.; Ryu, J. H.; Oh, S. M.; Lee, K. T. Tin Phosphide as a Promising Anode Material for Na-Ion Batteries. *Adv. Mater.* **2014**, *26*, 4139-4144.
- (68) Kovnir, K. A.; Kolen'ko, Y. V.; Ray, S. L., J.; Watanabe, T.; Itoh, M.; Yoshimura, M.; Shevelkov, A. V. A Facile High-yield Solvothermal Route to Tin Phosphide Sn₄P₃. *J. Solid State Chem.* **2006**, *179*, 3756–3762.
- (69) Kim, Y. U. L., C. K.; Sohn, H. J.; Kang, T. . Reaction Mechanism of Tin Phosphide Anode by Mechanochemical Method for Lithium Secondary Batteries. *J. Electrochem. Soc.* **2004**, *151*, 933-937.
- (70) Xie, Y.; Su, H.; Li, B.; Qian, Y. Solvothermal Preparation of Tin Phosphide Nanorods. *Mater. Res.* **2000**, *35*, 675–680.
- (71) Donohue, P. C. Synthesis, Structure, and Superconducting Properties of New High-Pressure forms of Tin Phosphide. *Inorg. Chem.* **1970**, *9*, 335-337.
- (72) Su, H. L.; Xie, Y.; Li, B.; Liu, X. M.; Qian, Y. T. A Novel One-Step Solvothermal Route to Nanocrystalline Sn₄P₃. *J. Solid State Chem.* **1999**, *146*, 110-113.
- (73) Devaiah, D.; Reddy, L. H.; Park, S.-E.; Reddy, B. M. Ceria–zirconia Mixed Oxides: Synthetic Methods and Applications. *Catal. Rev.* **2018**, *60*, 177–277.

- (74) Kim, Y.; Hwang, H.; Yoon, C. S.; Kim, M. G.; Cho, J. Reversible Lithium Intercalation in Teardrop-Shaped Ultrafine SnP_{0.94} Particles: An Anode Material for Lithium-Ion Batteries. *J. Adv. Mater.* **2007**, *19*, 92-96.
- (75) Warren, B. E.: *X-ray diffraction*: Dover, New York, 1990.
- (76) Borchert, H.; Shevchenko, E. V.; Robert, A.; Mekis, I.; Kornowski, A.; Grubel, G.; Weller, H. Determination of Nanocrystal Sizes: A Comparison of TEM, SAXS, and XRD Studies of Highly Monodisperse CoPt₃ Particles. *Langmuir* **2005**, *21*, 1931-1936.
- (77) Lee, M. X-Ray Diffraction for Materials Research. *Apple Academic Press Inc.:* Oakville, ON **2016**, p 289.
- (78) Cullity, B. D. Elements of X-ray Diffraction. . *Addison-Wesley Publishing Company, Inc.:* Reading, MA **1956**, P 514.
- (79) Williams, D. B.; Carter, C. B. Transmission Electron Microscopy A Textbook for Materials Science. . *Plenum Press: New York, NY* **1996**, P 729.
- (80) Van Der Heide, P. X-ray Photoelectron Spectroscopy An Introduction to Principles and Practices. . *John Wiley & Sons, Inc.:* Hoboken, NJ **2012**, P 241.
- (81) Devaiah, D.; Smirniotis, P. G. Effects of the Ce and Cr Contents in Fe–Ce–Cr Ferrite Spinels on the High-temperature Water-gas Shift Reaction. *Ind. Eng. Chem. Res.* **2017**, *56*, 1772–1781. .
- (82) Damma, D.; Boningari, T.; Smirniotis, P. G. High-temperature Water-gas Shift Over Fe/Ce/Co Spinel Catalysts: Study of the Promotional Effect of Ce and Co. *Mol. Catal.* **2018**, *451*, 20-32.
- (83) Aroca, R. Surface-Enhanced Vibrational Spectroscopy. *John Wiley & Sons Ltd:* West Sussex, England **2006**, P 233.

- (84) Schenk, G. H.: *Absorption of Light and Ultraviolet Radiation*; Allyn and Bacon Inc.: Boston, 1973.
- (85) Kovalev, D.; Diener, J.; Heckler, H.; Polisski, G.; Künzner, N.; Koch, F. Optical Absorption Cross Sections of Si Nanocrystals. **2000**, *61*, 4485-4487.
- (86) Tsuge, A.; Uwamino, Y.; Ishizuka, T.; Suzuki, K. Quantitative Analysis of Powdery Sample by Diffuse Reflectance Infrared Fourier Transform Spectrometry: Determination of the α -Component in Silicon Nitride. *Appl. Spectrosc.* **1991**, *45*, 1377–1380.
- (87) Nowak, M.; Kauch, B.; Szperlich, P. Determination of Energy Band Gap of Nanocrystalline SbSI Using Diffuse Reflectance Spectroscopy. *Rev. Sci. Instrum.* **2009**, *80*, 046107/1-046107/7.
- (88) Tauc, J.; Grigorovici, R.; Vancu, A. Optical Properties and Electronic Structure of Amorphous Germanium. *Phys. Status Solidi* **1966**, *15*, 627-637.
- (89) Klimov, V. I. Nanocrystal Quantum Dots. *2nd ed.*; Taylor and Francis Group, LLC: Boca Raton, FL **2010**, P 469.
- (90) Crooker, S. A.; Barrick, T.; Hollingsworth, J. A.; Klimov, V. I. Multiple Temperature Regimes of Radiative Decay in CdSe Nanocrystal Quantum Dots: Intrinsic Limits to the Dark-exciton Lifetime. *Appl. Phys. Lett.* **2003**, *82*, 2793-2795.
- (91) Crooker, S. A.; Barrick, T.; Hollingsworth, J. A.; Klimov, V. I. Multiple Temperature Regimes of Radiative Decay in CdSe Nanocrystal Quantum Dots: Intrinsic Limits to the Dark-Exciton Lifetime. *Appl. Phys. Lett.* **2003**, *82*, 2793/1-2793/8.
- (92) Zaera, F. New Advances in the Use of Infrared Absorption Spectroscopy for the Characterization of Heterogeneous Catalytic Reactions. *Chem. Soc. Rev.* **2014**, *43*, 7624–7663.

- (93) Norman, T. J.; Grant, C. D.; Magana, D.; Zhang, J. Z.; Liu, J.; Cao, D. L.; Bridges, F.; Van Buuren, A. Near Infrared Optical Absorption of Gold Nanoparticle Aggregates. *J. phys. Chem. B* **2002**, *106*, 7005-7012.
- (94) Hessel, C. M.; Reid, D.; Panthani, M. G.; Rasch, M. R.; Goodfellow, B. W.; Wei, J.; Fujii, H.; Akhavan, V.; Korgel, B. A. Synthesis of Ligand-Stabilized Silicon Nanocrystals with Size-Dependent Photoluminescence Spanning Visible to Near-Infrared Wavelengths. *Chem. Mater.* **2012**, *24*, 393-401.
- (95) Ruddy, D. A.; Johnson, J. C.; Smith, E. R.; Neale, N. R. Size and Bandgap Control in the Solution-Phase Synthesis of Near-Infrared-Emitting Germanium Nanocrystals. *ACS Nano* **2010**, *4*, 7459-7466.
- (96) Beard, M. C.; Knutsen, K. P.; Yu, P.; Luther, J. M.; Song, Q.; Metzger, W. K.; Ellingson, R. J.; Nozik, A. J. Multiple Exciton Generation in Colloidal Silicon Nanocrystals. *Nano Lett.* **2007**, *7*, 2506-2512.
- (97) Vaughn, D. D., II.; Schaak, R. E. Synthesis, Properties and Applications of Colloidal Germanium and Germanium-based Nanomaterials. *Chem. Soc. Rev.* **2013**, *42*, 2861-2879.
- (98) Nam, D.; Sukhdeo, D. S.; Gupta, S.; Kang, J.-H.; Brongersma, M. L.; Saraswat, K. C. Study of Carrier Statistics in Uniaxially Strained Ge for a Low-Threshold Ge Laser. *IEEE J. Sel. Topics Quantum Electron.* **2014**, *20*, 1500107/1- 1500107/7.
- (99) Sueess, M. J.; Geiger, R.; Minamisawa, R. A.; Schiefler, G.; Frigerio, J.; Chrastina, D.; Isella, G.; Spolenak, R.; Faist, J.; Sigg, H. Analysis of Enhanced Light Emission from Highly Strained Germanium Microbridges *Nat. Photonics* **2013**, *7*, 466-472.

- (100) Tolle, J.; Chizmeshya, A. V. G.; Fang, Y.-Y.; Kouvetakisa, J.; D'Costa, V. R.; Hu, C.-W.; Menéndez, J.; Tsong, I. S. T. Low Temperature Chemical Vapor Deposition of Si-Based Compounds via $\text{SiH}_3\text{SiH}_2\text{SiH}_3$: Metastable SiSn/GeSn/Si (100) Heteroepitaxial Structures. *Appl. Phys. Lett.* **2006**, *89*, 231924/1-231924/3.
- (101) Bhargava, N.; Coppinger, M.; Gupta, J. P.; Wielunski, L.; Kolodzey, J. Lattice Constant and Substitutional Composition of GeSn Alloys Grown by Molecular Beam Epitaxy *Appl. Phys. Lett.* **2013**, *103*, 041908/1-041908/4.
- (102) Wang, B.; Ouyang, G.; Yang, Y. H.; Yang, G. W. Anomalous Thermal Stability of Cubic Tin Confined in a Nanotube. *Appl. Phys. Lett.* **2007**, *90*, 121905/1-121905/7.
- (103) Yahyaoui, N.; Sfina, N.; Lazzari, J.-L.; Bournel, A.; Said, M. Wave-function engineering and absorption spectra in $\text{Si}_{0.16}\text{Ge}_{0.84}/\text{Ge}_{0.94}\text{Sn}_{0.06}/\text{Si}_{0.16}\text{Ge}_{0.84}$ strained on relaxed $\text{Si}_{0.10}\text{Ge}_{0.90}$ type I quantum well. *J. Appl. Phys.* **2014**, *115*, 033109/1-033109/9.
- (104) Liu, L.; Liang, R.; Wang, J.; Xu, J. Investigation on the Effective Mass of $\text{Ge}_{1-x}\text{Sn}_x$ Alloys and the Transferred-electron Effect. *Appl. Phys. Express* **2015**, *8*, 031301/1-031301/4.
- (105) Seifner, M. S.; Hernandez, S.; Bernardi, J.; Romano-R, A.; Sven Barth, S. Pushing the Composition Limit of Anisotropic $\text{Ge}_{1-x}\text{Sn}_x$ Nanostructures and Determination of Their Thermal Stability. *Chem. Mater.* **2017**, *29*, 9802–9813.
- (106) Kittel, C. Introduction to Solid State Physics, 8th ed. *Wiley: Hoboken, NJ*, **2005**, P 50.
- (107) Seifner, M. S.; Biegger, F.; Lugstein, A.; Bernardi, J.; Barth, S. Microwave-Assisted $\text{Ge}_{1-x}\text{Sn}_x$ Nanowire Synthesis: Precursor Species and Growth Regimes. *Chem. Mater.* **2015**, *27*, 6125–6130.

- (108) Barth, S.; Seifnera, M. S.; Bernardib, J. Microwave-assisted Solution–liquid–solid Growth of Ge_{1-x}Sn_x Nanowires with High Tin Content. *Chem. Commun.* **2015**, *51*, 12282-12285.
- (109) Biswas, S.; Doherty, J.; Saladukha, D.; Ramasse, Q.; Majumdar, D.; Upmanyu, M.; Singha, A.; Ochalski, T.; Morris, M. A.; Holmes, J. D. Non-equilibrium Induction of Tin in Germanium: Towards Direct Bandgap Ge_{1-x}Sn_x Nanowires. *Nat. Commun.* **2016**, *7*, 11405/1-11405/6.
- (110) Tabatabaei, K.; Lu, H.; Nolan, B. M.; Cen, X.; McCold, C. E.; Zhang, X.; Brutchey, R. L.; Benthem, K. V.; Hihath, J.; Kauzlarich, S. M. Bismuth Doping of Germanium Nanocrystals through Colloidal Chemistry. *Chem. Mater.* **2017**, *29*, 7353–7363.
- (111) Herd, S. R.; Chaudhari, P.; Brodsky, M. H. Metal Contact Induced Crystallization in Films of Amorphous Silicon and Germanium. *J. Non-Cryst. Solids* **1972**, *7*, 309-327.
- (112) Vaughn II, D. D.; Bondi, J. F.; Schaak, R. E. Colloidal Synthesis of Air-Stable Crystalline Germanium Nanoparticles with Tunable Sizes and Shapes. *Chem. Mater.* **2010**, *22*, 6103–6108.
- (113) Borchert, H.; Shevehenko, E. V.; Robert, A.; Mekis, I.; Kornowski, A.; Grubel, G.; Weller, H. Determination of Nanocrystal Sizes: A Comparison of TEM, SAXS, and XRD Studies of Highly Monodisperse CoPt₃ Particles. *Langmuir* **2005**, *21*, 1931-1936.
- (114) Chizmeshya, A. V. G.; Bauer, M. R.; Kouvetakis, J. Experimental and Theoretical Study of Deviations from Vegard's Law in the Sn_xGe_{1-x} System. *Chem. Mater.* **2003**, *15*, 2511–2519.

- (115) Volodin, V. A.; Marin, D. V.; Sachkov, V. A.; Gorokhov, E. B.; Rinnert, H.; Vergnat, M. Applying an Improved Phonon Confinement Model to the Analysis of Raman Spectra of Germanium Nanocrystals. *J. Exp. Theor. Phys.* **2014**, *118*, 65-71.
- (116) Oh, K. S.; Yang, K.-W.; Kim, H. T.; Lee, H.; Lee, J. C.; Sohn, Y.-S. Size Control of Crystalline Germanium Nanoparticles Using Inductively Coupled Nonthermal Plasma. *J. Nanoelectron. Optoelectron.* **2013**, *8*, 571–574.
- (117) Kalebaila, K. K.; Georgiev, D. G.; Brock, S. L. Synthesis and Characterization of Germanium Sulfide Aerogels. *J. Non-Cryst. Solids* **2006**, *352*, 232-240.
- (118) Devaiah, D.; Tsuzuki, T.; Boningari, T.; Smirniotisc, P. G.; Reddy, B. M. $\text{Ce}_{0.80}\text{M}_{0.12}\text{Sn}_{0.08}\text{O}_{2-\delta}$ (M = Hf, Zr, Pr, and La) Ternary Oxide Solid Solutions with Superior Properties for CO Oxidation. *RSC Adv.* **2015**, *5*, 30275-30285
- (119) Chandrappa, G. T.; Livage, J. Synthesis and Characterization of Mo-Oxide Nanoribbons. *Synth. React. Inorg., Met.-Org., Nano-Met. Chem.* **2006**, *36*, 23-28.
- (120) Biacchi, A. J.; Vaughn, D. D.; Schaak, R. E. Synthesis and Crystallographic Analysis of Shape-Controlled SnS Nanocrystal Photocatalysts: Evidence for a Pseudotetragonal Structural Modification. *J. Am. Chem. Soc.* **2013**, *135*, 11634-11644.
- (121) Olofsson, O. X-Ray Investigations of the Tin-Phosphorus System *Acta Chem. Scand.* **1970**, *24*, 1153-1162.
- (122) Katz, G.; Kohn, J. A.; Broder, J. D. Crystallographic Data for Tin Monophosphide. *Acta Cryst.* **1970**, *10*, 607-609.
- (123) Gullman, J. The Crystal Structure of SnP. *J. Solid State Chem.* **1990**, *87*, 202-207.

- (124) Gullman, J.; Olofsson, O. The Crystal Structure of SnP₃ and a Note on the Crystal Structure of GeP₃. *J. Solid State Chem.* **1972**, *5*, 441-445.
- (125) Liu, S.; Li, S.; Li, M.; Yan, L.; Li, H. Synthesis of Tin Phosphides (Sn₄P₃) and their High Photocatalytic Activities. *New J. Chem.* **2013**, *37*, 827-833.
- (126) Li, Z.; Ding, J.; Mitlin, D. Tin and Tin Compounds for Sodium Ion Battery Anodes: Phase Transformations and Performance. *Acc. Chem. Res.* **2015**, *48*, 1657-1665.
- (127) Qian, J.; Xiong, Y.; Cao, Y.; Ai, X.; Yang, H. Synergistic Na-Storage Reactions in Sn₄P₃ as a High-Capacity, Cycle-stable Anode of Na-Ion Batteries. *Nano Lett.* **2014**, *14*, 1865–1869.
- (128) Li, W.; Chou, S. L.; Wang, J. Z.; Kim, J. H.; Liu, H. K.; Dou, S. X. Sn₄+xP₃ @ Amorphous Sn-P Composites as Anodes for Sodium-Ion Batteries with Low Cost, High Capacity, Long Life, and Superior Rate Capability. *Mater.* **2014**, *26*, 4037– 4042.
- (129) Ueda, A.; Nagao, M.; Inoue, A.; Hayashi, A.; Seino, Y.; Ota, T.; Tatsumisago, M. Electrochemical Performance of All-Solid-State Lithium Batteries with Sn₄P₃ Negative Electrode. *J. Power Sources* **2013**, *244*, 597-600.
- (130) Ritscher, A. S., C.; Ipser, H. Pressure Dependence of the Tin-Phosphorus Phase Diagram. *Monatsh. Chem.* **2012**, *143*, 1593-1602.
- (131) Aso, K. K., H.; Hayashi, A.; Tatsumisago, M. SnP_{0.94} Active Material Synthesized in High-Boiling Solvents for All-Solid-State Lithium Batteries. *J. Ceram. Soc. Jpn.* **2010**, *118-124*.
- (132) Huang, M.; Feng, P. Y. Stability and electronic properties of Sn₃P₄. *Phys. Rev. B* **2004**, *70*, 184116/1-184116/5.

- (133) Binions, R.; Blackman, C. S.; Carmalt, C. J.; O'Neill, S. A.; P., P. I.; Molloy, K. C.; L., A. Tin Phosphide Coatings from the Atmospheric Pressure Chemical Vapour Deposition of SnX_4 (X=Cl or Br) and $\text{PR}_x\text{H}_{3-x}$ (R=Cyhex or phenyl). *Polyhedron* **2002**, *21*, 1943-1947.
- (134) Wang, J.; Johnston-Peck, A. C.; Tracy, J. B. Nickel Phosphide Nanoparticles with Hollow, Solid, and Amorphous Structures. *Chem. Mater.* **2009**, *21*, 4462– 4467.
- (135) Huang, Z.; Chen, Z.; Chen, Z.; Lv, C.; Meng, H.; Zhang, C. Ni_{12}P_5 Nanoparticles as An Efficient Catalyst for Hydrogen Generation via Electrolysis and Photoelectrolysis. *ACS Nano* **2014**, *8*, 8121-8129.
- (136) Wang, R.; Ratcliffe, C. I.; Wu, X.; Voznyy, O.; Tao, Y.; Yu, K. Magic-Sized Cd_3P_2 II–V Nanoparticles Exhibiting Bandgap Photoemission. *J. Phys. Chem.* **2009**, *113*, 17979–17982.
- (137) McPartlin, M.; Melen, R. L.; Naseri, V.; Wright, D. S. Formation and Rearrangement of SnII Phosphanediide Cages. *Chem.–Eur. J.* **2010**, *16*, 8854-8860.
- (138) Lu, X.; Tuan, H.-Y.; Chen, J.; Li, Z.-Y.; Korgel, B. A.; Xia, Y. Mechanistic Studies on the Galvanic Replacement Reaction between Multiply Twinned Particles of Ag and HAuCl_4 in an Organic Medium. *J. Am. Chem. Soc.* **2007**, *129*, 1733-1742.
- (139) Mobarok, M. H.; Buriak, J. M. Elucidating the Surface Chemistry of Zinc Phosphide Nanoparticles Through Ligand Exchange. *Chem. Mater.* **2014**, *26* 4653–4661.
- (140) Eckerlin, P. K., W. . Preparation and Crystal Structure of So-Called Sn_4P_3 Phases. *Z Anorg. Allg. Chem.* **1968**, *363*, 1-9.
- (141) Häggström, L.; Gullman, J.; Ericsson, T.; Wäppling, R. Mössbauer study of tin phosphides. *J. Solid State Chem.* **1975**, *13*, 204-207.

- (142) Lippens, P. E. Interpretation of the Sn-119 Mossbauer Isomer Shifts in Complex Tin Chalcogenides. *Phys. Rev. B* **1999**, *60*, 4576-4586.
- (143) Pan, Y. L., Y.; Liu, C. Nanostructures Nickel Phosphide Supported on Carbon Nanospheres: Synthesis and Application as an Efficient Electrocatalyst for Hydrogen Evolution. *J. Power Sources* **2015**, *285*, 169-177.
- (144) Kravchyk, K.; Protesescu, L.; Bodnarchuk, M. I.; Krumeich, F.; Yarema, M.; Walter, M.; Guntlin, C.; Kovalenko, M. V. Monodisperse and Inorganically Capped Sn and Sn/SnO₂ Nanocrystals for High-Performance Li-Ion Battery Anodes. *J. Am. Chem. Soc.* **2013**, *135*, 4199– 4202.

Vita

Venkatesham Tallapally

☎ 804-332-7094; ✉ tallapallyv@vcu.edu
520 West Franklin Street, Richmond, VA 23220

EDUCATION

Ph. D. Inorganic and Materials Chemistry (GPA 3.5/4.0), August 2018

Virginia Commonwealth University, Richmond, Virginia.

Dissertation: Colloidal Synthesis and Photophysical Characterization of Group IV Alloy and Group IV-V Semiconductor Nanocrystals: $\text{Ge}_{1-x}\text{Sn}_x$ and Sn-P Quantum Dots.

M. Sc. Organic Chemistry (GPA 3.8/4.0), May 2008, Kakatiya University, India.

B. Sc. Chemistry (GPA 3.9/4.0), May 2006, Osmania University, India.

RESEARCH EXPERIENCE AND PROFESSIONAL APPOINTMENTS

Graduate Research Assistant

Jan 2014 – Aug 2018

Advisor: Prof. Indika U. Arachchige

Virginia Commonwealth University, Richmond VA

- Developed a synthetic methodology to produce 3-6 nm $\text{Ge}_{1-x}\text{Sn}_x$ alloy quantum dots with composition tunable near-IR photoluminescence for potential applications in bio-imaging and sensing studies.
- Worked independently on wet chemical synthesis of ultra-small (2-3 nm) $\text{Ge}_{1-x}\text{Sn}_x$ alloy quantum dots with visible photoluminescence including optical characterization via steady-state and ultrafast spectroscopy and computational electronic structure simulations.
- Successfully investigated the role of SnCl_2 as tin source and co-reducing agent to produce $\text{Ge}_{1-x}\text{Sn}_x$ alloy nanostructures for Li-ion battery applications.
- Established the first colloidal synthetic strategy for trigonal Sn_3P_4 , rhombohedral Sn_4P_3 , and hexagonal SnP nanostructures with control over size, shape, and crystal structure.
- Developed a synthetic methodology for production of nanostructured Ni_3Mo , Ni_4Mo , and $\text{Ni}_{2-x}\text{Mo}_x\text{P}$ catalysts for photo-/electro-chemical water splitting.

Graduate Lab Managing

Jan 2014 – Aug 2018

Virginia Commonwealth University

- Trained junior graduate (3) and undergraduate (3) students in air-free colloidal synthesis of Group IV nanocrystals and metal phosphide nanostructures.
- Mentored undergraduate students (2) in directed study (CHEM 392) and independent study (CHEM 492) research courses.
- Trained users in diffuse reflectance spectroscopy, powder X-ray diffraction and assisted them to collect transmission electron microscopy images with their samples.
- Maintained LabStar glovebox, oversaw chemicals ordering and laboratory waste management.

Teaching Assistant

Aug 2013 – Aug 2016

Virginia Commonwealth University

- Performed laboratory sessions for inorganic, organic and general chemistry undergraduate classes.
- Graded weekly lab reports, exams, and prepared quizzes for lab sessions.
- Proctored and graded exams for undergraduate courses.

Research Fellow

June 2011- July 2013

Osmania University, India

- Worked with synthetic organic chemistry projects to produce heterocyclic compounds (isoindoline-1,3-dione and imidazoquinoline).
- Handled collaborative projects with senior students in synthesizing medicinal value organic compounds (ranolazine and crisaborole).

Research Assistant

May 2009- Dec 2010

RK Pharmaceuticals, India

- Experienced in handling air and moisture sensitive reagents under inert atmospheric conditions.
- Extensively experienced in interpreting IR, H^1 NMR, C^{13} NMR and Mass spectra of organic compounds produced via organic and organometallic syntheses.

Lecturer in Chemistry

June 2008- May 2009

Kakatiya University, India

- Taught elements of symmetry, coordination chemistry, organic reagents, stereochemistry, natural products, medicinal chemistry, pericyclic chemistry, and photochemistry for undergraduate and masters students.
- Conducted lab work on the synthesis of organic molecules and isolation of natural products.

FELLOWSHIPS & AWARDS

- Altria Graduate Assistantship in Chemistry (\$18,000, tuition, and fees) for academic year 2017-2018.
- Junior Research Fellowship (JRF) in chemical sciences, Council of Scientific and Industrial Research-University Grants Commission, India (2010).
- National Eligibility Test (NET) Lectureship Award in Chemical Sciences, Council of Scientific and Industrial Research-University Grants Commission, India (2010).
- Merit Scholarship in M.Sc. (Chemistry), Kakatiya University (2008).

INSTRUMENTATION AND TECHNICAL SKILLS

Extensively experienced in materials characterization via

- Powder X-Ray Diffraction (PXRD)
- Transmission Electron Microscopy (TEM)
- Scanning Electron Microscopy (SEM)
- X-Ray Photoelectron Spectroscopy (XPS)
- UV-visible-near IR spectroscopy
- Diffuse Reflectance Spectroscopy (DRS)
- Raman Spectroscopy
- Nuclear Magnetic Resonance (NMR)
- Infrared (IR) Spectroscopy.

DATA ANALYSIS

- Origin, Excel, MS office, and Chem draw

PUBLICATIONS

- (1) **Tallapally, V.**; Nakagawara, T. A.; Demchenko, D. O.; Özgür, Ü.; Arachchige, I. U. Ge_{1-x}Sn_x Alloy Quantum Dots with Composition-Tunable Energy Gaps and Near-Infrared Photoluminescence. *Nanoscale* **2018**, *Under Review*.
- (2) Demchenko, D. O.; **Tallapally, V.**; Esteves, R. J. A.; Hafiz, S.; Nakagawara, T. A.; Arachchige, I. U.; Özgür, Ü. Optical Transitions and Excitonic Properties of Ge_{1-x}Sn_x Alloy Quantum Dots. *J. Phys. Chem. C* **2017**, *121*, 18299–18306.
- (3) **Tallapally, V.**; Esteves R. J. A.; Nahar, L.; Arachchige, I. U. “Multivariate Synthesis of Tin Phosphide Nanoparticles: Temperature, Time, and Ligand Control of Size, Shape, and Crystal Structure” *Chem. Mater.* **2016**, *28*, 5406–5414.
(This article was one of the most read and downloaded in 2016)

PRESENTATIONS AT CONFERENCES

- (1) **Tallapally, Venkatesham.**; Esteves, Richard J.; Arachchige, Indika U. “Size, Shape, and Phase Control Synthesis of Crystalline and Amorphous Tin Phosphide Nanoparticles” 252nd ACS National Meeting, Philadelphia, PA, August 21-25, 2016, *oral presentation*.
- (2) **Tallapally, Venkatesham.**; Esteves, Richard J.; Arachchige, Indika U. “Tunable Size and Shape Control Synthesis of Crystalline and Amorphous Tin Phosphide Nanoparticles” 252nd ACS National Meeting, Philadelphia, PA, August 21-25, 2016, *poster presentation*.

REFERENCES

- (1) Dr. Indika U Arachchige, Director of Graduate Recruitment and Associate Professor, Department of Chemistry, Virginia Commonwealth University, Phone: +1 (804)-828-6855, Email: iuarachchige@vcu.edu.
- (2) Dr. Ram B. Gupta, Associate Dean for Research and Professor of Chemical and Life Science Engineering, Virginia Commonwealth University, Phone: +1 (334)-707-2013, Fax: (804) 828-9866, Email: rbgupta@vcu.edu.
- (3) Dr. Julio C Alvarez, Associate Professor and Director of Graduate Studies, Department of Chemistry, Virginia Commonwealth University, Phone: +1 (804)-828-3521, Email: jcalvarez2@vcu.edu.
- (4) Dr. Heather R. Lucas, Assistant Professor of Chemical Biology, Division of Inorganic Chemistry, Virginia Commonwealth University, Phone: +1 (804)-828-7512, Email: hrlucas@vcu.edu.